UNIVERSITY OF CALIFORNIA
RIVERSIDE

Electronic and Vibrational Properties of Low-Dimensional Heterogeneous Systems: Materials and Device Perspectives

A Dissertation submitted in partial satisfaction
of the requirements for the degree of

Doctor of Philosophy

in

Electrical Engineering

by

Mahesh Raj Neupane

March 2015

Dissertation Committee:
Dr. Roger K. Lake, Chairperson
Dr. Alexander A. Balandin
Dr. Ashok Mulchandani

The Dissertation of Mahesh Raj Neupane is approved:

Committee Chairperson

University of California, Riverside

Acknowledgments

First and foremost, I would like to express my sincere gratitude and appreciation to my supervisor Prof. Roger K. Lake for guiding me through my research work in the field of material and device modeling. Without his constant mentoring, this work would not be possible. I would also like to thank my lab-mates, Dr. Khalid Ashraf, Dr. Nicolas Burque, Dr. Mohammmed Khayer, Dr. K. Masum Habib, Dr. Somia Sylvia, Dr. Sonia Ahasan and Tom Helander for their friendship and support during my first few years. I would also like to thank Shan Shan, Supgeng Ge, Yi Zhou, Protik Das, and Soumya Biswas. A special thanks to Gen Yin, and Darshana Wickramaratne for joining me in our weekly group therapy sessions. Honestly, these sessions were very productive and fruitful. A sincere thanks goes to my collaborators: Dr. Rajib Rahman, Dr. Ferdows Zahid, Dr. Steven Cronin, Dr. Oliver Monti, Dr. Peter Sutter, Dr. Mihail Sigalas, Aris Sigorous, Rohan Dhall, Leah Kelly, and Robert Ionescu. Without their help and guidance, I would not have achieved all research goals. I would also like to thank my colleagues at the U.S. Army Research Lab, especially to my mentor Tanya and my supervisor Jan, for their support during the thesis writing process. I would like to thank my family for supporting me to pursue my dreams, particularly my brother for all the sacrifices he has done for my higher education, and also instilling confidence on me. Within all of their limitations they provided me with the best possible support. Last but not least, I would like to

thank my wife and son for being there with me during the emotional phases of my PhD journey.

The text of this dissertation, in part or in full, is a reprint of the material as it appears in the following journals and/or proceedings:

- SPIE Proceedings [1]. Reprinted with permission from [1]. © [2011] Society of Photo-Optical Instrumentation Engineering (SPIE).
- Journal of Applied Physics [2]. Reprinted with permission from [2]. © [2011] American Institute of Physics.
- Journal of Applied Physics [3]. Reprinted with permission from [3]. © [2011] American Institute of Physics.
- PCCP [4]. Reprinted with permission from [4]. © [2014] Royal Society of Physics (RSC).
- ACS Nano [5]. Reprinted with permission from [5]. © [2014] American Chemical Society (ACS).
- IEEE Nano [6]. Reprinted with permission from [6]. © [2014] IEEE.
- PCCP [7]. Reprinted with permission from [7]. © [2015] Royal Society of Physics(RSC).
- Advanced Materials [8]. Reprinted with permission from [8]. © [2015] John Wiley and Sons.

The co-author Roger K. Lake, listed in the above publications directed and supervised the research which forms the basis for this dissertation. The remaining co-authors listed provided technical expertise and support as collaborators. This

work is supported in part by FAME, one of the six centers of STARnet, a Semiconductor Research Corporation program sponsored by MARCO and DARPA, and the Department of Education GAAN Fellowship.

To my grandparents

ABSTRACT OF THE DISSERTATION

Electronic and Vibrational Properties of Low-Dimensional Heterogeneous Systems: Materials and Device Perspectives

by

Mahesh Raj Neupane

Doctor of Philosophy, Graduate Program in Electrical Engineering
University of California, Riverside, March 2015
Dr. Roger Lake, Chairperson

Due to the aggressive miniaturization of memory and logic devices, the current technologies based on silicon have nearly reached their ultimate size limit. One method to maintain the trend in device scaling observed by Moore's law is to create a heterostructure from existing materials and utilize the underlying electronic and optical properties. Another radical approach is the conceptualization of a new device design paradigm. The central objective of this thesis is to use both of these approaches to address issues associated with the aggressive scaling of memory and logic devices such as leakage current, leakage power, and minimizing gate oxide thickness and threshold voltage. In the first part of the dissertation, an atomistic, empirical tight binding method was used to perform a systematic investigation of the effect of physical (shape and size), and material dependent (heterogenity and strain) properties on the device related electronic and optical properties of the Germanium (Ge)/Silicon (Si) nanocrystal (NC) or quantum dot (QD). The device parameters pertaining to Ge-core/Si-shell NC-based floating gate memory and optical devices such as confinement energy, retention lifetimes and optical intensities are captured and analyzed.

For both the memory and optical device applications, regardless of the shape and size, the Ge-core is found to play an important role in modifying the confinement energy and carrier dynamics. However, the variation in the thickness of outer Si-shell layer had no or minimal effect on the overall device parameters.

In the second part of the dissertation, we present a systematic study of the effect of atomistic heterogeneity on the vibrational properties of quasi-2D systems and recently discovered 2D materials such as graphene, while investigating their applicabilities in future devices applications. At first, we investigate the vibrational properties of an experimentally observed misoriented bilayer graphene (MBG) system, a heterostructure where two graphene layers are rotated by a relative angle, using molecular dynamic (MD) method. The MD method includes temperature dependent phonon anharmonicity which correctly predicts misorientation angle (θ) dependent low-energy breathing modes, and establishes a correlation between the experimentally observed low frequency Raman modes. Using a similar method, we have also conceptualized a phononic circuit using quasi-2D materials constructed from group IV elements of the periodic table, mainly carbon (C), Germenium (Ge) and Silicon (Si) by modifying the phononic bandgap (PBG). We successfully demonstrated the realization of various phononic interconnects such as nano-scaled phononic resonators, waveguides and switches by simultaneously introducing defects of different types at various locations on the 3C-SiC and 3C-GeSi surfaces.

Finally, we have conceptualized a novel low power device called TMDC Excitonic Field Effect Transistor (TExFET), using other 2D materials namely, hexagonal boron nitride (h-BN) and Transition Metal Dichalcogenides (TMDC) by creating a TMDC/h-BN/TMDC heterstructure system. The characteristics of the TExFET device is explored with a combination of the variational principle and the mean field approximation. Our variational principle based calculation of the unscreened inter-

layer Coulombic forces in the TMDC/h-BN/TMDC system gives us an upper bound exciton gap in the order of 100 meV, mainly due to the isotropic electron and hole effective masses of the TMDC layers. Due to an effective exciton radius in the range of 2 nm, the TExFET could also be a device of choice for maintaining the device scaling trend. Further, when the effect of static screening between the layers is considered during self-consistent calculations, the interaction strength is reduced by $\sim 40\%$ to 60 meV, producing an excitonic gap suitable for low temperature, low power device applications.

Contents

Approval iii

Acknowledgments vi

Dedication vii

Abstract viii

1 Rationale 1

1.1 Introduction 1

1.1.1 Memory Devices 1

1.1.2 Two-Dimensional Materials 5

1.1.3 Next-generation Devices 9

1.2 Background and Motivation 16

1.3 Objective 24

1.4 Layout 25

2 Theoretical Methods 27

2.1 Atomistic Tight Binding Method 27

2.1.1 Overview 27

2.1.2 NEMO-3D 28

2.2 Classical Molecular Dynamics 32
2.2.1 Overview 32
2.2.2 Harmonic and Anharmonic Approximation 36
2.2.3 Fluctuation Dissipation Theory for Phonon Dispersion 38
2.3 First Principle Calculation- Density Functional Theory (DFT) 40

3 Electronic properties of spherical Ge-core/Si-shell nanocrystals 44
3.1 Introduction and Motivation 44
3.2 Objectives 46
3.3 Model and Theory 46
3.4 Results and Discussion 50
3.4.1 Hole confinement characteristics 50
3.4.2 Decay constant and tunneling mass 54
3.4.3 Hole Lifetimes 55
3.5 Conclusion 59

4 Electronic states of experimentally observed dome-shaped Ge/Si Nanocrystal with crescent-shaped Ge-cores 62
4.1 Introduction and Motivation 62
4.2 Objectives 63
4.3 Model and Theory 63
4.4 Results and Analysis 67
4.4.1 Carrier confinement characteristics 67
4.4.2 Confinement effects on the electronic states 68
4.4.3 Thermionic lifetime 69
4.5 Conclusion 71

5 Effect of Strain on the Electronic and Optical Properties of Ge/Si Dome Shaped Nanocrystal **74**

5.1 Introduction and motivation 74

5.2 Structure and Method 77

5.3 Results and Analysis 81

5.3.1 Strain characteristics 81

5.3.2 Electronic Properties 83

5.3.3 Optical Properties 88

5.4 Conclusion 91

6 Vibrational Properties of Misorientated Bilayer Graphene (MBG) system **92**

6.1 Introduction and Motivation 92

6.2 Models and Methods 96

6.3 Results and Discussion 99

6.4 Conclusion 113

7 Nanoscale Phononic Interconnects in THz Frequencies **115**

7.1 Motivation 115

7.2 Models and Methods 118

7.2.1 Models 118

7.2.2 Methods 119

7.2.3 Results and Discussion 122

7.3 Conclusion 136

8 TExFET- A device for future device applications **138**

8.1 Motivation 138

8.2 Model and Methods 140
8.2.1 EMA + Variational principle 142
8.2.2 Mean Field Approximation (MFA) 146
8.3 Results and Discussion 147
8.3.1 Binding energy (E_b) 147
8.3.2 Superfluid gap (Δ_{gap}) 151
8.4 Conclusion 153

9 Conclusion **155**

A Ge/Si QD Laser **196**
A.1 Introduction 196
A.1.1 Optical Properties 197
A.2 Conclusion 205

B Capping and core layer-dependent carrier dynamics on Ge/Si NC memory **207**
B.1 Introduction and Motivation 207
B.2 Model and Methods 208
B.3 Results and Discussion 209
B.4 Conclusion 211

List of Tables

6.1 Γ-centered Phonon Modes of Single Layer Graphene (SLG) 101

6.2 Low-frequency ZO' modes at Γ for MBG supercells 107

8.1 Material parameters used for binding energy calculation 148

8.2 **The effective Bohr radius** η_{min} 151

List of Figures

1.1 (Color online) A schematic of a p-Type Floating Gate Memory (FGM) device. 3

1.2 (Color online)a. A schematic of Ge/Si core-shell NC memory b. Band diagrams of a Si/Ge/Si core-shell memory at the conditions of b) flat band, c) programming, d) erasing, and e) retention. 4

1.3 (Color online) Graphene honeycomb lattice a. Graphene primitve cell containing A and B lattice sites. r_1 and r_2 are the primitve lattice vectors for graphene, b. Graphene Monolyaer formed after extending primitive cell extending x and y directions, and c-d. TEM and SEM images of a single layer Graphene, reproduced with permission from [9].© [2014] Nature 6

1.4 (Color online) 2D Crystal structurse a. Graphene monolayer b. Boron Nitride (BN) monolayer, and c) MoS_2 monolayer with the thickness of 3.16 A^o. Graphene and BN has hexagonal lattice structure. 7

1.5 (Color online) a. Scanning electron microscope image of a phononic crystal for surface acoustic waves, reproduced with permission from [10], © [2006] APS, and b. Phonon frequency vs scaled wave vector in the high symmetry KX direction for BAs (black) and Si (red) with experimental Raman data for BAs (black circles), reproduced with permission from [11], © [2006] APS. BAs has a large PBG, which is absent in Si. Note that the near-zone center acoustic velocities for BAs and Si are similar. However, the three acoustic branches [two transverse (TA1 and TA2) and one longitudinal (LA)] are bunched closer to one another in BAs than are the corresponding branches in Si. 10

1.6 (Color online) Electromagnetic spectrum (**top**). Atomic structures of hBN, MoS2, Black Phosphorous (BP) and graphene are shown in the bottom of the panel, left to right (**middle**). The crystalline directions (x and y) of anisotropic BP are indicated. The possible spectral ranges covered by different materials are indicated using coloured polygons. Bandstructure of single-layer hBN , MoS2 , BP, and graphene (**bottm**), reproduced with permission from [12]. © [2014] APS. 13

1.7 a) TYPE I band alignment b) TYPE II band alignment, and c) TYPE II broken gap band alignment 15

3.1 (Color online) Ge/Si core-shell NC (4 nm Ge-core and 5nm Si-shell around Ge-core). Total number atoms is 63976 (63448 Si atoms and 528 Ge atoms). The lighter gray dots are Si atoms and darker (red) dots are Ge atoms. 47

3.2 (Color online) Energy diagram and wave function distribution in the Ge/Si core-shell NC. The offsets shown in the band edges correspond to the bulk Si and Ge parameters used in the calculations. Confinement will alter the position of the energy levels. Dashed lines show the two different hole escape mechanisms resulting on the two lifetimes, τ_h^{th} and τ_h^T. 48

3.3 (Color online) Quantum confinement energy (ΔE_0 ($\circ$)) and barrier height (Φ_b ($\diamondsuit$)) as a function of Ge-core size. The number associated with each point on the Φ_b curve is the orbital number (n) associated with the barrier height. ΔE_{Ge} ($\square$) is the calculated quantum confinement energy using Eq. (1) from Ref. [13]. 51

3.4 (Color online) Magnitude of the wavefunctions squared plotted for (a) the highest localized state and (b) the highest delocalized state in the Si(5 nm)-Ge(4 nm)-Si(5 nm) NC. The values are taken from a two-dimensional slice through the center of the NC. In this case, $n = 63$. 52

3.5 (Color online) Localized hole effective mass m_w^* in the Ge-core region as a function of Ge-core size. 53

3.6 (Color online) Minimum energy gap (E_g), the valence band maximum E_0 and the conduction band minimum E_{c0}. as a function of the Ge-core size (nm) with a fixed 5 nm Si shell. 54

3.7 (Color online) (a) The magnitude squared of the HLO ($|\psi_0|^2$) plotted versus radial position in the Si shell and the superimposed exponential fit for the NC with a 4 nm Ge-core. (b) Ground state hole tunneling wave vector in the Si shell (κ) versus Ge-core diameter. (c) Parabolic tunneling effective mass (m_b^*) of the ground state hole in the Si-shell as a function of Ge-core size. 56

3.8 (Color online) Direct tunneling lifetime (dashed line) and thermionic lifetime (solid line) versus Ge-core diameter with a 5 nm Si shell. . . . 57

3.9 (Color online) Si shell size versus Ge-core size such that the quantum tunneling lifetime is equal to the thermionic emission lifetime. 57

3.10 Band diagram of the bulk Ge/Si/SiO_2 system. The dashed line illustrates the imaginary dispersion in the SiO_2 bandgap, and the horizontal line shows the energy at which κ_{ox}) is calculated from Eq. (3.7). The short-dashed green line illustrates the thermionic escape rate ($1/\tau_h^{th}$) that provides the attempt rate for quantum tunneling through the SiO_2. 60

3.11 (Color online) Total hole lifetime in the Ge/Si/SiO_2 system at SiO_2 thicknesses of 1, 2 and 3 nm. 61

4.1 (Color online) Front-view (a) and cross-sectional-view (b) of a dome-shaped Ge/Si NC with a Ge-core and Si-cap thickness of 3nm. The base diameter and the inner Si layer height is maintained at 5nm. The total number of atoms is 7696, with 2360 Si atoms in the capping layer, 1960 Ge atoms in the core layer and 3376 Si atoms in the inner layer. The lighter gray (red) dots are Ge atoms and the darker (yellow) dots are Si atoms. (c) Bulk energy level lineups. The energy values shown correspond to the band gap of the bulk Si and Ge materials. The valence and conduction band edges for the Ge and Si materials are labeled as E_V^{Ge} and E_V^{Si}, E_C^{Ge} and E_C^{Si}, respectively. Similarly, the valence band offset is identified as ΔE_V. The dotted arrow shows the thermionic hole escape mechanism with an escape rate of $1/\tau^{th}$. . . . 65

4.2 (Color online) Probability densities of the ground hole state, $|\Psi_0|^2$ (a,b), the lowest electron state, $|\Psi_e|^2$ (c,d), and both states superimposed (e,f). The red (light) and blue (dark) isosurfaces represent maximum and minimum probability densities, respectively. The Ge-core and Si-cap thickness is 3nm. The inner Si layer height and the base diameter are 5nm. The height of the NC is 11nm. In a-d, the two-dimensional cross-section of the probability density is taken through the center of the Ge-core region in the $x-y$ plane at $z = 6.5$nm. In e-f, the two-dimensional cross-section is taken through the center of the base in the $x-z$ plane at $y = 2.5$ nm. 67

4.3 Energy gap (a), and quantum confinement energy (ΔE) (b) as a function of Ge-core and Si-cap thickness. 70

4.4 Energy barrier height (Φ_b) (a), localized hole effective mass (m_w^*) in the Ge-core region (b), and thermionic lifetime (τ^{th}), as a function of Ge-core and Si-cap thickness. 72

5.1 (Color online) One of the simulated Ge/Si dome-shaped NC structures with a 20 nm base diameter (b) and 10 nm overall height (h). a) Front view b) Cross-section view and c) Extracted Ge-core. The base diameters of the simulated structures varies from a minimum value of 5 nm to the maximum value of 45 nm. The NC height is fixed at 10 nm. 75

5.2 (Color online) (a) In-plane strain E_{xx} and (b) out-of-plane strain E_{zz}, plotted along the [001] direction through the center of the NCs. The white and grey backgrounds correspond to the Si and Ge regions, respectively. The three different diameters are indicated in the legends. (c) Average in plane strain $\langle E_{xx} \rangle$ of the Ge and Si atoms. (d) Average out of plane strain $\langle E_{zz} \rangle$ of the Ge and Si atoms. (e) Average biaxial (solid line) and hydrostatic (dotted line) strain of the Ge and Si atoms, as a function of base diameter. 81

5.3 (Color online) Isosurface plots of the hydrostatic (I) and the biaxial (II) strain in a (100) plane cross-section through the NC center for the (a) smallest (5 nm), (b) intermediate (25 nm), and (c) largest (45 nm) dome-shaped Ge/Si NCs. The plane cuts through the Ge/Si interface at the center of the $x-y$ plane. The horizontal scales for the intermediate (b) and the largest (c) NCs are reduced by a factor of 2. 84

5.4 (Color online) Energy levels and optical transitions between the highest occupied state in the Ge core and the excited states in the Si base and cap. 85

5.5 (Color online) Cross sections of the orbitals of the highest occupied state H_0 and the three lowest excited states, E_0, E_1, and E_2, for diameters of 10, 15 and 25 nm. The first three rows are calculated with strain and the lower three rows are calculated without strain. The corresponding energies associated with each state are labeled. 87

5.6 (Color online) Electronic states of dome-shaped Ge/Si NC as a function of base diameter, (a) Energy gap (E_g) for unstrained (solid line) and strained (broken line) case, and (b) Strain induced shift in the occupied state (H_0) and the excited state (E_0) energies. 89

5.7 (Color online) Optical Properties of dome-shaped Ge/Si NCs as a function of base diameter (a) Wave function overlap between first three excited states (E_0, E_1, and E_2) and the ground state (H_0), and (b) Optical intensities between the the ground state H_0 and the excited states E_0, E_1, and E_2. For all the calculated transition intensities, Lorentzian broadening functions with the width of 10 meV are applied. 90

6.1 (Color online) Raman spectra of graphene sheet with different numbers of layers, reproduced with permission from [14]. © [2014] RSC. . . . 93

6.2 (Color online) Simulated models of bilayer graphene system, a. AB-stacked bilayer graphene, b. AA-stacked bilayer graphene, c. Misoriented Bilayer Graphene (MBG), d. Top view of MBG system illustrating Moire pattern, and e. MBG superlattice. Note that, MBG system with point-defect is not shown here. 97

6.3 (Color online) Phonon dispersions, a. Phonon dispersion of SLG in $\Gamma \rightarrow M$, b.Phonon dispersion of SLG in $\Gamma \rightarrow K$, and c. Phonon dispersion of AB-stacked bilayer system in $\Gamma \rightarrow M$. 102

6.4 (Color online) Phonon Dispersions for MBG supercell with $\Theta = 21.78°$ (a) and perfectly-aligned supercell (b). Dispersion for MBG supercell is overlaid over the dispersion of the Perfectly-aligned supercell (c), and the out-of-plane breathing modes (ZO') for both the supercells (d) 104

6.5 (Color online) Phonon Dispersions for MBG supercell with $\Theta = 21.7°$ (a), 27.79° (b), 13.17° (c), 9.43° (d), 7.34° (e), and 6° (f) 106

6.6 (Color online) a. Acoustic vibrations in MBG supercell with $\Theta = 21.78°$, and b. Low-energy modes (X) plotted on top of experimental Raman modes (From Pankaj Tharamani) 107

6.7 (Color online) Phonon density of states (PDOS) for AB-stacked bilayer (dotted-green), AA-stacked bilayer (solid-red) and $\Theta = 21^o$ (dotted-black) 109

6.8 (Color online) a. Lattice specific heat capacity C_v vs MBG Supercell size at T = 300K, and b. Relative difference in C_v between AB-stacked bilayer system and AA (dotted-red), $\Theta = 21.7^o$ (solid-blue) and $\Theta = 13^o$ (solid-green) 111

6.9 (Color online) a. Lattice specific heat capacity C_v vs MBG superlattice constructed using MBG with $\Theta = 21.7°$, and b. C_v for a pristine MBG with $\Theta = 21.7°$ (solid-blue) and defective MBG of same angle (dotted blue) 113

7.1 **a)** The primitive cell (triclinic) of the FCC lattice with a diatomic basis AB, where A is Si (Ge) and B is C (Si). **b)** The bulk structure of 3C-SiC, generated by 12 replications of the primitive cell **(a)**, in the x, y and z directions. **c)** The $< 111 >$ surface of SiC. Note that the atoms in the background (dark grey) are also Si atoms. 119

7.2 The TPDOS for (a) bulk GeSi and (b) bulk SiC calculated from the VACF method. 123

7.3 Phonon density of states of the bulk GeSi (a) and SiC (b) systems. The grey curves represent MD simulation results, the solid black curve with the hatched fill pattern represent first-principle results, and (c and d) the partial phonon density of states (PPDOS) of the bulk GeSi (c) and SiC (d) from MD simulations. The PPDOS for the C, Si and Ge atoms are represented with green, hatchet fill pattern and red curves, respectively. 124

7.4 The PPDOS of the <111> surfaces of 3C-GeSi and 3C-SiC. The PPDOS of the (a) Ge-Face, (b) Si-Face of GeSi. The PPDOS of the (c) Si-Face, (d) C-Face of SiC. For all the cases, the green, hatchet fill pattern and red curves correspond to the C, Si and Ge atoms respectively. 126

7.5 PPDOS of isolated substitutional and vacancy defects in the $< 111 >$ surface of 3C-GeSi and 3C-SiC. The PPDOS of the Ge-Face of GeSi surface with (a) a substitutional defect and (c) a single vacancy defect. The PPDOS of the Si-Face of SiC surface with (b) a substitutional defect and (d) a single vacancy defect. Inset on each figure illustrates the configurations for the corresponding case. For all the cases, the PPDOS corresponds to the atoms marked with the yellow arrows. The green, grey and red colors correspond to the C, Si and Ge atoms, respectively. 128

7.6 Atomistic representations of Ge-terminated surfaces of GeSi, with (a) one line, (b) two neighboring lines, and (c) three neighboring lines, with substitutional defects. The red and grey atoms correspond to Ge and Si respectively. d) The PPDOS of the atoms in the waveguides for one (grey), two (red), and three (blue) neighboring lines with vacancy defects. 130

7.7 Vacancy waveguides in the Ge-Face of the GeSi surface, (a) TYPE-S and (c) TYPE-D. PPDOS for the Si and Ge atoms in the TYPE-S (b) and TYPE-D (d) waveguides. The red and grey colors correspond to Ge and Si, respectively. 131

7.8 Illustration of the phonon propagation in complex phononic waveguides, which splits phonons into two paths (phonon-splitters, green circles), or modulates the direction (phonon-benders, dotted black circles). Complex phononic waveguides designed with (a) substitutional defects, and (b) with vacancy defects, in the Ge-Face of GeSi. The grey and red atoms are Si and Ge, respectively. The phonon propagation paths are illustrated using the zigzag lines. 134

7.9 Atomistic representations of a phononic switch designed by adding a Ge adatom (dark red atom marked with a yellow arrow) on the TYPE-S waveguide in the Ge-Face of GeSi. (b) The PPDOS of the Si atom (marked with a black arrow in (a)) that neighbors to the Ge adatom (switch). Note that the resonant peak at 8 THz is suppressed. 135

7.10 Substitutional defects (dark red) inside (a) and near (c) the TYPE-S vacancy waveguides in the Ge-Face of GeSi. The yellow arrow at (c) points to the substitutional defect. b) The PPDOS of the Ge atom marked with a black arrow in the configuration of (a). d) The PPDOS of the Ge atom marked with a black arrow in the configuration of (c). The red and white atoms represent the Ge and Si atoms, respectively, while the dark red atoms represent the substitutional defects (Si$\leftrightarrow$ Ge). 136

8.1 a) Model device architecture with two layers of MoS_2 separated by a thin film of boron nitride (BN). The top monolayer is biased with a positive voltage (V_p) and the bottom monolayer is biased with a negative voltage (V_n). 141

8.2 (Color online) Exciton binding (E_b)energy of homogeneous TMDC layers (a) and heterogenous TMDC layers (b), as a function of sandwiched boron nitride (BN) between two. The E_b of bilayer graphene system is also plotted for comparison and labelled as X. Band alignment of TMDC monolayers taken from Ref. [15] (c). Solid lines are obtained by PBE, and dashed lines are obtained by HSE06. The dotted lines indicate the water reduction (H+/H2) and oxidation (H2O/O2) potentials. The vacuum level is taken as zero reference. 149

8.3 (Color online) Superfluid gap (Δ_{gap}) of homogeneous TMDC layers (a) and heterogenous TMDC layers (b), as a function of sandwiched boron nitride (BN). 152

A.1 (Color online) Magnitude of the modulus squared of the optical matrix element $|M_{total}|^2$ plotted against the Ge core size for (a) unstrained and (b) strained case. The units for $|M_{total}|^2$ is given in eV/c, where c is speed of light. 199

A.2 (Color online) Transition energies (ΔE_{if}), in meV, between lowest electron state and first six highest hole states, as a function of strain and Ge core size (nm), with a fixed Si shell thickness of 5 nm. 201

A.3 (Color online) Transition rates between lowest electron level and first six highest holes states, as a function of strain and the Ge core size (nm) with a fixed 5 nm Si shell. 202

A.4 (Color online) Magnitude of Oscillator strength (OS_{if}) as a function of Ge core size and strain for the lowest electron state (E0) to a)Hole ground state (H0) b) First hole state (H1) c) Second hole state (H2), and d) Third hole state (H3). 203

A.5 (Color online) Lifetimes (a,b) and Current Densities (c,d) as a function of core size and temperature for both unstrained (left) and strained (right) conditions. 205

B.1 (Color online) Front-view (a) and cross-sectional-view (b) of a dome-shaped Ge/Si NC with a Ge-core and Si-cap thickness of 3nm. The base diameter and the inner Si layer height is maintained at 5nm. The lighter gray (red) dots are Ge atoms and the darker (yellow) dots are Si atoms. (c) Bulk energy level lineups. The energy values shown correspond to the band gap of the bulk Si and Ge materials. The valence and conduction band edges for the Ge and Si materials are labeled as E_V^{Ge} and E_V^{Si}, E_C^{Ge} and E_C^{Si}, respectively. Similarly, the valence band offset is identified as ΔE_V. The dotted arrow shows the thermionic hole escape mechanism with an escape rate of $1/\tau^{th}$. . . . 208

B.2 (Color online)(a) Minimum energy gap (E_g) as a function of as a function of Ge core and Si cap thickness. (b) Ground state hole energy (E_h) and Confinement energy (E_c) as a function of Ge core and Si cap thickness. The confinement energy (E_c) is defined as $E_c = E_v$ (Ge) - E_h, where E_v (Ge) is the bulk valence band edge of Ge. (c) Effective mass of hole inside the Ge core layer. 210

B.3 (Color online) (a) Probability densities ($|\psi|^2$) of localized and first delocalized hole states in the Ge core layer of a dome shaped Ge/Si core shell NC with Ge core and Si cap thicknesses of 3 nm and 2.5 nm, respectively. The n in the delocalized probability density represents the index of the first delocalized hole state. (b) The barrier height (ϕ_b) i.e. E_0 E_n, where E_0 is the ground state hole energy and En is the energy of the first delocalized hole states, as a function of Ge core and Si cap thickness.(c) Thermionic lifetime as function of Ge core and Si cap thickness 210

Chapter 1

Rationale

1.1 Introduction

1.1.1 Memory Devices

Since the evolution of the silicon era, semiconductor memory has become an integral component of modern electronic systems, where there is an ever-increasing need for the portable and energy efficient devices. The path followed by the industry to date is roughly governed by the Moore's observation in 1975 that the number of transistors on an integrated chip doubles every two years. His observation, which is now known as Moore's Law, states that a transistors must be scaled to smaller sizes to increase the transistor density which helps in adding more functionality per chip at lower cost. Such scaling laws provide guidelines for defining a smaller transistor with mostly improved or at least similar performance for the next technology node. In order to maintain this scaling trend, applied gate voltage and ratio between the ON and OFF current should be minimized and maximized, respectively. The current International Technology Roadmap for Semiconductors (ITRS) [16] also predicts an

end to the Moore's law, mainly due to the saturation of the applied gate voltage and limitation in the gate oxide thickness. Beyond complementary metal-oxide semiconductors (CMOS), several new approaches to information-processing and data-storage technologies and architectures are emerging to address the time-frame beyond . The miniaturization or down-scaling of devices, both logic and memory, has been aggressively pursued to achieve low power, high speed, and reliable and robust operational features. However, semiconductor memory, more importantly flash memory, scaling is far behind CMOS logic device scaling. Flash memory consists of a compact structure in which the selecting-element and the storage element are merged in an MOS-like structure. Because of the ever increasing scaling need and data retention time requirement of more than ten years, the nonvolatile flash memory (NVM) devices has become indispensable.

Magnetic memory [17], phase change memory [18], molecular memories [19], and floating gate memory [20] are the main types of NVM technology. Among these memory devices, floating gate memory is the only NVM compatible with the current CMOS processing technology. This memory type was first invented by Sze and Khang at Bell Labs in 1967 [21], where the floating gate layer is sandwiched between the control and tunneling oxide layers. The schematic of a floating gate memory device is shown in the Fig. 1.1. In this NVM, the floating gate layer acts as a charge storage or trapping layers, and charges can be stored through program operations and moved back to the substrate by means of erase operations. Floating gate NVM is also more reliable, offers higher density and requires lower production cost, making it a cheaper solution for stand-alone and embedded memory applications. In these devices, the floating gate is programmed by applying a large voltage at the control gate by lowering the potential barrier. Once carriers, electrons for n-type device and holes for the p-type device, are in the floating gate, they will stay in the potential

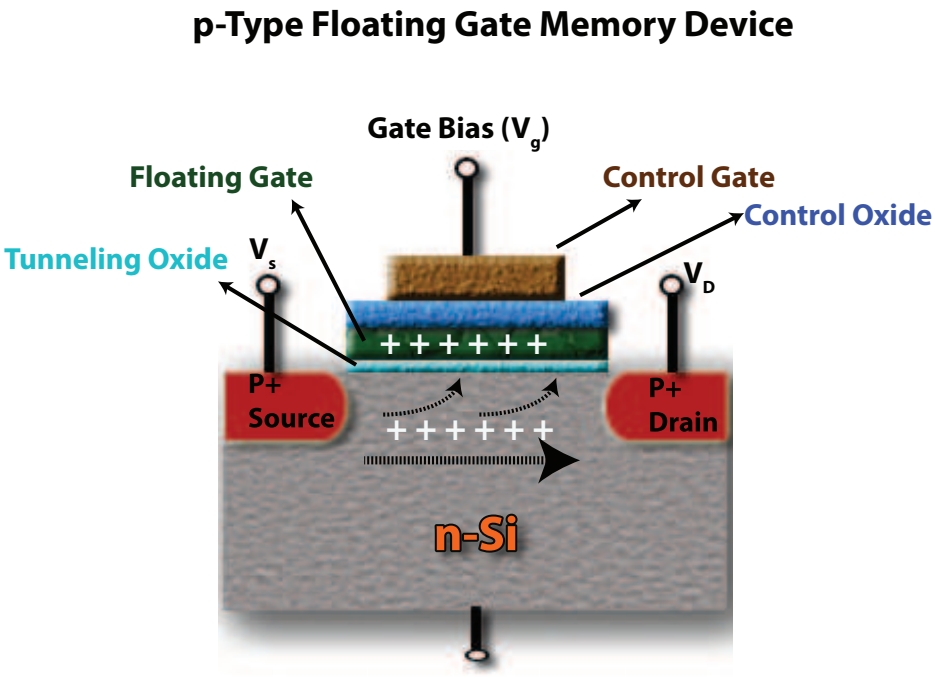

Figure 1.1: (Color online) A schematic of a p-Type Floating Gate Memory (FGM) device.

well formed between the control and gate oxide. The erasing mechanism is achieved by applying large negative (positive) voltage for n-type (p-type) device at the gate, and the electrons (holes) tunnel out by Fowler-Nordheim (FN) tunneling. However, conventional floating gate NVM suffers from physical limitations such as insufficient tunneling oxide thickness from the continual scaling of overall device structure. Since the floating gate, as a charge storing layer, is conductive, it is immune to the charge leakage, resulting in a serious reliability issue for memory applications.

Semiconductor nanocrystal memory is shown to have the potential to replace conventional floating gate flash memory by overcoming these shortcomings in the conventional floating gate non-volatile memory (NVM) [22]. In this type of NVM, nanocrystals (NC) or Quantum Dots (QDs) act as discrete charge storing sites that are embedded within the floating gate layer, as shown in the Fig.1.2

These NCs can confine charges, and exhibit many fascinating atomic-physics phe-

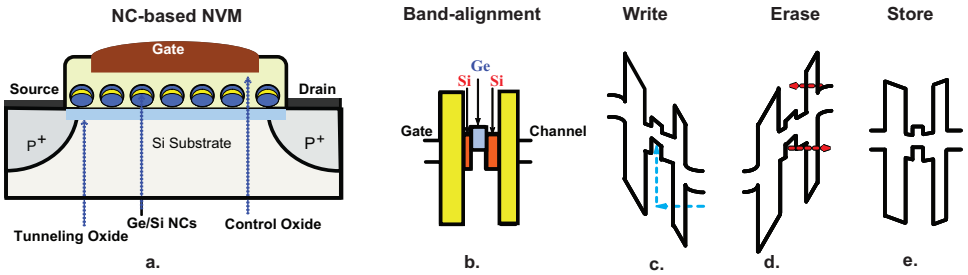

Figure 1.2: (Color online)a. A schematic of Ge/Si core-shell NC memory b. Band diagrams of a Si/Ge/Si core-shell memory at the conditions of b) flat band, c) programming, d) erasing, and e) retention.

nomena in the solid state which can be controlled by varying size, density, and work function. The tunable optical and electrical properties of these nanostructures have been explored and utilized in various applications, such as flash storage memory, quantum computing, and optical communication. In experiment, the key device element, i.e. NCs layer can easily be fabricated at low temperature. Due to the localization of the charge into electrically discrete nodes and thinner tunneling oxide, NC-based NVM devices possess various advantageous properties such as longer retention time and higher endurance as compared to the traditional NVM. Currently, NC-based NVM can be classified into three major categories, determined by the materials used: (i) semiconductor [23], (ii) metal [24], and (iii) high- dielectric [25] nanocrystals. Due to the simple fabrication process and compatibility with the existing semiconductor industry, semiconductor NC-based memory, mainly Si and Ge NCs, are widely being used [20].

Metal-oxide-semiconductor (MOS) nonvolatile memory devices based on nanocrystals (NC), especially using Si as the material for NCs [23], have attracted attention due to their potential to utilize evolutionary nanotechnology, within the existing Si device fabrication schemes. In these memory devices, NC's are embedded in the oxide layer of the MOS memory [26]. Due to the localization of the charge into electrically

discrete nodes and thinner tunneling oxide, these devices possess various advantageous properties. Low-power consumption and high storage density, up to 1 Tbit/inch, can be obtained in comparison with conventional non-volatile flash memories [27]. Further studies of Si NC embedded non-volatile memories (NVM) by Zhao et al. suggested that the magnitudes of valence and/or conduction band offsets between the Si and SiO_2 characterize the amount of leaked charge into the substrate [28]. In order to minimize this leakage charge and to handle the trade-off between programming speed and retention time due to the scaling limitation of the oxide layer in the Si NC embedded memories, Ge/Si core-shell NC based memory devices were first proposed in Ref. [29]. In this device, the Si shell acts as an additional barrier layer during the tunneling of holes confined in the Ge core. The memory characteristics and advantages of using Ge/Si heterostructure as the material for NC will be discussed later.

1.1.2 Two-Dimensional Materials

Low-dimensional materials in general and two-dimensional (2-D) layered materials in particular are interesting from a technological standpoint not only because they provide access to novel physical phenomena, but also because of their unique electrical, optical, mechanical, and chemical properties. Graphene, a sheet of carbon atoms arranged in a honeycomb structure, is a path-breaking 2-D material, which has been proposed as a candidate for the channel material of future electronic devices [30]. An atomistic view of a graphene primitive cell, a thin sheet of monolayer graphene, and images of experimentally observed graphene samples characterized by TEM and SEM [31] are illustrated in Fig. 1.3. Monolayer graphene has a unique linear band structure near its charge neutrality point, and has served as a platform for many studies of two-dimensional physics, including quantum Hall effects [32]. Defect-free

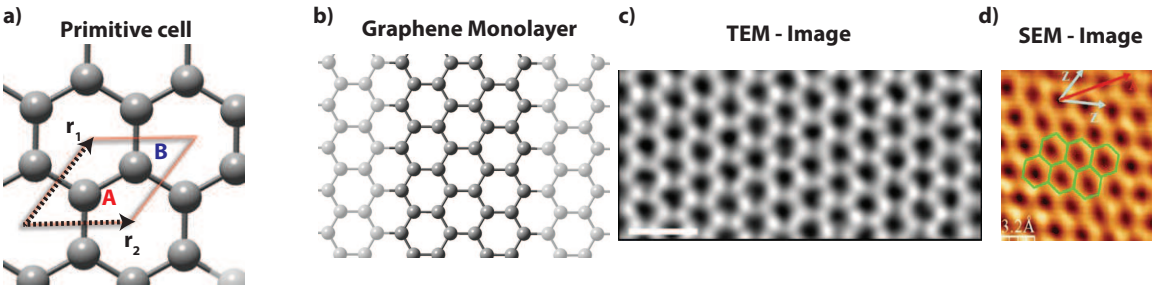

Figure 1.3: (Color online) Graphene honeycomb lattice a. Graphene primitve cell containing A and B lattice sites. r_1 and r_2 are the primitve lattice vectors for graphene, b. Graphene Monolyaer formed after extending primitive cell extending x and y directions, and c-d. TEM and SEM images of a single layer Graphene, reproduced with permission from [9].© [2014] Nature

graphene also exhibits very high carrier mobility [33].

Although graphene has many exceptional electronic, thermoelectric and mechanical properties, lack of an intrinsic bandgap reduces its utility for conventional electronic device applications. In addition to graphene, hexagonal boron nitride (h-BN) (shown in Fig. 1.4.b), and more recently TMDC comprised of MX2 (M = Mo, W, and Sn and X = S, Se, and Te) are receiving an increasing amount of scientific attention as promising candidates for various future nanoelectronic applications [34]. TMDC materials exist in a large number of different polymorphs of MX2, but the basic crystal structure consists of a sheet of metal atoms M, sandwiched by two sheets of chalcogens X. The coordination of the metal can be either trigonal prismatic (D_{3h} symmetry, H) or approximately octahedral (D_{3d} symmetry, T). Atomistic representation of MoS_2, a commonly studied TMDC system, is shown in Fig. 1.4.c.

Due to the weak van der Waals bonding between the chalcogenide planes, these materials can be exfoliated via mechanical [35] or liquid techniques [36] or grown in atomically precise layers using van-der-Waal epitaxy [37]. There is no reconstruction of the chalcogenide layers after exfoliation, and the layers are chemically inert. Thus, single trilayers of high quality transition metal dichalcogenide films can be placed

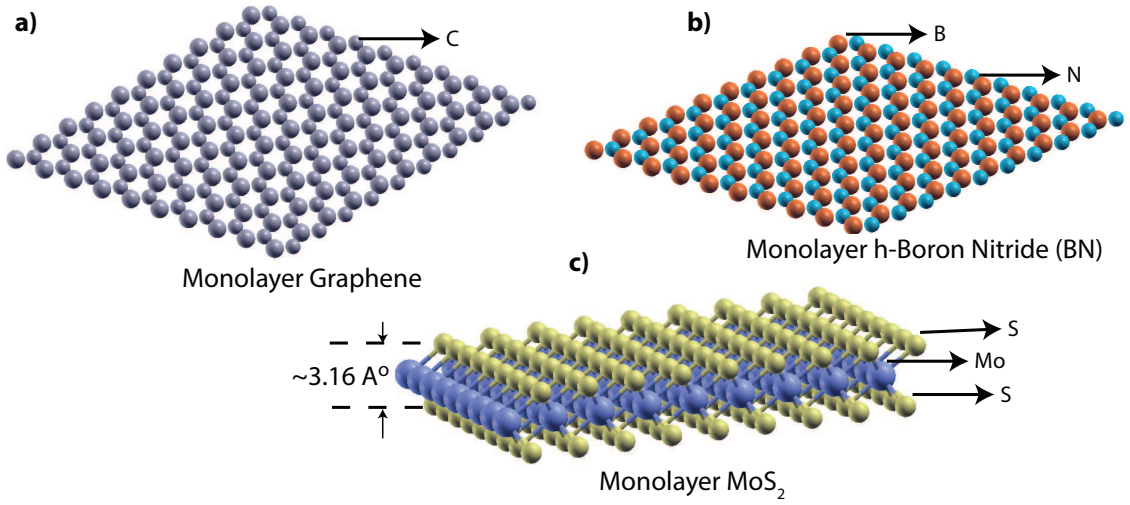

Figure 1.4: (Color online) 2D Crystal structurse a. Graphene monolayer b. Boron Nitride (BN) monolayer, and c) MoS_2 monolayer with the thickness of 3.16 A^o. Graphene and BN has hexagonal lattice structure.

on substrates to be utilized in a range of device applications [38–41]. Unlike other artificial 2D materials, they are typically stable if removed from a supporting substrate. In addition, when these materials are placed on top of a bulk or 2D surface, it interacts with the surface with weak van der Waals interactions, without disrupting its in-plane covalent bonding. It is a dispersive force that acts even between neutral bodies at large separations, and it results from the non-zero dipole-dipole attraction stemming from transient quantum dipole fluctuation. The weak interlayer bonding permits intercalation of metal atoms, ions, or even organic molecule, which can introduce dramatic changes in the physical properties of the host.

Misoriented Bilayer Graphene (MBG) system

A feature common among all 2-D materials consisting of a hexagonal lattice structure is that when layers are stacked together, either by mechanical stacking, chemical vapor deposition (CVD) or epitaxial growth, a relative rotation between the layers is introduced due to inter-layer van-der-Waal (vdW) forces [42–44] In the case of bilayer graphene, misorientation between the two layers produces a misoriented bilayer graphene (MBG) system. In the MBG, it is established that the individual layers with a relative rotation angle greater than 20^o are electronically decoupled [45–48]. An interesting property of MBG from the application point of view is that the inter layer coupling is decreased [49] and the Fermi velocity is reduced, as a function of misorientation angle [50]. Recent theoretical and experimental studies on MBG also suggest that inter-layer resistance between the layers is in the order of several kilo-ohms and are mainly dominated by the phonon-mediated interlayer resistance [51].

An often cited technological roadblock to this scaling trend is the increased levels of power dissipation which lead to self-heating of devices and local hot-spot formations. In semiconducting materials, the thermal conductivity is mainly influenced by

the lattice thermal conductivity. In addition, heat dissipation in transistors occurs in a two-step process in which electrons in the transistor channel emit phonons (a quanta of lattice vibration), that carry the heat away from the active region. The phonon transport mechanisms are of critical importance as they determine the self-heating that occurs within the device. Low-energy acoustic phonon modes are responsible for conducting heat in the low-dimensional materials and devices. The thermal resistance between the layers arises from three-phonon scattering, in which one phonon decays into two or two phonons combine into one, with the strength of the interaction determined by cubic term of the interatomic force constants [52]. The scattering is only possible when each three-phonon process must satisfy momentum and energy conservation. Understanding how the misorientation affects the low-energy acoustic phonon modes in the MBG is essential for widening the applicability of MBG in other applications such as thermal management and as thermoelectric devices. The second part of the dissertation primarily focused on identifying the correlation between the vibrational and associated lattice-dependent thermoelectric properties and the misorientation angle, through a phonon engineering approach. In this of work, the phonon dispersion, phonon density of states and lattice specific heat capacity is determined for a variety of misorientation angles. These values are compared with previously calculated theoretical and experimentally observed values.

1.1.3 Next-generation Devices

Phononics Devices

Phonons are incoherent particles that can be observed as heat and noise, and are usually minimized or removed from the surface. In recent years, however, there has been few efforts on not only creating phonons, but also trapping and making them

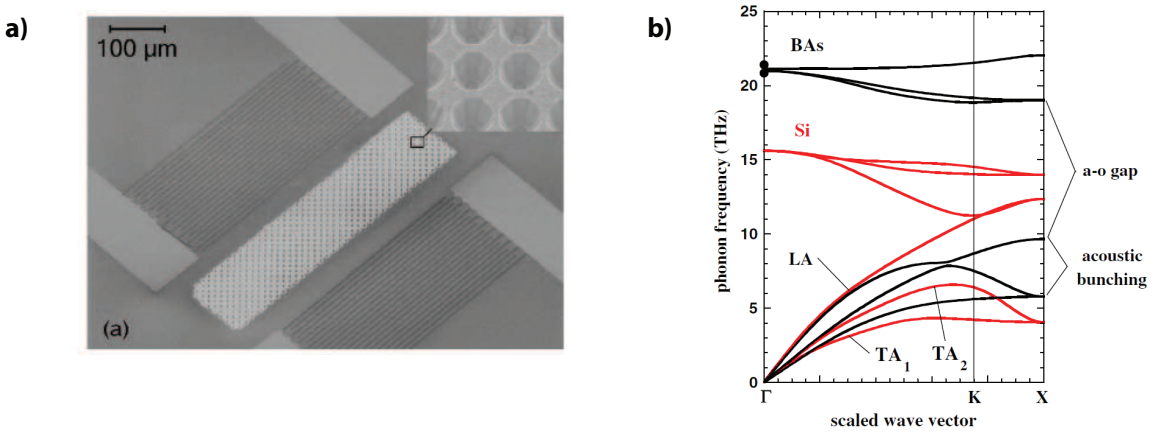

Figure 1.5: (Color online) a. Scanning electron microscope image of a phononic crystal for surface acoustic waves, reproduced with permission from [10], © [2006] APS, and b. Phonon frequency vs scaled wave vector in the high symmetry KX direction for BAs (black) and Si (red) with experimental Raman data for BAs (black circles), reproduced with permission from [11], © [2006] APS. BAs has a large PBG, which is absent in Si. Note that the near-zone center acoustic velocities for BAs and Si are similar. However, the three acoustic branches [two transverse (TA1 and TA2) and one longitudinal (LA)] are bunched closer to one another in BAs than are the corresponding branches in Si.

coherent. Phononics or phonon engineering involves the control and manipulation of phonon interactions and transport in the host crystal known as Phononic Crystal (PnC). PnCs are artificial composite materials made of periodic distribution of inclusions embedded in a matrix with different elastic constants and atomic mass, as shown in the Fig. 1.5a.

Due to periodicity, these materials may exhibit phononic band gaps (PBGs)– a frequency region where no acoustic or elastic phonon propagation is allowed. Even so, the PBG can be tuned by material composition, lattice spacing, crystal-packing arrangement, crystal orientation, and size of the elements comprising the crystal. The widths of PBG, and their locations in the frequency domain, depend on the topology of the unit cell, material-wise or geometry-wise. The opening of PBG due to the material miss-match is illustrated in the Fig. 1.5b. As can be seen in the Fig.

1.5.b, the Boron-Arsenide (BAs) phonon dispersion curve has the combined energy of two acoustic phonons which is often smaller than that of a single optical phonon. The atomic mass of As is $70X$ higher than that of B. The large energy gap comes from this difference in atomic mass between boron and arsenic. Due to the large PBG, the process of optical phonon decaying into two acoustic phonons is forbidden, which results in the large phonon mean free path (MFP). In the silicon (Si), however, the optical phonons decays into the acoustic phonons, while closing the PBG. The scattering events often involve an optical phonon which is a high-frequency vibration of the atoms within a single primitive unit cell, and leads to shorter MFP.

In PnC, phonons travel through the lattice of the host materials as a wave, similar to the way sound passes through the air. The unique dispersion properties can be used to design phononic devices like waveguides, cavities or switches. One of the recent applications of PnC has been a phononic waveguide where the boundaries for the confined phonons are defined using surrounding two-dimensional crystal lattice [53]. Most of the recent work in this area has been using III-V materials (GaAs, AlAs and AlGaAs) at the larger dimension ranging from millimeter to micrometer [54]. With electronic and photonic devices already into the nanoscale, phononic devices and corresponding circuit elements are also needed to scale into the sub-nanometer range in order to become compatible with their electronic and photonic counterparts. We have extended the phonon engineering study in the low dimensional system by designing and analysing phononic circuits in the systems composed of group V elements (Si,Ge, and C) in the periodic table. To create phononic circuit elements such as resonators, waveguides, and switches, isolated and linear substitutional and vacancy defects are created in the $\langle 111 \rangle$ surface of the quasi-2D GeSi and SiC heterogeneous system. Furthermore, the mechanisms behind the creation of phononic components based on defects involve that only evanescent waves are present outside the defect, so

that energy confinement can be guaranteed.

TMDC Excitonic Field Effect Transistor (TExFET)

As the size and speed of the CMOS transistors continue to scale, power dissipation becomes the bottleneck for the scaling trend. Leakage current is the main source of power dissipation and dynamic power loss, and increases exponentially under constant field and the scaled supply voltage. In the conventional MOSFET devices, the switching speed is defined by the order of ON/OFF current ratio which is heavily influenced by the leakage current. To circumvent the issue of leakage current, various unconventional Si-based device designs such as High-K Multigate Field Effect Transistor (HK/MG FET) [55], Homogeneous Junction Field Effect Transistor (HomJFET) [56], Heterogeneous Junction Field Effect Transistor (HetJFET) [57], FinFET [58], and Tunnelling Field Effect Transistor (TFET) [59–61] are being proposed. These device designs provide solution to the problem of leakage current and power dissipation through thinner effective oxide thickness, tighter electrostatic control, and modulation channel doping which might help in short-term device scaling. For a long-term solution to the device scaling problem, a revolutionary solution could be provided by designing devices based on alternative state variables, such as spin, phase, and wave. With the advent of naturally occurring 2D materials such as h-BN and TMDCs, the field of device engineering is being served with the opportunity and challenge of designing scaled devices with them. The electronic structure of TMDs strongly depends on the number of valence electrons in the metal and its coordination environment. Most of the semiconductor TMDs in the bulk form have an indirect energy gap in the energy range between 1.2 to 1.7 eV. However, a single layer TMDCs has a large direct energy gap, a feature which has quickly attracted attention for use in nanoscale electronic and photonic devices. Some of the intrinsic optoelectronic

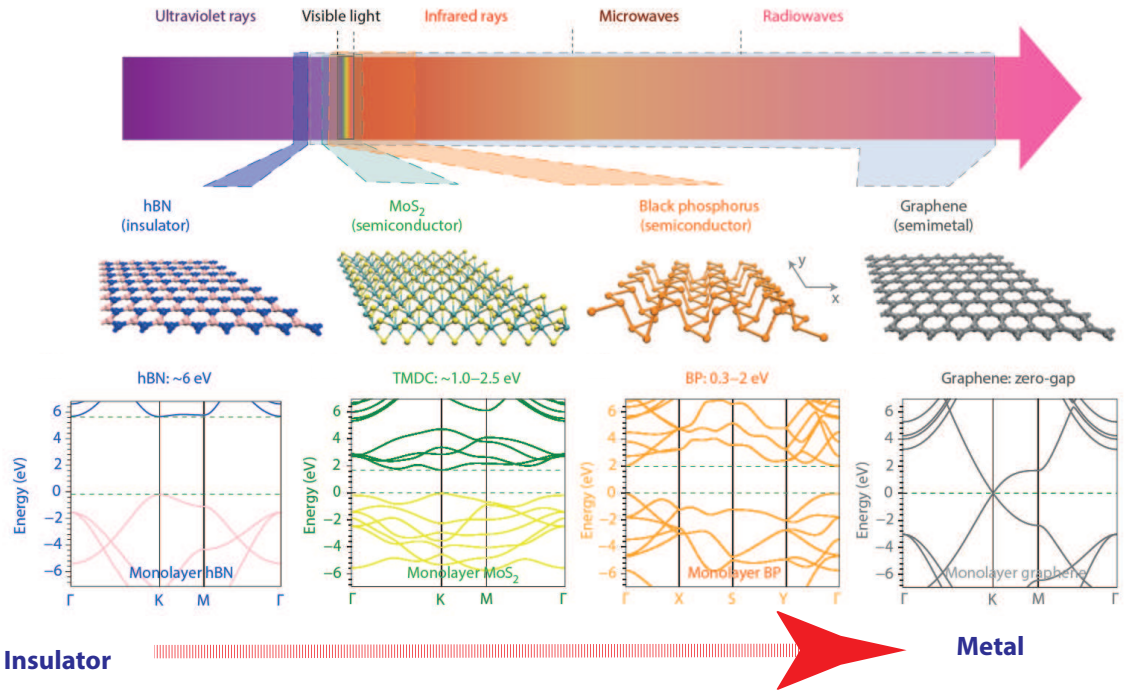

Figure 1.6: (Color online) Electromagnetic spectrum (**top**). Atomic structures of hBN, MoS2, Black Phosphorous (BP) and graphene are shown in the bottom of the panel, left to right (**middle**). The crystalline directions (x and y) of anisotropic BP are indicated. The possible spectral ranges covered by different materials are indicated using coloured polygons. Bandstructure of single-layer hBN , MoS2 , BP, and graphene (**bottm**), reproduced with permission from [12]. © [2014] APS.

properties of 2D materials and their possible application domains is illustrated in the Fig. 1.6

Ultrathin TMDC, mainly MoS_2 has been successfully fabricated into field-effect transistors (FET) with high on-off ratios [38,62], and being investigated for its chemical sensing [63], and photovoltaic properties [40]. Although these proof-of-concept devices have shown great potentials as a potential channel material, materials related issues such as intrinsic heavier carrier effective mass, lower carrier mobility, and higher contact-resistance prevents them from being a industry standard channel materials for a device. Alternatively, many interesting intrinsic material properties make these 2D materials discrete, atomically thin "building blocks [64]" that can be combined

to form complex structures with unexplored feature and functionality [65]. Heterogeneities in 2D materials, including variations in layer number and stacking order, may be the another avenue of customizing variety of unique optical and electronic properties.

In general, semiconductor quantum wells for the electron/hole are formed when two semi-conducting surfaces or layers are stacked on top of each other, and heterostructure properties depends on the energy offsets between the conduction and valence bands of these layers. TYPE I and TYPE II are the most widely utilized band lineups between two semi-conducting surfaces. In the TYPE-I band lineup, electrons and holes are confined within the same layer (Fig. 1.7.a). Conversely, in the TYPE-II band lineup, both the carriers are localized in the two adjacent layers, as shown in Fig.1.7.b. Column III-V materials are the most widely used materials to form these staggered potentials, and are regarded as one of the leading candidates to overcome the performance limitations of silicon-based devices for ultra high-speed and ultra-low power applications. Furthermore, a selected combinations of these column III and V materials, such as GaSb/InAs/GaSb, also form a new type of TYPE-II potentials known as broken-gap TYPE-II potential, as shown in Fig.1.7.c. This type of potential profile posseses various interesting properties: conduction and valence band hybridization due to coupling at the interface and spatial separation of electrons and holes. This spatial separation of opposite charges leads to the formation of stable electron-hole pair bounded by Coloumbic force and are known as excitons. Existing theoretical studies on exciton condensation in bilayer graphene systems have focused on utilizing the enhanced tunneling current for device functionality. In this study, we utilize the collective excitonic state formed between two oppositely doped parallel segments of TMDC monolayer films as a collective state variable for information processing where we propose TMDC Excitonic Field Effect Transistor (TExFET) as

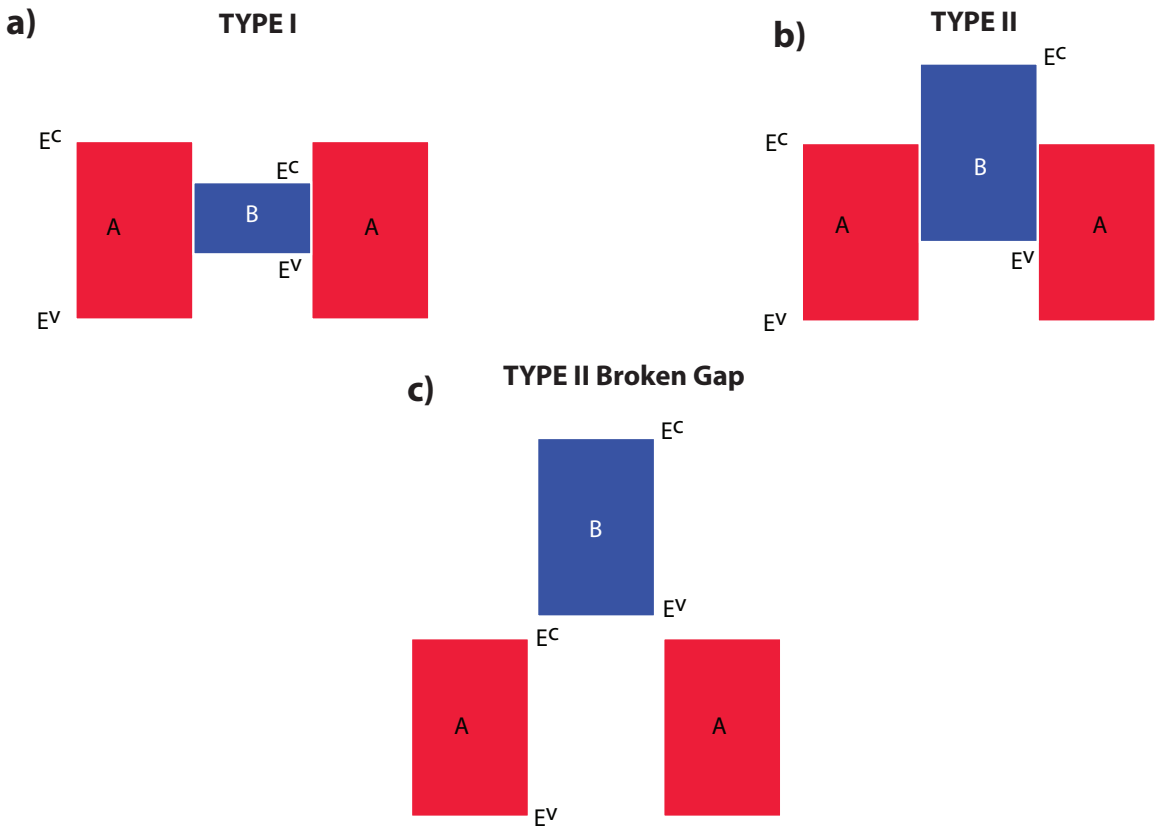

Figure 1.7: a) TYPE I band alignment b) TYPE II band alignment, and c) TYPE II broken gap band alignment

an exotic new device design.

TExFET, a low power device, is designed by creating heterostructure between hexagonal boron nitride (h-BN) and Transition Metal Dichalcogenides (TMDC), and is based on the novel concept of many-body physics and governed by a new collective-state variable known as excitons. When Coulomb interaction between electrons in the n-type branch and holes in the p-type branch is made sufficiently strong, the system undergoes a phase transition from independently mobile electrons and holes to an electrically insulating excitonic insulator state, with an energy gap in the single particle excitation spectrum. This coherent state formation might support ultra-low power operation by allowing on/off switching by shifting the energy of the ensemble charge instead of the individual charge [66]. Recombination of electrons and holes is suppressed through the spatial separation of charges with opposite polarity. The effective strength of the Coulomb interactions, sometime referred as the magnitude of the binding energy, can be tuned using a gate voltage to modify the charge concentration. The device functions as a function of the gate voltage, from a highly conductive state that allows for fast switching into the off-state once the conditions for the formation of a collective excitonic state are satisfied.

1.2 Background and Motivation

The device scaling trend, however, demands a detailed understanding of not only the chemistry of low dimensional materials but also, the underlining physics of the conceptualized device. So far, the transistor scaling trend is supported and enabled by three different factors: advanced lithography technique, discovery of new materials, and architectural innovation. The scaling of silicon metal-oxide-semiconductor field-effect transistor (MOSFET) is approaching its fundamental limits, and hence,

the need for alternative channel materials and device architectures is growing fast. Rather than vying to replace silicon based transistors, one of the conventional approaches to maintain the device scaling trend is to create nanostructure with new design and functionalities from existing materials. Heterostructure-based nanostructures created by combining existing materials and designs could also contribute to this effort. By exploiting the underlining physics of heterostructures and conceptualizing new device design with it, one could also extend the life of current technologies to new applications domains such as memory, optical and communication.

In parallel with the logic devices, post-CMOS memory devices should also scale and be compatible with existing technology. An ideal highly scaled post-CMOS memory device should have higher density, faster read/write speeds, lower cost, and also should be non-volatile in nature. One of the critical challenges in the memory device design is to meet the demand of scalability and compatibility with the evolving logic devices with new materials and operational principles. Among these memory designs, non-volatile floating gate memory (NVM) devices have attracted attention due to their potential to take advantage of the nanotechnology, while being highly scalable and compatible with current Si-based device fabrication technologies. In the past decade significant focus has been put on the emerging memories field to find a possible alternative to NVM. The emerging NVMs, such as NC-based NVM, phase-change memory (PRAM) [18], ferroelectric RAM (FeRAM) [67], magnetic spin-torque-transfer RAM (STT-MRAM) [68], and resistive memory (ReRAM) [69], are showing potential to achieve high cycling capability and lower power per bit for both read and write operations.

Some commercial applications, such as cellular phones, have recently started to use these NVMs, demonstrating that reliability and cost competitiveness in emerging memories is becoming a reality. In recent years, NC-based NVM with Si NCs

as the charging sites have evolved as a leading NVM design because of low-power consumption, high storage density, and better support for scaling, in comparison to the conventional NVM [27]. Though Si NC-based NVM improves upon the charge retention lifetime, there exists an inherent trade-off between the program/erase and retention times. A thinner tunneling dielectric is required for faster program/erase operation, whereas a thicker tunneling oxide is favorable to achieve an acceptable retention time of 10 years. Most of the recent research on NC-based NVM has focused on addressing this trade-off. One of the proposed solution is based on material science, where high-dielectric (K) materials have been proposed as the tunneling dielectric material [25]. The use of high-K dielectric materials as a tunneling oxide reduces the equivalent oxide thickness (EOT) and improves the retention time, without maintaining the program/erase time. An alternative approach is to create an asymmetrical barrier between the storage nodes and the substrate by engineering the shape (either the depth or the structure) of the potential well where the charges are stored. Ge/Si core-shell NC based memory devices have been proposed and identified as suitable candidate material system for creating of an asymmetric barrier which leads to a small barrier for writing and a large barrier for retention [23]. In this device, the Si shell acts as an additional barrier layer during the tunneling of holes confined in the Ge core.

In addition, bulk Ge and Si when joined together form a Type-II heterojunction [70]. In such a heterojunction, electrons and holes are spatially separated between the shell and the core region respectively and hence, the hole lifetime in the core region increases due to the minimal electron-hole recombination [70]. C-V measurement on the Si_xGe_{1-x}/Si system also confirms the longer hole retention, even with ultra thin oxide thickness, owing to the higher valence band offset between Ge and Si [71]. Utilizing this band alignment property of Ge/Si heterojunction, Sousa and et al.

compared hole and electron based operation of alloy based Si_xGe_{1-x} non-volatile memory (NVM) [72]. The dependence of the read/write characteristics on the oxide (SiO_2) thickness on Ge/Si core-shell NC have also been investigated by Yang and colleagues [73]. Kanman and et al. [74], experimentally demonstrated retention time and writing/erasing speed dependency on the NC size, and also on the size induced shift of the band edge in a Ge/Si NC. Likharev [75] reported that the barrier thickness is transparent during the write/erase cycle and the applied voltage has little or no effect. Recently, a series of studies of the effect of electric field and interface trap density on the electron and hole dynamics for the Ge NC / SiO_2 system have been reported [76], [77], [78].

Theoretically, Niquet and et al. performed atomistic, empirical tight-binding calculations of the electronic structure of isolated Ge nanocrystals, and they determined analytical expressions for the electron and hole confinement energies as a function of nanocrystal size [13]. However, atomistic modeling of Ge/Si core-shell structures for realistic shapes and sizes has been limited. An atomistic, full-bandstructure model is required to calculate the valence band states of a strongly confined structure.

One could also contribute to the solution to the scaling problem by envisioning new materials and device design paradigms governed by novel physics. Since its discovery in 2005 by Profs. Geim and Novosolov's group at University of Manchester, graphene, a 2D material, is being studied extensively as an alternative channel materials for future device applications [30]. High thermal conductivity [79], carrier mobility, and long coherence length [30, 80, 81] make graphene a very attractive material for next-generation thermoelectric, electronic, and optical devices. The graphene transistors showed good scalability of the gate length, and the potential performance with higher cut off frequency. However, lack of appreciable energy gap in graphene [81,82] hinders any effort to use it in real device application. Due to the lack of energy gap, graphene-

based transistor can not provide sufficient current on/off ratio of at least 10^4, as recommended by recent ITRS report for the next generation logic device [16]. To open up the energy gap, various methods such as edge patterning and functionalization [83–85], application of an electrical field, chemical doping [86–88], and stacking of two monolayers to form a bilayer system [89–91] have been implemented.

A bilayer graphene consists of two layers of graphene where each has two sublattices, namely A and B, where the breaking of the inversion symmetry between the layers produces an energy gap [81] Recent theory predicts that stacking two monolayers into a bilayer does not affect the overall graphene properties but opens an energy gap of 56 meV [92]; experimental evidences suggest otherwise. The typical mobility of charge carriers in the bilayer graphene is found to be substantially smaller than in a single layer graphene [33]. This is mainly due to structural defects, which may appear during growth or processing [93] and the existence of the relative misorientation between the layers, forming misoriented bilayer graphene (MBG) [43]. A recent experiment showed that in MBG with twist angles greater than 10°, the low-energy carriers behave as massless Dirac Fermions with a reduced Fermi velocity compared to that of single layer graphene, and that for twist angles greater than 20°, the layers are effectively decoupled and act as independent layers [48]. Calculations, based on density functional theory [42, 43, 46, 47], empirical tight binding [94] and continuum [45] models for such rotated bilayers also confirms the experimental observations.

Since a perfectly aligned bilayer graphene in experiment is far from being a reality, deviations from perfection can be useful in some applications, as they make it possible to tailor the local properties of graphene to achieve new functionalities. The physics of MBG has been studied extensively for electronic and optical device applications [95], its usage as a thermoelectric materials has been limited. Recent experimental calculation of the thermal conductivity on MBG suggests some reduc-

tion in the thermal conductivity due to the misorientation angle, as compared to the perfectly stacked bilayer sample [96]. The reduction in the thermal conductivity was attributed to low-energy acoustic modes. An earlier theoretical study phonon modes suggests that arbitrarily rotating the misorientation angle in a bilayer graphene sample leads to a huge change in the frequencies of the optical modes [97]. Similarly, a theoretical thermal properties analysis of MBG using the harmonic approximation reveals a strong correlation between the misorientation angle and thermal properties. In these studies, attempts were made to correlate the experimentally observed Raman modes, at room temperature, to that of zero temperature harmonic approximation based calculations. Since the sensitivity of low-energy phonon modes to the temperature has already been observed experimentally and verified theoretically, an anharmonic atomistic approximation is required to characterize the misorientation dependent low energy modes in the MBG. Understanding the vibrational and thermoelectric properties of MBG and investigating it's applicability in the thermoelectric application is one of the motivation of this dissertation.

In the longer term, a new device design technology, capable of providing additional scaling of the size, reduction in cost, and minimization of power dissipation together with increased data processing, would have invaluable impact. To obtain scaled-devices with higher performance at lower power consumptions, the replacement of charge-based CMOS transistors by novel types of devices may become necessary. While seeking new device designs, it is also important to understand not only the material properties at the atomistic level but also the operational characteristics, while performing complex logic functions. At the fundamental level, the operational principles of all the devices are represented by a physical properties, also known as state variables, of entities such as particles, quasi-particles, and collections of particles. The most common state variables are charge, mass and voltage etc., and can attain

several values during operation, resulting in the state of the device. In an ultimate-scaled CMOS device, however, these conventional state variables become obsolete, and alternative state variables such as spin (spintronics), acoustic vibrations, i.e. phonon (phononics), photons (photonics), or collective states variables (excitons) might be relevant for information processing.

In the last two section of dissertation, we propose two novel device concepts: phononic devices and excitonic devices. Electronic and optical interconnect design tradeoffs are well researched and understood. However, the concept of phononic device is relatively new, where the quanta of lattice vibration i.e. phonons act as a state variable, and the control and manipulation of phonon leads to device operation. Since phonons are quantum objects, it can also carry information, and may provide new avenue for quantum computation [98]. In an ideal crystal environment, it could play a role analogous to photons, though they may propagate with the much slower speed of sound. Phononic crystals (PnCs) have attracted a lot of interest over the last two decades due to their possible applications in sensors and radio frequency (RF) filters and the ability to control acoustic and elastic waves [99]. Although research utilizing engineered materials and their heterostructures in this field of engineering started as early as 1992 [100], it is only recently that there has been intense effort to analyze and manipulate phonons at the nanoscale in order to design nanodevices operating at terahertz (THz) frequencies. To realize and integrate the phononic devices with the existing conventional device architectures, phononic interconnect components such as waveguides, resonators, and switches are needed. In this study, we propose and analyze various phononic interconnect components, such as nano-scaled phononic resonators, waveguides and switches, realized on [111] surfaces of group IV elements, such as 3C-SiC and 3C-GeSi (the surfaces with the highest density) by introducing defects on the surface of these materials. In these phononic components, in particular,

by varying the defect concentration and by changing their location, the lower bandgap edge can be swept in frequency and the resulting change in the lifetime, density of states, and localization of the trapped acoustic waves.

The observation of exciton phenomenon was first theoretically predicted by Lozovik and Yudon [101], as a follow up to Keldysh and Kopaev's proposal on semimetallic system in 1965. It was predicted that strong Coulomb interaction between spatially separated electrons and holes can lead to the condensation of excitons with large radii. The EC in closely coupled two-dimensional (2D) electron-hole bilayer system have been a topic of continued research [102–104]. Experimental investigation based on this prediction have been focused on the III-IV systems, mainly, GaSb/InAs [105, 106] and GaAs material systems [107, 108], mainly for optical device applications.

In a quest for an alternative system to the semiconductor double quantum well (DQW) systems, bilayer graphene structures are currently being explored for use in ultralow-power transistors [109–112]. This graphene based system is based on the theoretically predicted possibility of room temperature superfluidity in two adjacent layers of graphene. This allows electrons in one layer to pair with holes in an adjacent layer, resulting in electron-hole pairs i.e. excitons at room temperature. The study of the exciton states in has been performed primarily for a single quantum well and with III-V materials, where exciton lifetime in the of picosecond was observed, mainly due to lighter effective mass and surface induced scattering in the heterojunction. [113] Thus far, the Bose condensate of excitons has only been observed at low temperatures and high magnetic fields in GaAs/AlGaAs double-quantum well systems, with an exception of recent attempts on bi-layer graphene [114] In the bilayer graphene, due to the lack of a sizable bandgap in graphene, direct optical observation demonstrating the existence of such excitons is challenging **??**. In addition, existing theoretical stud-

ies on exciton condensation in bilayer graphene systems have focused on utilizing the enhanced tunneling current for device functionality. Recently, formation of type II band-alignment of in TMD heterojunctions was also predicted by the earlier theoretical studies **??**. Encouraged by this development, we envision, TExFET, a low power device. This device is designed using hexagonal boron nitride (h-BN) and Transition Metal Dichalcogenides (TMDC) layers. In this device architecture, multilayer h-BN are sandwiched between two monolayer of TMDC and the device is based on the novel concept of many-body physics and governed by excitons acting as a collective-state variable. The device related parameters suitable for future device application will be discussed later.

1.3 Objective

In general, there are mainly two device related issues associated with the characterization of Ge/Si NC-based memory and optical devices. First, the impact of physical (shape and size) parameters on the electronic and optical properties on the charge retention and optical properties has not been elucidated. Secondly, since these NCs are typically formed by random nucleation and growth process, impact of strain due to heterogeneous surface on the relevant device parameters is not well understood. The objectives of the first section of dissertation are: (1) to model the experimental Ge/Si quantum dot topologies at the atomistic scale (2) to understand the shape and strain effects on the essential underlying physics and parameters such as carrier confinement, and lifetime and (3) to assess the potential use of these Ge/Si quantum dots in the memory and optical applications, while providing the theoretical insight to the experimental findings. In order to achieve aforementioned objectives, we employ the empirical tight binding (ETB) method, as implemented in the NEMO-3D

simulator [115].

MBG has interesting electronic and optical properties that can be combined with other 2D materials and can potentially be used as a channel material in the post CMOS devices. In general, the thermal resistance in the channel is mainly due to interfaces and defects that scatter phonons, reducing the effective thermal conductivity of the channel materials by orders of magnitude from their intrinsic values. Although physics of the MBG is well understood, the systematic study of vibrational properties that includes the anharmonic effects is still lacking. Quantitative study of thermoelectric properties such as phonon density of states, and lattice specific heat is also an important issue for both the device and thermoelectric interface material applications. Second part of the dissertation will provide answer aforementioned open questions regarding vibrational and thermoelectric properties using a classical molecular dynamics (MD) method as implemented in LAMMPS [116].

To support the continuous scaling and to meet the demand for low-power devices, we are also required to envision new device concepts using bottom-up of device design scheme, starting from atom. In the final part of the dissertation, we will conceptualize two next-generation devices phononic and TeXFET based on the novel concept of phononic engineering and many-body physics. For this study, we will utilize a classical molecular dynamics (MD) method as implemented in LAMMPS [116], first principle calculation using VASP [117], variational principle [118], and mean field approximation [119].

1.4 Layout

The rest of this dissertation is organized as follows. In chapter **??**, a systematic study of the electronic and memory device related properties of spherical Ge-core/Si-

shell NCs is presented. It is shown that changing the radius of the Ge-core size increases the memory retention lifetime. Utilizing the analytical formalism developed in **??**, we will focus our study on realistic experimentally observed crescent-shaped Ge-core/Si-shell NCs in chapter 4. In chapter 5, the optical properties of large scale experimentally relevant dome-shaped Ge-core/Si-shell NCs for a variety of base diameter, while fixing the overall height, is studied. In chapter 6, the misorientation dependent vibrational and thermoelectric properties of experimentally observed misoriented bilayer graphene (MBG) is presented. A correlation between the low-energy Raman modes observed in the experiment and low-energy phonon modes evaluated in our theoretical study is established. In chapter 7, a novel phononic device concept and associated components is presented using phonon engineering technique. Using various atomistic defects on quasi-2D surfaces, phononic circuit components such as resonators, waveguides and switches are created on $\langle 111 \rangle$ surface of the quasi-2D GeSi and SiC systems. Another novel electronic device, TExFET using TMDC and h-BN as the materials is conceptualized in chapter 8. A correlation between the exciton binding energy and the thickness of the h-BN layer sandwiched between TMDC layers is established. Furthermore, a preliminary observation on the effect of static screening, effective masses, and chemical potentials on the superfluid-gap of TExFET will presented. Finally, we summarize the key findings of this thesis in the chapter 9. In Appendix, A the effect of varying the core thickness on the fundamental optical properties and leakage current out of NC-based laser is analyzed. Effect of capping layer variation on the confinement properties of dome-shaped Ge-core/Si-shell NCs is presented in Appendix B

Chapter 2

Theoretical Methods

2.1 Atomistic Tight Binding Method

2.1.1 Overview

Major challenges in modeling QDs and calculating electronic structure are that these nanostructures are much larger than conventional molecules, however they do not possess fundamental symmetry of periodic bulk or planar structures. In addition, strain originating from the lattice mismatch between materials penetrates in the vicinity of the interface. Furthermore, the interface roughness, the alloy randomness and the atomistic granularity demands for an atomistic treatment of the simulated domain in electronic structure calculations. Most of the current or past theoretical calculations are based on the use of the continuum approach such as effective mass approximation (EMA) or k.p model, which fails to include any or some of the aforementioned effects necessary to capture the essential physics, thus resulting in inaccurate predictions. The Pseudo-potential approach is an atomistic approach, and hence, minimizes the shortcomings of EMA and k.p methods. However, due to the inclusion of macroscopic

details, the single particle states and energies calculations are computationally expensive for large more realistic systems. Empirical tight binding model is a powerful tool that captures the atomistic description of the simulated systems treating the electrons as tightly bound particles. In this approach, the Hamiltonian describing the system consists of the overlap between different localized states in the presence of the ionic potentials. However, these states are the localized orbitals of the valence electrons and might not be the same as the atomic orbitals of the corresponding valence electrons of an isolated atoms. In this method, the tight binding Hamiltonian contains the matrix elements between various orbitals localized at the different sites, and can be evaluated by empirical methods. The matrix elements are treated as fitting parameters to reproduce the bulk band structure. This is a powerful tool that captures atomistic description of the simulated system by assuming electrons as tightly bound particle to their ions.

2.1.2 NEMO-3D

NEMO-3D is an atomistic simulation package that models the nanostructures atomistically using above mentioned tight binding model. Spin effects are included in its fundamental atomistic tight binding representation i.e. in the Hamiltonian. The electronic structure calculation of Ge/Si dome-shaped NCs using the tight binding approach should include an accurate representation of the atomic position in the Hamiltonian because the atom positions are shifted from the ideal bulk positions in order to minimize the overall strain energy of the system. In our model, we use a valence force field method (VFFM) with Keating potential for the energy minimization, in which the total strain energy is expressed in terms of the positions of its nearest neighbor and then added up for all atoms. The local atomic strain energy with Keat-

ing potential at each atomic position is given by the energy sum of bond-stretching interaction and bond-bending interaction [115],

$$U_{VFF} = U(bond - stretching) + U(bond - bending) \tag{2.1}$$

where,

$$U(bond - stretching) = \frac{1}{4}\sum_{i}[\frac{\alpha_{ij}}{4}\sum_{j}\frac{(\mathbf{r}_{ij}.\mathbf{r}_{ij} - 3d_{ij}^2)^2}{d_{ij}^2}] \tag{2.2}$$

and

$$U(bond - bending) = \frac{1}{4}\sum_{j}[\sum_{j}\sum_{k\neq j}\frac{\beta_{ijk}(\mathbf{r}_{ij}.\mathbf{r}_{ik} + 3d_{ij}d_{ik})^2}{2d_{ij}d_{ik}}] \tag{2.3}$$

where the sums over j and k run over the four tetrahedrally coordinated nearest neighbor atoms, $\mathbf{r}_{ij}$ denotes the distance vector from the ith atom towards jth neighbor and d_{ij} is the lattice constant between i and j elements. Eq. 2.2 and Eq. 2.3 are non-zero when the bond length and angle is altered from the strain-free state.α and β represent the force constant for bond-length (stretching) and bond-distortion(bending) in the bulk zinc-blend materials, respectively and are calculated using anharmonic correction as in the reference [115]. The strain domain has fixed boundary conditions on the bottom plane, and open boundary condition on the top surface. The electronic domain assumes closed boundary conditions. Finally, local strain energy calculated for each atomic site using the energy correction from the Eq.2.1.

The single-particle energies and wave functions are calculated using an empirical nearest-neighbor tight-binding model. The underlying idea of this approach is the selection of a basis consisting of atomic orbitals (such as s, p, d, and s*) centered on each atom. These orbitals are further treated as a basis set for the Hamiltonian,

which assumes the following form:

$$H|\Psi_n\rangle = \varepsilon_n|\Psi_n\rangle \tag{2.4}$$

The electron eigenvalues ε_n is a complex dependence on atomic coordinates. In order to find the sets of ε_n, we need to construct and diagonalize the Hamiltonion matrix H_{mn} which is defined as,

$$H_{mn} = \langle\Psi_m|H|\Psi_n\rangle \tag{2.5}$$

Since the true eigenfunctions $\{\Psi_n\}$ of the Hamiltonian are unknown, we need to expand them in a simpler basis. One of the naturally available basis is the linear combination of atomic orbitals (LCAO) basis. The $\{\Psi_n\}$ in the LCAO basis looks like,

$$|\Psi_n\rangle = \sum_{i,\alpha} C_n^{i,\alpha}|\phi_{i\alpha}\rangle \tag{2.6}$$

Here, index i spans of all the atomic sites and index α spans over all the basis orbitals on each atomic sites. For example, in the case of Si, the minimal atomic orbital basis to be the valence s, p_x, p_y and p_z orbitals located on every atom in the given system. With this basis, the total number of basis functions will be of 4N. In our nearest neighbor TB approximation, the basis function $|\phi_{i\alpha}$ is assumed to be orthogonal to each other. By substituting Eq. 2.6 into Eq. 2.5, we can obtain the matrix element of H_{mn} as a linear combination of matrix elements between the basis orbitals,

$$H_{mn} = \langle\Psi_{i\alpha}|H|\Psi_{j\beta}\rangle \tag{2.7}$$

If the simplest case of two Si atoms with their p_x, p_y and p_z orbitals parallel to each other respectively, and p_z orbitals lying on the same axis, matrix elements $H_{i\alpha,j\beta}$ can be all represented by a small set of terms that only depends on the interatomic distance, R_{ij}. Two different diagonal terms are atomic orbital energies ϵ_s and ϵ_p and the four off-diagonal terms are "hopping parameters." In the orthogonal basis, all the p-functions perpendicular to each other will vanish. Thus, the key elements required for the Hamiltonian matrix construction are hopping parameters and their dependence on interatomic distance. In the empirical TB approach, these terms are fitted to the results of first principles calculations and parameterized in the form of simple functions depending on distance. Most of the systems under consideration in this approach have zincblende lattice structure. The parameterizations of all bonds using analytical forms of directional cosines for various tight-binding models is given in Ref. [120].

NEMO 3-D provides the user with choices of the $sp^3d^5s^*$, sp^3s^*, and single s-orbital models with and without spin, in Zincblende, Wurtzite, and simple cubic lattices. The strain energy calculated using VFF model is included in the total nearest neighbor tight-binding Hamiltonian and solved using Lancoz algorithm for the eigen energies and eigen states [115]. In the case of a strained system, like Ge/Si, the atomic positions deviate from the ideal (bulk) crystal lattice. This, in turn, leads to distortion not only in the bond directions, but also in the bond lengths. The new interaction parameters are calculated analytically from the relaxed atom positions. The 20-band nearest-neighbor tight-binding model is thus parametrized by 34 energy constants and 33 strain parameters, which need to be established by fitting the computed electronic properties of materials to those measured experimentally. This is done by considering bulk semiconductor crystals (such as Ge or Si) under strain. The summation in the Hamiltonian for these systems is done over the primitive

crystallographic unit cell only. The model makes it possible to compute the band structure of the semiconductor throughout the entire Brilliuon zone. For the purpose of the fitting procedure, however, only the band energies and effective masses at high symmetry points and along the Δ line from Γ to X are targeted, and the tight-binding parameters are adjusted until a set of values closely reproducing these target values is found.

2.2 Classical Molecular Dynamics

2.2.1 Overview

Over the past few years, molecular dynamics (MD) has emerged as a powerful tools for computing thermophysical properties such as zero-point energy, lattice heat capacity and thermal conductivity, etc. of a classical many body system. Because of its portability and scalability, MD simulation has been used to studies such as the thermal conductivities of a variety of bulk and composite solids [121], the fracturing of semiconductor nanowires [122], protein folding [123], and supercritical phase change [124]. The main strength of MD simulation is that it describes a system with atomic-scale resolution, providing a level of detail that is either difficult or impossible to attain in an experiment. With this atomistic resolution, it is possible to elucidate the physics underlying macroscopically observable properties and phenomena. In an MD simulation, the positions and momenta of a set of atoms are allowed to evolve from an initial configuration by numerically integrating Newton's equations of motion, as follows [125]:

$$\sum_{j=1;j!=i}^{N} F_{ij} = m + i\frac{d^2 r_i}{dt^2} i = 1....N \tag{2.8}$$

where F_{ij} is the force exerted on an atom i caused by atom j and m_i and r_i are the mass and position of atom i, respectively. By using the Lagrangian or Hamiltonian equations of motion, all the degrees of freedom of an atom's trajectory, including rotational motion, can be obtained in one vector of generalized conditions, r. The system's Lagrangian is defined as the energy difference between th kinetic and potential energies,

$$L(t, r, r') = K(r, r') - V(r) \tag{2.9}$$

here r' is the time derivative of r or the generalized velocity. The Lagrange equation of motion is given by,

$$\frac{1}{dt} d\frac{L}{dr'_i} - \frac{L}{r_i} \tag{2.10}$$

the subscript i denotes the generalized coordinates for each atom. The Hamiltonian, a function of the generalized coordinate vector r and corresponding momentum p, describes the total energy of the system,

$$H(t, r, p) = K(p) - V(r) \tag{2.11}$$

where the generalized momentum, p is derived from the Lagrangian by differentiating with respect to the generalized velocity,

$$p = d\frac{L}{dr'_i} \tag{2.12}$$

The Hamilton equations of motion are given by

$$p'_i = d\frac{H}{dr_i} r'_i = d\frac{H}{dp_i} \tag{2.13}$$

Any of the equations of motions 2.11 2.12 and 2.13 can be used to describe the atom's

trajectory.

The only required input to an MD simulation is a suitable method for specifying the atomic interactions. Such specification is typically made using empirically-derived inter-atomic potential functions, which are element- specific and are valid only for a range of atomic configurations similar to those used during the potential development. In recent years, $ab-initio$ density functional theory (DFT)-based approaches have become an attractive alternative to empirical inter-atomic potential functions because they are valid for all atomic configurations and elements. However, this approach is only practical for systems containing less than 100 atoms and simulations with durations less than a picosecond (10^{-12} second) because of the computational cost. Because of these limitations, empirical interatomic potentials are used in MD simulations.

Since the details of the electron positions and momenta are neglected, MD simulations are suitable for calculations in which the effect of electron transport are negligible. Some of the materials satisfying this condition are dielectrics and semiconductors because the thermal transport is dominated by the lattice vibration i.e. phonons. In addition, because the simulating system is governed by the Newtonian equations of motion, the atomic dynamics in an MD simulation are strictly classical, neglecting any quantum effects. There has been few attempts on adding, quantum correction to the MD-predicted thermal properties [126]. The quantum-corrected MD computes the energy of interaction from the electronic structure of material instead of an interatomic potential, which adds to the computational cost. Though this is more accurate than the classical MD, it is still a classical method because the nuclei obey Newtonian mechanics. Classical MD is also computationally demanding because the dynamics are averaged over hundreds of thousands or millions of time steps and several different initial configurations of atomic positions and momenta are required

to give a good statistical description of the atomic behaviour. To achieve statistically meaningful results, one needs to simulate a large number of atoms over enough time steps to achieve statistically meaningful results, which can be difficult or even impossible depending on the computational resources available. The major advantages of the MD method are that, other than the interatomic potential, no assumptions or approximations are needed and the method is intuitive.

In classical MD, the qualitative and quantitative description of a system and their thermophysical properties relies on the ability of the interatomic potentials to describe the interaction between the atoms. The interactomic potentials are, however, are limited to being as good as the extracted force constants, either from experiments or $ab - initio$ simulations. MD simulations of atoms have potentials that can be categorized as pair, many-body, and force fields. Among them, pair potential is the simplest potential which describes the interaction between two atoms. Coulomb's, Lennard-Jones (L-J), and Morse potentials are some of the examples of this type of potential. Lennard-Jones potential is widely used to describe a non-bonded interactions, but fails to describe the interactions associated with covalent bonds and long-range interaction [127]. In a realistic system, such as graphite, diamond, nanotube, the interaction between two carbon atoms depends not only on the distance between the atoms, but also on the atoms surrounding the pair. Many-body potentials and force-fields describe both the covalent bonds and the long-range interactions quite well. Some of the widely used many-body potentials are Tersoff potential, reactive empirical bond-order (REBO) potential and bond order potential (BOP). The Tersoff potential is the first potential that considered bond-order and allowed for bonds to be formed and broken during the simulation, which is useful in studying chemical reactions, where it also considers the bond angle between atoms [128]. The REBO potential is a type of Tersoff potential that is good at modeling the interactions in

hydrocarbons and graphite [129]. The REBO potential was further extended to include L-J terms to account for intermolecular interactions and radial interactions, and known as adaptive intermolecular REBO (AIREBO) [130]. In the scope of this work, we will mainly utilize long-range bond-order potential (LCBOP), an extension to the BOP, which includes both the angular and coordination dependent short-range part accounting for the strong covalent interactions and a radial long-range part describing the weak interactions responsible, e.g., for the interplanar binding in graphite [131].

2.2.2 Harmonic and Anharmonic Approximation

The MD method does not explicitly consider the energy carriers during lattice dynamics calculation. Instead, phonons arise from correlated atomic motion and electrons are omitted. The atomistic resolution provided by MD simulation allows for direct observation of the changes in phonon properties which drive the observed phonon-mediated transport. This includes the phonon dispersion, which contains information essential to thermal transport, including the temperature dependence of phonon energies and velocities of each phonon modes. The vibrational properties from a MD simulation is evaluated using two approximations: harmonic and anharmonic.

Harmonic approximation is a means of computing the vibrational frequencies and modes available in a crystal lattice. These vibrations are known as phonons. Harmonic lattice dynamic is a well known technique of calculation many thermophysical properties of crystals. In this approximation, the atoms in a crystal are assumed to sit at their zero temperature equilibrium positions and are also assumed to interact through Hooke's law. In other words, the crystal is modeled as a system of linear chains connecting atomic masses. This method is only valid when the atom vibration is smaller than the spring between neighboring atoms. The spring constants,

or force constants, can be determined by twice differentiating the potential energy (P.E) with respect to the average atomic positions at zero temperature. The phonon dispersion, and phonon density of states (PDOS) predicted from this approach is based on an assumption of equipartition of kinetic and potential energy between normal modes. Consequently, the harmonic specific heats (C_v) which utilizes both the phonon frequency and phonon density of states (PDOS) are significantly different at low temperatures, where quantum effects are important. The harmonic approximation is exact in the limit of zero atomic motion and is never exactly fulfilled in a quantum system (due to zero-point motion). As the atomic motion increases due to finite temperature, the spacing between the average positions of the atoms in a crystal can change with temperature, leading to thermal expansion/contraction. In addition, prediction of the experimentally measured specific heat would require taking into account the temperature dependence and coupling of the normal modes. This issue is solved by using quasi-harmonic lattice dynamics, where the second-order derivatives of the potential energy is taken with respect to the average, finite-temperature atomic positions. This extension of harmonic approximation accounts for the effects of thermal expansion/contraction on the phonon frequencies but still neglects the effects of finite atomic motion.

Anharmonic approximation is the natural extension of quasi-harmonic lattice dynamics and includes both the finite temperature and finite atomic motion effects. In this approximation, higher order derivatives (usually third and fourth orders) of potential energy are included as a perturbation to the quasi-harmonic frequencies. The inclusion of higher order derivatives adds contributions from three and four-phonon processes to the quasi-harmonic frequencies. This study involves the calculation of an-harmonic vibrational properties calculated with force constants measured directly from the MD simulations at finite temperature and pressure using the formalism

developed by Kong and coworkers [132], described in 2.2.3. In this formalism, the anharmonic phonon dispersion is calculated during MD simulations by monitoring atomic displacement, which adds minimal computational overhead to simulations. This provides several benefits over the other lattice dynamics techniques, including that no assumptions are made about the degree of anharmonicity and both elastic and inelastic phonon scattering processes are intrinsically included in MD simulations. Furthermore, these calculations can be made on-the-fly during simulations, without the needed for lengthy, independent simulations.

2.2.3 Fluctuation Dissipation Theory for Phonon Dispersion

In this approach, the phonon dispersion relation is calculated with the force constants measured directly from the MD simulations at finite temperature and pressure by extending the theory of lattice dynamics. The dynamical matrix in the lattice dynamics is written as,

$$D^{jj'}_{\alpha,\beta} = \frac{1}{\sqrt{m_j m_{j'}}} \sum_{l'} \phi^{jl,j'l'}_{\alpha\beta} exp(i\mathbf{q}.[r(j'l') - r(jl)]) \tag{2.14}$$

where α and β = 1, 2, 3 denote x, y, and z directions, j denotes an atom in the l-th unit cell, m_j is the mass of the $j-th$ atom, $\phi^{jl,j'l'}$ is the 3N X 3N force constant matrix where N is the total number of atoms in a unit cell, $\mathbf{r}$ is the atomic position vector, and $\mathbf{q}$ is the phonon wave vector.

The eigenvalues of the dynamical matrix are the square of the phonon frequencies at specified wave vectors, which provides the dispersion relationship

$$\omega^2(\mathbf{q}) e^j_\alpha(q) = \sum_{j',\beta} D^{jj'}_{\alpha,\beta}(\mathbf{q}) e^{j'}_\beta(q) \tag{2.15}$$

where e(q) is the polarization vector.

The effect of anaharmonicity in the dispersion is included through the calculation of the force constant matrix $\phi_{\alpha\beta}$. In a harmonic or quasi-harmonic approximation, the force constants are evaluated using analytical expressions related to the second derivative of the total potential energy. In this thesis, however, the force constant matrix is directly measured from the MD simulation using fluctuation-dissipation theorem which provides the basis to functionally relate the displacement of atoms due to thermal vibrations, v , to the elastic Green's functions [132]

$$G^{jj'}_{\alpha,\beta}(\mathbf{q}) = \langle v^{*jl}_{\alpha} v^{j'l'}_{\beta} \rangle, \tag{2.16}$$

from which the force constants can be calculated

$$\phi^{jl,j'l'}_{\alpha\beta} = K_b T[G^{-1}]jl, j'l'_{\alpha\beta}, \tag{2.17}$$

where K_b is the Boltzmann constant, and T is temperature. For mathematical simplicity, the atomic displacements in real space are Fourier transformed into reciprocal space,

$$\tilde{\mathbf{v}}^{j}_{\alpha}(\mathbf{q}) = \frac{1}{\sqrt{L}} \sum_{l} \mathbf{v}^{jl}_{\alpha} exp(i\mathbf{q}.\mathbf{r}_l), \tag{2.18}$$

where L is the total number of unit cells. In the reciprocal space, the Green's function is given by,

$$\tilde{G}^{jj'}_{\alpha,\beta}(\mathbf{q}) = \langle \tilde{v}^{*j}_{\alpha} \tilde{v}^{j'}_{\beta} \rangle, \tag{2.19}$$

and the force constant matrix is defined as

$$\tilde{\phi}^{jl,j'l'}_{\alpha\beta} = K_b T[\tilde{G}^{-1}]jl, j'l'_{\alpha\beta}, \tag{2.20}$$

which is the functional form of the Fourier transform of the force constant matrix

in real space.

$$\tilde{\phi}_{\alpha\beta}^{jl,j'l'} = \sum_{l'} \phi_{\alpha\beta}^{\prime jl,j'l'} exp(i\mathbf{q}.[\mathbf{r}(j'l') - r(jl)]), \tag{2.21}$$

To ensure translational invariance, the acoustic sum rule at the zone-center γ point is applied as follows [132]:

$$\sum_{j'} \tilde{\phi}_{\alpha\beta}^{jl,j'l'}(q = \gamma) = 0, \tag{2.22}$$

The details of this approach are more thoroughly discussed in Refs. [133, 134]

2.3 First Principle Calculation- Density Functional Theory (DFT)

Density functional theory (DFT), which is based on the Hohenberg-Kohn theorem [135], states that all ground state properties of a many-body system can be completely determined through the ground-state charge density. The central concept of DFT is to describe a system of interacting quantum particles via its charge density rather than its many-body wave function. For a system of N electrons in a solid, this means that the key quantity depends on three spatial coordinates rather than 3N degrees of freedom. Moving from many-body wave functions to charge density significantly reduces the computational complexity and gives the possibility of developing algorithms that allow very large systems to be treated.

The Hamiltonian of a system of interacting electrons and ions is given by,

$$H = -\sum_i \frac{\hbar^2}{2\ M_i} \nabla_{R_i}^2 - \sum_j \frac{\hbar^2}{2\ m_e} \nabla_{r_j}^2 + \frac{1}{2} \sum_{i=!j} \frac{Z_i\ Z_j\ e^2}{|R_i - R_k|} + \frac{1}{2} \sum_{k=!l} \frac{e^2}{|r_k - r_l|} - \sum_{i,k} \frac{Z_i\ e^2}{|R_i - r_k|} \tag{2.23}$$

i, and j are the indices that run through all the ions, and k, and l are the indices for

electrons. R_i and r_k are the ion and electron positions, respectively. Z_i is the atomic number of ion i. The first and the second terms are the ion and electron kinetic energies, respectively. The third term and fourth terms are the Coulomb interaction between ions and between electrons, respectively. The final term is the potential energy between ions and electrons.

Utilizing the Hohenberg-Kohn theorem, Kohn and Sham introduced a method to minimize the energy functional with respect to charge density to find the ground state energy under the constraint that the total number of electrons is constant [136]. The Kohn-Sham equations for ground state electron-energy can be re-written as,

$$H_{KS}\ \psi(R_i, Rj, ..., r_k, rl, ...) = \epsilon_i \psi(R_i, Rj, ..., r_k, rl, ...), \tag{2.24}$$

where, the Kohn-Sham H_{KS} is given by,

$$H_{KS} = \{\frac{1}{2}\nabla^2 + V_{KS}(R_i, Rj, ..., r_k, rl, ...)\}\psi(R_i, Rj, ..., r_k, rl, ...) = \epsilon_i \psi(R_i, Rj, ..., r_k, rl, ...), \tag{2.25}$$

where $\psi(R_i, Rj, ..., r_k, rl, ...)$ is the single-particle wave function and ϵ_i can be the inhomogeneous energy. The ψ satisfies,

$$\sum_{i=1} \psi_i^* \psi_i = \sigma, \tag{2.26}$$

The Kohn-Sham method is an exact description of the ground state properties of many-electron systems provided the equations 2.25 and 2.26 are solved self-consistently, because $V_{KS}(r)$ depends on the density through the exchange-correlation potential $V_{XC}(r)$ and the density depends on the wavefunctions. So far the Kohn-Sham approach has mapped the original interacting system to a non-interacting

system with an effective Kohn-Sham single-particle potential $V_{KS}(r)$, and the two systems have the same ground-state density. In practice, however, the exchange-correlation functional is unknown that causes its difficulties and demands further approximations. In order to obtain a satisfactory description of a real system, it is important to have an accurate functional for exchange correlation energy. Two of the most widely used approximations for the exchange-correlation potential are the local density approximation (LDA) [135, 137, 138] and the generalized gradient approximation (GGA) [139].

In the LDA, the exchange-correlation energy per electron at a given point is taken to be the same as that for a homogeneous electron gas with density equal to that at the point. Most LDA formulas use analytic forms for ϵ, fit to accurate quantum simulation results of the correlation energy at intermediate density, and designed to reproduce the exact result at the high- and low-density limits. In principle, the LDA should work best in systems where the density varies slowly, with some exception where it turns out it surprisingly work well even in some systems with rapidly varying electron density. In general, the LDA tends to underestimate bond length by 1-2%, overestimate binding energies by 10-50% , and underestimate band gaps by 50%. The inhomogeneity in the electron density can be addressed by using GGA approximation. In this approximation, the correlation functional depend not only on the local density but also it's local gradient. It generally works better than LDA in predicting bond lengths, crystal lattice constants, binding energies, and so on, but often over estimates. However, for the system with the localized and correlated electrons, both the GGA and LDA tends to produce wrong results.

The bandgap under (over) estimation with GGA(LDA) is corrected by using hybrid functionals. They are a class of approximations to the exchange-correlation energy functional in density functional theory (DFT) that incorporate a portion of

exact exchange from Hartree-Fock theory with exchange and correlation from other sources (*ab-initio* or empirical). The exact exchange energy functional is expressed in terms of the Kohn-Sham orbitals rather than the density, so is termed an implicit density functional. A hybrid exchange-correlation functional is constructed as a linear combination of Hartree- Fock, an exact exchange functional, and any number of exchange and correlation explicit density functionals. The parameters determining the weight of each individual functional are typically specified by fitting the functional's predictions to experimental or accurately calculated thermo chemical data. There are several version of hybrid functionals used like B3LYP **??**, PBE0 [140] and HSE [141] etc.

Chapter 3

Electronic properties of spherical Ge-core/Si-shell nanocrystals

3.1 Introduction and Motivation

Metal-oxide-semiconductor (MOS) nonvolatile memory devices based on nanocrystals (NC), especially using Si as the material for NCs [23], have attracted attention due to their potential to take advantage of the evolutionary nanotechnology, within the existing Si device fabrication schemes. In these memory devices, NC's are embedded in the oxide layer of the MOS memories [26]. Due to the localization of the charge into electrically discrete nodes and thinner tunneling oxide, these devices possess various advantageous properties. Low-power consumption and high storage density, up to 1 Tbit/inch, can be obtained in comparison with conventional non-volatile flash memories [27].

Further studies of Si NC embedded non-volatile memories (NVM) by Zhao et al. suggested that the valence/conduction band offset between the Si and SiO_2 substrate is responsible for the leakage of the stored charges into the substrate [28]. In order

to handle the trade-off between the programming speed and the retention time due to the scaling limitation of the oxide layer in the Si NC embedded memories, Ge/Si core-shell NC based memory devices were first proposed in Ref. [29]. In this device, the Si-shell acts as an additional barrier layer during the tunneling of holes confined in the Ge-core. In addition, bulk Ge and Si when joined together form a Type-II heterojunction [70]. In such a heterojunction, electrons and holes are spatially separated between the shell and the core region respectively and hence, the hole life time in the core region increases due to the minimal electron-hole recombination [70]. C-V measurement on Si_xGe_{1-x}/Si system also confirms the longer hole retention, even with ultra thin oxide thickness, owing to the higher valence band offset between Ge and Si [71]. Utilizing this band alignment property of Ge/Si heterojunction, Sousa and et al. compared hole and electron based operation of alloy based Si_xGe_{1-x} non-volatile memory (NVM) [72]. The dependence of the read/write characteristics on the oxide (SiO_2) thickness on Ge/Si core-shell NC have been investigated [73]. Kanman and et al. [74], experimentally demonstrated retention time and writing/erasing speed dependency on the NC size, and also on the size induced shift of the band edge in a Ge/Si NC. Likharev [75] reported that the barrier thickness is transparent during the write/erase cycle and the applied voltage has little or no effect. Recently, a series of studies of the effect of electric field and interface trap density on the electron and hole dynamics for the Ge NC / SiO_2 system have been reported [76], [77], [78].

Theoretically, Niquet and et al. performed atomistic, empirical tight-binding calculations of the electronic structure of isolated Ge nanocrystals, and they determined analytical expressions for the electron and hole confinement energies as a function of nanocrystal size [13]. However, atomistic modeling of Ge/Si core-shell structures for realistic shapes and sizes has been limited. An atomistic, full-bandstructure model is required to calculate the valence band states of a strongly confined structure. In

such structures, bulk light-hole and heavy-hole masses can have little meaning [142].

3.2 Objectives

In this section, we present the theory and models used to simulate and calculate the electronic properties of the Ge/Si core-shell heterostructure NCs and the hole lifetimes in a NC-based NVM device application. We carry out a computational study of the low-energy electronic states in Ge/Si core-shell nanocrystals using a full-band, $sp^3d^5s^*$ model implemented in NEMO3D [115]. Barrier heights are determined from the calculated energy levels. Decay constants are determined from the wavefunctions and used to calculate hole lifetimes as a function of Ge core diameter.

3.3 Model and Theory

In this section, we present the theory and models used to simulate and calculate the electronic properties of the Ge/Si core-shell heterostructure NCs and the hole lifetimes. Fig. B.1 shows one of the simulated structures with a Ge core diameter of 4 nm. Free-standing spherical Ge/Si core-shell NCs with core diameters ranging from 1-7.5 nm are considered. The thickness of the Si shell is maintained at 5 nm around the Ge core region. Strain is not considered because the Ge/Si core-shell NC considered here is free standing. The surfaces of NC structures are faceted. The electronic states are modeled using the $sp^3d^5s^*$, nearest-neighbor, empirical-tight-binding model with spin-orbit(SO) coupling as implemented in NEMO3D, and described in detail in section **??**. The energies of the dangling bonds at the surface are shifted by 20 eV so that the effect of the dangling bonds on the density of states near the bandgap is negligible [143]. The largest NC contains 120,376 atoms. With 20 orbitals per atom

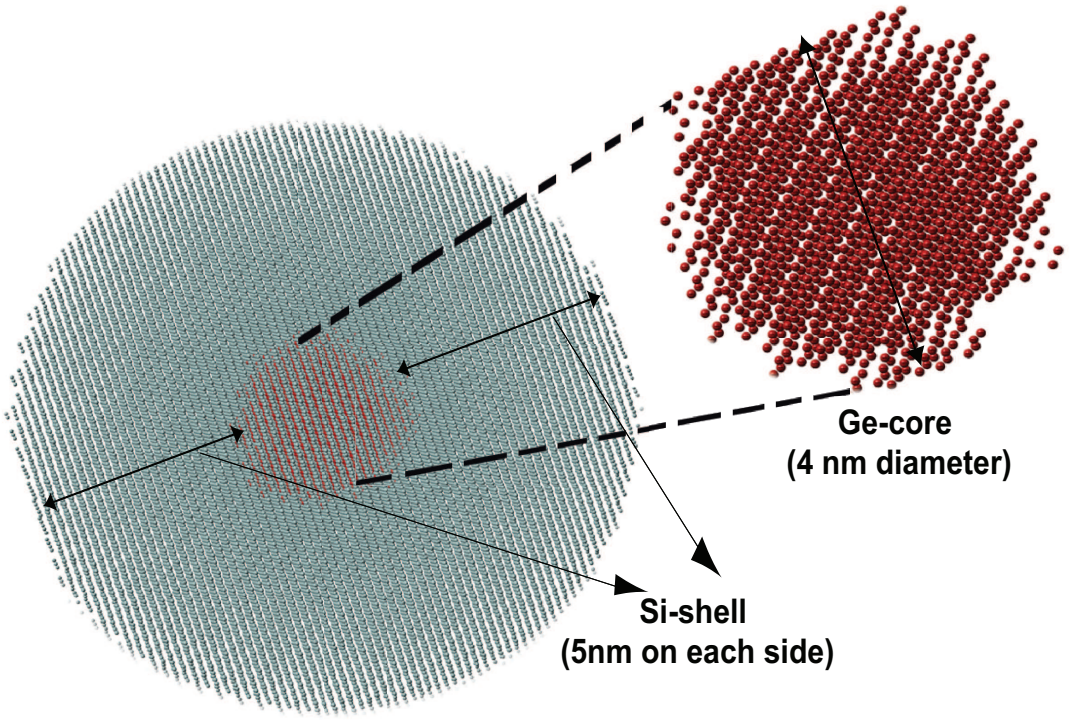

Figure 3.1: (Color online) Ge/Si core-shell NC (4 nm Ge-core and 5nm Si-shell around Ge-core). Total number atoms is 63976 (63448 Si atoms and 528 Ge atoms). The lighter gray dots are Si atoms and darker (red) dots are Ge atoms.

(10 orbitals $\times$ 2 spins), the total size of the basis is 2.4×10^6, however the Hamiltonian is very sparse. The eigenvalues and eigenstates are solved using a Lanczos algorithm. This model and implementation in NEMO3D has proven its reliability in predicting the electronic properties of nano-structures [144].

As shown in Fig. 3.2, the Ge core forms a quantum well for holes.

During a write process, the quantum well charges with holes. $|\Psi_0|^2$ is the spatial probability density of the highest energy orbital of the valence-band states. It is confined in the Ge core and exponentially decays in the Si shell. We refer to this state as the highest localized orbital (HLO) with an energy of E_0. The other state, $|\Psi_n|^2$, is the probability density of the highest delocalized orbital (HDO). This is the highest energy hole state that does not exponentially decay in the Si shell, i.e. it

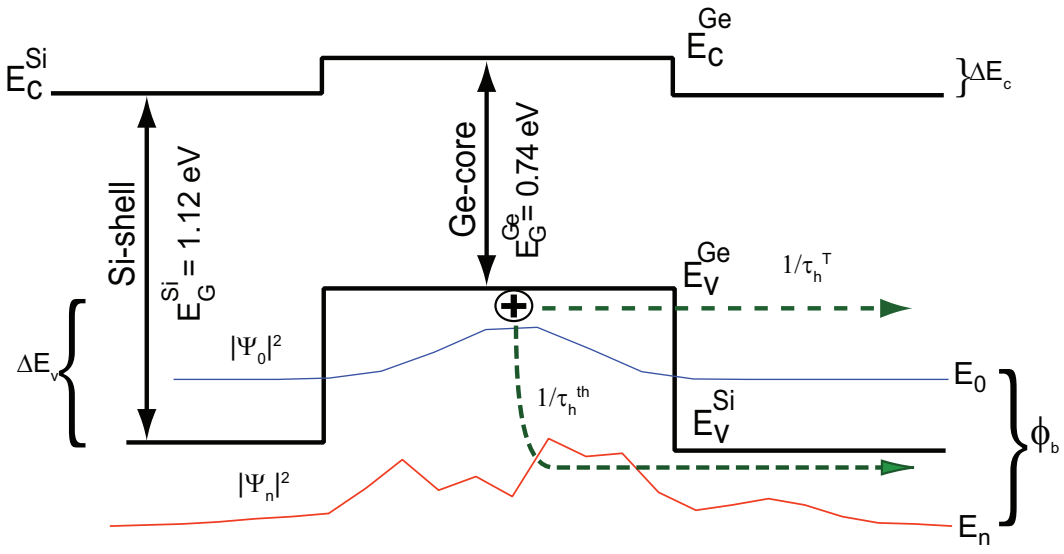

Figure 3.2: (Color online) Energy diagram and wave function distribution in the Ge/Si core-shell NC. The offsets shown in the band edges correspond to the bulk Si and Ge parameters used in the calculations. Confinement will alter the position of the energy levels. Dashed lines show the two different hole escape mechanisms resulting on the two lifetimes, τ_h^{th} and τ_h^T.

is delocalized throughout the Ge/Si NC. The corresponding energy is E_n where the quantum number n varies depending on the size of the Ge core. The energy difference between these two states gives the barrier height for thermionic emission of a hole in the HLO. A hole in the HLO escapes out of the Ge core through the Si shell either by direct tunneling or by thermionic emission.

Single-hole lifetimes are calculated with semi-classical and WKB approximations using the energy levels calculated numerically. The thermionic emission lifetime is determined by the height of the barrier over which the hole is emitted. Schneider and von Klitzing derived the thermionic emission lifetime (τ^{th}) in a quantum well as a function of the quantum-well width W as [145]

$$\tau_h^{th} = W\sqrt{\frac{2\pi m_w^*}{k_B T}}\exp\left(\frac{\Phi_b}{k_B T}\right) \tag{3.1}$$

where, m_w^* is the effective mass of the well i.e Ge core, k_B is Boltzmann's constant, and Φ_b is the potential barrier height. The potential barrier height is calculated from the energy difference between the HLO and HDO,

$$\Phi_b(E) = E_0 - E_n \tag{3.2}$$

The temperature (T) is maintained at room temperature (300 K).

The tunneling lifetime is the time spent by the hole inside the Ge core before tunneling out through the finite potential Si barrier. Following the analysis of [146], the tunneling lifetime (τ_h^T) of a localized hole tunneling through the the Si barrier is calculated using a WKB approximation [147],

$$\tau_h^T = W\sqrt{\frac{3m_w^*}{2\Delta E_0}}\exp\left(2\kappa t_{Si}\right) \tag{3.3}$$

where t_{Si} is the Si barrier thickness, κ is the evanescent wavevector in the Si, and m_w^* is the effective mass of the hole inside the Ge core. The prefactor in front of the exponential is the inverse of the attempt rate to tunnel out through the Si shell in the z direction. Since the quantization energy, ΔE_0, is three-dimensional, we divide it by a factor of 3 to get the kinetic energy related to the velocity in the z direction. ΔE_0 is the confinement energy of the HLO calculated as $\Delta E_0 = E_v^{Ge} - E_0$, where E_v^{Ge} is the bulk valence band edge of Ge. Since m_w^* is not known, we approximate it using the expression for the lowest energy level in a three-dimensional box with infinite potential confinement given by Eq. (4.2),

$$m_w^* \approx \frac{3\hbar^2}{2\Delta E_0}\left(\frac{\pi}{W}\right)^2 \tag{3.4}$$

3.4 Results and Discussion

This section illustrates the charge localization and delocalization of the wave functions within the Ge-Si Quantum well followed by the core-size variation effect on the bandgap, effective masses, decay factor, barrier height, quantum confinement energy, and lifetimes (both direct tunneling and thermionic). Finally, total lifetime of localized charge in the presence of tunnel oxide (SiO_2) is calculated.

3.4.1 Hole confinement characteristics

Fig. 4.3 shows the effect of the Ge core size on the quantum confinement energy, ΔE_0, and the barrier height, Φ_b. Core sizes range from 1 nm to 7.5 nm and the Si shell is fixed at 5 nm. The hole quantization energy, ΔE_0, drops from a maximum of 0.75 eV for the 1 nm core to 0.13 eV for the 7.5 nm core. Also plotted is the hole quantum confinement energy labeled ΔE_{Ge} calculated using the analytical expression

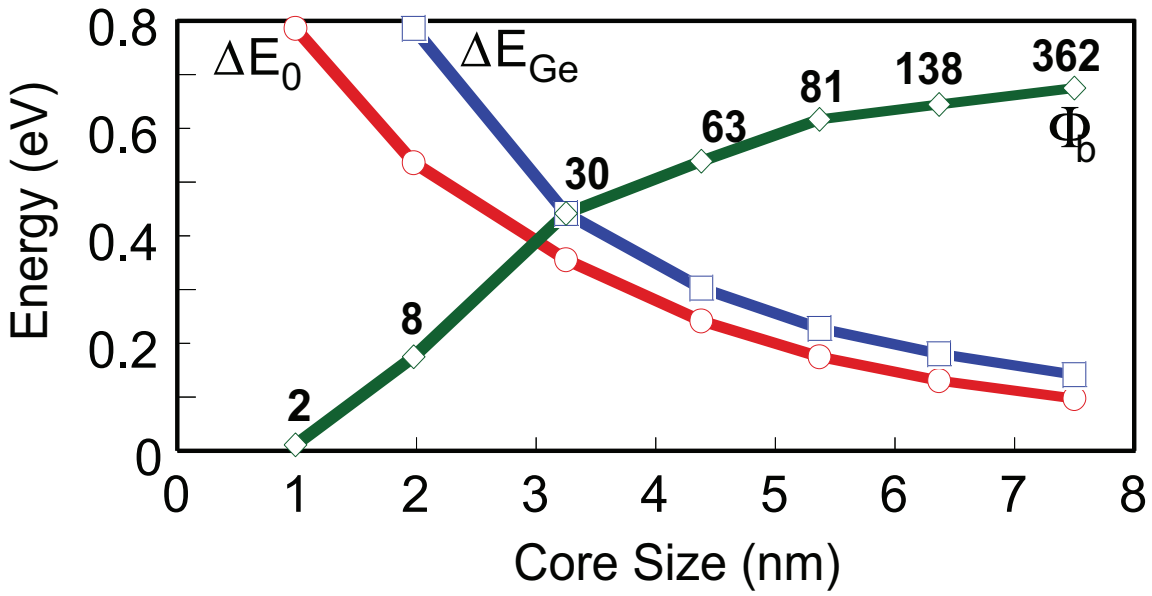

Figure 3.3: (Color online) Quantum confinement energy (ΔE_0 ($\circ$)) and barrier height (Φ_b ($\diamondsuit$)) as a function of Ge-core size. The number associated with each point on the Φ_b curve is the orbital number (n) associated with the barrier height. ΔE_{Ge} ($\square$) is the calculated quantum confinement energy using Eq. (1) from Ref. [13].

given in Eq. (1) of Ref. [13]. For larger diameters, the two values ΔE_0 and ΔE_{Ge} are in good agreement. At smaller diameters, the two values diverge as expected since the calculation of Ref. [13] was for an isolated Ge nanocrystal. In our Ge/Si core-shell nanocrystals, the hole confinement energy is limited to approximately the valence band offset of Ge and Si.

The barrier height rises from 12 meV for the 1 nm core to 0.67 eV for the 7.5 nm core. The numbers along the Φ_b curve indicate the quantum number n of the highest delocalized state used to calculate the barrier height from Eq. (A.6). For the 1 nm Ge core NC, there is essentially no hole confinement in the Ge core.

In earlier works [148] [28], the barrier height was formulated by calculating the difference between the bulk valence band edge of Si and Ge. In our approach, the finite barrier height Φ_b is calculated by taking the energy difference between the

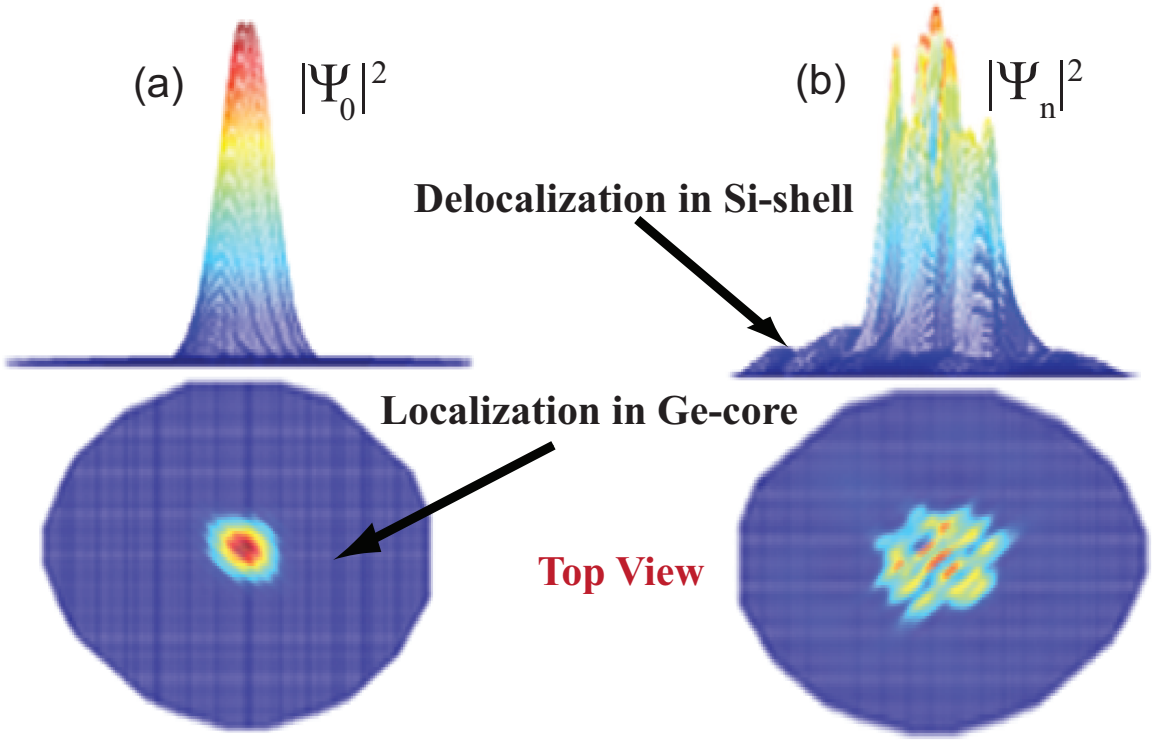

Figure 3.4: (Color online) Magnitude of the wavefunctions squared plotted for (a) the highest localized state and (b) the highest delocalized state in the Si(5 nm)-Ge(4 nm)-Si(5 nm) NC. The values are taken from a two-dimensional slice through the center of the NC. In this case, $n = 63$.

ground state energy of the HLO and the HDO using Eq. (A.6). In order to correctly identify the HDO, several hundred excited states are calculated and analyzed. Plots of $|\psi_0|^2$ and $|\psi_n|^2$ are shown in the Fig. 3.4 for a 4 nm Ge core. The energy (E_n) of $|\psi_n|^2$ defines the top of the barrier for thermionic emission of holes.

The localized hole effective mass in the Ge core region is calculated using Eq. (4.2), and plotted against the Ge core diameter in the Fig. 3.5. In the Ge/Si core-shell NC, the localized hole effective mass (m_w^*) decreases with the Ge core diameter, from $0.54m_0$ at 2 nm to $0.21m_0$ at 7.5 nm. The latter value is smaller than the Ge bulk hole heavy mass of $0.33m_0$ [149]. The 1 nm Ge core NC has a confinement energy of 12 meV, so the infinite potential confinement of Eq. (4.2) is not applicable.

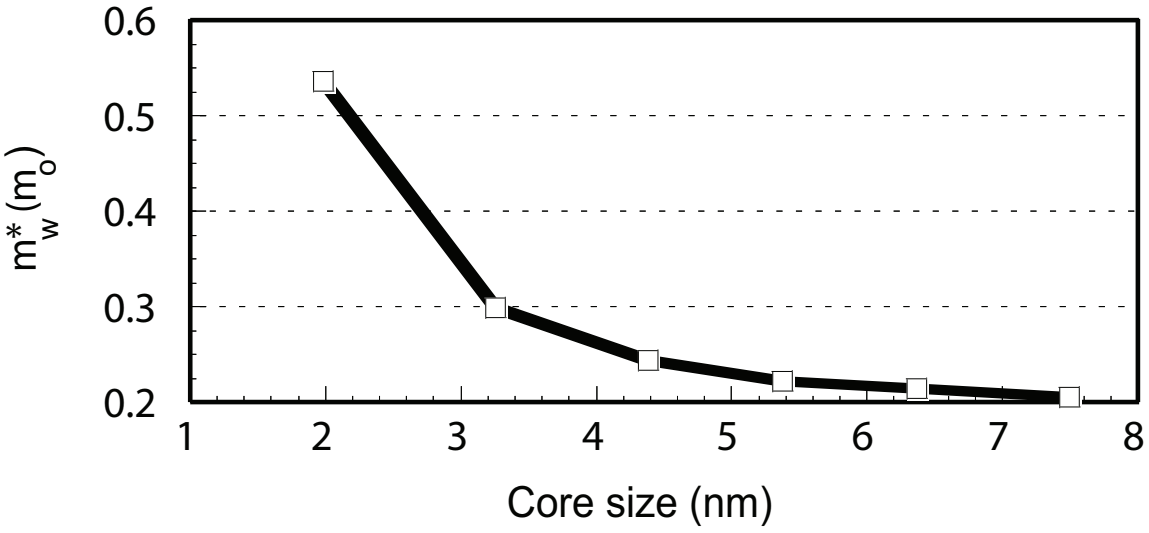

Figure 3.5: (Color online) Localized hole effective mass m^*_w in the Ge-core region as a function of Ge-core size.

Fig. 3.6 shows the calculated bandgap versus Ge core diameter for a fixed 5 nm Si shell. The bandgap is calculated from ground state electron and hole energy levels, $E_g = E_{c0}\text{-}E_0$, where E_{c0} is the energy of the lowest conduction band state. Also shown in Fig. 3.6 are E_{c0} and E_0. Increasing the size of the Ge core reduces quantum confinement of the hole energy E_0, but it has little effect on E_{c0}. This behavior is to be expected from the Type-II band lineup shown in Fig. 3.2. The quantization of the conduction band state is determined by the overall diameter of the NC which starts at 11 nm for a 1 nm Ge core. The confinement energy of a conduction band state in an 11 nm Si NC is very small. The observed decrement of the energy gap with the increasing core size is qualitatively consistent with the experimental results reported by [150] and [151]. At a core size of 1 nm, the bandgap is slightly greater than the bulk bandgap of Si (1.12 eV) [149]. At a core size of 4 nm, the energy gap is close to the bulk Ge bandgap. At the largest core size of 7.5 nm, the bandgap is 0.5 eV which is below the bulk Ge bandgap. This decrease below the bulk bandgap of Ge results

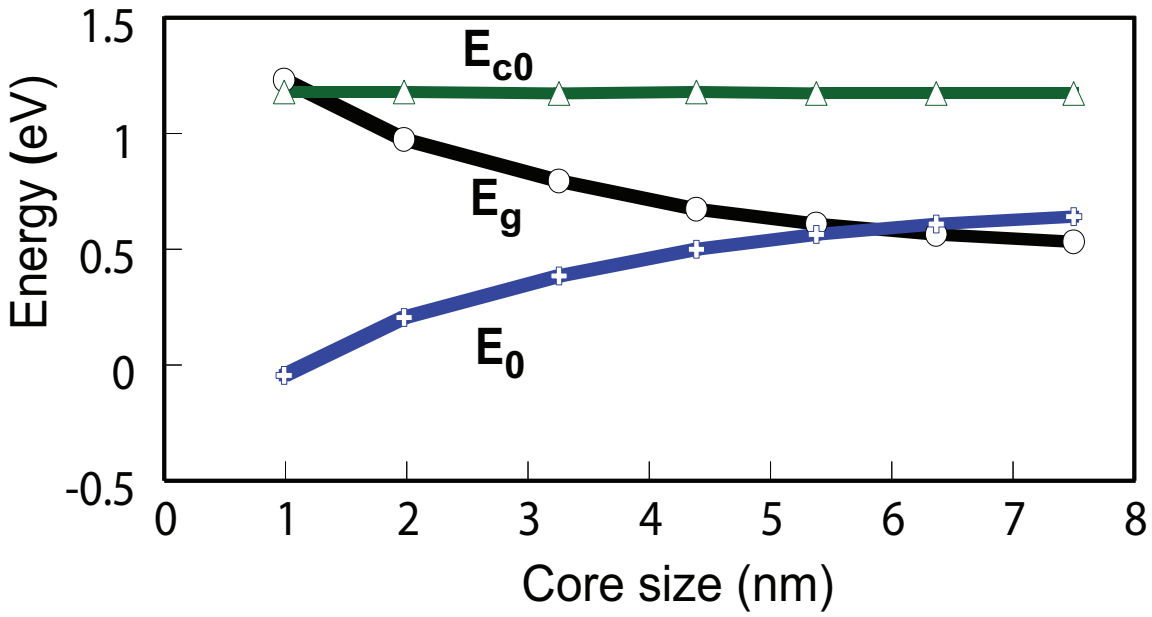

Figure 3.6: (Color online) Minimum energy gap (E_g), the valence band maximum E_0 and the conduction band minimum E_{c0}. as a function of the Ge-core size (nm) with a fixed 5 nm Si shell.

from the Type-II band offset shown in Fig. 3.2.

3.4.2 Decay constant and tunneling mass

The calculation of the direct tunneling lifetime in Eq. (3.3) requires the evanescent decay wavevector (κ) in the Si barrier which is not known. Since the bulk hole effective masses are meaningless in the NCs, κ must be evaluated numerically. To do so, we plot the magnitude of the wavefunction squared of the HLO in the Si barrier region and fit it to an exponential as shown in Fig. 3.7(a). The fit gives the value for κ for each different core size. The values are plotted versus core size in Fig. 3.7(b). As the core size increases, the confinement energy decreases, the barrier height increases, and κ increases as one would expect.

In analytical models, it is common to use a 'tunneling mass' to obtain the evanescent wavevector [152]. Using the values of κ from Fig. 3.7(b) and the values of Φ_b

from Fig. 4.3, we calculate the parabolic tunneling mass from

$$\kappa = \sqrt{\frac{2m_b^*\Phi_b}{\hbar^2}} \tag{3.5}$$

and plot it versus core diameter in Fig. 3.7(c). For all diameters, the parabolic tunneling mass is much heavier than the heavy hole mass of Si.

3.4.3 Hole Lifetimes

Using the decay constants from Fig. 3.7(b) and the barrier heights from Fig. 4.3, the lifetimes corresponding to thermionic emission and quantum tunneling are calculated from Eqs. (A.6) and (3.3), respectively. The results are plotted in Fig. 3.8. With a 5 nm Si shell, the hole lifetimes are limited by thermionic emission. The quantum tunneling lifetimes are many orders of magnitude larger. Thus, a 5 nm thick Si shell is unnecessary. Reducing the shell thickness reduces the overall NC size, increases packing density, and increases the capacitive coupling to the Si channel. For memory applications, the thickness of the Si shell should be reduced so that the quantum tunneling lifetime is comparable to the thermionic emission lifetime.

To estimate the Si shell thickness such that the quantum tunneling lifetime is equal to the thermionic emission lifetime, τ_h^T in Eq. (3.3) is set equal to τ_h^{th}, and then solved for Si shell thickness (t_{Si}). The Si shell thickness, as a function of Ge core size is plotted in Fig. 3.9. This estimate can be viewed as a zero order approximation, since changing the Si shell thickness, changes the quantization energy ΔE_0 which changes the decay constant κ. These effects are ignored in the estimate shown in Fig. 3.9.

In a NC memory, the hole must also escape through the SiO_2. To determine the total lifetime including the effect of the SiO_2, we assume that the Si shell is thick

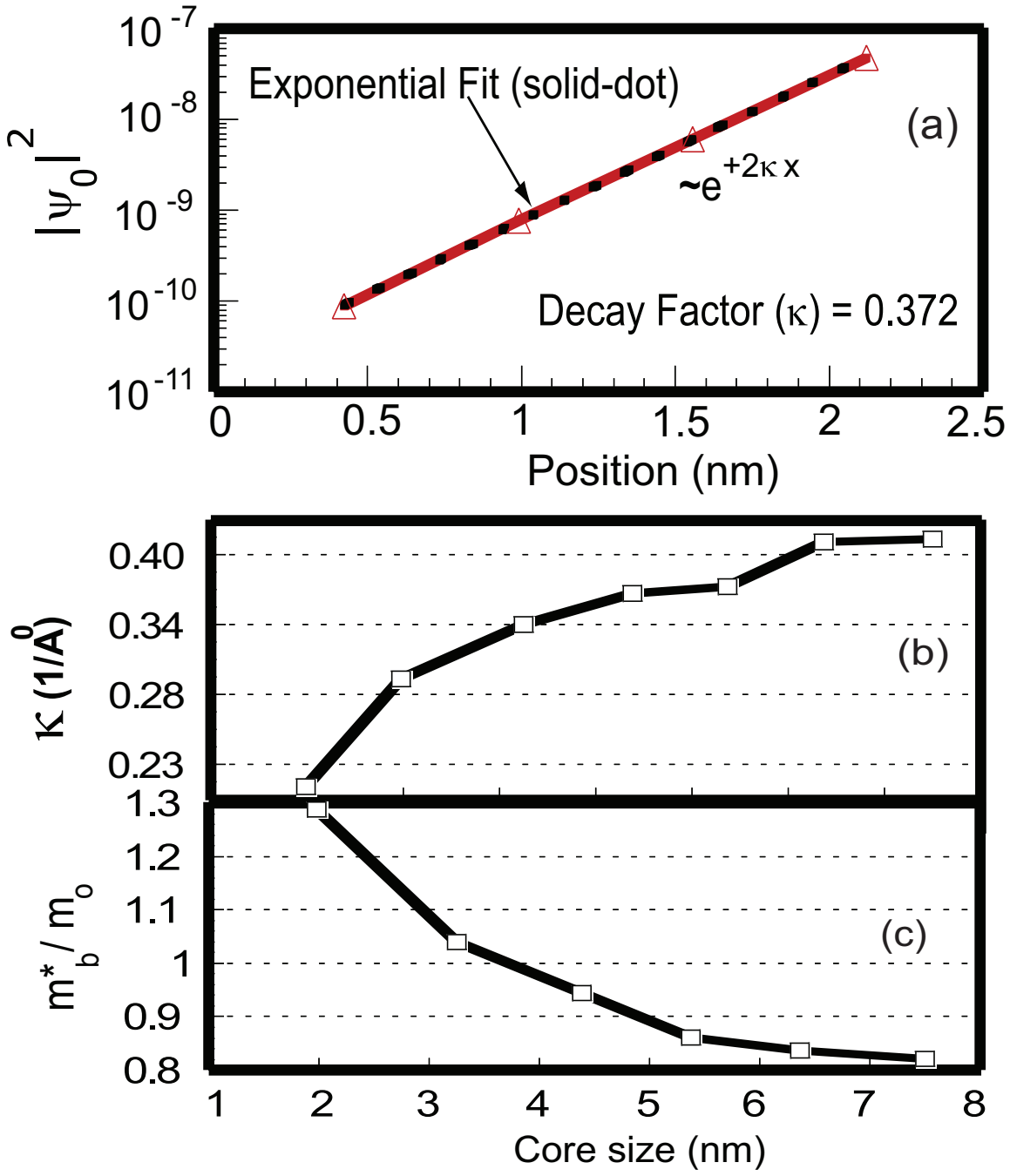

Figure 3.7: (Color online) (a) The magnitude squared of the HLO ($|\psi_0|^2$) plotted versus radial position in the Si shell and the superimposed exponential fit for the NC with a 4 nm Ge-core. (b) Ground state hole tunneling wave vector in the Si shell (κ) versus Ge-core diameter. (c) Parabolic tunneling effective mass (m_b^*) of the ground state hole in the Si-shell as a function of Ge-core size.

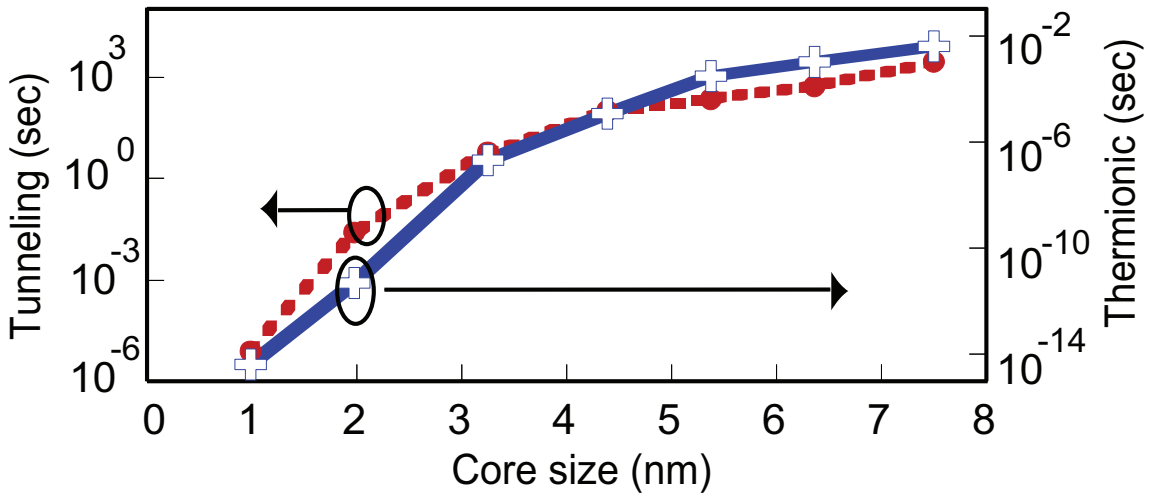

Figure 3.8: (Color online) Direct tunneling lifetime (dashed line) and thermionic lifetime (solid line) versus Ge-core diameter with a 5 nm Si shell.

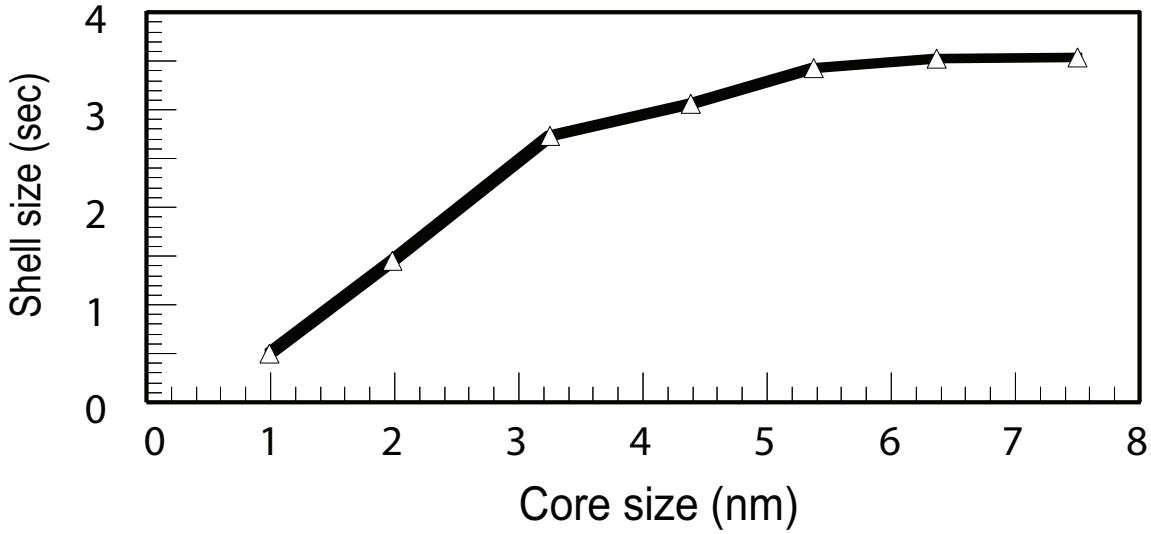

Figure 3.9: (Color online) Si shell size versus Ge-core size such that the quantum tunneling lifetime is equal to the thermionic emission lifetime.

enough such that escape from the Ge core through the Si shell is limited by thermionic emission. After thermionic emission out of the Ge core, the hole must then tunnel through the SiO_2 tunnel barrier. The hole tunneling mechanism from the Ge/Si/SiO_2 system is shown schematically using bulk band alignments and the 2-band, imaginary dispersion in the SiO_2 bandgap in Fig. 3.10. This lifetime can be calculated using the WKB expression of Eq. (3.3) replacing the prefactor to the exponential with the thermionic emission lifetime of Eq. (A.5). The prefactor is the inverse of the attempt rate for tunneling. Substituting the thermionic emission expression in for the attempt rate physically means that the attempt rate for tunneling through the SiO_2 is the thermionic emission escape rate out of the Ge core. Thus, the expression used to calculate the total hole lifetime including the effect of the SiO_2 is,

$$\tau_{\text{total}} = W\sqrt{\frac{2\pi m_w^*}{k_B T}}\exp\left(\frac{\Phi_b}{k_B T}\right)\exp\left(2\kappa_{ox} t_{ox}\right) \tag{3.6}$$

where, κ_{ox} is the decay constant in the SiO_2 and t_{ox} is the SiO_2 thickness.

Thus, the effect of the Ge core is to increase the hole lifetime by a factor of $\exp\left(\frac{\Phi_b}{k_B T}\right)$ compared to the hole lifetime in an all-Si NC. For example a 4 nm Ge core with a thermionic barrier of 0.5 eV increases the hole lifetime by a factor of 2×10^8 at room temperature compared to the lifetime of a pure Si NC.

Once a hole escapes from the Ge core, it is in the HDO state with energy E_n. At this energy, κ_{ox} is determined analytically using Kane's two-band model described in Ref. [153],

$$\kappa_{ox} = \sqrt{\frac{2m_{ox}^*}{\hbar^2 E_g}(E_c - E_n)(E_n - E_v)} \tag{3.7}$$

with parameters values of $m_{ox}^* = 0.6m_0$, E_g = 9 eV, E_v = -4.84 eV and E_c =4.24 eV, taken from Ref. [153]. The decay constants in the SiO_2 are practically independent

of the Ge core size. The decay constants for the minimum and maximum Ge core sizes of 1 nm and 7.5 nm are 0.5918 $Å^{-1}$ and 0.5916 $Å^{-1}$, respectively.

The total lifetimes, calculated for three different oxide thicknesses are plotted versus Ge core size in Fig. 3.11. The short lifetime of ~ 1 second for the thin oxide (1 nm) is consistent with the experimental result reported for Ge:SiO_2/Si system [78]. The retention lifetime of ten years (3×10^8 s), required for a practical QD based non-volatile memory device, is achieved with a SiO_2 thickness of 3 nm and a Ge core size of 3 nm.

3.5 Conclusion

The electronic states of ideal Ge-core/Si-shell NCs are calculated for a fixed 5 nm Si shell and Ge cores ranging from 1 nm - 7.5 nm diameters. Calculations are performed atomistically using a nearest-neighbor, $sp^3d^5s^*$ tight-binding model as implemented in NEMO3D. The wavefunctions and energies are used to determine decay constants and barrier heights for calculations of quantum-tunneling and thermionic emission lifetimes. For a Ge core diameter of 3 nm and a Si shell thickness of ≥ 3 nm, the escape rate of a hole out of the Ge core is given by the thermionic emission rate. This then becomes the attempt rate for tunneling through the SiO_2. The thermionic barrier presented by the Si shell increases the hole lifetime by a factor of $\exp\left(\frac{\Phi_b}{k_B T}\right)$ compared to the hole lifetime in an all-Si NC. A retention lifetime of 10 years is achieved with a SiO_2 thickness of 3 nm, a Ge core size of ≥ 3 nm, and a Si shell thickness of ≥ 3 nm.

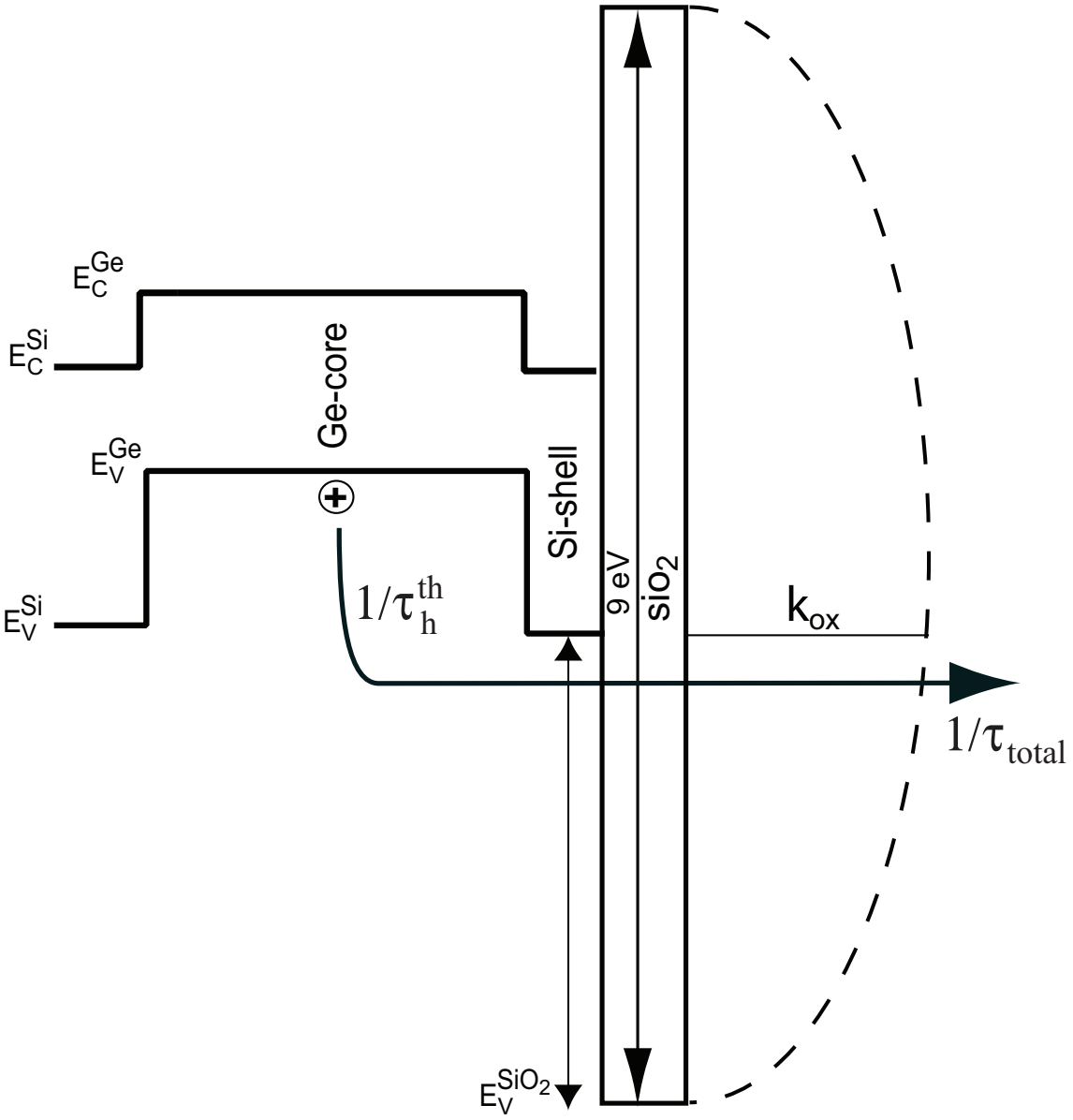

Figure 3.10: Band diagram of the bulk Ge/Si/SiO_2 system. The dashed line illustrates the imaginary dispersion in the SiO_2 bandgap, and the horizontal line shows the energy at which κ_{ox}) is calculated from Eq. (3.7). The short-dashed green line illustrates the thermionic escape rate ($1/\tau_h^{th}$) that provides the attempt rate for quantum tunneling through the SiO_2.

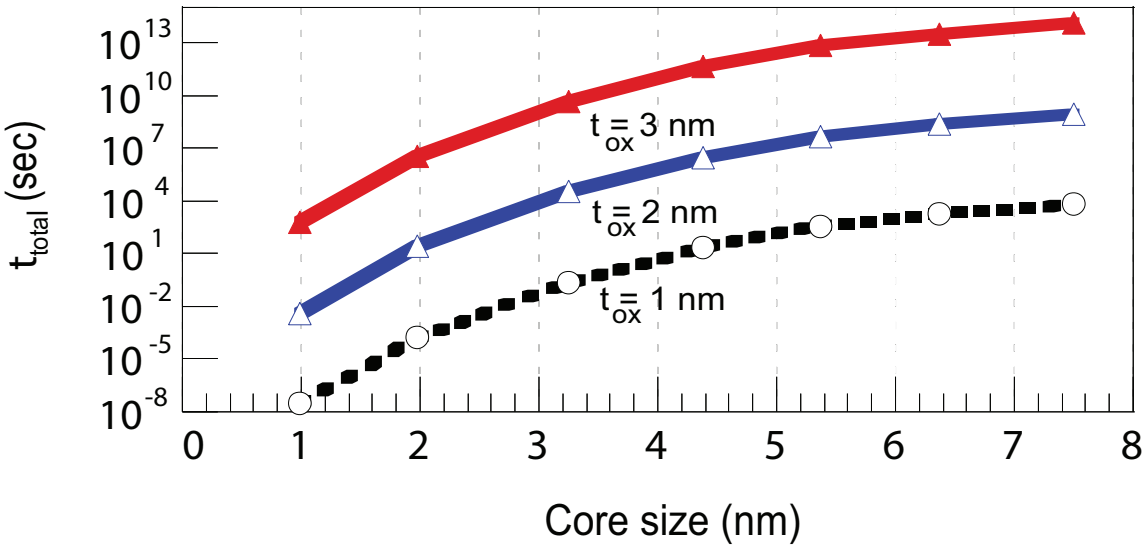

Figure 3.11: (Color online) Total hole lifetime in the Ge/Si/SiO_2 system at SiO_2 thicknesses of 1, 2 and 3 nm.

Chapter 4

Electronic states of experimentally observed dome-shaped Ge/Si Nanocrystal with crescent-shaped Ge-cores

4.1 Introduction and Motivation

Several experimental groups [154–157] have reported the observation of dome-shaped Ge/Si NCs because of the atomistic heterogenity between the Ge and Si layer. Instead of ideal spherical Ge-core, experimental characterization reveals a crescent-shaped Ge-core in the dome-shaped Ge/Si NCs. In these nanostructures, the Si-cap thickness, the crescent-shaped Ge-core thickness, and the overall size distribution of Ge/Si dome shaped structures influence various device parameters, such as confinement energies, activation energies, and carrier lifetimes. Early theoretical works [26, 72, 158] have provided a simplistic explanation of the retention mechanism based on the smaller

bandgap of Ge with respect to Si using continuum models, ignoring strain and shape effects. However to include atomic scale inhomogeneities strain and shape effects at these nanostructures, an atomistic model should also be considered.

4.2 Objectives

In this work, we carry out such an atomistic study of the low-energy electronic states in realistically dome shaped Ge/Si core-shell NCs with experimentally observed crescent-shaped Ge-cores. Energy levels and related parameters are used to calculate hole lifetimes as a function of Ge-core and Si-cap thickness.

4.3 Model and Theory

The specific type of heterostructure NC studied is shown in Fig. B.1. The inner Si layer forms when Si is grown on the SiO_2 substrate. It has been found to have little influence on the overall electronic properties of the system [159]. The Si-capping layer prevents Ge atoms from being oxidized during the control oxide growth [160], and it preserves the dome shape and size during growth [161, 162]. A maximum Si-capping layer thickness of 3.5 nm is chosen based on previous theoretical [2, 163] and experimental work [164] on Ge/Si core-shell nanocrystals where it was shown that beyond this thickness, the carrier dynamics and other related electronic properties remain constant. The Si layers serve as the barriers for the hole in the Ge-core layer forming a TYPE-II heterojunction as illustrated in Fig. B.1.c.

The electronic states are modeled using 20-band $sp^3d^5s^*$ nearest-neighbor, empirical-tight-binding model with spin-orbit (SO) coupling as implemented in NEMO3D and described in Ref. [120]. The strain due to the lattice mismatch between Ge and Si

is calculated using the valence-force-field (VFF) model with Keating potentials, and included in the Hamiltonian during the electronic structure calculation. The surfaces of the NC structures are faceted. The energies of the dangling bonds at the surface are shifted by 20 eV so that the effect of the dangling bonds on the density of states near the energy gap is negligible [143]. The largest simulated NC contains 8440 atoms. With 20 orbitals per atom (10 orbitals $\times$ 2 spins), the total size of the basis is 1.688×10^5, however the Hamiltonian is very sparse. The eigenvalues and eigenstates are solved using the Lanczos algorithm. The accuracy of these models has been tested through quantitative agreement of simulations with experimental data in SiGe systems [165], strained InGaAs quantum dots [166], and a single impurity in Si FinFets [144].

The nanocrystal consists of a inner Si layer, a crescent-shaped Ge-core, and a Si cap as shown in Fig. B.1. The Si atoms and Ge atoms in both the frontal view (Fig. B.1.a) and the cross-sectional view (Fig. B.1.b) are marked with light (yellow) and dark (red), respectively. For all nanocrystals, the diameter of the base is fixed at 5nm. The maximum Ge-core thickness in the vertical direction is varied from 1 - 3.5nm. Hereafter, this vertical thickness is referred as the Ge-core thickness. The maximum Si cap thickness is also varied from 1 - 3.5nm. The inner Si layer height is fixed at 5nm. The nanocrystals are grown in the [100] direction.

A schematic band diagram is shown in Fig. B.1.c. The valence band edges and conduction band edges for the Ge/Si materials are labeled as E_V^{Ge} / E_V^{Si} and E_C^{Ge} / E_C^{Si}, respectively. The valence band offset is labeled as ΔE_V. The bulk bandgaps of Ge and Si are 0.74 and 1.12 eV, respectively. The thermionic emission process of the hole escaping from the Ge-core region to the Si-region is represented by the dotted arrow. The corresponding escape rate is $1/\tau^{th}$.

The thermionic emission lifetime is determined using semi-classical and WKB

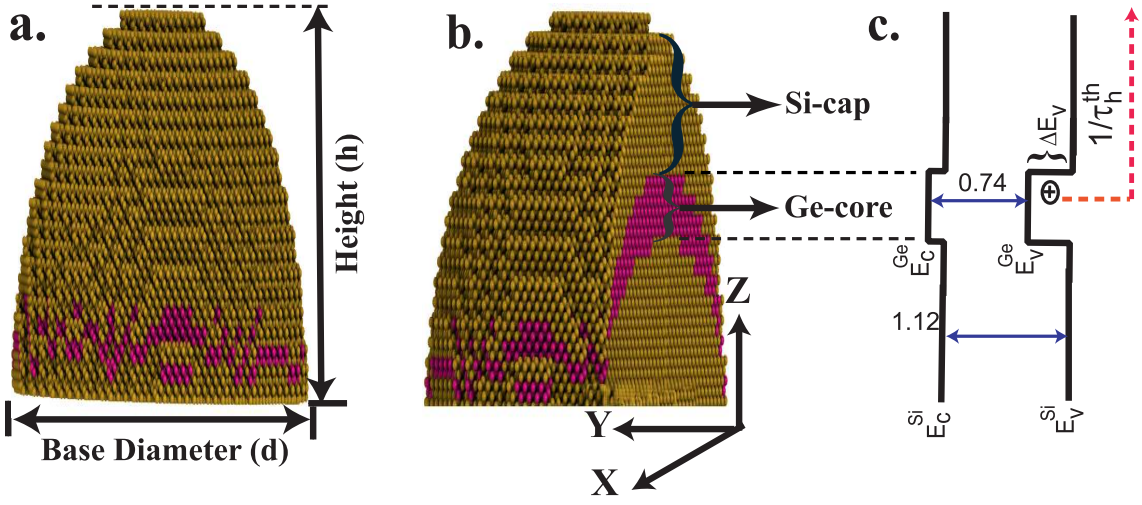

Figure 4.1: (Color online) Front-view (a) and cross-sectional-view (b) of a dome-shaped Ge/Si NC with a Ge-core and Si-cap thickness of 3nm. The base diameter and the inner Si layer height is maintained at 5nm. The total number of atoms is 7696, with 2360 Si atoms in the capping layer, 1960 Ge atoms in the core layer and 3376 Si atoms in the inner layer. The lighter gray (red) dots are Ge atoms and the darker (yellow) dots are Si atoms. (c) Bulk energy level lineups. The energy values shown correspond to the band gap of the bulk Si and Ge materials. The valence and conduction band edges for the Ge and Si materials are labeled as E_V^{Ge} and E_V^{Si}, E_C^{Ge} and E_C^{Si}, respectively. Similarly, the valence band offset is identified as ΔE_V. The dotted arrow shows the thermionic hole escape mechanism with an escape rate of $1/\tau^{th}$.

approximations with the numerically calculated energy levels as input. Schneider and von Klitzing derived the thermionic emission lifetime (τ^{th}) in a quantum well as a function of the quantum-well width, W, as [145],

$$\tau^{th} = W\sqrt{\frac{2\pi m_w^*}{k_B T}}\ \exp\left(\frac{\Phi_b}{k_B T}\right) \tag{4.1}$$

where, m_w^* is the hole effective mass in the well, k_B is Boltzmann's constant, and Φ_b is the potential barrier height. Here, the quantum-well width W is the maximum vertical thickness of the Ge-core. The temperature $T = 300$K. Since m_w^* is not known, we approximate it using the expression for the lowest energy level with infinite potential confinement as,

$$m_w^* \approx \frac{\hbar^2}{2\Delta E}\left(\frac{\pi}{W}\right)^2 \tag{4.2}$$

where, ΔE is the confinement energy defined as,

$$\Delta E = E_V^{Ge} - E_0 \tag{4.3}$$

where E_0 is the ground state of the hole. The barrier height, Φ_b is calculated from

$$\Phi_b = E_0 - E_V^{Si} \tag{4.4}$$

where, E_V^{Si} is the valence band edge of the bulk Si . Based on earlier published results on the spherical Si/Ge/Si system, we find that E_V^{Si} is a good approximation to the energy of the first delocalized hole state with an energy below the Si valence band edge [2].

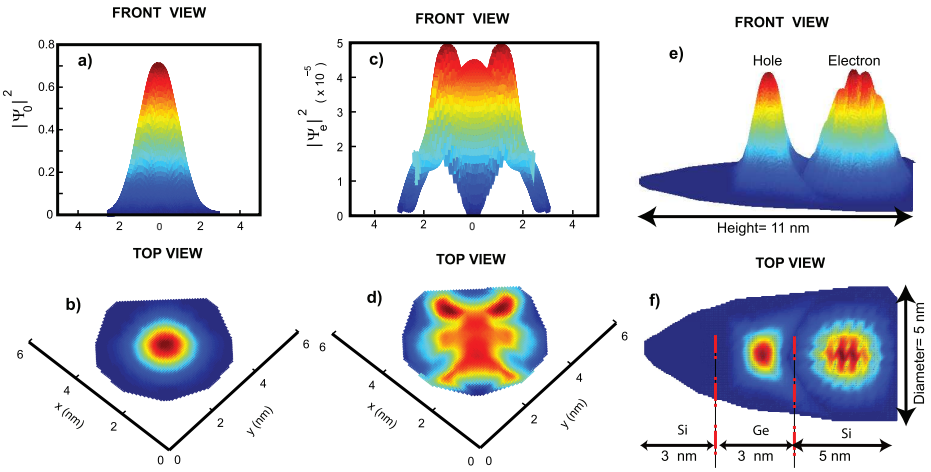

Figure 4.2: (Color online) Probability densities of the ground hole state, $|\Psi_0|^2$ (a,b), the lowest electron state, $|\Psi_e|^2$ (c,d), and both states superimposed (e,f). The red (light) and blue (dark) isosurfaces represent maximum and minimum probability densities, respectively. The Ge-core and Si-cap thickness is 3nm. The inner Si layer height and the base diameter are 5nm. The height of the NC is 11nm. In a-d, the two-dimensional cross-section of the probability density is taken through the center of the Ge-core region in the $x-y$ plane at $z = 6.5$nm. In e-f, the two-dimensional cross-section is taken through the center of the base in the $x-z$ plane at $y = 2.5$ nm.

4.4 Results and Analysis

This section illustrates the effect of the core and cap size variation on the energy gap, effective mass, barrier height, quantum confinement energy, and thermionic life time.

4.4.1 Carrier confinement characteristics

Si and Ge form a TYPE-II band alignment. A deep quantum well for holes in the Ge-core region is formed by the large valence band offset between the valence bands of Ge and Si. A shallow quantum well for electrons is formed in the Si region by the small conduction band offset between the conduction bands of Ge and Si .

The depth of the potential wells formed in the Ge-core region, for both the holes and electrons, can be verified by analyzing the probability densities of the ground

state and excited state, in the core region.

The existence and spatial separation of the electron and hole quantum wells result in localization and spatial separation of the electron and hole wavefunctions. Fig. 4.2.(a-d) shows a cross-section of the hole and electron probability densities in the $x - y$ plane taken at the center of the Ge-core region with a Ge-core and Si-cap thickness of 3nm and an inner Si layer height and the base diameter of 5nm. The probability density ($|\Psi_0|^2$) of the hole state is strongly localized in the Ge-core as shown in Fig. 4.2.(a,b). The probability density of the electron state in that same spatial region is five orders of magnitude smaller as shown in Fig. 4.2.(c,d). The electron wavefunction is localized in the inner Si layer. The spatial separation of the electron and hole wavefunctions is evident in Fig. 4.2.(e,f) in which the electron and hole probabilities are superimposed on a single vertical cross-section of the NC. This spatial separation affects optical properties such as oscillator strengths and electron and hole recombination times.

4.4.2 Confinement effects on the electronic states

The energy difference between the ground state hole and ground state electron states, also known as energy gap, is primarily a function of the Ge-core thickness and varies little with the thickness of the Si-cap. Fig. 4.3.a shows the effect of the Ge-core and Si-cap thickness on the energy gap. The maximum energy gap is 1.1 eV when both the core and cap layers are 1nm thick, and the minimum energy gap is 0.78 eV when both the core and cap are 3.5nm. The energy gap remains high between 1 eV to 1.1 eV when the Ge-core thickness is maintained at 1nm, independent of the Si capping layer thickness. This result is consistent with the experimentally observed value of 0.80 eV for a 0.9nm Ge-core thickness when the Si-capping layer thickness

is greater than 5nm [167]. When the Ge-core thickness increases beyond 3nm, the energy gap approaches the bulk Ge energy gap of 0.75 eV, consistent with other published results [2, 13, 168].

The hole confinement energy, ΔE, is also primarily dependent on the Ge-core thickness and independent of the Si-cap thickness, as shown in Fig. 4.3.b. For any fixed Ge-core thickness, ΔE decreases by at most ~ 0.035 eV as the Si-cap thickness increases from 1nm to 3.5nm. Increasing the Ge-core thickness from 1nm to 3.5nm reduces ΔE by 50%. For a 3.5nm Si-cap thickness, ΔE decreases from 0.48 to 0.25 eV as the Ge-core thickness increases from 1nm to 3.5nm.

4.4.3 Thermionic lifetime

As the Ge-core thickness increases, the hole confinement energy decreases and the barrier height for the hole to escape from the quantum well increases. The calculated barrier height (Φ_b) is plotted against the Ge-core and Si-cap thickness in the Fig. 4.4.a. Φ_b increases from 0.28 to 0.51 eV as the Ge-core thickness increases from 1nm to 3.5nm with a Si-cap thickness of 3.5nm. Barrier heights of 0.28 and 0.39 eV for the 1 and 1.5nm thick Ge-cores and 3.5nm thick Si-cap are in line with the experimentally measured activation energies for the 1–1.5nm high Ge NCs sandwiched between two thick Si-spacer layers [169]. For Ge-core thicknesses greater than 3nm, Φ_b saturates consistent with other reports [2, 163, 170]. The maximum change in Φ_b as the Si-cap thickness increases from 1nm to 3.5nm is 10%, and this insensitivity to cap thickness is consistent with photoluminescence measurements [156, 170].

The hole effective mass (m_w^*), calculated from Eq. 4.2, is a strong function of the Ge-core thickness (W) as shown in Fig. 4.4.b. In a parabolic band model, the confinement energy is inversely proportional to the square of the confinement,

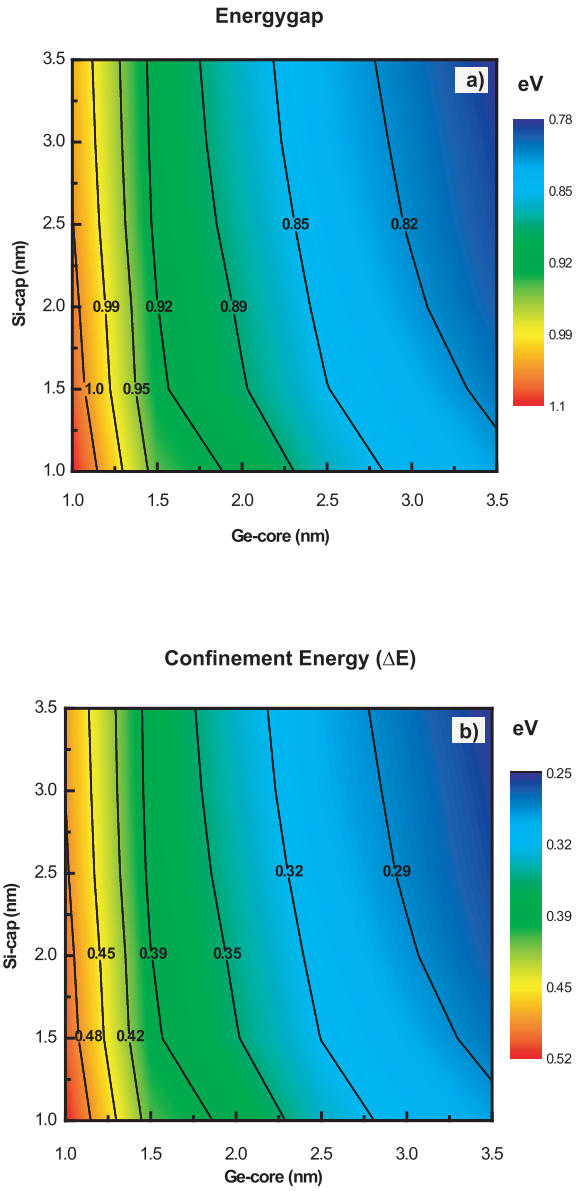

Figure 4.3: Energy gap (a), and quantum confinement energy (ΔE) (b) as a function of Ge-core and Si-cap thickness.

$\Delta E \propto (1/W)^2$. Thus, Eq. (4.2) gives a constant value for m_w^* in a parabolic band model. The dependence of m_w^* on W shows the large nonparabolicity of the hole energy dispersion. The hole effective mass is 0.7 m_0 when W = 1nm, and it drops to 0.1 m_0 when W = 3.5nm. This minimum value lies between the Ge effective mass values of the bulk heavy-hole and the bulk light-hole indicating mixing of the two states.

The thermionic lifetime of the hole (τ^{th}) depends exponentially on the Ge-core thickness through the exponential dependence on barrier height in Eq. A.5, and this dependence is shown in Fig.4.4.c. With a 3.5nm Si cap, as the Ge-core thickness increases from 1nm to 3.5nm, the thermionic hole lifetime increases from 10^{-9} s to 10^{-5} s. The Ge-core increases the lifetime of a hole by a factor of $\exp\left(\frac{\Phi_b}{k_B T}\right)$ compared to the lifetime of a hole in an all-Si NC. For example, a 3.5nm Ge-core, with a 3.5nm Si-cap, has a thermionic hole barrier of 0.51 eV, which increases the hole lifetime by 3×10^8 at room temperature compared to the lifetime of a hole in a pure Si NC.

4.5 Conclusion

The electronic states in realistically shaped Ge/Si core-shell NCs with crescent-shaped Ge-cores have been calculated with an atomistic model. The electron and hole wavefunctions are spatially separated. The hole wavefunction is localized in the Ge-core and the electron wavefunction is localized in the inner Si region. The effect of the Ge-core and Si-cap thickness on the energy gap, confinement energy, energy barrier height, effective mass, and thermionic hole lifetime are determined. As the Ge crescent thickness increases from 1nm to 3.5nm with a 3.5nm Si cap, the hole confinement energy decreases from 0.52 to 0.28 eV, the barrier height for a hole to escape into the Si valence band increases from 0.25 to 0.51 eV, and the resulting thermionic hole

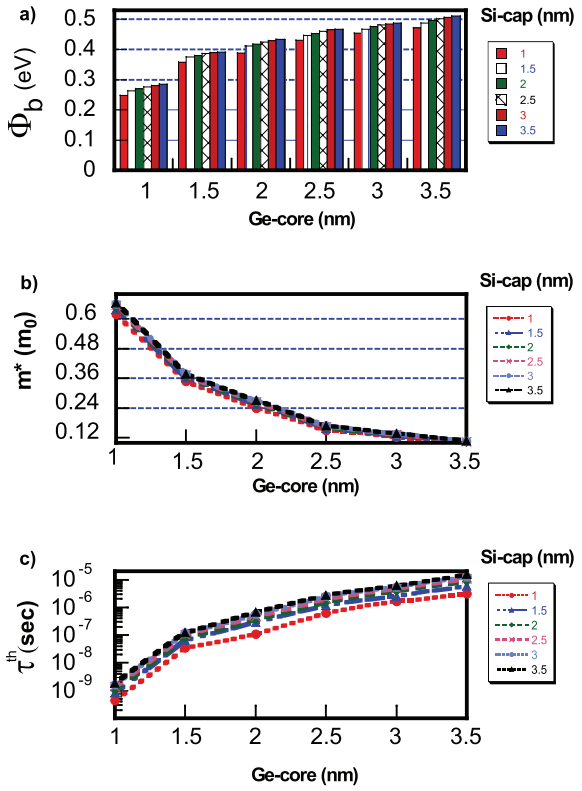

Figure 4.4: Energy barrier height (Φ_b) (a), localized hole effective mass (m_w^*) in the Ge-core region (b), and thermionic lifetime (τ^{th}), as a function of Ge-core and Si-cap thickness.

lifetime increases from 10^{-9} to 10^{-5} s. For the largest NC with Ge-core and Si-cap thickness of 3.5nm, the thermionic lifetime is on the order of 10 microseconds. The thermionic barrier presented by the Si shell increases the hole lifetime by a factor of $\exp\left(\frac{\Phi_b}{k_B T}\right)$ compared to the thermionic hole lifetime in an all-Si NC. The maximum increase is 3×10^8 at $T = 300$K.

Chapter 5

Effect of Strain on the Electronic and Optical Properties of Ge/Si Dome Shaped Nanocrystal

5.1 Introduction and motivation

Aggressive scaling and the demand for high speed electronic and photonic devices have resulted in a large effort to understand carrier dynamics in heterostructure based nanostructures, such as InAs/GaAs [171–173], CdTe/CdSe [174,175] and Ge/Si [1–3, 160, 176–184]. Ge/Si based nanostructures are of interest due to their compatibility with the existing silicon-based technology. Furthermore, Ge/Si nanostructures with various shapes (domes, wire, lens, and pyramids) have been fabricated and integrated in optical and electrical devices using advanced fabrication techniques such as molecular beam epitaxy (MBE) [185], self-assembly, [186–188] and chemical vapor deposition (CVD) [160]. These devices exhibit size dependent characteristics and show potential for future devices

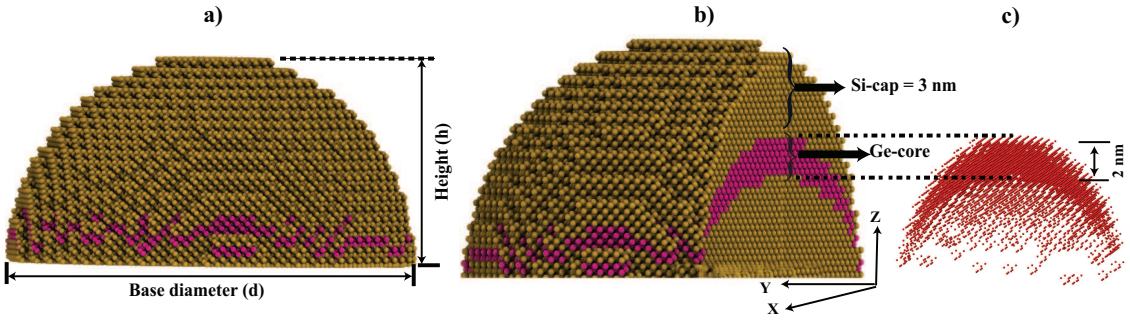

Figure 5.1: (Color online) One of the simulated Ge/Si dome-shaped NC structures with a 20 nm base diameter (b) and 10 nm overall height (h). a) Front view b) Cross-section view and c) Extracted Ge-core. The base diameters of the simulated structures varies from a minimum value of 5 nm to the maximum value of 45 nm. The NC height is fixed at 10 nm.

such as thin-film field effect transistors [177], flash memory [160, 179], DotFETs [189], photodetectors [190], solar cells [191, 192], and quantum computers [181, 182, 193, 194]. Inter-level optical transitions in Ge/Si NCs have attracted interest due to the TYPE-II band alignment at the Ge and Si interface causing the holes and electrons to be spatially separated in the Ge and Si regions, respectively. There is significant effort to exploit these complex nanostructures to maximize the performance of future devices [195–199].

Researchers have recently been successful in fabricating high quality Ge/Si NCs of different lateral dimensions and shapes in both single and multiple layers [185, 200–203]. Of the various experimentally observed NC shapes, hut-shaped and dome-shaped Ge/Si NCs have unique electronic and optical properties [204]. Dome-shaped Ge/Si NCs with the curved bounding facets can relieve strain more efficiently compared to the hut, pyramid, or ring shaped NCs [205].

Because of the 4.1% lattice mismatch between Si and Ge, the strain plays a key role in determining the energy levels [206, 207]. Strain can shift both the conduction and valence states, alter the energy gap [208, 209], change the carrier dynamics [1, 3],

modulate optical properties, and modify spin relaxation times [210]. In general, the strain distribution in Ge/Si NCs influences the shape and depth of the potential wells for electronic excitations, charge confinement, and carrier dynamics [194].

Designing optoelectronic devices using Ge/Si NCs benefits from an atomistic model in both the Ge-core and the surrounding Si regions. When evaluating the polarization dependent interlevel transitions, a fully atomistic treatment is necessary to capture atomistic effects at the Ge/Si interface that can mix electronic levels and modify the polarization [211]. Several theoretical works have supported experimental findings [212, 213], however, there are few large-scale, atomistic studies that include strain inhomogeneity while matching experimental shapes and sizes [214]. Lavchiev and et al. observed a huge discrepancy between experimental and theoretical findings in the optical and electrical properties of dome and pyramid shaped, Si-capped, Ge NCs embedded in the Si-matrix [215]. They attributed this discrepancy to their model's inability to realize the atomistic representation of the experimental structure. Recently, Usman et al. published an extensive theoretical study on III-V NCs highlighting the importance of strain and shape on the overall optoelectronic properties [166, 172, 216, 217]. However, similar studies of the Ge/Si system are lacking.

The diameter and the aspect ratio (AR), the ratio of the height (h) to the base diameter (d), determine the overall stability of the NC [196]. A decrease in the aspect ratio corresponds to a morphological transition from a dome to an energetically favorable superdome resulting from excessive Ge deposition [202, 218, 219]. Recently, good control over the height of a Ge/Si NC system has been demonstrated with less control over the diameter [220–224]. This motivates our study of the diameter dependent properties of Ge/Si NCs. The atomistic structure of the 20 nm diameter NC is shown in Fig. 5.1. The NC cross-section in Fig. 5.1(b) shows the half-moon like Ge-core sandwiched between the two Si layers. The Ge core is extracted and illustrated in

Fig. 5.1(c). This crescent shaped Ge-core has been observed experimentally by Lee et al. [202]. Experimentally, the Si-capping layer is used not only to prevent Ge atoms from being oxidized during the control oxide growth, [160] but also to preserve the dome shape and size during growth [161, 162]. Prior experimental studies of Ge/Si heterostructures demonstrated sharp interfaces with minimal intermixing [225, 226]. We leave the investigation of intermixing at the interface for a future study. The Ge and Si interfaces are inhomogeneously strained due to the lattice mismatch between Si and Ge.

We present a systematic computational study of the confinement and strain effects on the electrical and optical properties of Ge/Si dome-shaped NCs with crescent-shaped Ge-cores. The spatially resolved strain distribution is calculated atomistically throughout the structure. The strain modulated energy-level and energy gap shifts are determined. Optical transition rates are calculated. The effect of the lattice strain on the electronic properties of dome-shaped Ge/Si NCs is analyzed by making one-to-one comparisons of device properties calculated from strained and unstrained systems. Electronic structure calculations are performed with NEMO3D [115]. The accuracy of the models have been verified by comparison with experimental data in SiGe systems [165], strained InGaAs quantum dots [166], a single impurity in Si FinFets [144, 227, 228] and Si-based single electron transistors [229, 230].

5.2 Structure and Method

The growth direction of the NCs is the [001] direction. The heights of all NCs are fixed at 10 nm, and the diameters are varied from 5 nm to 45 nm. The thicknesses of the base, core, and cap at the center of the NCs are fixed and they taper towards the perimeter as shown in Figs. 5.1(b,c). At the NC center, the thickness of the base,

core, and cap are 5 nm, 2 nm, and 3 nm, respectively.

Geometry relaxation uses an atomistic valence force field (VFF) model with additional interaction terms included in the Keating model, and the minimization procedure employs the conjugate gradient technique [115, 231–234]. This approach has been extensively used to model strain in complex quantum dots and other nanostructures, and it has qualitatively compared well with the various experimental data [144, 165, 177, 228, 229]. During relaxation, the z-position of the bottom layer of the Si atoms is fixed, and they are free to move in x and y. Free boundary conditions are applied at all other surfaces. These boundary conditions approximate those during growth of a NC on an amorphous SiO_2 layer as is done in NC memory applications [160, 179].

Once the structure is relaxed to its minimum energy configuration, the strain components for all of the atomic sites are calculated using the formalism introduced by Pryor and co-workers [231]. In the relaxed structure, each atom is surrounded by 4 nearest neighbors at positions $\mathbf{R}_j$ in a strained tetrahedron. The strained tetrahedron edges given by the difference vectors $\mathbf{R}_{i,j} = \mathbf{R}_j - \mathbf{R}_i$ are related to the unstrained tetrahedron edges $\mathbf{R}^0_{i,j} = \mathbf{R}^0_j - \mathbf{R}^0_i$ by the strain tensor as

$$\begin{bmatrix} \mathbf{R}_{1,2} & \mathbf{R}_{2,3} & \mathbf{R}_{3,4} \end{bmatrix} = \begin{bmatrix} \mathbf{I} & + & \mathbf{E} \end{bmatrix} \begin{bmatrix} \mathbf{R}^0_{1,2} & \mathbf{R}^0_{2,3} & \mathbf{R}^0_{3,4} \end{bmatrix} \tag{5.1}$$

where each column $\mathbf{R}_{i,j}$ is a column vector of the x, y, z components of the vector $\mathbf{R}_{i,j}$. $\mathbf{I}$ is the identity matrix and $\mathbf{E}$ is the strain tensor. After solving Eq. (5.1) for the strain tensor, the resulting in-plane strains (E_{xx} and E_{yy}) and the out-of-plane strain (E_{zz}), at each atomic site, are used to calculate the hydrostatic strain $\epsilon_H = E_{xx} + E_{yy} + E_{zz}$ and the biaxial strain $\epsilon_b = E_{xx} + E_{yy} - 2E_{zz}$.

The electronic structure is calculated by solving for the eigenvalues and eigenstates

of an atomistic tight-binding Hamiltonian with a 20-band $sp^3d^5s^*$ basis including spin-orbit coupling (SO) as implemented in NEMO3D [235]. The SO splitting of the split-off hole band in bulk Si and Ge is 40 and 300 meV, respectively. Without the SO interaction, the bulk valence bands have 3-fold orbital degeneracy, with each band at Γ being a pure bonding $|p_x\rangle$, $|p_y\rangle$, or $|p_z\rangle$ state. The SO interaction reduces the orbital degeneracy to 2-fold, and it also mixes the orbitals. Even in bulk, one must include the SO interaction to get a qualitatively correct valence band for these semiconductors. In our system, the valence band becomes quantized states localized in the Ge core. The SO interaction qualitatively changes the level spacing and orbital composition of these levels.

The energies of the dangling bonds at the surface are increased by 20 eV to move the surface states away from the low-energy interior states of interest around the energy gap. These boundary conditions mimic the physical passivation of dangling bonds with H atoms, and they are described in detail in Refs. [143, 236]. They have been used extensively on nanocrystals, quantum wells, and nanowires [165, 227, 237]. The largest simulated NC contains 745176 atoms. With 20 orbitals per atom (10 orbitals $\times$ 2 spins), the total size of the basis is 1.4903×10^7, however the Hamiltonian is very sparse. The eigenvalues and eigenstates are solved using the Lanczos algorithm [115]. For the smaller NCs with diameters $\leq$ 20 nm, a block-Lanczos algorithm was also used for energies near the energy gap to ensure that no eigenenergies were missed [238].

In order to quantify the strain contribution to the electronic and optical properties, the eigenenergies and wave functions are calculated twice, once using the tight-binding parameters of the relaxed structure, and once using the tight-binding parameters of the un-relaxed structure. For the un-relaxed structure, bulk Si and Ge tight-binding parameters are used, and the Si-Ge interface is treated using average values in a virtual

crystal type approximation. Calculations of the electronic states in the un-relaxed and relaxed structures will be referred to as the un-strained and strained calculations, respectively. The unstrained calculations used the tight binding parameters for bulk Si and Ge described in Ref. [239]. Calculations of the strained structures used modified tight-binding parameters [240] that incorporate changes in the bond length and bond angle on the nearest neighbor matrix elements and also include modification to the on-site orbital energies that lift orbital degeneracy in the presence of strain. The resulting wavefunctions and energy levels are used to determine other device related parameters such as energy gaps, momentum matrix elements, and optical transition rates [166, 241].

The spontaneous emission rate $\Gamma(\omega)$ between an excited state and the ground state is calculated using Fermi's golden rule,

$$\Gamma(\omega) = \frac{e^2}{\epsilon_o \hbar^2 m_o^2 \pi c^3} \hbar\omega_{if} |\langle i|P_\nu|f\rangle|^2 \tag{5.2}$$

where, e is the electron charge, m_o is the bare electron mass, ϵ_o is the absolute dielectric permittivity of a vacuum, c is the speed of light, P is the momentum operator, ν is the polarization, $|i\rangle$ is the initial state, $|f\rangle$ is the final state, and $\hbar\omega_{if}$ is their energy difference. As part of the analysis, we define the envelope function at each atomic site n,

$$C_n{}^2 = \sum_{i=1}^{20} |\psi_{n,i}|^2 \tag{5.3}$$

where $|\psi_{n,i}|^2$ is the probability density of orbital i at atomic site n. The envelope functions for the initial state C^i and final state C^f are then used to calculate the

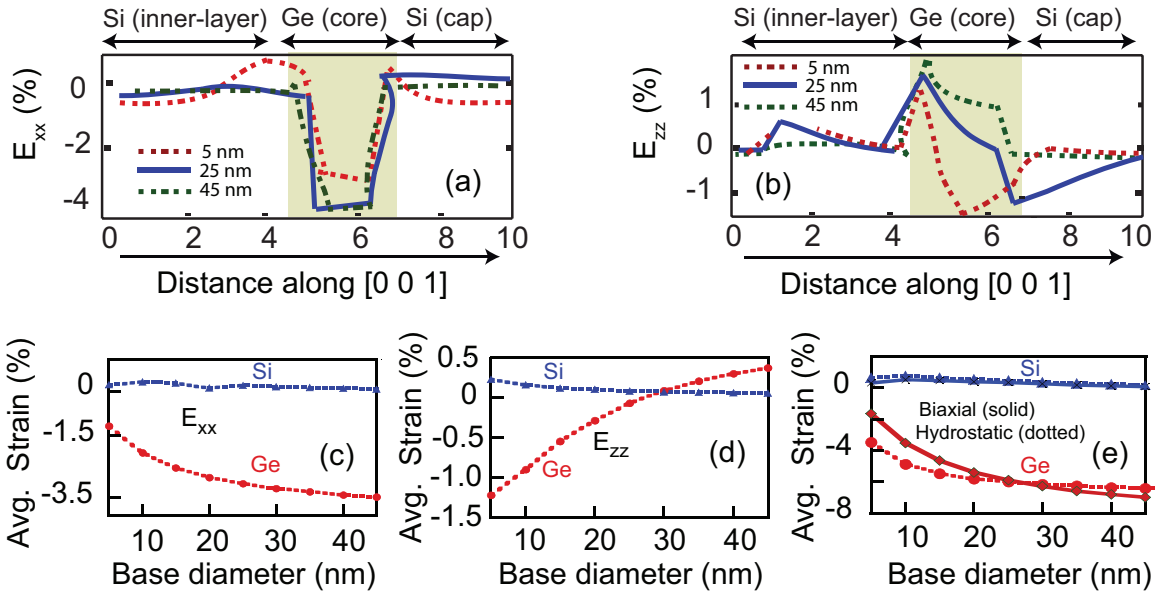

Figure 5.2: (Color online) (a) In-plane strain E_{xx} and (b) out-of-plane strain E_{zz}, plotted along the [001] direction through the center of the NCs. The white and grey backgrounds correspond to the Si and Ge regions, respectively. The three different diameters are indicated in the legends. (c) Average in plane strain $\langle E_{xx} \rangle$ of the Ge and Si atoms. (d) Average out of plane strain $\langle E_{zz} \rangle$ of the Ge and Si atoms. (e) Average biaxial (solid line) and hydrostatic (dotted line) strain of the Ge and Si atoms, as a function of base diameter.

spatial overlap of the two wavefunctions as,

$$\text{Overlap} = \mid \sum_{i=1}^{N} {C_n}^i \cdot {C_n}^f \mid^2 \tag{5.4}$$

where N is the total number of atoms in the structure.

5.3 Results and Analysis

5.3.1 Strain characteristics

The strain components at each atomic site are calculated using Eq. (5.1). The in-plane strain E_{xx} and the out-of-plane strain E_{zz} plotted in the [001] direction

through the center of the NC are shown in Fig. 5.2(a,b) for 3 different diameter NCs. The positive and negative strain values correspond to tensile and compressive strain, respectively. There is a general trend of an abrupt change in E_{xx} and E_{zz} while passing through the Si / Ge interfaces at the bottom and top of the Ge core. Since the Ge lattice constant is greater than the Si lattice constant, the Ge-core layer is compressed parallel to the interface giving negative values for E_{xx} and E_{yy}. E_{zz} becomes positive in order to maintain the Poisson ratio.

For the smaller NCs, the Ge atoms are, on average, compressed in all 3 directions as shown in the plots of the average strain in Figs. 5.2(c,d). In these plots, the values of the strain have been averaged over all of the Ge atoms and all of the Si atoms in the NC. Because of the high curvature of the Ge region in the smaller NCs, the physical distinction between E_{xx} and E_{zz} becomes blurred since the Ge atoms curve around the Si base. Once the base diameter becomes larger than 30 nm, the average strain takes on the character expected for a planar structure with $\langle E_{xx} \rangle < 0$ and $\langle E_{zz} \rangle > 0$. The average hydrostatic and biaxial strain in the Ge region is always negative as shown in Fig. 5.2(e). The average hydrostatic strain is 3.8% for a 5 nm NC and increases to 6% for a 45 nm NC. Due to the relatively large Si base region, the strain averaged over all of the Si atoms is small.

Iso-surface plots of the hydrostatic and biaxial strain of the Ge/Si NCs are shown for the smallest (5 nm), medium (25 nm), and largest (45 nm) diameter NCs in Fig. 5.3. The cross-sectional plane is taken through the NC center. For the smallest 5 nm diameter NC with an AR of 2, the local hydrostatic and biaxial strain distribution in the Ge and Si regions are the most inhomogeneous. The Si base, immediately underneath the Ge core, experiences the largest hydrostatic strain of 1.2% of all of the NCs. Conversely, the magnitude of the hydrostatic strain in the Ge core is the least among all of the NCs. In this smallest NC, the magnitude of the strain is shared most

equally between the Si and Ge regions. As the diameter increases, and the volume of the Si base becomes much larger than the volume of the Ge core, the NC more resembles a planar heterostructure, and the strain becomes more localized in the Ge region. The general trend in the strain distribution is consistent with other theoretical and experimental results for similar lattice mismatched systems [161, 210, 225].

5.3.2 Electronic Properties

A schematic illustration of the energy levels and their spatial location in the Ge/Si NCs is shown in Fig. 5.4. Bulk Si and Ge form a type-II energy level alignment. The valance band offset of 0.70 eV creates a deep potential well in the Ge-core region which strongly localizes the occupied valence states of the NC. The unoccupied excited states localize in the Si base and in the Si cap. Whether an excited state is in the base or the cap depends on the size of the NC and the strain. The energy splitting of ≤ 15 meV between the three excited states E_0, E_1 and E_2 is small. Optical transitions that will be analyzed are shown.

To obtain insight into the energy and positions of the wavefunctions as a function of NC diameter and strain, we plot in Fig. 5.5 the colored iso-surfaces of the probability densities corresponding to the energies H_0, E_0, E_1, and E_2 for both the strained and unstrained NCs. The magnitude of the momentum matrix elements between the highest occupied level H_0 and first three excited states E_0, E_1 and E_2 are a few orders of magnitude larger than those between the second highest occupied level H_1 and E_0, E_1 and E_2. Hence, our study only focuses on these lowest-energy and more optically favorable transitions. For all of the NCs, with or without strain, the wavefunction ψ_{H_0} of the highest occupied state is localized in the Ge core. The strain only lowers its energy level. The energy differences between the highest 3 occupied states of the

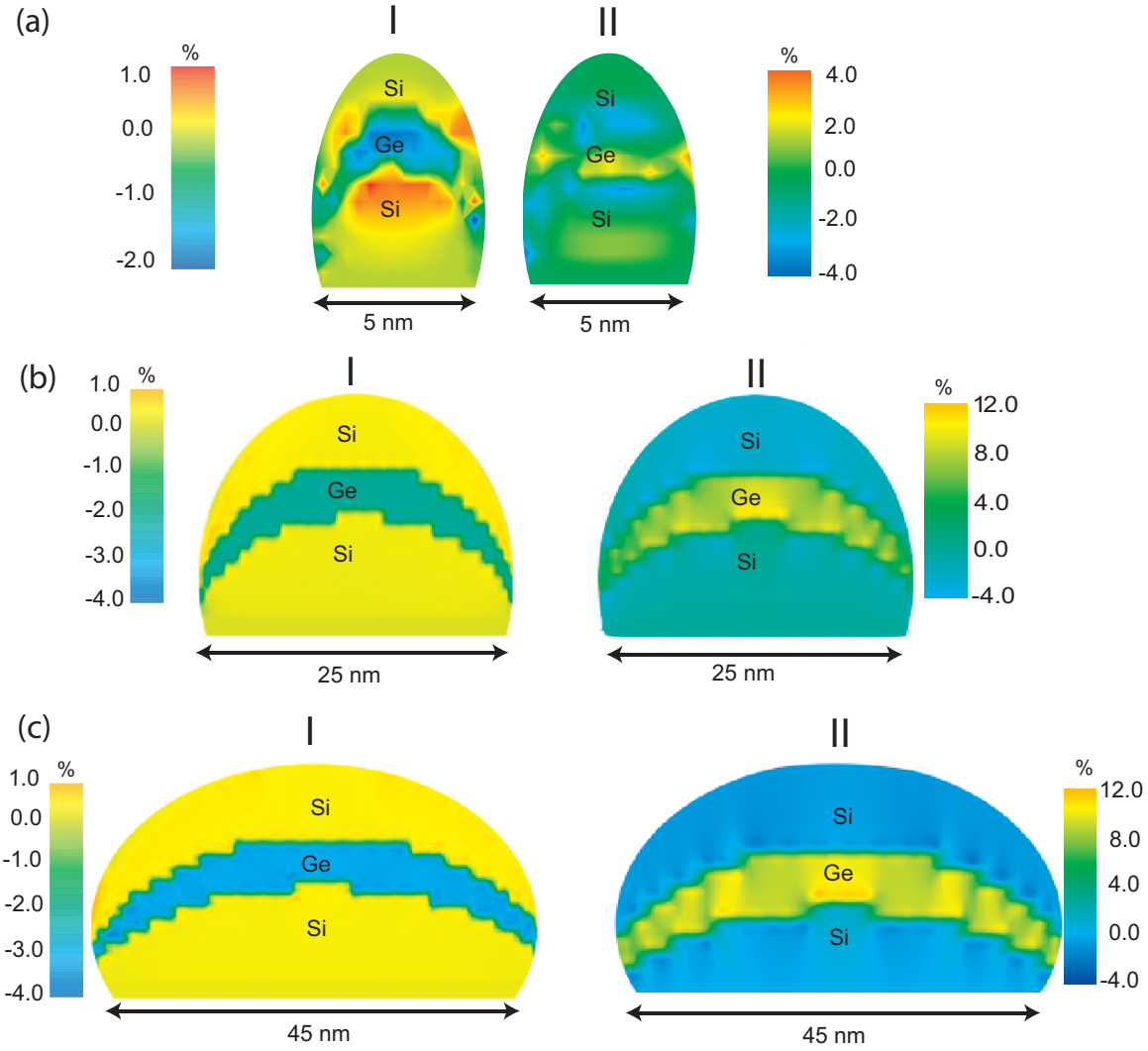

Figure 5.3: (Color online) Isosurface plots of the hydrostatic (I) and the biaxial (II) strain in a (100) plane cross-section through the NC center for the (a) smallest (5 nm), (b) intermediate (25 nm), and (c) largest (45 nm) dome-shaped Ge/Si NCs. The plane cuts through the Ge/Si interface at the center of the $x - y$ plane. The horizontal scales for the intermediate (b) and the largest (c) NCs are reduced by a factor of 2.

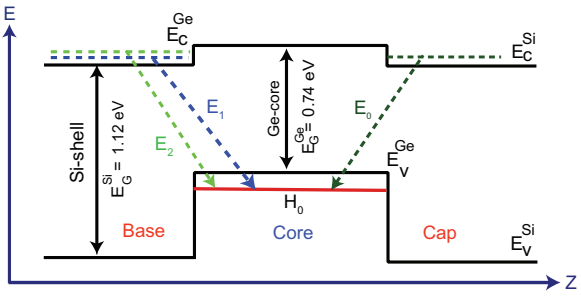

Figure 5.4: (Color online) Energy levels and optical transitions between the highest occupied state in the Ge core and the excited states in the Si base and cap.

strained (unstrained) NCs are 5 (3) meV for the largest NC and 50 (25) meV for the smallest NC.

The quantum confinement and strain both lift the degeneracy of the lowest excited state. In all cases, with or without strain, the lowest excited state is non-degenerate. For the strained NCs, the first two excited states differ in energy by 2 - 4 meV with the maximum difference of 4 meV occuring in the 15 nm diameter NC. For the unstrained NCs, the energy splitting of the two lowest excited states is 1 meV. Thus, the strain enhances the splitting of the lowest excited state by a factor of 2 to 4. These values are similar or slightly larger than the splitting in strained GeSi/Si/GeSi QWs [178], GeSi QDs [180] and disordered Si QD's [184],and within the energy resolution limits of the advanced techniques like photon assisted tunneling [242]. This energy splitting of the excited states in a Ge/Si NC was observed experimentally for a Ge NC of height $\sim$ 2 nm and base diameter of $\sim$ 10 nm, sandwiched between two strained Si-layers [243]. The meV energy differences arise from the breaking of the bulk Si X-valley degeneracy due to the quantum confinement, and they are consistent with earlier studies of confined Si structures using both atomistic and analytical models [142, 144, 165, 178, 184, 237]. These small energy level splittings have been of interest primarily for applications in quantum computing.

As the NC diameter increases from 10 nm to 25 nm, the localization of the excited states move. Consider the two lowest, nearly-degenerate excited states of the strained NCs. In the 10 nm NC, ψ_{E_0} is localized in the Si base, and ψ_{E_1} is localized in the Si cap. At 15 nm, ψ_{E_0} and ψ_{E_1} are both localized in the base, and at 25 nm, they are both localized in the cap. They both remain localized in the cap for all larger diameters. A similar switching between cap and base occurs in the unstrained NCs, however, the positions of ψ_{E1} and ψ_{E2} are the opposite of those in the strained NCs. For both the strained and unstrained NCs, the lowest two excited states reside in the cap for diameters ≥ 25 nm. The third level is about 7 meV above the first two for the larger NCs and only 1 meV above the second level for the 10 nm strained NC. The excited state wavefunctions in the cap have a larger spatial overlap with the occupied wavefunction in the Ge core than do the excited state wavefunctions in the base. This property affects the optical matrix elements.

To understand the effects of strain and confinement on the fundamental energy gap, the individual energy levels and the fundamental energy gaps are plotted versus diameter for both the strained and unstrained NCs. The energy difference between the lowest excited state ψ_{E0} and the highest occupied state ψ_{H0} is defined as the energy gap E_g, and it is plotted in Fig. 5.6(a) as a function of the base diameter. The change in the E_g with diameter is primarily the result of the change in the occupied state energy $H0$ with diameter. Confinement and compressive strain work together to lower the energy of the occupied state in the Ge core. For the smaller NCs ≤ 15 nm diameter, the confinement energy is larger than the strain energy. Beyond 15 nm, the strain energy dominates. The strain induced shift in E_g for the smallest NC is 35 meV and it reaches a maximum value of 128 meV for the largest NC. The plot of the strain-induced shifts of the individual energy levels given in Fig. 5.6b, shows that the strain-induced increase in the energy gap is dominated by the strain-induced lowering

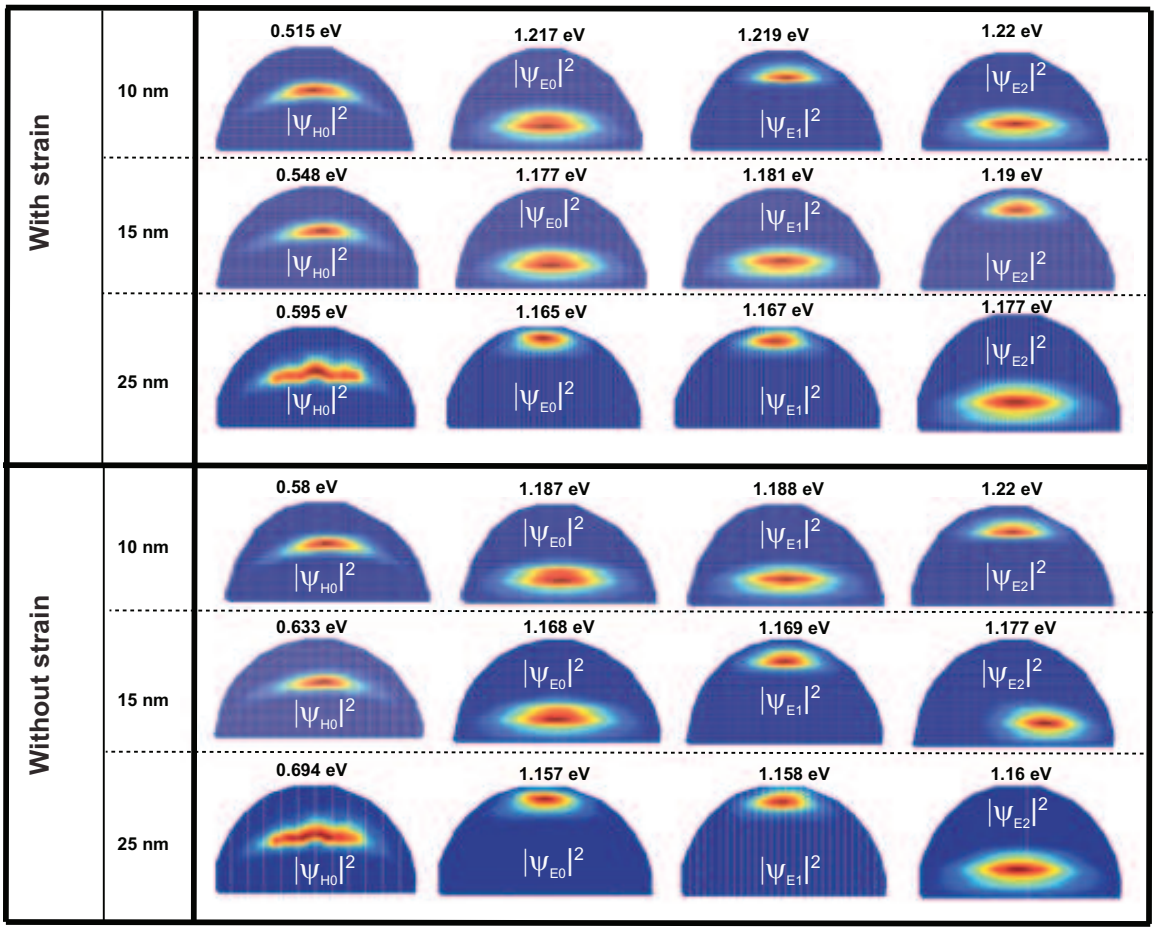

Figure 5.5: (Color online) Cross sections of the orbitals of the highest occupied state H_0 and the three lowest excited states, E_0, E_1, and E_2, for diameters of 10, 15 and 25 nm. The first three rows are calculated with strain and the lower three rows are calculated without strain. The corresponding energies associated with each state are labeled.

of the occupied state localized in the Ge core. The strain lowers the eigenenergies of the highest occupied states H_0 by 38 meV in the 5 nm NC and by 120 meV in the 45 nm NC. These values were compared to the predictions of deformation potential theory using the average strain components described in the previous section and the deformation potentials from Ref. [244]. The deformation potential theory lowers the energies of the highest occupied states of the 5 nm and 45 nm NCs by 45 meV and 100 meV, respectively, which is consistent with the above values of 38 meV and 120 meV. The effect of strain on the energies of the excited states localized in the Si base and cap is relatively small compared to its effect on the energies of the occupied states localized in the Ge core. For diameters greater than 20 nm, the strain raises the lowest excited state energy E_0 by about 10 meV.

5.3.3 Optical Properties

The closely spaced excited states with energy spacing less than 15 meV can all contribute to the overall optical emission intensity [172]. The interlevel emission transition rate $\Gamma(\omega)$ is a function of the transition energy and the momentum matrix element. Since the initial and final wavefunctions are localized in different regions of the NC, some of the diameter dependent trends of $\Gamma(\omega)$ can be understood by considering the overlap of the occupied and excited state wave function envelopes. Fig. A.3(a) shows the wave function overlap between the occupied state (ψ_{H_0}) and first three excited states (ψ_{E_0}, ψ_{E1} and ψ_{E_2}) for the strained NCs calculated from Eq. (5.4). The wave function overlaps for the smallest Ge/Si NC are around 0.1. For the smallest NCs, ψ_{E_0} is localized in the Si base. As the base size increases, ψ_{E_0} moves away from ψ_{H_0} in the Ge core, and the overlap decreases. At 20 nm, ψ_{E_0} shifts from the Si base to the Si cap where it stays for all larger diameters. Therefore, as

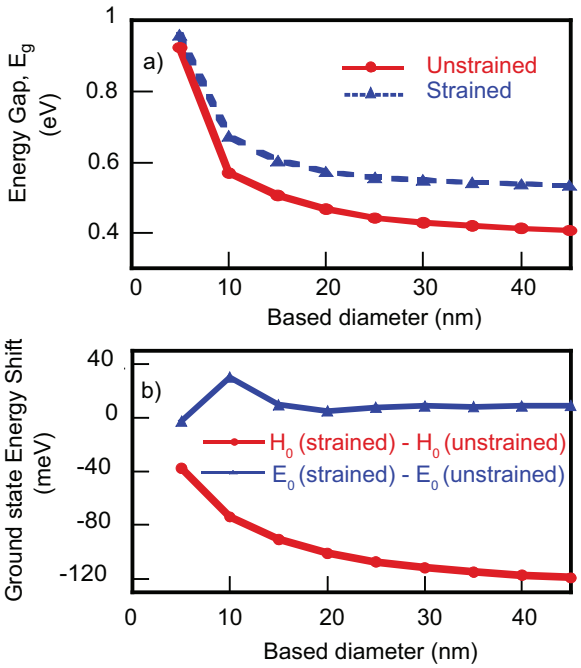

Figure 5.6: (Color online) Electronic states of dome-shaped Ge/Si NC as a function of base diameter, (a) Energy gap (E_g) for unstrained (solid line) and strained (broken line) case, and (b) Strain induced shift in the occupied state (H_0) and the excited state (E_0) energies.

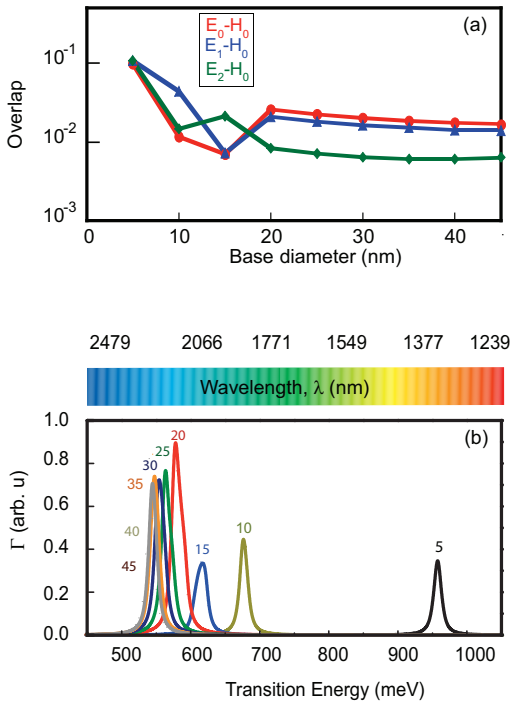

Figure 5.7: (Color online) Optical Properties of dome-shaped Ge/Si NCs as a function of base diameter (a) Wave function overlap between first three excited states (E_0, E_1, and E_2) and the ground state (H_0), and (b) Optical intensities between the the ground state H_0 and the excited states E_0, E_1, and E_2. For all the calculated transition intensities, Lorentzian broadening functions with the width of 10 meV are applied.

the diameter increases from 20 nm, the overlap is a smooth function of diameter and slightly decreases. The abrupt jumps in the wavefunction overlap moving from one diameter to the next result from the electronic state switching from the base to the cap or vice-versa. This also explains why, in the 15 nm NC, the overlap of ψ_{E_2} with ψ_{H_0} is larger than that of ψ_{E_0} or ψ_{E_1} with ψ_{H_0}. This is the one diameter where ψ_{E_2} is localized in the cap and ψ_{E_0} and ψ_{E_1} are localized in the base.

The transition rates $\Gamma(\omega)$ between the first three excited states, E_0, E_1 and E_2, and the ground state H_0 for in-plane polarization are calculated using Eq. (5.2). The discrete spectrum is convolved with a 10 meV Lorentzian broadening function and plotted in Fig. A.3(b). For the smallest 5 nm NC, the rate between the highest occu-

pied state and the lowest excited state dominates, and the peak energy (wavelength) associated with this transition lies at 960 meV (1292 nm). As the diameter is increased, the transition spectrum red-shifts following the trend in the energy gap and reaches a minimum of approximately 550 meV for NC diameters $\geq$ 25 nm. For these larger NCs, the magnitude of the emission rate is approximately two times larger than that of the 5 nm NC. This enhancement results from an increased magnitude of the momentum matrix elements between the initial and final states.

5.4 Conclusion

Dome-shaped Ge-core/Si-shell nanocrystals with crescent shaped Ge cores and base diameters ranging from 5 nm to 45 nm have been simulated atomistically to determine the effect of quantum confinement and strain on the electrical and optical properties. Strain and confinement work together to lower the occupied state energies in the Ge core. Strain increases the energy gap by approximately 100 meV for NCs with base diameters greater than 15 nm, and the increase is a result of the downward shift of the occupied state in the Ge core. Confinement and strain break the degeneracy of the lowest excited state and split it into two states separated by a few meV. In the smaller NCs with base diameters below 15 nm, one of the states can be in the base and the other in the cap. For diameters $\geq$ 20 nm, the two lowest excited states are localized in the Si cap for both the strained and unstrained NCs. The fundamental energy gap and emission spectrum varies from 960 meV for the 5 nm NC to 550 meV for the largest NC with most of the variation occurring between 5 nm and 20 nm.

Chapter 6

Vibrational Properties of Misorientated Bilayer Graphene (MBG) system

6.1 Introduction and Motivation

Single layer graphene (SLG) is the most widely used vdW material. It consists of two-dimensional sheet of sp^2 carbon atoms and has many unique electrical, optical and thermal properties. The Billouin zone (BZ) of SLG is also a honeycomb lattice with rotational symmetry. Conventionally, in single layer graphene, band gap opening and modification of the linear dispersion of the bands was observed by (a) applying external field, (b) introducing surface adsorption [245, 246], and (c) modulating graphene-substrate interaction [247, 248]. SLG exhibits the highest thermal conductivity among existing 2D materials [249]. The exceptional thermal properties of SLG are partially due to its unique phonon transport mechanism where phonon energy spectra are quantized. There are three acoustic phonon branches, i.e. the

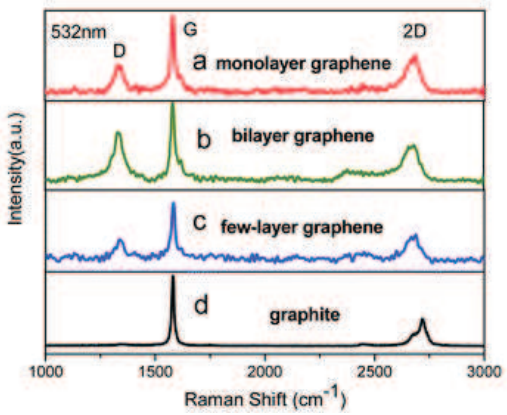

Figure 6.1: (Color online) Raman spectra of graphene sheet with different numbers of layers, reproduced with permission from [14]. © [2014] RSC.

in-plane longitudinal acoustic (LA) and transverse acoustic (TA) branches and the out-of-plane flexural or z-axis acoustic (ZA) branch, which contribute to the thermal conductivity in SLG. Depending on the physical proximity of SLG and the surrounding temperature, the LA and ZA modes contribute differently to the total lattice thermal conductivity. For example, in a supported SLG, the ZA branch contribute up to 77% of the total thermal conductivity. In a suspended SLG, however, the ZA branch can contribute as much as 90% of the thermal conductivity at room temperature [250], mainly due to the high specific heat and long mean scattering time of ZA phonons. Theoretical calculation of lattice thermal conductivity of graphene at room temperature, using Boltzmann transport equation (BTE), reveals that the contribution from the ZA branch is greater than the combined TA and LA contributions.

In experiment, the thermal properties in any 2D system, including SLG, is mainly characterized by using Raman spectroscopy. Raman spectrum for single and bilayer graphene with G, a primary in-plane vibrational mode, D, first-order overtone of a different in-plane vibration, and 2D, second-order overtone of a different in-plane vibration, peaks is illustrated in Fig. 6.1. D and 2D peaks positions are dispersive.

The D peak of SLG appears only in small or highly-defected crystals of graphene or graphite. It is not Raman active in extended crystals because it involves double-resonant scattering of a single phonon with non-zero crystal momentum ($q \neq 0$). Absence of this mode in SLG signifies the existence of extended defect-free lattices, where crystal momentum is conserved. The 2D peak, on the other hand, is present in large, low-defect SLG samples, along with the ubiquitous G peak of graphitic materials The 2D peak occurs due to a double-resonance, two-phonon process. In clean extended crystals, single-phonon Raman peaks are insensitive to the energy of the incident laser, because the phonon crystal momentum is fixed at $q = 0$, and thus the phonon energy does not vary with laser energy. However, in a two-phonon process the phonons can have nonzero, opposite crystal momenta, q and -q, since their sum still adds to zero.

In SLG, a careful analysis of G, D and 2D peaks from Raman spectroscopy reveals lattice-specific properties such as phonon-phonon interaction, electron-phonon interaction and thermal conductivity. The G band near 1485 cm^1 is a first-order Raman peak in SLG related to the scattering of in-plane transverse (TO) or longitudinal (LO) optical phonons at the Γ point of the BZ. Similarly, the pronounced 2D band in the range of $2500-2800$ cm^1 is a second-order Raman peak, associated with the scattering of two TO phonons around the K point of the BZ. The ratio between G and 2D peaks is sensitive to the number of atomic layers in few layer graphene [251]. The spectral position, height and shape of the peaks also give useful insight about the quality of the graphene samples. In addition, temperature dependence of the Raman peaks was instrumental for the first measurement of the thermal conductivity of graphene [249]. Hence, Raman spectroscopy has become the tool for surface meteorology for the graphene and graphene-like 2D materials.

Mechanical stacking of monolayer of vdW materials, such as SLG, on a substrate

or on another layer is known to lead to misorientation and structural imperfections, at the interface [252–254]. Though a perfectly AB-stacked bilayer graphene has massive charge carriers with zero band gap, a few degrees of misorientation is sufficient to decouple the individual layers exhibiting the massless linear dispersion similar to that of monolayer graphene [45–48]. This misoriented graphene bilayer (MBG) system also exhibits other intriguing intrinsic properties such as renormalized Fermi velocity [255, 256], electronic localization [257], and van Hove singularities [258, 259]. Experimental and theoretical studies on MBG suggest that these electronically decoupled graphene bilayers exhibit interesting electronic [51, 255] and magneto-transport properties [260, 261]. However, the zero-energy-gap character, similar to SLG, has impeded the application of MBG in modern electronic devices.

Although twisting only weakly affects the interlayer interaction, it breaks the symmetry of the Bernal stacking present in perfectly aligned AB bilayer system, resulting in an intriguing dependence of the electronic and thermal properties on the rotation angle Θ. Since the coherent interlayer coupling can be so small, the interlayer, room-temperature conductance for all but the smallest misorientation angles is dominated by phonon-assisted transport mediated by an out-of-plane beating mode of the bilayer with phonon energies ranging from 10 meV to 30 meV as the misorientation angle varies from 0° to 30° [262].

Recent Raman measurement of multi-layer graphene suggests appearance of low-energy phonon peaks [263]. Raman studies of MBG also demonstrate a strong resonant G-peak when the excitation energy matches the energy separation of the van Hove singularities that form at the overlapping Dirac cones [264, 265]. In these studies, the theoretical analysis assumed that the phonon dispersion of the MBG was identical to the unperturbed phonon dispersion of single layer graphene. The fact that the calculations qualitatively matched the trends in the experimental results

is consistent with the hypothesis of phonon decoupling between the rotated layers. The effect of misorientation angle on the phonon dispersion of MBG is still an open question, and the effect of misorientation angle on the thermal properties has yet to be studied. These two questions are intimately related since heat is carried by the phonons. The cross-plane coupling of the low-energy phonons is also responsible for the dimensional cross-over from 3D to 2D observed in the in-plane thermal conductivity of few layer graphene [266]. These modes are also sensitive both to the number of atomic layers and interlayer coupling, where the possibility of using them for noncontact characterization of the stacking order in multilayer graphene and MBG has been proposed [267]. The objectives of this study is to: (1) understand how the phonon dispersion MBG differs from that of SLG and AB-stacked bilayer graphene, (2) to reproduce experimentally observed Raman modes in MBG, and (3) to explore the applicability of MBG as a thermoelectric materials by analyzing the thermophysical properties.

6.2 Models and Methods

Bilayer graphene, in theory, can have two lattice configurations namely, AB and AA, depending upon the relative position of the atoms on each layer. Both of these stacking orders show unique electronic and optical properties. In AB-stacked bilayer graphene, the two graphene layers are such that the A-triangular sub-lattice of the top (bottom) layer lies exactly on top of the B-sub-lattice of bottom (top) layer, as shown in the Fig. 6.2.a. While, in an AA-stacked bilayer system, both triangular sub-lattices (A and B) of the top layer lie exactly on top of two sub-lattices of the bottom graphene layer, as shown in the Fig. 6.2.b. However, the AB-stacked bilayer system was found to be more stable than the AA-stacked bilayer system [268]. Hence, using

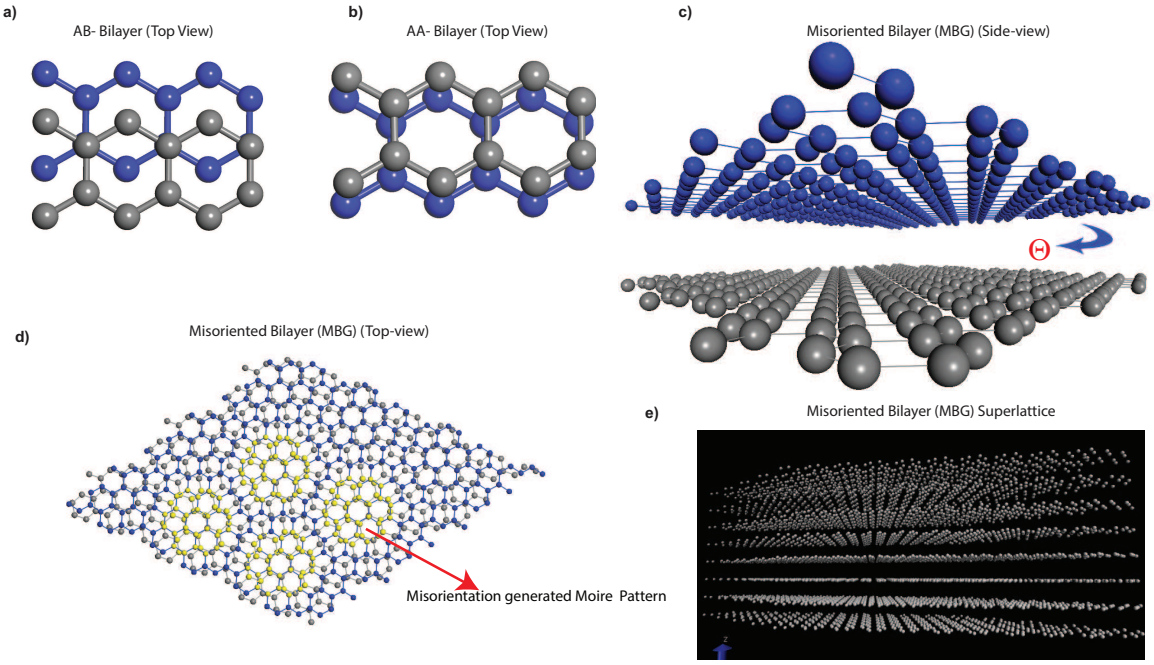

Figure 6.2: (Color online) Simulated models of bilayer graphene system, a. AB-stacked bilayer graphene, b. AA-stacked bilayer graphene, c. Misoriented Bilayer Graphene (MBG), d. Top view of MBG system illustrating Moire pattern, and e. MBG superlattice. Note that, MBG system with point-defect is not shown here.

the AB-stacked primitive cell, we construct experimentally observed commensurate MBG supercells by following the method described in Ref. [47]. One of the simulated MPG supercells is illustrated in Fig. 6.2.c, where the top layer is misoriented with a misorientation angle $(\Theta) = 9^o$ relative to the bottom layer, giving rise to hexagonal *Móire* patterns which are highlighted in Fig. 6.2.d. Naturally occurring multi-layer graphene systems forming misoriented supperlattice is also depicted in Fig. 6.2.e.

To maintain the periodic commensurability, the length of the supercell lattice vector l_v increases exponentially with decreasing Θ. Since BZ is reduced by a factor of $1/l_v$, comparing the phonon dispersion of SLG against that of MBG is not straightforward. In addition, BZ folding due to commensurate supercell formation prevents a direct comparison of phonon characteristics of AB-stacked bilayer graphene with that of MBG. In this study, we will perform a system study of phonon dispersion and

density of states (DOS) of MBG, as a function of misorientation angle, Θ, using anharmonic MD method as implemented in LAMMPS and described in detail in Chapter 2. The pair-wise interactions were computed with the ReaxFF, Airebo and LCBOP potentials for the in-plane and out-of-plane CC interactions. All of the MD simulations are performed within the framework of the isothermal-isobaric ensemble (NPT), with a fixed number of atoms N, constant pressure P, constant temperature T, and a time step of 0.8 femtosecond (fs). Periodic boundary conditions are applied in all direction and the crystal is initially equilibrated at a predefined temperature via a velocity scaling routine. Prior to sampling the dynamical matrix, all simulations run for 200,000 time steps using a Noose-Hoover thermostat under NPT ensemble at 300K. Pressure is maintained at 1 bar. Following equilibration, constant number, volume, and energy (NVE) integration is performed along with the application of a Langevin thermostat. The dynamical matrix is then sampled 500,000 times at intervals of 5 time steps. The friction and random force provided by the Langevin thermostat allowed for faster convergence of the dispersion relations, although comparable results were achieved with longer NVE simulations without a Langevin thermostat.

In a 2D system, the transport of acoustic phonons is altered due to scattering by other phonons, lattice defects, impurities, conduction electrons and interfaces. These different scattering events significantly affect the net phonon mean free path l and hence the thermal conductivity K. Using the phonon frequencies and phonon density of states (PDOS) calculated using the fluctuation-dissipation theorem, the thermodynamic properties of a given materials can be determined. The lattice specific heat capacity C_v is one of the key parameters that characterizes the thermal properties of materials which is directly related to the lattice thermal conductivity through the

following relation from kinetic theory [269],

$$K_l = \frac{1}{3} C_v v l \tag{6.1}$$

where v is the phonon group velocity and l is the phonon mean free path. The specific heat at constant volume, C_v, contributed by each phonon branch is obtained by integrating over the PDOS with a convolution factor that reflects the energy and occupation of each phonon state,

$$C_v(T) = 3\ K_b \int_0^{w_{max}} [\frac{\hbar}{K_b T}]^2 \frac{e^{\frac{\hbar\omega}{K_b T}}}{(e^{\frac{\hbar\omega}{K_b T}} - 1)^2} D(\omega) d\omega, \tag{6.2}$$

where $D(\omega)$, is the PDOS, and $\hbar$ is the Plank's constant divided by 2π. Above formalisms for the phonon dispersion and lattice specific heat capacity calculations are implemented in the FixPhonon package [132], as implemented in the Large-scale Atomic/Molecular Massively Parallel Simulator (LAMMPS) code [116].

6.3 Results and Discussion

Empirical Potential Verification

The potential is an algebraic (or numerical) function that can be used to calculate the potential energies and forces (through its derivative) associated with the particles in the system. The Potential, which could include the two-body and three-body interactions, can be obtained by fitting a chosen functional form to experimental data, or to the results of *ab-initio* calculations. The increasing application of MD simulations to the study of phonon and other related characteristics is often met with a shortage of empirical potentials parametrized specifically to reproduce accurate phonon

properties. The comparison of thermophysical properties, either between interatomic potentials, or between simulation and experiment, therefore depends strongly on the parametrization of the empirical potential used in simulations. Since the quality of phonon frequencies depends on the in-plane and out-of-plane C-C interactions, the potentials defining these interactions need a systematic validation. One way to achieve the validation is to compare the observed frequencies against frequencies from an accurate theoretical method such as first principle methods. In order to identify a suitable potentials for the MBG simulations, first analyze the phonon dispersion of SLG using Tersoff potential, adaptive intermolecular reactive bond order (AIREBO) potential, and long-range carbon bond order potential potential (LCBOP).

Since one of the objectives of this study is to re-produce and provide some theoretical understandings of experimentally observed Γ-centered Raman modes of MBG, the potential verification is focused at optical frequencies at around Γ point of BZ. In general, all three potentials produce qualitatively similar phonon spectra for a SLG. However, the Tersoff potential overestimates the maximum optical frequencies (TO and LO) at Γ by 35% when compared to the first principle calculation. The discrepancies in the optical frequencies is mainly due to the use of parameters that are reproduced by fitting the bulk modulus of graphite, while ignoring long-range interactions. Similar limitation of this potential was also identified during a recent study, where the temperature dependent phonon dispersion and transport was compared against experiment and first principle calculations [134]. AIREBO potential also overestimates the maximum optical frequencies (TO and LO) at Γ, though only by 30%. Although AIREBO is an extension of the Tersoff potential, this potential does include torsional interaction [131]. The incapability of early BOPs to properly describe multilayer graphitic materials was noted by Los and Fasolino [270]. However, the maximum optical frequencies obtained by LCBOP potentials (1450 cm^{-1})

Table 6.1: Γ-centered Phonon Modes of Single Layer Graphene (SLG)

	LCBOP			From Experiment [271]			From DFT calculation [272]		
Mode	Γ	M	K	Γ	M	K	Γ	M	K
TO	1450	1353	1400	1550	1320	1500	1581-1597	1396-1442	1289-1371
LO	1450	1236	1000	1550	1210	1100	1581-1597	1346-1380	1220-1246
ZO	780	601	501	790	550	380	825-890	636-640	535-539
LA	0	935	1000	0	1200	1100	-	1315-1347	1220-1246
TA	0	601	900	0	680	1000	-	618-634	994-1004
ZA	0	284	334	0	280	380	-	472-476	535-539

is only off by 9% , as compared to the experimentally observed maximum optical frequency (1600 cm^{-1}). LCBOP is an appropriately parametrized mix of a short-range Brenner-like bond order potential and a long-range, radial potential. It's inclusion of a long-range interaction provides a good description of the interlayer properties over a range of interlayer distances, as compared to experimental and/or *ab-initio* data. Γ-centered Phonon Modes of SLG calculated using the LCBOP potential are presented on Table-6.1 along with the data from experiment [271] and first principle calculation [272].

Since the parameters for the LCBOP potential was initially parametrized for the interlayer interaction over the range of interlayer distances in a graphitic system, this could also provide an adequate description of the modulating vdW-gap in the MBG system. The phonon dispersions for both the SLG and AB-stacked graphene bilayer system are presented in Fig. 6.3. All the phonon modes, including degenerate modes in AB-stacked bilayer system, are labelled accordingly. For the AB-stacked bilayer system, inter-layer breathing mode, labelled as ZO' (or ZA), describes the coupling between the layers. LCBOP correctly predicts the location of ZO' mode at around 100 cm^{-1}, which is consistent with experiment [271] and DFT calculation using perturbation theory [272].

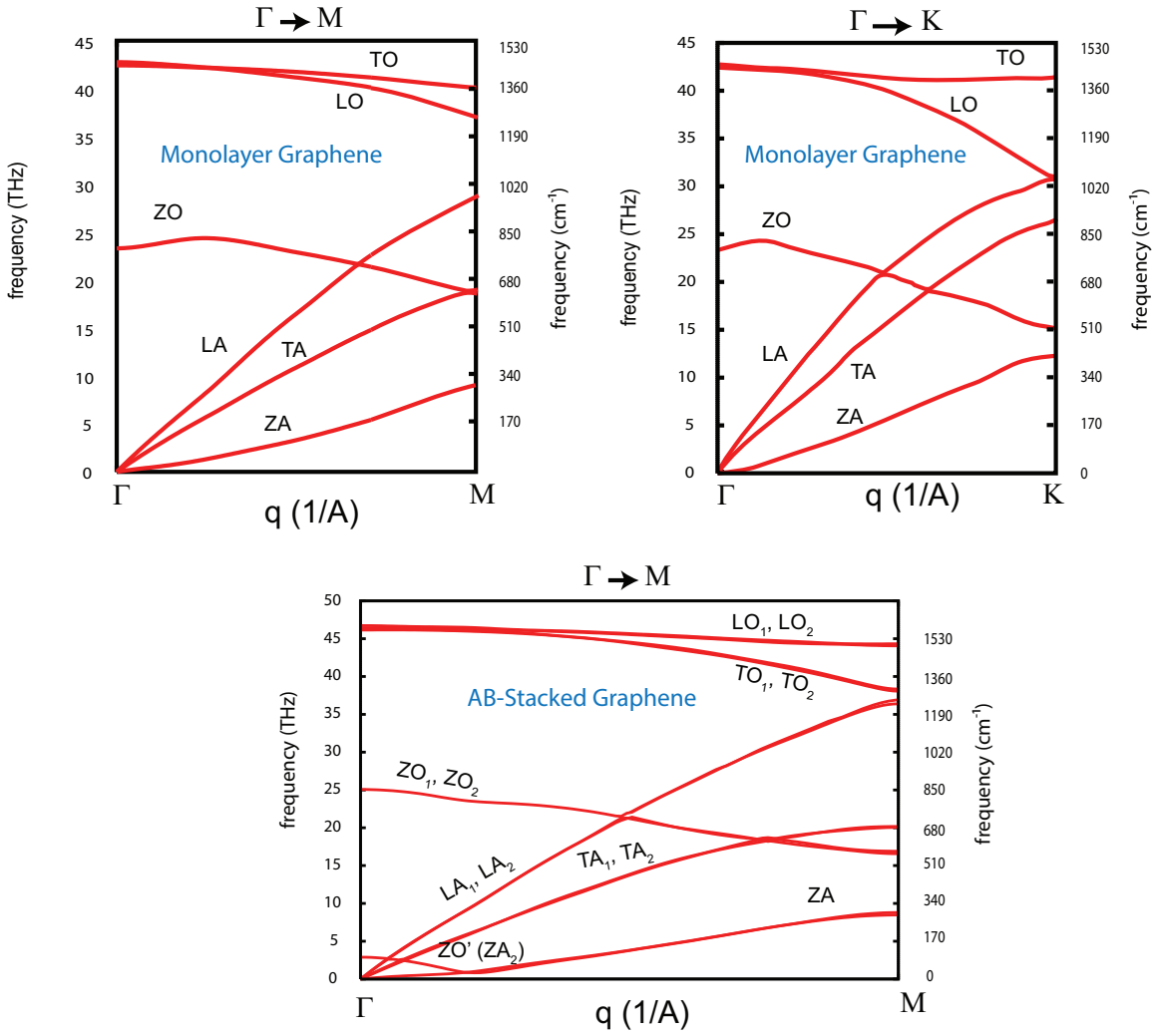

Figure 6.3: (Color online) Phonon dispersions, a. Phonon dispersion of SLG in $\Gamma \rightarrow M$, b.Phonon dispersion of SLG in $\Gamma \rightarrow K$, and c. Phonon dispersion of AB-stacked bilayer system in $\Gamma \rightarrow M$.

Phonon Dispersion

The directions in the BZ of MBG depend strongly on the rotational angle and do not coincide with the directions in the BZ of SLG or AB-stacked graphene. The misorientation influences the phonon spectra of MBG owing to two reasons: (i) modification of the weak van der Waals interlayer interaction and (ii) alteration of BZ size leading to phonon momentum change. To gain a fundamental understanding of misorientation on the phonon frequencies, we start our phonon dispersion calculation with the smallest MBG supercell consisting of 28 atoms, which occurs when the top and bottom layers are misoriented with a relative Θ of 21°. In addition, to isolate the effect of misorientation from the increasing lattice sites, we calculate phonon dispersion of MBG supercell and compare it to that of a AB-stacked supercell with the same number of lattice sites. After identifying the LCBOP potential as a suitable potential for a multi-layer 2D system like MBG, we perform a systematic study of vibrational properties such as phonon dispersion, and density of states in the MBG system, as a function of misorientation angle Θ. The phonon dispersions for a MBG supercell with $\Theta = 21.78°$ is illustrated in Fig. 6.4.a.

Qualitatively, the phonon dispersion curve for both the MBG supercell with $\Theta = 21.78°$ and the perfectly-aligned supercell have similar features. Lattice-induced folded phonon modes have similar frequencies, with an exception of out-of-plane ZO' modes. ZO' mode frequency for the MBG increases by 17 cm^{-1}, as compared to the perfectly-aligned supercell. A similar frequency shift for the ZO' mode was also observed in earlier theoretical studies using the harmonic approximations, attributing it to the weak inter-layer coupling [251, 273, 274].

When the misorientation angle Θ decreases, the MBZ supercell size increases to maintain the long-range periodicity. Consequently, the total number of phonon modes

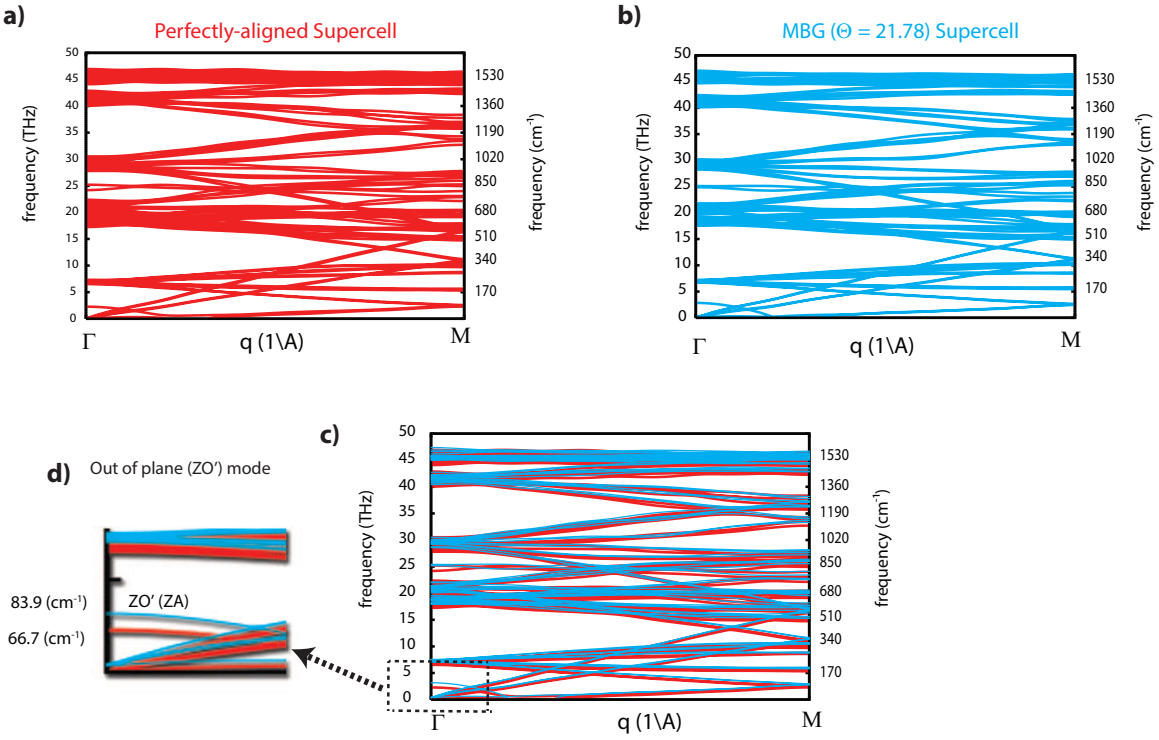

Figure 6.4: (Color online) Phonon Dispersions for MBG supercell with $\Theta = 21.78°$ (a) and perfectly-aligned supercell (b). Dispersion for MBG supercell is overlaid over the dispersion of the Perfectly-aligned supercell (c), and the out-of-plane breathing modes (ZO') for both the supercells (d)

in the dispersion curve increases with increasing number of lattice sites by a factor of 3N, where N is the number of lattice sites. Increasing the number of lattice sites also adds to the complexity of the dispersion curve due to folded phonon spectrum at the Γ point of the BZ. To analyze the misorientation angle dependent evolution of the phonon dispersion in MBG and to establish correlation between misorientation angle and low-energy phonon modes below the ZO' mode, we perform phonon dispersion calculations for other commensurate angles between 0° and 30°. Phonon dispersions for $\Theta = 21.78°$, $27.79°$, $13.1°$, $9.43°$, $7.34°$, $11°$, and $6.0°$ are presented in Fig. 6.5

Low-frequency modes

Low-frequency or energy modes arise from out-of-plane relative motions of the two graphene layers, and these modes are sensitive to both the inter-layer coupling and the temperature. In experiment, this mode can be explained by the double resonance mechanism and may be activated by MBG lattice that lacks long-range translational symmetry [273]. The dependence of the frequency and line width of this mode on the twisting angle reveals a degree of overlap of the two Dirac cones that belong to the two layers in the MBG. In the MBG, the identification of the Raman active ZO mode from the complex dispersion curve, as shown in the Fig. 6.5, is a non-trivial process. We identify these low-frequency ZO' modes, in any given MBG system, by analyzing the direction and the magnitude of the out-of-pane force constants on each layer of the MBG, as shown in the Fig. 6.6.a. Since in the ZO mode the top and bottom layers move in opposite directions, resulting in expansion of the MBG system leading to the weak inter-layer coupling. Low-frequency ZO' modes for all the simulated MBG system is tabulated in Table- 6.2.

Fig. 6.6.b compares the experimentally observed low-energy Raman modes with our theoretical observations. It can been seen that, our model successfully reproduces

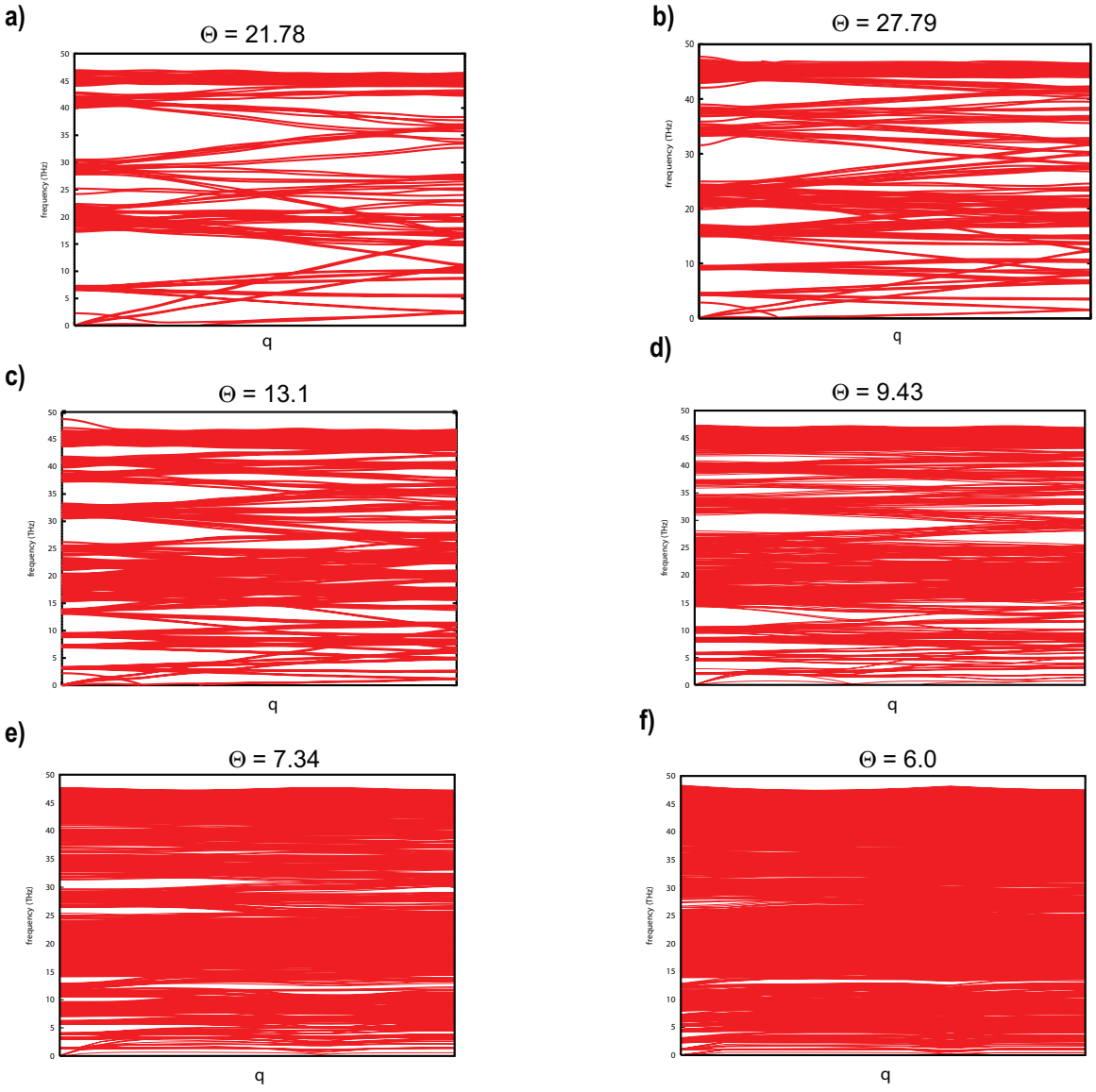

Figure 6.5: (Color online) Phonon Dispersions for MBG supercell with $\Theta = 21.7°$ (a), 27.79° (b), 13.17° (c), 9.43° (d), 7.34° (e), and 6° (f)

Table 6.2: Low-frequency ZO' modes at Γ for MBG supercells

Misorientation Angle (Θ)	**No. of atoms in the Super-cell**	**Length of the Lattice Vectors** (A^o)	**Low-frequency ZO' Modes** cm^{-1} (meV)
AB	4	2.46	94 (11.7)
21.78°	28	6.51	94.188 (11.7)
27.79°	54	8.87	95.19 (11.8)
13.17°	76	10.72	94 (11.7)
9.43°	148	14.96	96.86 (12)
7.34°	244	19.21	96.8 (12)
6°	364	23.46	88.5(11)

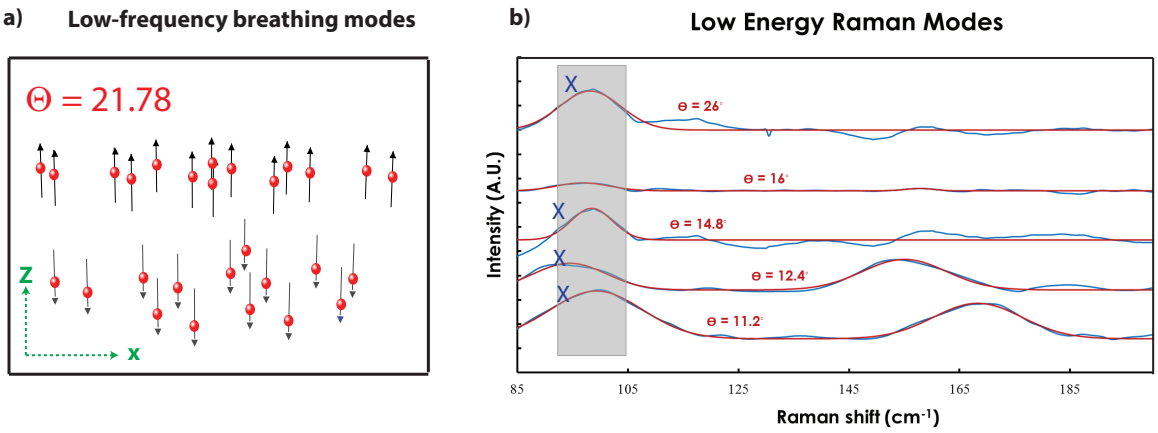

Figure 6.6: (Color online) a. Acoustic vibrations in MBG supercell with Θ = 21.78°, and b. Low-energy modes (X) plotted on top of experimental Raman modes (From Pankaj Tharamani)

the low-energy modes observed in experiment.

Phonon Density of States (PDOS)

Phonons generally affect the thermal, optical, mechanical, and electrical properties of materials. While the phonon density of states (PDOS) is primarily a function of the local atomic structure, it is also sensitive to atomic-level strain and disorder. Misorientation also adds topological disorder to the perfectly-stacked bilayer system. At lower dimension, deviations of the PDOS from the corresponding bulk structure have also been observed, both in experiment and theory. Phonon confinement due to finite size or quantum phenomena comes from the discreteness of electron states and band-gap variation due to confinement. Grain boundaries and confinement effects affect the optical modes at the Γ where the momentum (q) = 0. However, phonons away from the Γ where the momentum is not zero, also contributes to the total PDOS. A study providing a fundamental understanding of PDOS shift due to the misorientation and the supercell size appears to be a worthwhile task. An extreme case of a rotational disorder in a bilayer graphene exists when the two layers are in AA-stacking, which resembles $\Theta = 60^o$ in the MBG. In order to understand the effect of rotational disorder in the phonon dispersion, PDOS for nominal disorder (AB-stacked bilayer), a moderate disorder ($\Theta = 21^o$) and an extreme disorder (AA-stacked bilayer) is presented in Fig. 6.7.

PDOS for the nominal disorder (AB-stacked bilayer) and extreme disorder (AA-stacked bilayer) show no variation of the peak maximum of the optical modes. Rotational disorder, however, shifts the TO peak to a lower frequency. Essentially, two major features can be observed, namely the broadening of the acoustical branch and a red-shift of the MBG optical frequency, mainly due to the grain size- or supercell size-induced confinement effect. Above all, our observation of a weak dependence of

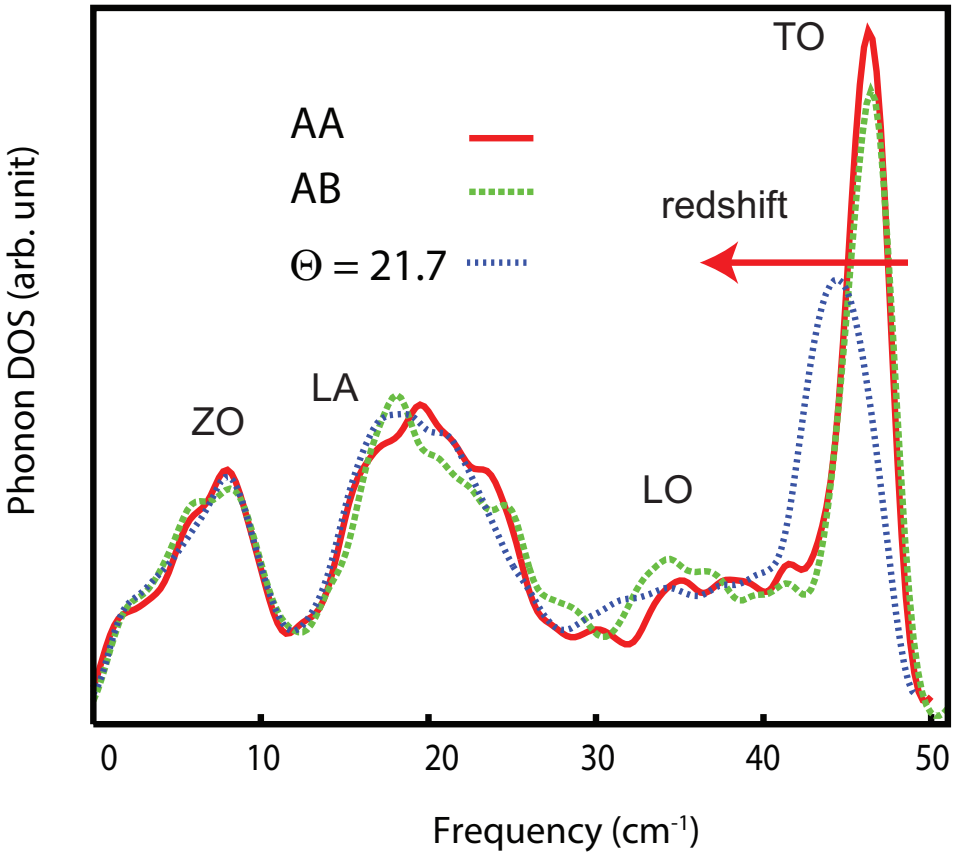

Figure 6.7: (Color online) Phonon density of states (PDOS) for AB-stacked bilayer (dotted-green), AA-stacked bilayer (solid-red) and $\Theta = 21^o$ (dotted-black)

PDOS on the misorientation angle is consistent with the earlier theoretical calculation based on harmonic lattice dynamics [251].

Lattice Specific Heat Capacity (C_v)

From our PDOS analysis, we have observed that the supercell size is the strongest contributor to the increases in the acoustic modes of the PDOS, due to the general broadening of the PDOS in those regions. The increase of the acoustic low frequency modes in the PDOS will cause a direct change in the specific heat and the related thermal properties. Though there are few reported research efforts on identifying the correlation between the misorientation angle and thermal properties, both theoretically and experimentally. Theoretical efforts are mainly based on the harmonic approximation that ignores temperature effect. Here, we report, for the first time, a systematic study of thermal properties such as specific heat, C_v, or thermal conductivity of MBG using the anharmonic approximation, which is plotted in Fig. 6.8. The C_v in the bilayer graphene can be tuned by introducing misorientation between the layers, by increasing the number of layers in the MBG, and by introducing defects.

We found that the C_v for the MBG follows the classical Dulong-Petit law, where the magnitude of C_v increases linearly at the low temperature. This is an expected "classical" behavior of solids at high temperature when all six atomic degree of motion (three translational and three vibrational) are excited and each carries $\frac{1}{2}K_bT$ energy. For temperatures above 1500K, the value of C_v starts saturating to a constant value. We also evaluated the low temperature C_v of SLG, which is higher than that in graphite due to a discrepancy in the DOS. This difference in C_v vanishes at higher temperatures.

Since we are interested in the thermal properties of MBG at room temperature, we evaluate C_v at room temperature as a function of supercell size (number of atoms) in

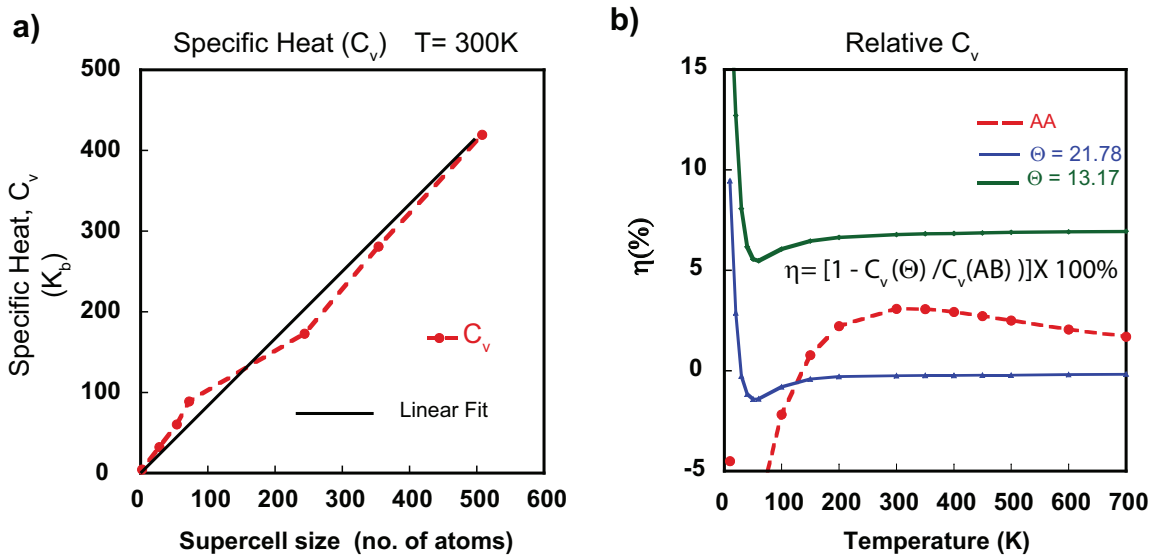

Figure 6.8: (Color online) a. Lattice specific heat capacity C_v vs MBG Supercell size at T = 300K, and b. Relative difference in C_v between AB-stacked bilayer system and AA (dotted-red), $\Theta = 21.7^o$ (solid-blue) and $\Theta = 13^o$ (solid-green)

Fig. 6.8.a. C_v shows a linear dependency on the supercell size, which is consistent with the scaling law of thermal conductivity. In addition, in order to understand the effect of misorientation on the thermal properties of MBG, we evaluate a relative specific heat parameter $\eta = [1 - C_v(\Theta)/C_v(AB)]$ X 100 %. At low temperature (< 700 K), η is evaluated and plotted in Fig. 6.8. b, where we observed that the lattice specific heat capacity depends on the misorientation angle, which mainly comes from the misorientation-dependent low-frequency phonon modes. Similar observations were also reported recently by Nika and et al [275]. They attributed this modulation of interlayer coupling due to strain.

In experiment, the exotic properties of monolayer graphene are not always beneficial for the realization of graphene devices or interconnects and, in many cases, few-layer graphene (FLG) or vertical supperlattice has more favorable properties for practical applications. Contrary to the SLG, FLG exhibit much lower thermal conductivity due to the weak van der Waals interaction between the layers [276]. In the

FLG, van der Waals interactions between the layers are also responsible for the misorientation between the layers, forming MBG superlattice. A large number of studies on the in-plane thermal properties for supported FLG has already been reported. The layer dependent thermoelectric properties in the MBG has rarely been reported.

To elucidate the effect layer stacking on the thermoelectric properties of MBG, we calculate the C_v for the MBG superlattice with $\Theta = 21.7^o$. C_v as a function of both the temperature and number of layers is plotted in Fig. 6.9.a. In the MBG superlattice, the C_v , which is directly propotional to the thermal conductivity (K), increases with the temperature. At low temperature range($< 50K$), the observed behavior of $C_v \propto T^2$ is due to the "bond bending" character of out-of-plane vibration between the layers because, at low temperature, $C_v \approx T^{\frac{d}{n}}$ for phonon dispersion $\approx q^n$. Thus the low-temperature C_v contains information about both the dimensionality of the system and the phonon dispersion. The in-plane low-energy frequency modes corresponds to layer sliding, and make a minor contribution to heat capacity at low temperature. At room temperature, the C_v for 6L MBG superlattice with $\Theta = 21.7^\circ$ 30% higher than that of MBG $\Theta = 21.7^\circ$ because of the higher PDOS at low phonon frequencies given by the weak coupling between the layers in the 6L MBG superlattice. A similar behavior is expected for an isolated graphene sheet at room temperature, when all of its flexural ZA modes should be thermally excited.

The phonon propagation in an atomically thin graphene sheet is likely to be very sensitive to surface or edge or defects. To understand the effect of point-defect on MBG, we have calculated C_v for the defective MBG with $\Theta = 21.7^\circ$ as well as pristine MBG. As can be seen from Fig. 6.9.b, MBG with a point defect also follows the follows the classical Dulong-Petit law. In general, the defective MBG which had lower C_v, as compared to its pristine MBG.

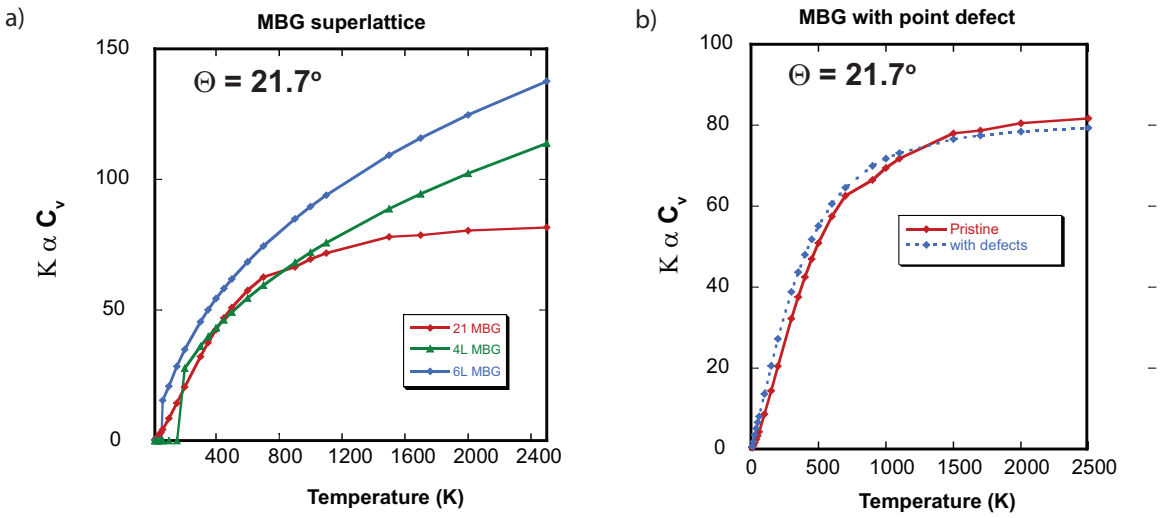

Figure 6.9: (Color online) a. Lattice specific heat capacity C_v vs MBG superlattice constructed using MBG with $\Theta = 21.7°$, and b. C_v for a pristine MBG with $\Theta = 21.7°$ (solid-blue) and defective MBG of same angle (dotted blue)

6.4 Conclusion

We successfully modeled the experimentally observed misoriented bilayer system and studied their vibrational and thermal properties, as a function of misorientation angle. In order to include the temperature effect, we have utilized the anharmonic approximation implemented in the Fixphonon package integrated in the MD method. Phonon dispersion characteristics for both the MBG supercell with $\Theta = 21.78°$ and perfectly-aligned supercell have similar features. Lattice-induced folded phonon modes have similar frequencies, with an exception of out-of-plane ZO' modes. ZO' mode frequency for the MBG increases by 17 cm^{-1}, as compared perfectly-aligned supercell, owing it to the weak inter-layer coupling. Anharmonic approximation successfully predicts all the experimentally observed low-frequency Raman modes around 100 cm^{-1} ($\approx$12 meV). The broadening of the acoustical branch and a redshift of the MBG optical frequency was observed, mainly due to the grain size- or supercell size-induced confinement effect.

The lattice specific heat capacity, C_v, for the MBG follows the classical Dulong-Petit law. C_v shows a linear dependency on the supercell size, which is consistent with the scaling law of thermal conductivity. In conclusion, we have demonstrated the possibility of using the topology-based phonon engineering technique to engineer vibrational and thermal properties in 2D materials with hexagonal lattice.

Chapter 7

Nanoscale Phononic Interconnects in THz Frequencies

7.1 Motivation

Phononics or phonon engineering involves the control and manipulation of phonon inter-actions and transport [277]. With the advent of naturally occurring two-dimensional (2D) van-der Waals materials such as graphene, transition metal dichalcogenides (TMDC) and artificially made 2D materials, this field of engineering is becoming a very interesting research area with applications ranging from the macroscale to the nanoscale [278]. Although research utilizing engineered materials and their heterostructures in this field of engineering started as early as 1992 [100, 279], it is only recently that there has been intense effort to analyze and manipulate phonons at the nanoscale in order to design nanodevices operating at terahertz (THz) frequencies. In analogy with the corresponding electronic and photonic devices, there are studies of thermal diodes and rectification [280–283], thermal memory [284] and charge density wave transistors [285, 286]. With the realization of these types of devices,

phononic computing will appear as an alternative computing paradigm to the conventional electronic and optical computing, increasing our ability to manipulate and store information in the nanoscale.

Parallel to phononic device research, there is an effort to manipulate phonons and the thermal conductivity for improved thermoelectric properties. The materials studied in those works are carbon based such as carbon nanotubes, graphene, and graphene composites. Several studies with silicon based materials have also shown that, due to the confinement-induced changes, the phonons and lattice thermal conductivity are significantly modified in nanoscale systems, such as silicon membranes [287], two dimensional phononic crystals, [288–290] and silicon surfaces with silicon posts [291].

Electronic and optical interconnect design trade-offs are well researched and understood [292]. However, to realize and integrate the phononic devices with the existing conventional de-vice architectures, phononic interconnect components such as waveguides, resonators, and switches are needed. In this study, we propose and analyze various phononic interconnect com-ponents, such as nano-scaled phononic resonators, waveguides and switches, realized on ¡111¿ surfaces of group IV elements, such as 3C-SiC and 3C-GeSi (the surfaces with the highest density) by introducing defects on the surface of these materials. These materials are widely used in the optoelectronics devices [293–297]. The growth of ordered systems with alternating atoms, similar to the SiC and GeSi systems, are commonly achieved using advanced deposition techniques such as molecular beam epitaxy (MBE) [298], atomic layer deposition (ALD) [299], self-assembly [300] and chemical vapor deposition (CVD) [301]. The appearance of phononic band gaps (PBG) is very important for the creation of localized states around the defects and these materials are expected to have wide PBG [302, 303]. The defects are introduced either by removing (vacancy defects) or

by replacing atoms (substitutional defects). The removal and placement of individual atoms and lines of atoms in Si has been demonstrated [297, 304, 305]. The process of defect introduction leads to the generation of strongly localized vibrational modes around the defects which could be used as resonating sites in the resonator. Furthermore, removing or replacing lines of atoms creates phononic waveguides through which phonons can propagate. By engineering specific defects near these waveguides, the propagation of the phonons can also be controlled and manipulated leading to the realization of a phononic switch. Though it is possible to design such defect-based phononic components in the bulk materials, in this study, we focus on the realization of the phononic interconnect components on the surfaces of these materials.

In our study, we use molecular dynamics (MD) simulations, as implemented in the LAMMPS code [116] for our calculations of the partial phonon density of states, and the total density of states (TPDOS). We choose the Tersoff potential as our potential of choice [306,307]. This method has been used in our prior work on similar systems and tends to produce vibrational and structural properties, which were in good agreement with more rigorous first principle calculations [308]. Though the initial frequency offsets in phononic band gap (PBG) edges and higher frequency phonons are up to 30%, further optimization and fitting led to the reduction in those offsets to less than 5% [302]. We validate our MD produced vibrational properties with those from the first principle calculations [308] for smaller systems, and they are qualitatively and quantitatively in good agreement.

7.2 Models and Methods

7.2.1 Models

For our simulations, the base cell of choice was the primitive cell of the FCC Bravais lattice (triclinic) with a diatomic basis AB, were A is Si (Ge) and B is C (Si) for the cases of the 3C-SiC and 3C-GeSi crystals, respectively (see Fig. 7.1). By replicating the base cell several times along the x, y and z directions, supercells with thousands of atoms were generated with their faces parallel to the $< 111 >$ crystallographic plane. For bulk systems, the size of the structures was made equal to the size of the simulation box, as shown in Fig. 1b, and the barostat was set to relax the system in all directions. The $< 111 >$ surface (see Fig. 1c), was constructed by replicating the base cell five times in the z-direction, and several times in the x- and y- directions. In order to avoid spurious interaction in the z-direction, a large enough vacuum gap was maintained above the supercell, so that the atoms in the top will not feel the interactions from the atoms in the bottom (due to the PBC along the z-axis), and thus behave as surface atoms. Systems with vacuum gaps 5A$\circ$ showed the exact same behavior as systems with very large vacuum gaps. Consequently, the structure becomes periodic along the x- and y- directions, and hence, the volume and pressure relaxes only along these directions. In order to avoid any unwanted surface effects related to the thickness of the structures, and to eliminate any thickness dependent frequency changes, as discussed in Refs. [288, 309], we test the effect of thickness dependence. Increasing the thickness of GeSi surface from $\approx$6 to $\approx$ 16 A$\circ$, leads to the on average blue-shifts of 0.3 THz in the phonon DOS. However, increasing the thickness further leads to a negligible change ($\approx$0.05 THz) in the phonon spectra. Hence to minimize the required simulation time and computational resources, we have used five unit cells ($\approx$13 A$\circ$ for SiC and $\approx$16 A$\circ$ for GeSi) to model the structures

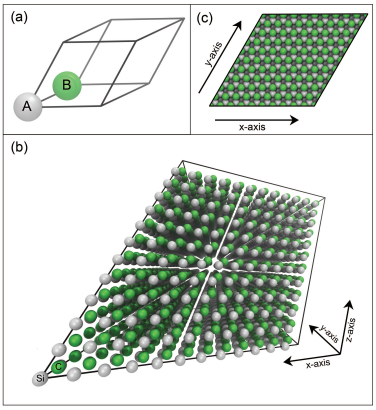

Figure 7.1: **a)** The primitive cell (triclinic) of the FCC lattice with a diatomic basis AB, where A is Si (Ge) and B is C (Si). **b)** The bulk structure of 3C-SiC, generated by 12 replications of the primitive cell **(a)**, in the x, y and z directions. **c)** The $< 111 >$ surface of SiC. Note that the atoms in the background (dark grey) are also Si atoms.

with infinite thickness. This confirms that the examined surfaces should behave as the surfaces of the bulk materials in the range of THz frequencies.

7.2.2 Methods

DFT Calculation

DFT calculations were performed using the generalized gradient approximation (GGA) employing the exchange-correlation functional of Perdew, Berke, and Ernzerhof (PBE) [308] expanding the wavefunction on plane-wave basis sets. We used standard Vanderbilt ultrasoft pseudopotentials [310]. The plane wave basis set cut-off is 240 eV. For the sampling of the Brillouin zone, we use a 661 MonkhorstPack mesh. Tight convergence criteria have been imposed for the total (self-consistent) energy per atom at 2x10-5 eV/atom, while the threshold on the forces is set to 10-3 eV/. For the phonon DOS calculations, the dynamical matrix elements were calculated in the first Brillouin zone on a 661 q-point mesh using a supercell of about 10 . A suitable Gaus-

sian broadening of the dynamic matrix eigenvalues was used for the creation of the phonon DOS curves with a full width at half maximum of 3.3 cm-1. The calculations have been performed using the electronic structure calculation package QUANTUM ESPRESSO [311].

MD Calculation

Molecular dynamics (MD) simulations were performed with the LAMMPS code [116], to study the vibrational properties both of the bulk and the surface of the SiC and GeSi crystals. The pair-wise interactions were computed with the Tersoff potentials for the C-C, C-Si, Si-Si, Si-Ge and Ge-Ge interactions [306, 307]. All of the MD simulations are performed within the framework of the isothermal-isobaric ensemble (NPT), with a fixed number of atoms N, constant pressure P, constant temperature T, and a time step of 0.8 femtosecond (fs). The temperature of the system was held constant at 300 K using the Nose Hoover thermostat [312, 313]. The Nose Hoover thermostat allows for fluctuations of the temperature with a distribution close to the canonical distribution, thus probing the canonical ensemble quite accurately. The effective relaxation time affects the coupling with the internal heat bath. A long results in slower convergence to the canonical ensemble, and for a short , can result in large, high-frequency fluctuation in the temperature. In our simulations, we used an effective relaxation time of 0. ps, which gives a good convergence and small temperature fluctuation. The pressure of the system was maintained at 1 bar with the Nose Hoover barostat, and a relaxation time of 1 ps [116].

Phonon Density of States Calculation

The phonon density of states was calculated independently using two different methods. In the first method, the finite temperature phonon DOS was calculated by the

Fourier transformation of the velocity time autocorrelation function (VACF) [302],

$$D(w) = \int_0^{inf} d\tau e^{iw\tau} \frac{1}{N} \sum_{i=1}^{N} \frac{1}{t_{max}} \sum_{t_0=1}^{t_{max}} v(t_0).v_i(t_0+\tau) \tag{7.1}$$

where v_i is the velocity of the i^{th} atom, N is the number of the selected atoms, and t_0 is the initial time step. For the total phonon density of states (TPDOS), the structures were allowed to relax for 160 ps ($2x10^5$ time steps), and then the velocities of the all the atoms in the system (N_{system}) were captured every 3.2 fs (4 time steps), for a total time of 13.1 ps (214 time steps). To evaluate the TPDOS, These captured velocities were input into the (Eq. 7.2.2). For the partial phonon density of states (PPDOS) calculation, the velocities of specified groups of atoms ($1 \leq N \leq Nsystem$), or single atoms (N=1) were captured instead and then used in the Eq. 7.2.2. In order to improve the accuracy of the PPDOS and avoid any statistical sampling issue, the size of the statistical sample is increased by capturing the velocities of the selected atoms in 10 independent iterations instead of one, and then averaging the calculated velocity autocorrelation functions. In order to check the consistency of the observed results and avoid any relaxation time dependent results, we also performed test simulations at longer relaxation times, and found no direct correlation between the relaxation time and quality of the phonon spectra.

In the second method, we used the FixPhonon module available in the LAMMPS distribution [116,132,133]. In this module, prior to analyzing the lattice vibrations of the given system, the system was equilibrated at room temperature by calibrating at various time scales. The instantaneous positions of atoms in the equilibrated system were transformed into reciprocal space to obtain the Greens function. After a certain number of measurements, the time average of the Greens function was evaluated,

and, for a long enough simulations, the time average was equivalent to an ensemble average. The force constant matrices were then deduced, and the dynamical matrices were constructed from them. During the dynamic matrix calculation, at a given temperature and pressure, the systems were equilibrated for 10^6 MD steps, and then the time average of the phonon frequencies were calculated for $6x10^6$ MD steps. Using the eigen-values of these dynamical matrices, the TPDOS and PPDOS were computed. In order to observe smoother DOS, a dense wave vector is recommended [309], thus in our simulations we replicated our supercell several times and then used an even denser wave vector in the post-processing stage. This requirement increases the size of the supercell from 20-50 atoms to approximately $5X10^3$ to 10^4 atoms.

For all the structures in this study, both the VACF and FixPhonon methods produced qualitatively and quantitatively similar vibrational properties. Though the VACF method is free from any requirement of supercell replication and hence, intensive computing resources, the phonon spectra were relatively noisier than the one produced by the FixPhonon method. Irrespective of the higher computational cost, throughout this study, we present the FixPhonon method since the results were of higher quality, though all of our results were verified with both methods.

7.2.3 Results and Discussion

Model Verification

Bulk PDOS Molecular dynamics (MD) is an empirical atomistic model, and its empirical parameters should be calibrated and verified either against available experimental data and/or data from the first principle calculation. Since there is a lack of the experimental data on our system, we compare our bulk GeSi and SiC vibrational properties with those obtained from first principle (or DFT) calculations. The solid

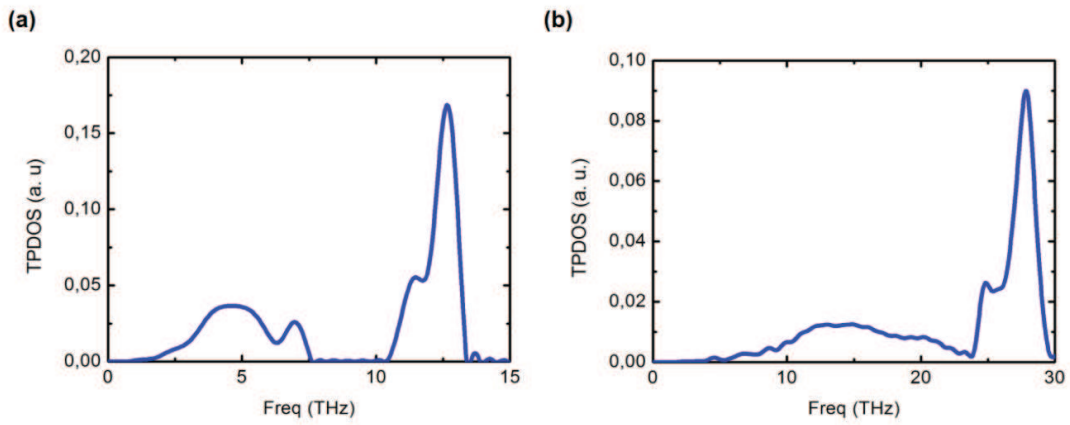

Figure 7.2: The TPDOS for (a) bulk GeSi and (b) bulk SiC calculated from the VACF method.

black curve with the hatched fill pattern in the figure 7.2.3.a shows the DFT TPDOS for GeSi with a phononic band gap (PBG) between 8.3 and 10.7 THz and a maximum frequency at approximately 13.5 THz. The solid grey region shows the MD TPDOS with a PBG between 7.8 and 10.3 THz and a maximum frequency at 13.8 THz. The TPDOS of the bulk SiC and GeSi from the VACF method are presented in Fig. 7.2.3.

The first principle calculated PBG for bulk SiC (solid curve with hatched fill in Fig. 7.2.3.b) is between 16.7 and 19.2 THz, and the maximum frequency phonon is at around 27 THz. The MD simulations (Fig. 7.2.3.b, grey region) give a PBG between 22.3 and 23.9 THz and a maximum phonon frequency at 29 THz. The PBG resulting from the MD simulation is shifted by 20-30% to-wards higher frequencies with a width 36% smaller than the result from the first-principle calculation. It is clear that the interatomic potential **??** does not describe the lattice dynamics and inter-layer coupling of SiC as accurately as for GeSi. However, as will become clear from the rest of our results, the trends are the same for both GeSi and SiC indicating the validity of the calculations.

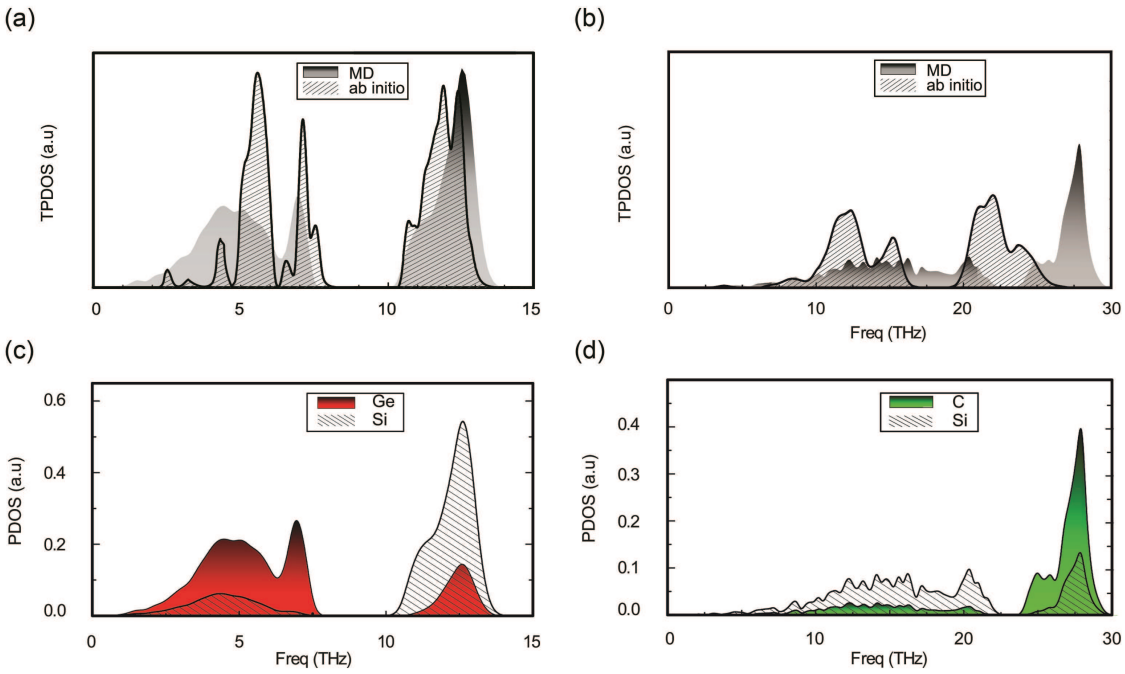

Figure 7.3: Phonon density of states of the bulk GeSi (a) and SiC (b) systems. The grey curves represent MD simulation results, the solid black curve with the hatched fill pattern represent first-principle results, and (c and d) the partial phonon density of states (PPDOS) of the bulk GeSi (c) and SiC (d) from MD simulations. The PPDOS for the C, Si and Ge atoms are represented with green, hatchet fill pattern and red curves, respectively.

Though the first principle method for the SiC system produces better results, it is computationally expensive, as compared to the MD method. In addition, most of our examined structures have several thousand atoms, and hence, analyzing the vibrational properties using first principle method is not feasible, mainly due to the computational time and memory constraints. Figures 2c and 2d illustrate the partial density of states (PPDOS) of bulk GeSi and bulk SiC, respectively, calculated using the MD method.

Surface PDOS Figure 7.1.c illustrates the atomistic view of the $< 111 >$ surface of 3C-SiC, similar to the $< 111 >$ surface of 3C-GeSi. The constructed surfaces have

two possible configurations based on the type of atoms covering the surface. In the first configuration, the surface is covered with the lighter atoms i.e. Si-Face (C-Face) for the cases of GeSi (SiC), as shown in Fig. 7.1.c. In the second configuration, the heavier atoms are on the surface Ge-Face (Si-Face) for GeSi (SiC). The PPDOS of the Ge-Face surface of GeSi in (Fig. 7.2.3.a) is qualitatively similar to the bulk GeSi (Fig. 7.2.3.c), with a slight blue-shift (≈0.5 THz) in the maximum phonon frequency. In contrast, the PPDOS of the Si-Face (Fig. 7.2.3.b) shows a new surface state inside the PBG around 8 THz. This feature is also observed in the SiC case. When the heavy atom (Si) is in the surface (Si-Face), the PPDOS (Fig. 7.2.3.c) is similar to that of bulk SiC (Fig. 7.2.3.b) with a slight red-shift of the PBG by 0.5 THz. Interestingly the PPDOS of the C-terminated surface shows a maximum fre-quency peak at about 30 to 37 THz, well above the highest frequency phonon of the bulk SiC, while the PBG is significantly reduced (23 to 23.5 THz), as is illustrated in figure 7.2.3.d. The C atoms in 3C-SiC crystals with randomly induced substitutional defects have a total of five possible configurations, since they neighbor with zero to four C atoms (and consequently with four to zero Si atoms). When the C atoms neighbor with four other C atoms by forming the diamond configuration, the observed maximum phonon frequencies are at 33 THz. In the case where the C atoms neighbor with four Si atoms (SiC configuration), the PPDOS has maximum phonon frequencies at 29 THz (Fig. 7.2.3.d). This is mainly due to the damping of the higher frequency vibration of the lighter C atoms when surrounded by the heavier Si atoms. This also ap-plies to the atoms in the surface. In the C terminated surface of SiC, the C atoms neighbor with just three Si atoms instead of four (the configuration in the bulk), and thus, the phonon branches of these atoms tend to shift in higher frequencies. Similar suppression and release of the phonon branches is also observed in the GeSi system. It is important to point out that, these surface states appear either inside the PBG, or

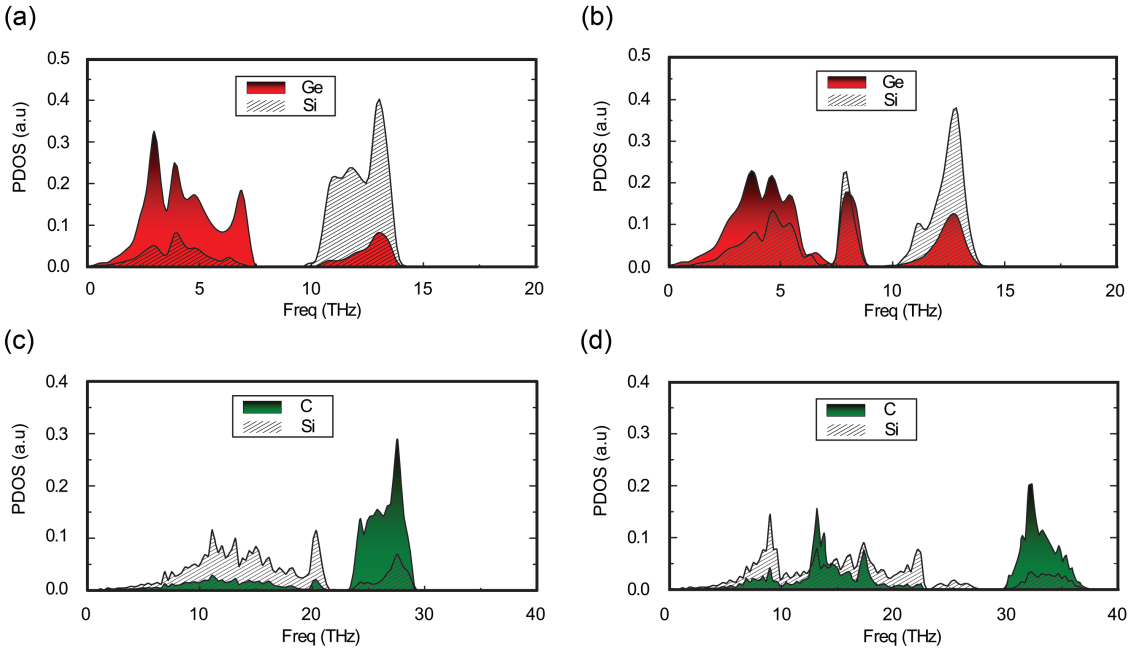

Figure 7.4: The PPDOS of the <111> surfaces of 3C-GeSi and 3C-SiC. The PPDOS of the (a) Ge-Face, (b) Si-Face of GeSi. The PPDOS of the (c) Si-Face, (d) C-Face of SiC. For all the cases, the green, hatchet fill pattern and red curves correspond to the C, Si and Ge atoms respectively.

above the maximum frequency phonon of the bulk. These states, if excited, will not leak in the bulk region but instead will propagate in the surface. In the rest of this study, these surface states will be used for designing the resonators (isolated defects), the waveguides (lines with defects) and the switches (defects in the waveguides), that enhance the propagation of the phonons.

Circuit Components

Resonators The resonators can be created on the surface either by introducing single substitutional or vacancy defects. In the first type of resonator, a substitutional defect was introduced by exchanging one Ge atom with one Si atom in the Ge-Face of the GeSi surface (see the inset in Fig. 7.2.3.a). The introduction of the substitutional defect gives rise to two new phonon states: (a) one around 8 THz (inside the PBG of both the bulk GeSi and the $< 111 >$ Ge-Face) and (b) another around 16 THz (above the highest frequency phonon of both the bulk GeSi and the Ge-Face surface). These states are well localized around the defect. Substitutional defects in the $< 111 >$ Si-Face of the SiC surface exhibit similar behaviour. The PPDOS of the replaced atom (Si $\leftrightarrow$ C), as shown in (Fig. 7.2.3.b), features a PBG between 22 and 23 THz. The observed frequency maxima is around 38 THz (above the maximum phonon frequency of both the bulk SiC and the $< 111 >$ Si-surface of the SiC).

The second type of resonator was designed by introducing a single vacancy defect in the Ge-Face of the GeSi surface (inset in Fig. 7.2.3.c). The PPDOS for the neighboring Si atom (marked with an arrow in the inset of Fig. 7.2.3.c) exhibits a peak at around 8 THz. This peak is inside the PBG of both the bulk GeSi (Fig. 7.2.3.c) and the $< 111 >$ Ge terminated surface (Fig. 7.2.3.b). Albeit the steeper maximum peak, the overall PPDOS feature is similar to the case of the Si-Face of the GeSi surface, as shown in the figure 3b, because, in both cases, the examined

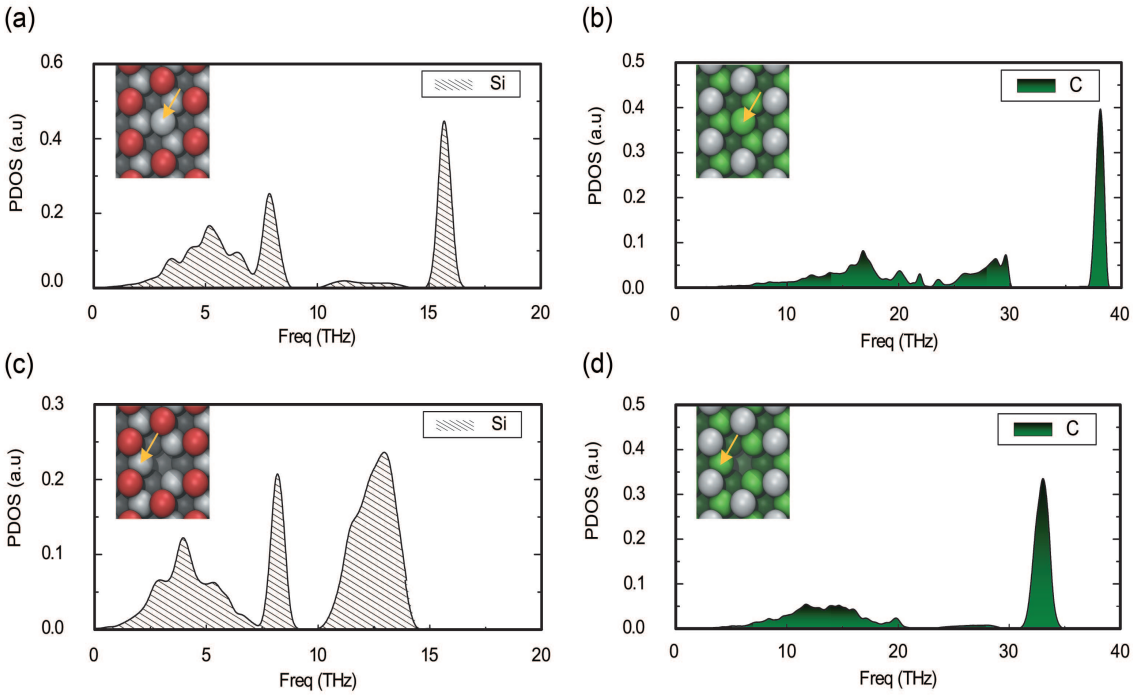

Figure 7.5: PPDOS of isolated substitutional and vacancy defects in the $< 111 >$ surface of 3C-GeSi and 3C-SiC. The PPDOS of the Ge-Face of GeSi surface with (a) a substitutional defect and (c) a single vacancy defect. The PPDOS of the Si-Face of SiC surface with (b) a substitutional defect and (d) a single vacancy defect. Inset on each figure illustrates the configurations for the corresponding case. For all the cases, the PPDOS corresponds to the atoms marked with the yellow arrows. The green, grey and red colors correspond to the C, Si and Ge atoms, respectively.

Si atoms share the same local configuration (both of them neighbor with three Ge atoms). In the case of the Si-Face of SiC, the PPDOS of the C atom located near the vacancy (marked with an arrow in the inset of Fig 7.2.3d) exhibits a well-defined peak at around 33 THz. The peak is well above the maxima in the phonon frequencies of both the bulk SiC (Fig. 7.2.3.d) and the ¡111¿ Si-surfaced SiC (refer to Fig. 7.2.3.c). Similar to the substitutional induced defect states, the phonons corresponding to vacancy defects are well localized around the defects.

Waveguides Similar to the resonators, we have designed waveguides by creating lines with substitutional or vacancy defects in the $< 111 >$ surfaces of GeSi and SiC. Initially, a single line of Ge atoms was replaced with Si atoms (see Fig. 7.2.3a) in the Ge-Face of GeSi. The PPDOS of the Si atoms in the line features two well defined peaks at around 8 and 16 THz, as illustrated in figure 7.2.3.d (grey curve). The PPDOS of this waveguide is similar to the PPDOS of the Si resonator, as shown in the figure 7.2.3.a. Since these states are absent in the phonon DOS of the bulk and the Ge-Face, they will be able to propagate only along the line of Si defects on the Ge-surface of GeSi. As the width of the waveguide increases to two and three Si atoms, as shown in figures 7.2.3.b and 7.2.3.c, the highest frequency phonons appear at around 17 and 17.2 THz, respectively, as illustrated in the figure 7.2.3.d (red and blue curves). For the two and three atoms widths, the lowest bounds of the PBG shifts to higher frequencies at around 9.7 and 9.9 THz, respectively, leading to the reduction of the PBG gaps, while the higher edges remains unaltered. For four and more atom widths of the waveguide, the PBG width of the PPDOS remains constant. Note that, these states were also observed in the PPDOS of the neighboring Si atoms, just below the defect line. Similar results were also obtained for the waveguides with the substitutional defects in the Si-Face of SiC.

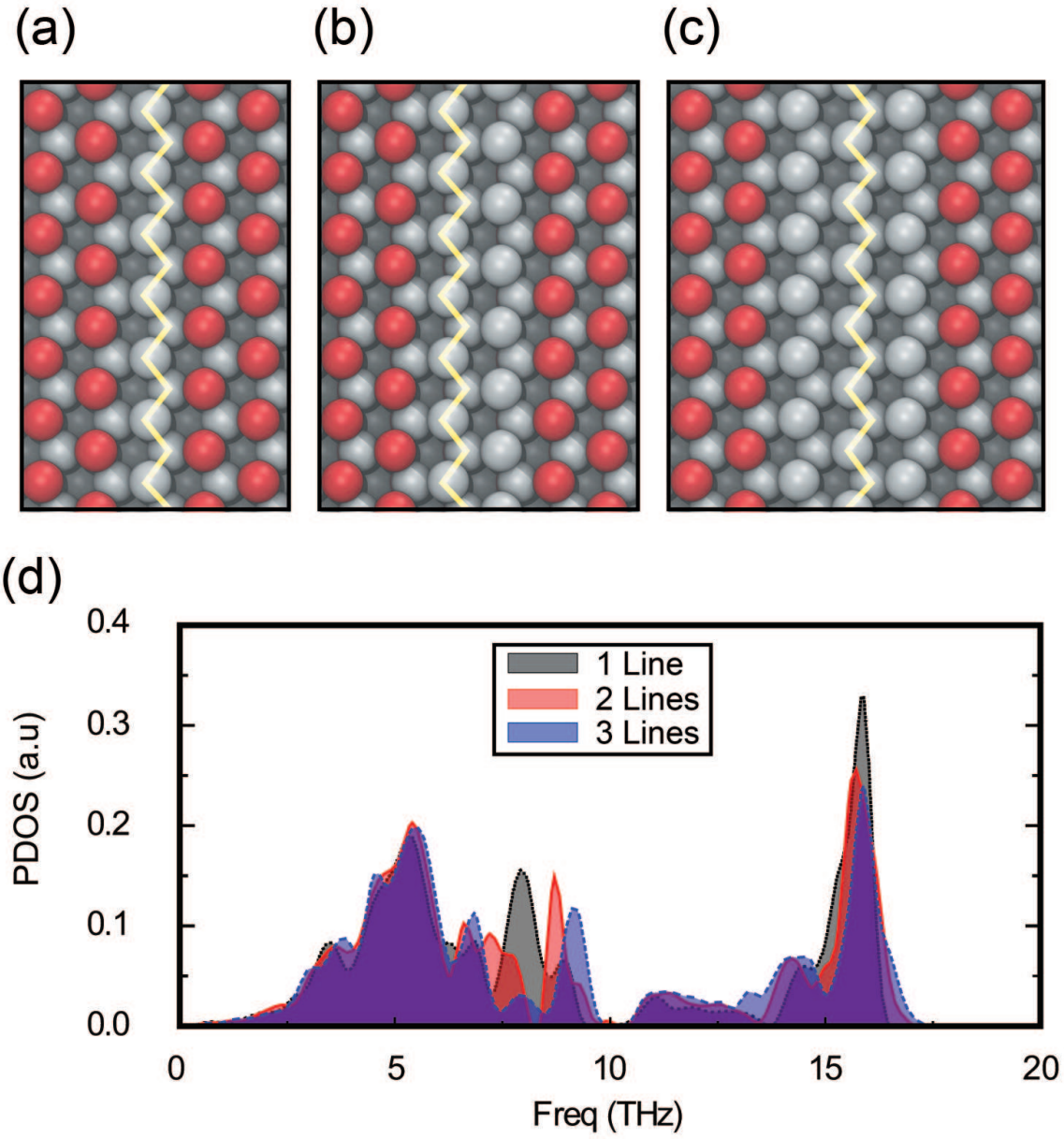

Figure 7.6: Atomistic representations of Ge-terminated surfaces of GeSi, with (a) one line, (b) two neighboring lines, and (c) three neighboring lines, with substitutional defects. The red and grey atoms correspond to Ge and Si respectively. d) The PPDOS of the atoms in the waveguides for one (grey), two (red), and three (blue) neighboring lines with vacancy defects.

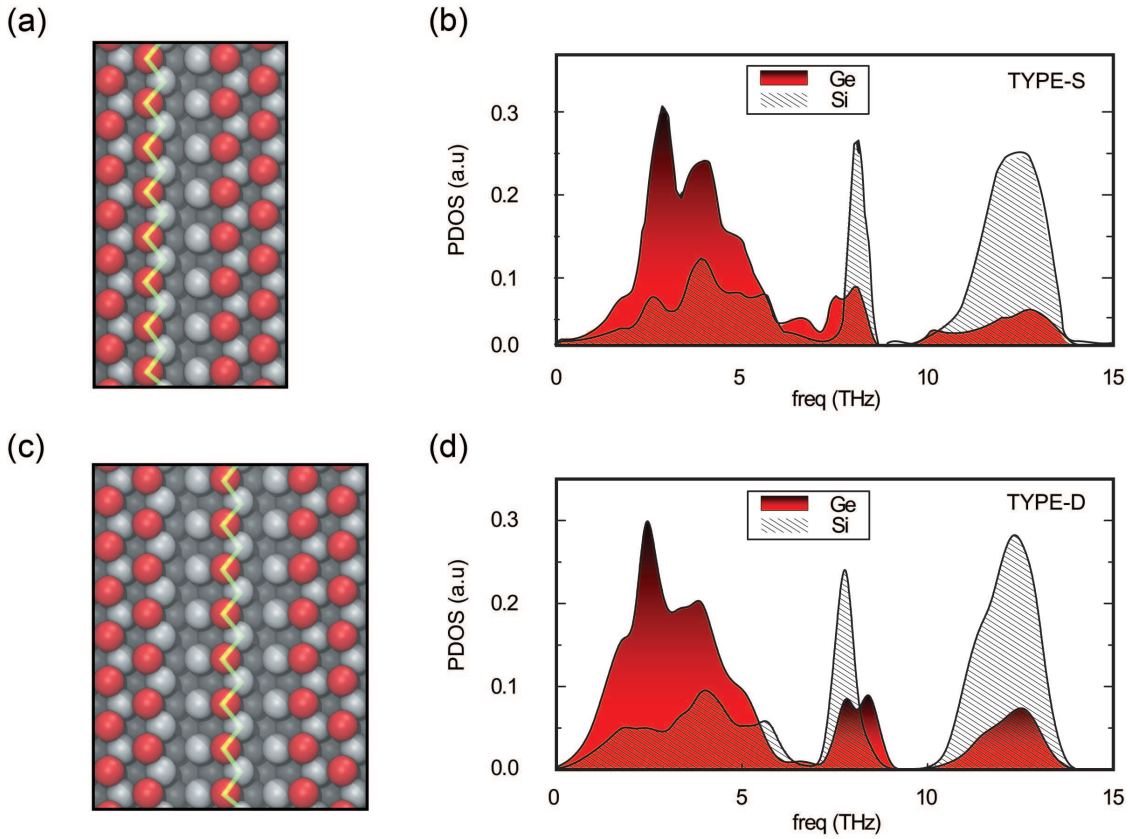

Figure 7.7: Vacancy waveguides in the Ge-Face of the GeSi surface, (a) TYPE-S and (c) TYPE-D. PPDOS for the Si and Ge atoms in the TYPE-S (b) and TYPE-D (d) waveguides. The red and grey colors correspond to Ge and Si, respectively.

Introducing substitutional defects using C atoms along a single line completely fills the PBGs of the bulk SiC and the Si-Face SiC. Consequently, few new states emerge in between 33.5 to 40 THz, well above the phonon frequency maxima of the bulk GeSi, and hence, a new PBG appears in between 30.5 and 33.5 THz. By increasing the width of the waveguide to two Si atoms, the newly formed PBG of the single line is partially filled with the new states. Further increment of the line-width leads to the filling of the gap and the disappearance of the PBG.

Besides substitutional defects, waveguides can also be designed by removing lines of atoms (vacancy defects) from the surface. Initially a waveguide with a line with

vacancy defects in the Ge-Face of the GeSi is designed, as shown in figure 7.7.a. Hereafter, we call this type of wave-guides as TYPE-S. The PPDOS of either a Si atom just below the defect line or a Ge atom next to the defect line shows a peak at around 8.2 THz as in figure. 7.7.b. Unlike the waveguide from substitutional defects, it does not exhibit any additional mode above the maximum phonon frequencies of either the bulk GeSi, or the $< 111 >$ Ge-surface of GeSi.

Removing two or more neighboring lines of Ge atoms from the $< 111 >$ Ge-Face of the GeSi makes the Si atoms just below those defect lines unstable, and they detach from the rest of the structure at room temperature. This is expected because these atoms, after losing three of their neighbors, become unstable due to the reduction of their bonding energies. Beside this case, all the other cases studied above were stable. Another possible type of stable waveguide (TYPE-D) can be created by removing two lines of Ge atoms in each side of a Ge line, as shown in figure 7.7.c. The PPDOS of this wave guide, as illustrated in figure 7.7d, displays similar behavior to that of the single line vacancies in the Ge-Face of GeSi (Fig. 7.7.b), with a peak at 7.8 THz. However, it has an additional narrow peak at around 8.5 THz.

In addition to the linear waveguides, controlled addition or removal of defects in the surface could lead to the realization of a phononic component that could not only modulate the phonons but also, split and redirect the propagation into different directions. This phononic wave-guides, which could modulate phonons, is an analogous component to the electrical or optical waveguides [292]. Figure 7.8 illustrate such structures made from substitutional and vacancy defects. The top structure (dotted black circles in Figs. 7.8.a, and 7.8.b) bends the propagation path of the propagating phonons, and we call this phononic component a phonon-bender. Similarly, the bottom structure (green-dotted circles in Figs. 7.8.a, and 7.8.b) splits the propagating phonons, and this component is known as the phonon-splitter. When the propagat-

ing phonons reach the phonon-bender they could either change direction (120 turn). Similarly, when the propagated phonons reach the phonon-splitter, they will split in two different directions. Using this method of inducing the substitutional defects, one can design phonon-splitters that could split the transmitting phonons in many different directions. Note that, a Ge atom is missing from the top of the waveguide with the vacancy defects (Fig. 7.8.b). This intentional removal of Ge atom is needed because the Si atoms in the waveguide are required to neighbor with only three Ge atoms to sus-tain the resonant peak at 8 THz frequency.

Switches By inducing defects at the waveguides, one can also enhance the propagation of the phonons, and design phononic switches, an analogous to an electronic and optical switches. Here, we have designed the phononic switch by placing adatoms in the middle of the vacancy waveguide, as shown in figure 7.9.a. The PPDOS of a Si atom (marked with the black arrow) that neighbors to a Ge adatom (marked with the yellow arrow) placed in the middle of a vacancy waveguide, at the Ge-terminated surface, is shown in the figure 7.9b. In this structure, there is no resonant peak in the frequency region between 7 and 10 THz, indicating the blocking of the guiding mode at around 8 THz, which was present in the simple waveguide case (refer to the Fig. 7.7b). Using this property, one can envision a phononic component having a $< 111 >$ Ge-terminated surface of GeSi with a vacancy waveguide and a scanning tunneling microscope (STM) tip consisting of Ge atoms that can be tuned in or out of the waveguide. The novelty of these types of components would be their ability to allow or block the propagation of phonons along the waveguide at the atomic-level.

Besides adatoms defects, we also investigated the possibility of using other kinds of defects within the waveguide. Since the phonons can only be transmitted through the atoms that are located either below or next to the waveguide, introducing a vacancy

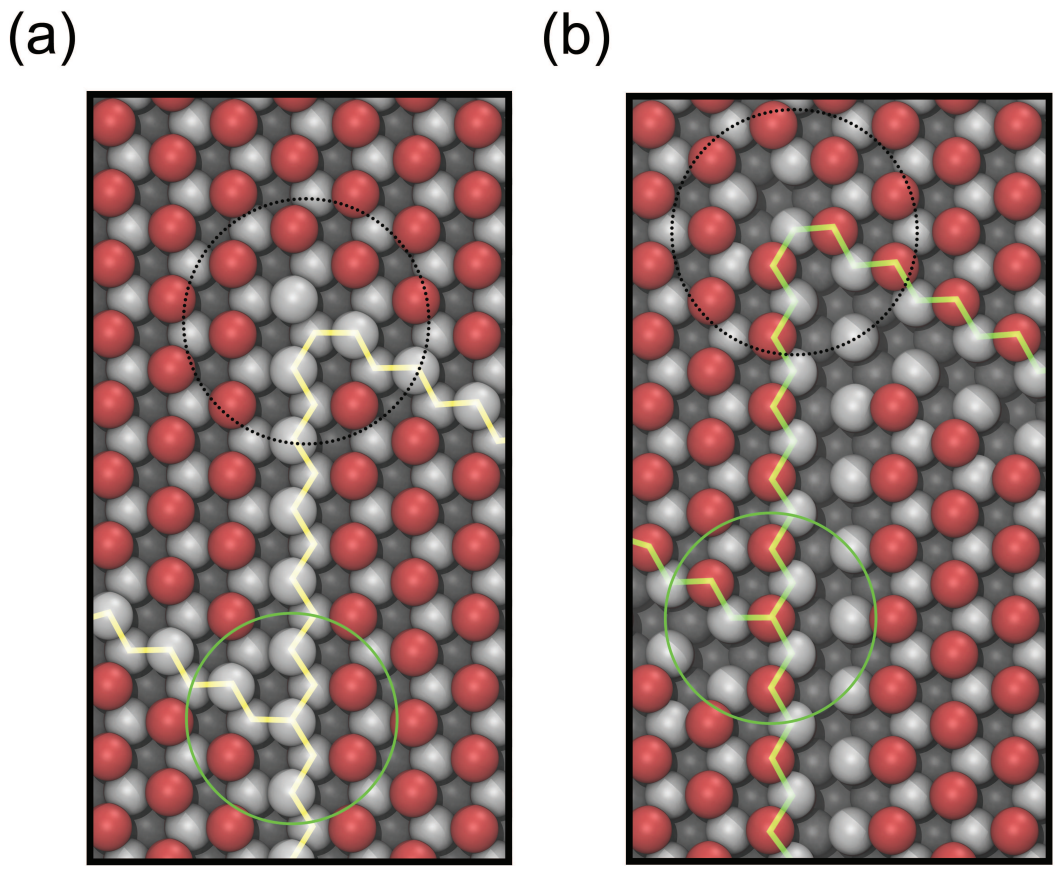

Figure 7.8: Illustration of the phonon propagation in complex phononic waveguides, which splits phonons into two paths (phonon-splitters, green circles), or modulates the direction (phonon-benders, dotted black circles). Complex phononic waveguides designed with (a) substitutional defects, and (b) with vacancy defects, in the Ge-Face of GeSi. The grey and red atoms are Si and Ge, respectively. The phonon propagation paths are illustrated using the zigzag lines.

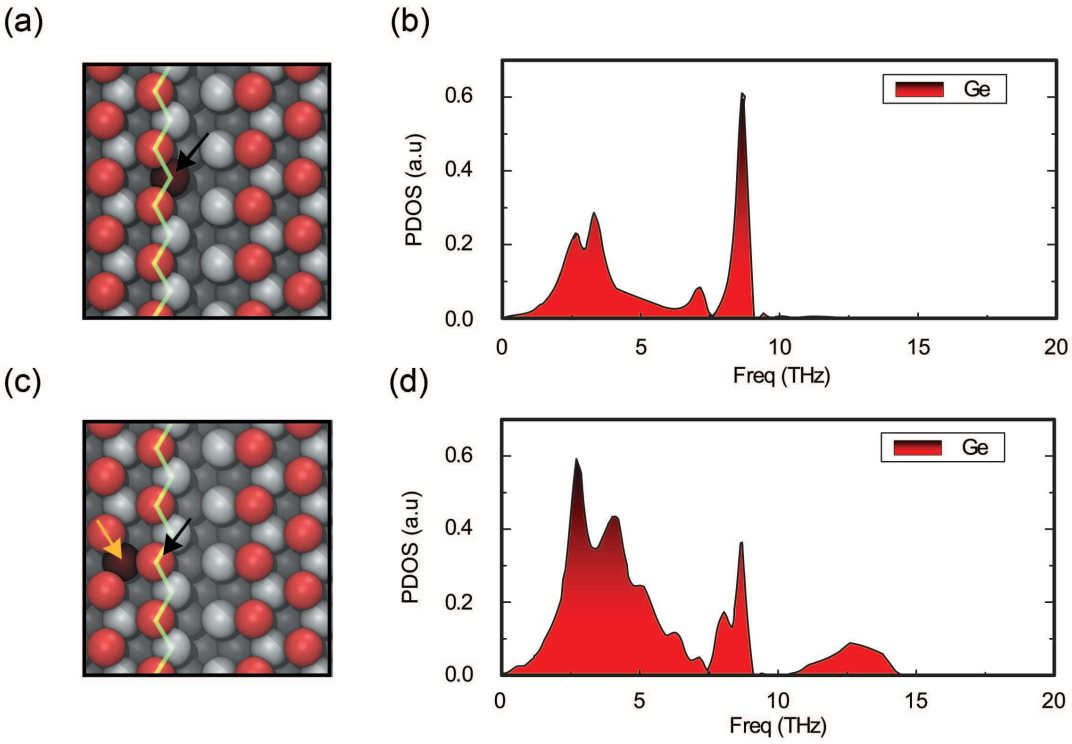

Figure 7.9: Atomistic representations of a phononic switch designed by adding a Ge adatom (dark red atom marked with a yellow arrow) on the TYPE-S waveguide in the Ge-Face of GeSi. (b) The PPDOS of the Si atom (marked with a black arrow in (a)) that neighbors to the Ge adatom (switch). Note that the resonant peak at 8 THz is suppressed.

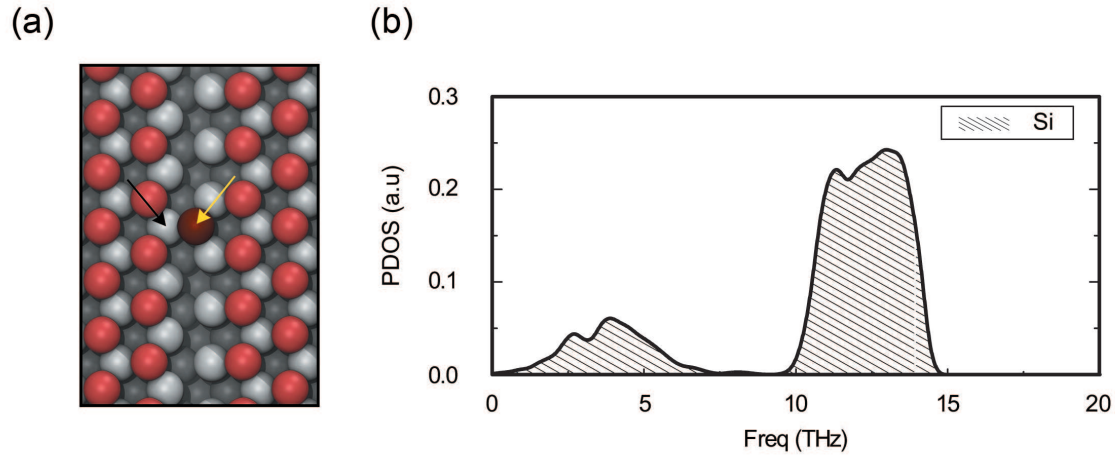

Figure 7.10: Substitutional defects (dark red) inside (a) and near (c) the TYPE-S vacancy waveguides in the Ge-Face of GeSi. The yellow arrow at (c) points to the substitutional defect. b) The PPDOS of the Ge atom marked with a black arrow in the configuration of (a). d) The PPDOS of the Ge atom marked with a black arrow in the configuration of (c). The red and white atoms represent the Ge and Si atoms, respectively, while the dark red atoms represent the substitutional defects (Si↔ Ge).

defect in the waveguide blocks the propagation of the phonons in its entirety. On the other hand, substitutional defects within the waveguide do not seem to block the phonon transmission. We also observed that, by exchanging a Si atom with a Ge atom either within (Fig. 7.10.a) or near (Fig. 7.10.c) the waveguide does not affect the resonant peak at ≈8 THz, thus the phonons are allowed to propagate without any scattering. This confirms that, introduction of random substitutional defects, through natural diffusion, should not block the transmission of the phonons, and hence, the waveguide should continue to be functional.

7.3 Conclusion

Phononic interconnects on the $< 111 >$ surface of the 3C-SiC and 3C-GeSi system were conceptualized and designed using defect engineering techniques with the frame-

work of atomistic molecular dynamics (MD) method. The existence of phononic band gaps within the phonon spectrum of the bulk 3C-SiC and 3C-GeSi was confirmed by both the first-principle and MD simulations with semi-empirical potentials. The agreement between the two methods was good for the case of 3C-GeSi and moderate for the 3C-SiC case, mainly due to the inaccuracies in the Si-C interaction parameters in the Tersoffs potential. The PPDOS on the $< 111 >$ surface of these sys-tems reveals the possibility of generating the new surface states within the phononic band gap (especially for the case where the lighter atoms are in the surface). These surface states, which are decoupled from the bulk states, are used to design phononic interconnects, such as resonators (isolated defects), waveguides (lines with defects), and switches (adatoms within the waveguide). In conjunction with electronic and/or photonic interconnects, these proposed phononic interconnects could be used in the current and future devices, while expanding overall computing and memory capabilities.

Although the present study demonstrates the possibility of realizing phononic interconnects in the atomic scale, there are several important issues that need to be addressed before they can be integrated in the current and future technologies. Some of these issues are excitation frequency, coupling losses, propagation losses, optimum materials and structures, and surface passivation.

Chapter 8

TExFET- A device for future device applications

8.1 Motivation

The possibility of achieving a Bose-Einstein condensate (BEC) of electron-hole pairs in a system that consists of two spatially separated layers of electrons and holes has been a topic of continued research since its initial inception [101, 314]. Initial experimental studies have focused on the use of two-dimensional electron systems confined in GaAs/AlGaAs double quantum well structures to observe evidence of exciton condensation [108, 315]. In these systems, recombination of electrons and holes is suppressed due to the spatial separation of charge with a spacer layer, forming indirect exciton. A bias applied independently to each layer can be used to balance or unbalance the charge concentrations between layers thus controlling the effective strength of the Coulomb interactions, referred as the exciton binding energy. The formation of excitons is exponentially suppressed once the thickness of the insulating barrier exceeds the effective Bohr radius of the exciton [101,316]. Thus far, the exciton

condensate in GaAs/AlGaAs double-quantum well systems has only been observed at low temperatures in the quantum Hall regime [108, 315]. Furthermore the binding energy of the excitons in GaAs quantum wells has been theoretically predicted to be ~ 4.5 meV [118,316]. But despite ultrahigh-quality materials, and insulating barriers as thin as 1 nm, the superfluid has not yet been definitively observed without any external field.

The advent of graphene as the prototypical two-dimensional material led to a resurgence in the exploration of exciton condensation in double layer quantum well structures. Theoretical predictions of spontaneous condensation of excitons at room temperature have been suggested in bilayer graphene structures. The possibility of achieving strong interlayer interactions in atomically thin vdW heterostructures has also led to a number of proposals to utilize this many-body collective state as ultra-low power transistors in post-CMOS devices [16, 110, 111, 317]. Recently, the bilayer pseudospin field-effect transistor (BiSFET) was proposed, and the possibility of exciton condensation at room-temperature was demonstrated, albeit theoretically [110]. In principle, the switching energy per device in the BISFET could be on the scale of 10^{-18} J, over two orders of magnitude below estimates for "end-of the roadmap" CMOS transistors. In the BISFET, high and potentially room temperature condensation is favored mainly because two graphene sheets are closely spaced, leading to stronger Coulomb interaction. Symmetric electron and hole band structures over the energy ranges of interest that allow accurate nesting between the electron and hole two-dimensional Fermi surfaces. A low density of states in the graphene which leads to the required high Fermi energies relative to the Dirac points at relatively low carrier densities.

Experimental realization of the room temperature superfluidicity using BISFET is hindered by a number of the fundamental challenges. These challenges include

choosing the appropriate dielectric materials, minimizing the spacing between dielectric layers while still limiting the bare/single-electron coupling between the layers, understanding the effects of charge imbalance and screening. The problem of charge imbalance is crucial because, if not handled properly, it could lead to suppression of condensed exciton. Electron-impurity scattering, lattice scattering, or from the presence of inhomogeneity in the charge density distribution lead to charge imbalance between the layers. Screening effects the sperfluidic gap formation mainly due to the free-carrier screening induced by the gates around the graphene layers. To minimize this effect, vacuums and/or a very low-k dielectrics near the region of condensation, including above and below the graphene layers is needed.

The emergence of monolayer semiconducting transition metal dichalcogenides has introduced a new platform in which atomically-thin hetero-layered devices can be envisioned. The TExFET addresses some of the issues associated with BISFET, and relies on the superfluidity to excitonic insulator state transition, which results in the formation of a gap that switches the device from a highly conductive state to an "off" state [16]. As a complement to the BiSFET structure, in this study, we model the properties of an exciton condensate in monolayer MoS_2, $MoSe_2$, WS_2 and WSe_2 films separated by an atomically thin insulating layer. The availability of atomically thin dielectric layers such as boron nitride (BN) allows for strong electron-hole coupling between the spatially separated monolayers [318].

8.2 Model and Methods

Our system consists of two TMDC layers embedded in a dielectric media, analogous to the bi-layer graphene system. Our study is limited to a single trilayer of 2H-MoS_2, 2H-$MoTe_2$, 2H-$MoSe_2$, 2H-WS_2 and 2H-WSe_2 with boron nitride sandwiched

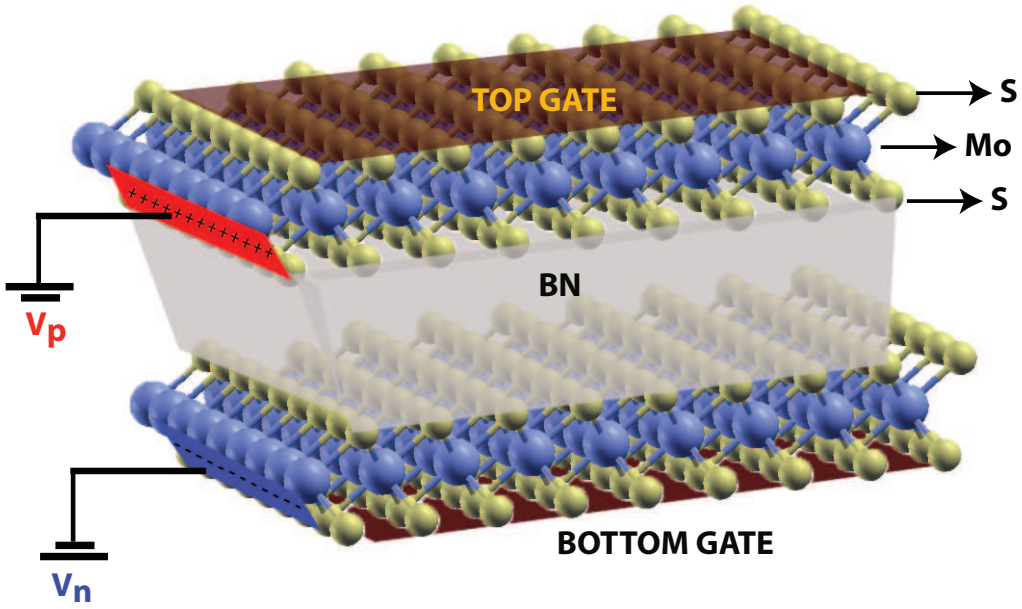

Figure 8.1: a) Model device architecture with two layers of MoS_2 separated by a thin film of boron nitride (BN). The top monolayer is biased with a positive voltage (V_p) and the bottom monolayer is biased with a negative voltage (V_n).

between the semi-infinite slabs. Figure 8.1 shows the atomic structure of the coupled quantum well (CQW) system we will study. Each monolayer is terminated with an independent set of metal contacts from which current may be injected and extracted. The charge imbalance due to contact resistance is ignored by assuming similar top and bottom gates. The carrier concentration in each TMDC layer is controlled by gating them independently. In order to form exciton condensation and hence, drive the condensate current, the drag-counterflow configuration is used while applying bias voltage. In this configuration, a positive voltage is applied to the top contact and an equal negative bias is applied to the bottom layer. We assume the use of ideal contacts within this study, which ignores unintentional doping of the TMDC layers. In this study, we employ two methods: a) Effective mass approximation (EMA) coupled with variational principle, and b) mean field approximation (MFA).

8.2.1 EMA + Variational principle

An effective mass model is used to calculate the exciton binding energy and effective Bohr radius in this model structure. Prior calculations of exciton binding energies in separated quantum well structures have utilized a range of methods ranging from effective mass approximations [118] to more rigorous many-body calculations. As illustrated in our model, paired electron and holes of masses m_e and m_h are moving on a surface of a CQW consisting of two quantum wells with thickness l_w and separated by a thin potential barrier with thickness Δ, as illustrated in the Fig. 8.1. Traditionally, the excitonic condensate states and corresponding energies are calculated using rigorous and accurate many-body [319], and Monte-Carlo [320] methods. However, for excitons of large radius and smaller binding energies, in comparison with the bandgap, the effective mass approach provides a suitable approximation of these properties. In this approximation, the total Hamiltonion for a spatially separated electron-hole pairs in a CQW separated by a thin potential barrier consists of a kinetic energy term (H_{KE}) and a Coulomb interaction term (H_{Coul}) which can be written in the following form:

$$H_{tot} = H_{KE} + H_{Coul} \tag{8.1}$$

and the Schrodinger equation for the exciton envelope function is given by:

$$[H_{KE} - H_{Coul}]\Theta(x_e, y_e, x_h, y_h, z_e, z_h) = E_b\Theta(x_e, y_e, x_h, y_h, z_e, z_h) \tag{8.2}$$

where $\Theta(x_e, y_e, x_h, y_h, z_e, z_h)$ is the exciton envelope function. The exciton binding energy (E_b) is given as the sum of the kinetic (E (KE)) and Columbic (E (Coul))

energies. The single particle kinetic energy term is written as follows:

$$E(KE) = \left[\frac{p_{z_e}^2}{2\ m_e} + \frac{p_{z_h}^2}{2\ m_h} + \frac{P_X^2 + P_Y^2}{2\ (m_e + m_h)} + \frac{p_x^2 + p_y^2}{2\ \mu}\right] \Theta(x_e, y_e, x_h, y_h, z_e, z_h) \quad (8.3)$$

where, m_e and m_h are effective masses in the upper and lower quantum well. z_e and z_h are the physical separation of the charges in the z-direction or confinement direction. P is the center-of-mass momentum and μ is the reduced electron-hole mass. The electron-hole Coulomb interaction energy is given by,

$$E(Coul) = -\left[\frac{e^2}{\kappa[x^2 + y^2 + (z_e - Z_h)^2]^{1/2}}\right] \Theta(x_e, y_e, x_h, y_h, z_e, z_h) \quad (8.4)$$

where κ is the effective dielectric constant, which can be taken as the average of dielectric constants of the QW and the insulating materials, as long as the image-charge effects are neglected. The exciton envelope wave function can be separated as follows:

$$\Theta(x_e, y_e, x_h, y_h, z_e, z_h) = \Psi_e(x_e, y_e)\Psi_h(x_h, y_h)\Psi(z) \quad (8.5)$$

where Ψ_e and Ψ_h are electron and hole wave functions in the upper and lower quantum well, respectively, and are identical in shape. $\Psi(z)$ is the exciton wave function in the confined direction. The Eq.8.5 describes the correlation of the electron and hole relative motion. The exciton wave function in the z-direction ($\Psi(z)$) can be further separated as,

$$\Psi(z) = \Psi(z_e)\Psi(z_h) \quad (8.6)$$

with

$$\Psi(z_h) = N_h sin\left(\frac{\pi * z_h}{l_w}\right) \quad (8.7)$$

and

$$\Psi(z_e) = N_e sin\left(\frac{\pi * (z_e - l_w - \Delta)}{l_w}\right) \tag{8.8}$$

where z_e and z_h are the relative distance between the electron and the holes. Δ is the distance between the two quantum wells, and N_e and N_h are the normalizing constants for electron and hole wavefunctions, respectively.

The kinetic energy of the particle does not depend on X, Y, P_X, and P_Y because they are good quantum numbers, and only account for the 2D character of the exciton motion in the layer plane. The independent motion of electrons and holes does not contribute to the exciton condensation. The electron-hole relative kinetic energy that competes with the Coulomb attraction to form the electron-hole binding state is given as,

$$E(KE) = -\frac{\hbar^2}{2\ \mu}\int\int\left[\Theta^*(x,y)\left(\frac{\partial^2}{\partial\ x^2} + \frac{\partial^2}{\partial\ y^2}\right)\ \Theta(x,y)\partial\ x\partial\ y\right] \tag{8.9}$$

The band anisotropy and the correction due to the band non-parabolicity are important since the parallel mass determines the energy in the plane and perpendicular mass determines the quantization energy in the quantized plane. The effect of band anisotropy is included by calculating density of states effective mass for both the electron and holes as,

$$m^*_{dos} = (m^*_x.m^*_y)^{1/2} \tag{8.10}$$

where m^*_x and m^*_y are the effective masses in the x and y directions. This approach normalizes any intrinsic mass anisotropy effect within a layer. The inclusion of the Columbic term in the model Hamiltonian leads to a non-separable differential equation which cannot be solved analytically. A variational procedure is used to calculate the eigenfunction and eigenvalues of the exciton Hamiltonian with the Gaussian type trial

wave function for electrons/holes as,

$$\Psi(x,y) = exp\left[-\frac{(x^2+y^2)}{2*\eta}\right] \tag{8.11}$$

where η is the variational parameters responsible for electron-hole relative motion in the z-direction. Applying the envelope trial function to Eq. 8.9, the expectation value of the electron-hole kinetic energy is simplified as:

$$E(KE) = -\frac{\hbar^2}{\mu * \eta^2} \tag{8.12}$$

By substituting Eq. 8.6 and Eq. 8.11 into the electron-hole Coulomb interaction energy equation i.e. Eq.8.4, the expectation value of the Coulomb potential energy is given by the four dimensional integration,

$$E(Coul) = -\frac{e^2}{\kappa}\int\int\int\int dx\ dy\ dz_e\ dz_h\ N_h^2\ N_e^2 sin^2\left(\frac{\pi * z_h}{l_w}\right)\ sin\left(\frac{\pi*(z_e - l_w - \Delta)}{l_w}\right) exp\left(-\frac{(x^2+y^2)}{2*\eta}\frac{1}{[x^2+y^2+(z_e-Z_h)^2]^{1/2}}\right)$$

Above equation along with the Eq. 8.12 is solved numerically, and the ground-state binding energy in the coupled DQW is obtained by minimizing the total energy by varying the variational parameter (η):

$$E_b = min\{E(KE) + E(Coul)\} \tag{8.13}$$

The minimum η for which E_b is maximum characterizes the effective Bohr radius of the coupled excitonic system. In terms of the device scaling limit, the smaller the value of η, the better scaled would be our TExFET device.

8.2.2 Mean Field Approximation (MFA)

In this study, we employ mean field approximation (MFA) to calculate effective interaction between the electrons and holes residing in two monolayers of TMDC separated by a h-BN layer with a finite thickness. The electron-hole 2D bilayer system forming exciton can be described by the mean-field Hamiltonian of the following form:

$$H^{MF} = \frac{1}{A}\sum_{k,e/h} \xi_k c^{\dagger}_{k,e/h} c_{k,e/h} V^{ij}(|k-k'|) \tag{8.14}$$

k, and k' are two-dimensional wave vectors in the layers, A is the quantization area, $\xi_k = k^2/(2m^*_{e/h}) - \mu_e - \mu_h$ is the quadratic band for the electrons and holes effective masses and chemical potential $\mu_{e/h}$. $V^{ij}(|k-k'|)$ is the Coulomb interaction between electrons and holes in the two layers.

For the unscreened interaction, the effective electron-hole interaction is defined as:

$$V^0(k'-k) = v_q e^{d\ |k-k'|} \tag{8.15}$$

where $v_q = \frac{2\ \pi\ e^2}{\epsilon_r \epsilon_0 |k-k'|}$ is the bare Coulomb interaction, screened by a surrounding medium with thickness d and dielectric perimitivity ϵ_r. The formation of a condensate of interlayer electron-hole pairs gives rise to a direct response of charge density in one layer on the electric field in the other layer, described by anomalous polarizability $\prod_e(h)$. Within the random phase approximation (RPA), the behavior of the system is determined only by the screened interaction between electrons and holes as [321,322],

$$V^s(k'-k) = \frac{V^0(k'-k)}{1 - v_q\left[\prod_e + \prod_e\right] + v_q^2 \prod_e \prod_h [1 - e^{-2d|k-k'|}]} \tag{8.16}$$

where $\prod_e$ and $\prod_e$ are the polarizabilities for the electrons and holes, and in the

parabolic approximation, are defined as by $\prod_e = \frac{2m_e}{\pi\hbar^2}$ and $\prod_h = \frac{m_h}{\pi\hbar^2}$, respectively. The most favorable condition for the electron-hole pairing is achieved at small interlayer separation distance, when $(k - k')\ d << 1$. In this case, the Eq. 8.16 reduces to,

$$V^s(k' - k) = \frac{V^0(k' - k)}{1 - v_q\left[\prod_e + \prod_e\right]} \tag{8.17}$$

The superconducting BCS gap equation for the parabolic band structure is given by,

$$\Delta_{k'} = \sum V^{ij}(|k - k'|)\frac{\Delta_k}{2E_{k'}} \tag{8.18}$$

where,

$$E_{k'} = \sqrt{\xi_k^2 + \Delta_{k'}} \tag{8.19}$$

The parameters used to calculate the exciton binding energy for each of the TMD materials studied are defined in Table **??**.

8.3 Results and Discussion

8.3.1 Binding energy (E_b)

Recent, field dependent measurements conducted on the 2D heterostructures like TExFET revealed interesting physical properties of the interlayer exciton with a much longer lifetime compared to intralayer excitons [323]. The interlayer exciton binding energy calculation in the TExFET device (Eq. 8.13) requires suitable material parameters such as effective masses, band alignment, and dielectric constant, which are extracted from the DFT calcuations. The quality of these parameters depends on the accuracy of a DFT calculation, which in turn relies on the underlying theory. In semiconducting materials which have a parabolic energy dispersion, the electron and

Table 8.1: Material parameters used for binding energy calculation

Material	ϵ_R	m_e (m_o)	m_h (m_o)	ϵ_{eff}	2D Bohr radius (a_B) (nm)
Graphene	3	0.049	0.049	3.4	7.89
2H-MoS_2	3.43	0.406	0.485	3.86	0.665
2H-$MoSe_2$	4.74	0.435	0.503	4.52	0.77
2H-$MoTe_2$	5.76	0.50	0.57	5.03	0.789
2H-WS_2	4.13	0.33	0.30	4.21	1
2H-WSe_2	4.63	0.3585	0.303	4.46	0.9

hole effective masses are characterized by the shape of the dispersion near the conduction and valence band edges, respectively. In order to correctly capture the shaper of the dispersion, we employ HSE functionals within the DFT calculation using VASP. The material parameters extracted from our DFT calculations for all the materials of interest are listed in Table 8.1. Carrier effective masses for the TMDC are averages of the longitudinal and transverse effective masses calculated using Eq. 8.10. This approach normalizes any intrinsic mass anisotropy effect within a layer. Graphene effective mass is calculated using the approach adopted by Gilbert and Shumay's in Ref. [66].

Though the parabolic dispersion in the graphene system under an applied electric field has not been confirmed by experiment, the theoretical calculation does predict field dependent parabolicity in the linear dispersion near the Dirac point. The field induced parabolicity, though theoretically, gives a finite effective mass that can be used in our model. This will be used to compare the E_b of a system composed of graphene layers and separated by h-BN with our system that has TMDC layers separated by h-BN.

The 2D Bohr radius a_B, which gives an upper-bound to the effective exciton Bohr radius (a_B), is an intrinsic material property which is a function of effective dielectric

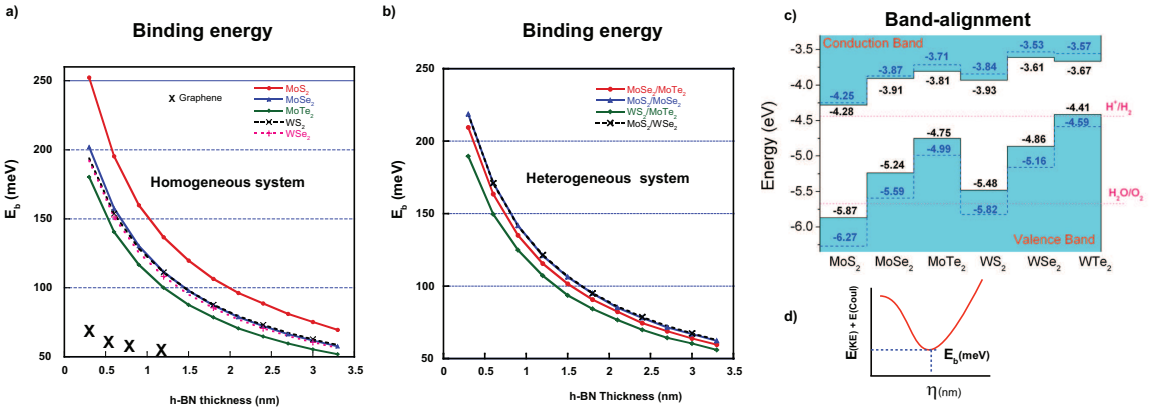

Figure 8.2: (Color online) Exciton binding (E_b)energy of homogeneous TMDC layers (a) and heterogenous TMDC layers (b), as a function of sandwiched boron nitride (BN) between two. The E_b of bilayer graphene system is also plotted for comparison and labelled as X. Band alignment of TMDC monolayers taken from Ref. [15] (c). Solid lines are obtained by PBE, and dashed lines are obtained by HSE06. The dotted lines indicate the water reduction (H+/H2) and oxidation (H2O/O2) potentials. The vacuum level is taken as zero reference.

constant (ϵ_{eff}) and the carrier effective mass (m^*). As can be seen from Table 8.1, the a_B is the largest for Graphene. Using this, we can obtain a lower bound of the E_b using the Hydrogeneic model, which relates E_b *to* $\frac{e^2}{\epsilon_r\ a_B}$. Using $a_B = 7.89$ nm and $\epsilon_{eff} = 3\epsilon_0$, the evaluated lower bound of E_b for the bilayer graphene system is $\approx 21\ meV$. With the a_B of 0.665 nm and $\epsilon_{eff} = 3.43\epsilon_0$, the lower bound of E_b is $\approx 213\ meV$ for MoS_2. Since the effective dielectric constants are of the same order, the difference in the lower bound of E_b between graphene and TMDC's comes from the difference in the carrier effective masses.

The binding energy (E_b) as a function of h-BN layer thickness for two TMDC monolayers of similar type, hereafter called the homogeneous system, is plotted in the Fig. 8.2. a. The E_b for a bilayer graphene system separated by a h-BN layer is also plotted for comparison. In the homogeneous TMDC system, the E_b decreases monotonically with the h-BN layer thickness because of the weaker Coulombic interaction between the electrons and holes. For a monolayer h-BN thickness of $\approx 0.4nm$,

the E_b for the bilayer graphene is only $\frac{1}{3}E_b$ of MoS_2. Because of the largest electron and hole combined effective mass, the E_b for the MoS_2 is $\approx 40\%$ higher than the other TMDCs,

The material selection for a heterogeneous system depends on factors such as the relative valence band offset (VBO) and conduction band offset (CBO) between the valence and conduction bands of the top and bottom layers and the isotropic carrier effective mass. An ideal system that could form the strongest electron-hole pair with the largest binding energy values would posses a staggered or broken-gap band alignment. In this type of band alignment, the conduction band energy level of the bottom (top) layer coincides with the valence band energy level of the top (bottom) layer. The higher conduction or valence band offsets between the top and bottom layer signifies the larger broken-gap feature, which is a preferred band-alignment for exciton formation.

We have identified several heterogeneous TMDC systems by analyzing the band alignment from the Ref. [15] (shown in Fig. 8.2.c) which meet these two criterion. The material combinations used for this study are $MoSe_2/MoS_2$, $MoS_2/MoSe_2$, $WS_2/MoTe_2$, and MoS_2/WSe_2. As in the homogeneous system, the E_b's for the heterogeneous TMDC systems strongly depend on the BN layer thickness. For a BN layer thickness of 0.4 nm, which is an equivalent to one monolayer of TMDC, E_b is in the energy range between 180 to 230 meV, where the 2H-MoS_2 posses the maximum binding energy of 250 meV. Earlier, it was reported that a 2 nm (approximately four monolayers) of h-BN is sufficient to suppress the interlayer tunnelling. At this thickness, for both the homogeneous and heterogenous systems, we observe binding energies in the range of 75-100 meV, which is three times higher than the room temperature thermal energy i.e. KT. Since the interlayer screening is ignored, the observed E_b energy range represents the optimistic case.

Table 8.2: **The effective Bohr radius** η_{min}

	Effective Bohr Radius (η_{min}) (nm)				
	h-BN Thickness (No of Layer)				
System	1	2	3	4	5
MoS_2 / MoS_2	2	2.32	3	3.88	4.31
$MoSe_2$ / $MoSe_2$	1.9	2.5	3.1	3.59	3.81
$MoTe_2$ / $MoTe_2$	1.97	2.52	3.1	3.49	3.8
WS_2 / WS_2	2.2	2.4	2.78	3.2	3.4
WSe_2 / WSe_2	2.07	2.7	3.15	3.3	3.6
MoS_2 / $MoSe_2$	2.1	2.7	3.2	3.7	4
MoS_2 / $MoTe_2$	2.24	2.8	3.2	3.55	3.9
MoS_2 / WSe_2	2.17	2.7	3.07	3.55	3.9
WS_2 / $MoTe_2$	2.10	2.52	2.9	3.3	3.6

For all the material combinations and for h-BN layer thickness up to five monolayers, the effective Bohr radius η_{min} values are presented in Table 8.2. The effective Bohr radius η_{min} is defined as an inter-particle optimum distance when the sum of E(KE) and E(Coul) becomes minimum i.e. at E_b energy point, as shown in Fig. 8.2.d. The η_{min} signifies the scalability aspect of the TExFET devices. For example, if the system has three layer of h-BN in between two MoS_2 layers, the exciton can be formed at the optimum separation distance of η_{min} = 2.32 nm. This optimum distance is $\frac{1}{3}$ of the graphene bilayer system with the same h-BN layer thickness.

8.3.2 Superfluid gap (Δ_{gap})

Electron-hole Fermi surface nesting and the precise control of the potentials and doping densities in each layer are the most important requirements for the observation of the superfluidic gap Δ_{gap} in the TexFET. In our TexFET system, the degree of Fermi surface nesting is characterized by the difference in the electron and hole effective masses. The magnitude of the gate potential is primarily characterized by the absolute energy difference (ΔE) between the conduction band edge of the negatively

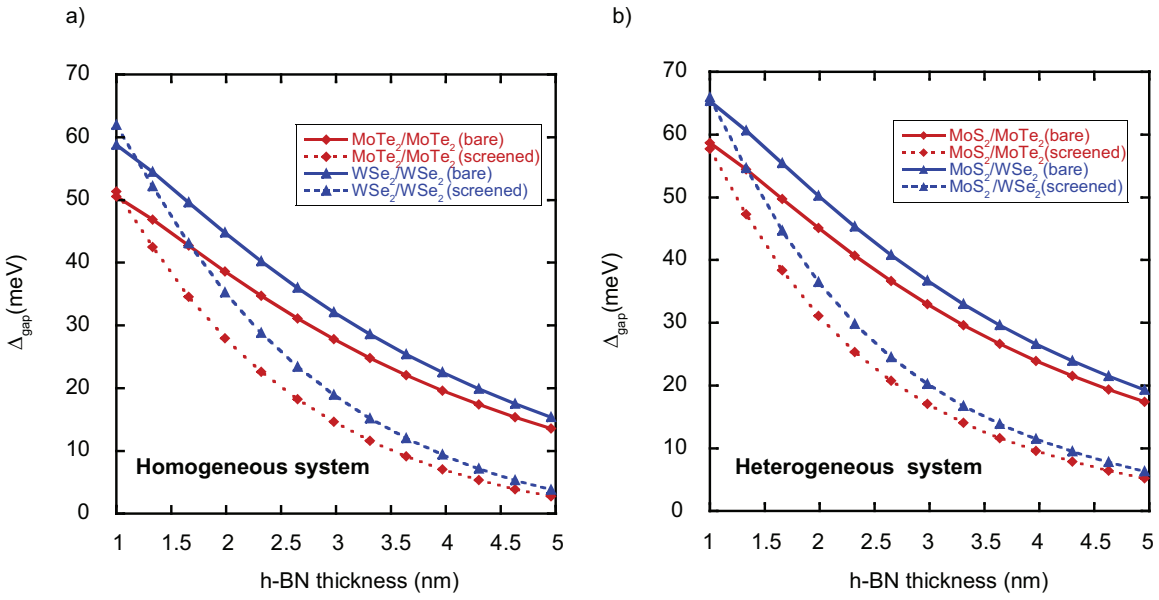

Figure 8.3: (Color online) Superfluid gap (Δ_{gap}) of homogeneous TMDC layers (a) and heterogenous TMDC layers (b), as a function of sandwiched boron nitride (BN).

doped layer and the valence band edge of the positively doped layer. In order to realize the optimum Δ_{gap}, beside minimum h-BN thickness, a material combination system with a minimum effective mass mismatch (or largest Fermi surface nesting) is needed. We have identified two homogeneous systems, $MoTe_2/MoTe_2$, and WSe_2/WSe_2, that meets these criterion. In the case of the homogeneous system, the ΔE is equal to the energy gap of the material. In spite of possessing the heaviest and lightest carrier effective masses, the electron and hole mass mismatch in both the $MoTe_2$ and WSe_2 is only 15%, which will lead to nearly nested Fermi-surfaces. The Δ_{gap} for the homogeneous systems, with and without screening effect, as a function of h-BN layer thickness is plotted in Fig. 8.3.a.

When selecting suitable materials for a heterogeneous system, in addition to the effective mismatch, the ΔE between the layers also needs an attention, because this energy parameter determines the amount of voltage needed to form exciton condensation. Among the available TMDCs data, we have also identified the minimum ΔE

= ≈75 meV between MoS_2 and $MoTe_2$ using the absolute value of band edge energies from the band-alignment plot presented in the Fig. **??**.c. ΔE = ≈91 meV between MoS_2 and WSe_2 also makes MoS_2/WSe_2 suitable for the superfluidic gap formation. In both cases, the carrier effective mass mismatch is greater than 25 %.

Screening, for both the homogeneous and heterogeneous systems, reduces the magnitude of Δ_{gap}. The reduction in Δ_{gap} due to screening effect is negligible ($\lessapprox 10\%$) for the h-BN thickness between 1 and 1.5 nm. However, when the h-BN thickness increases beyond 1.7 nm, screening reduces the Δ_{gap} by $\approx 40\%$. With the increasing h-BN thickness, screening decreases and saturates the Δ_{gap} faster, as compared to the unscreened case.

For the homogeneous system of $MoTe_2/MoTe_2$, a $\Delta_{gap} \approx 26$ meV is observed for the h-BN thickness of 2 nm. Δ_{gap} of similar magnitude, for WSe_2/WSe_2, is observed for the h-BN thickness of 2.5 nm. In the heterogeneous systems, Δ_{gap} also decreases with increasing h-BN thickness. Since the effective mass mismatch between the $MoS_2/MoTe_2$ and MoS_2/WSe_2 systems is similar, the 10% difference in the Δ_{gap} between $MoS_2/MoTe_2$ and MoS_2/WSe_2 is mainly due to the dielectric mismatch. For all the cases, a room temperature superconducting gap of ≈ 26 meV is a possibility when the h-BN thickness is less than 3 nm.

8.4 Conclusion

TMDCs with their large effective mass offer a possible route to room temperature exciton condensation in bilayer structures and gate controlled switching of a quantum phase transition. The unscreened inter-layer Coulombic forces in the TExFET system, with TMDC/h-BN/TMDC heterostructure, gives us an upper bound exciton gap in the order of $\approx 70\ meV$ for a h-BN thickness of 2 nm, mainly due to the isotropic

electron and hole effective masses and the smaller effective dielectric constants of the TMDC layers. Though any inter and intra-layer screening effects might reduce the large exciton gap by 50%, the gap is still sufficient suitable for low temperature, low power device applications. The observed effective exciton radii is in the range of 2 nm, the TExFET could also be a device of choice for extending the device scaling trend. Existence of superfluidic gap in this device architecture is demonstrated. For both the homogeneous and heterogeneous systems, the superfluidic gap of ≈ 26 meV is observed when the thickness of the h-BN layer is maintained in between 2 and 2.5 nm.

At 2 nm h-BN thickness, the effect of static screening between the layers reduces the superfluidic gap in TExFET by $\approx 40\%$. Although the reduction in the superfluidic gap is significant in these systems, the possiblity room temperature superfluidity still exists.

Chapter 9

Conclusion

There is rapidly growing interest in next-generation memory and optical devices by formed using heterostructures between existing materials such as Si and Ge. In this type of heterostructure, the strain, along with the quantum confinement effect, influences overall device properties. A widely used heterostructure is Ge/Si nanocrystal. In the core-shell Ge/Si nanocrystal or quantum dot, where a Ge layer forms core-region which is encapsulated between Si-shell layers. The effect of Ge/Si heterogenity on the carrier dynamics has been studied extensively both theoretically and experimentally. In theoretical studies, however, the details associated with atomistic strain details were not included during the electronic and optical properties calculation because of the scaling limitation of the model. Here, we utilized a method and model that includes strain at the interface during electronic structure calculations.

Using a full-band, $sp^3d^5s^*$ model implemented in NEMO3D, we simulated and calculated the electronic properties of the Ge/Si core-shell heterostructure NCs and the hole lifetimes in a NC-based NVM device application, Barrier height, a crucial parameter that determines the carrier dynamic, is determined from the calculated energy levels. Decay constants are determined from the wavefunctions and used to

calculate hole lifetimes as a function of Ge core diameter.

Several experimental groups have reported the observation of dome-shaped Ge/Si NCs because of the atomistic heterogenity between the Ge and Si layer. Instead of an ideal spherical Ge-core, experimental characterization reveals a crescent-shaped Ge-core in a dome-shaped Ge/Si NCs. Early theoretical works have provided a simplistic explanation of the retention mechanism based on the smaller bandgap of Ge with respect to Si using continuum models, ignoring strain and shape effects. However, atomic scale inhomogeneous of the interface strain and assymetric shape effects on these nanostructures play a crucial role in determining the carrier dynamics. Using a similar method utilized for spherical system, we study the effect of a crescent-shaped Ge-core on the carrier dynamics, in the dome-shaped Ge/Si NCs . Energy levels and related parameters are used to calculate hole lifetimes as a function of Ge-core and Si-cap thickness. In addition, we also employ a similar method to investigate the effects of strain and confinement on the energy levels and emission spectra of dome-shaped, Ge-core/Si-shell nanocrystals (NCs) with diameters ranging from 5 to 45 nm.

Phononics or phonon engineering involves the control and manipulation of phonons. With an increasing focus on design and development of non-charge based devices, phononic computing is emerging as an alternative computing paradigm to conventional electronic and optical computing, increasing our ability to manipulate and store information in the nanoscale. To realize these phononic devices within existing conventional architectures, phononic components such as waveguides, resonators, and switches are needed. In this study, we propose and analyze various phononic circuit building blocks, such as nano-scaled phononic resonators, waveguides and switches, realized on the $< 111 >$ surfaces of group IV elements, such as 3C-SiC and 3C-GeSi. This is achieved by simultaneously introducing defects of various types, and by varying their specific locations on the surface. To calculate the defect-induced vibrational

properties, such as the phononic bandgap, the total phonon density of states, and the partial phonon density of states, we used molecular dynamics with semi-empirical potentials. Our study reveals the possibility of designing phononic circuit elements through defect engineering.

Parallel to phononic device research, there is an effort to manipulate phonons and the thermal conductivity for improved thermoelectric properties. The materials studied are carbon-based system such as carbon nanotubes, graphene, and graphene composites. There is also a rapidly growing interest in vertically stacked van der Waals materials, such as graphene and h-BN, for electronic as well as themoelectric device applications. Graphene is most well studied and well understood van der Waals material. The electronic structure and vibrational properties of monolayer and bilayer graphene has been studied extensively both theoretically and experimentally. However, in vertically stacked van der Waals material devices the interfaces between different materials will, in general, be misoriented with respect to each other. Experimentally observed misoriented graphene bilayer system form a moire superlattice with periodic potentials and posses a monolayer-like electronic structure near the Dirac point combined with the appearance of low-energy van Hove singularities (vHs), Thermoelectric and vibrational properties measurement in the misoriented graphene bilayer system was conducted using Raman spectroscopy. In this work, we present a systematic theoretical study of misorientation on the vibrational properties of a misoriented graphene bilayer system. Our simulations show that an anharmonic approximation is suitable for predicting low-energy phonon modes observed in experiments. The possibility of tuning vibrational and thermoelectric properties through a relative misorientation between the layers in stacked vdW layer was demonstrated and discussed.

Finally, we have conceptualized a novel low power device called TExFET (TMDC

Excitonic Field Effect Transistor), using other 2D materials namely, hexagonal boron nitride (h-BN) and Transition Metal Dichalcogenides (TMDC) by creating a TMDC/h-BN/TMDC heterstructure system. The characteristics of the TExFET device is explored with a combination of the variational principle and the mean field approximation. Variational principle based calculations of the unscreened inter-layer Coulombic forces in the TMDC/h-BN/TMDC system gives us an upper bound exciton gap in the order of 100 meV which is mainly due to the isotropic electron and hole effective masses of the TMDC layers. Due to the observed sub-nanometer effective exciton radius, the TExFET could also be a device of choice for maintaining the device scaling trend. The combined effects of h-BN thickness, effective mass missmatch and static screening on the excitonic gap is quantified and discussed in detail.

The critical findings of this work are summarized as follows:

- In a spherical Ge/Si core-shell NCs with a Ge core diameter of 3 nm and a Si shell thickness of $\geq$ 3 nm, the escape rate of a hole out of the Ge core is given by the thermionic emission rate. This then becomes the attempt rate for tunneling through the SiO_2. The thermionic barrier presented by the Si shell increases the hole lifetime by a factor of $\exp\left(\frac{\Phi_b}{k_B T}\right)$ compared to the hole lifetime in an all-Si NC. Thus, a retention lifetime of 10 years is achieved with a SiO_2 thickness of 3 nm, a Ge core size of $\geq$ 3 nm, and a Si shell thickness of $\geq$ 3 nm.

- In the Ge/Si NCs with crescent-shaped Ge-core, as the Ge crescent thickness increases from 1 nm to 3.5 nm with a 3.5 nm Si cap, the hole confinement energy decreases from 0.52 to 0.28 eV, the barrier height for a hole to escape into the Si valence band increases from 0.25 to 0.51 eV, and the resulting thermionic hole lifetime increases from 10^{-9} to 10^{-5} s. For the largest NC with Ge-core and Si-cap thickness of 3.5nm, the thermionic lifetime is on the order of 10

microseconds. The thermionic barrier presented by the Si shell increases the hole lifetime by a factor of $\exp\left(\frac{\Phi_b}{k_B T}\right)$ compared to the thermionic hole lifetime in an all-Si NC. The maximum increase is 3×10^8 at $T = 300$K..

- In the dome-shaped Ge/Si NCs, strain and confinement work together to lower the occupied state energies in the Ge core. Strain increases the energy gap by approximately 100 meV for NCs with base diameters greater than 15 nm, and the increase is a result of the downward shift of the occupied state in the Ge core. Confinement and strain break the degeneracy of the lowest excited state and split it into two states separated by a few meV. In the smaller NCs with base diameters below 15 nm, one of the states can be in the base and the other in the cap. For diameters ≥ 20 nm, the two lowest excited states are localized in the Si cap for both the strained and unstrained NCs. The fundamental energy gap and emission spectrum varies from 960 meV for the 5 nm NC to 550 meV for the largest NC with most of the variation occurring between 5 nm and 20 nm.

- The existence of phononic band gaps within the phonon spectrum of the bulk 3C-SiC and 3C-GeSi was confirmed by both first-principle and MD simulations with semi-empirical potentials. The PPDOS on the $< 111 >$ surface of these sys-tems reveals the possibility of generating the new surface states within the phononic band gap (especially for the case where the lighter atoms are in the surface). These surface states, which are decoupled from the bulk states, are used to design phononic interconnects, such as resonators (isolated defects), waveguides (lines with defects), and switches (adatoms within the waveguide).

  Although the present study demonstrates the possibility of realizing phononic interconnects in the atomic scale, there are several important issues that need

to be addressed before they can be integrated in the current and future technologies.

- Phonon dispersion characteristics for both the MBG supercell with $\Theta = 21.78°$ and perfectly-aligned supercell have similar features. Lattice-induced folded phonon modes have similar frequencies, with an exception of out-of-plane ZO' modes. ZO' mode frequency for the MBG increases by 17 cm^{-1}, as compared perfectly-aligned supercell, owing it to the weak inter-layer coupling.

- Anharmonic successfully predicts all the experimentally observed low-frequency Raman modes around 100 cm^{-1} ($\approx$12 meV). The broadening of the acoustical branch and a redshift of the MBG optical frequency was observed, mainly due to the grain size- or supercell size-induced confinement effect.

- The lattice specific heat capacity, C_v, for the MBG follows the classical Dulong-Petit law. C_v shows a linear dependency on the supercell size, which is consistent with the scaling law of thermal conductivity.

- The TMDCs with their large effective mass offer a possible route to room temperature exciton condensation in bilayer structures and gate controlled switching of a quantum phase transition. The unscreened inter-layer Coulombic forces in the TExFET system, with TMDC/h-BN/TMDC heterostructure, gives us an upper bound exciton gap in the order of $\approx$70 meV for a h-BN thickness of 2 nm, mainly due to the isotropic electron and hole effective masses and the smaller effective dielectric constants of the TMDC layers.

- Though any inter and intra-layer screening effects might reduce the large exciton gap by 50%, the gap is still sufficient suitable for low temperature, low power device applications. The observed effective exciton radii is in the range of 2 nm,

the TExFET could also be a device of choice for extending the device scaling trend.

- Existence of superfluidic gap in this device architecture is demonstrated. For both the homogeneous and heterogeneous systems, the superfluidic gap of ≈ 26 meV is observed when the thickness of the h-BN layer is maintained in between 2 and 2.5 nm.

  At 2 nm h-BN thickness, the effect of static screening between the layers reduces the superfluidic gap in TexFET by $\approx 40\%$.

- Although the reduction in the superfluidic gap is significant in these systems, the possibility of room temperature superfluidity still exists.

Bibliography

[1] M. R. Neupane, R. Rahman, and R. K. Lake, "Carrier leakage in Ge/Si core-shell nanocrystals for lasers: core size and strain effects," *Proc. SPIE*, vol. 8102, pp. 81 020P–81 020P–8, 2011. [Online]. Available: http://dx.doi.org/10.1117/12.894153

[2] M. R. Neupane, R. K. Lake, and R. Rahman, "Core size dependence of the confinement energies, barrier heights, and hole lifetimes in Ge-core/Si-shell nanocrystals," *Journal of Applied Physics*, vol. 110, no. 7, p. 074306, 2011. [Online]. Available: http://link.aip.org/link/?JAP/110/074306/1

[3] M. R.Neupane, R. K. Lake, and R. Rahman, "Electronic states of Ge/Si nanocrystals with crescent-shaped Ge-cores," *Journal of Applied Physics*, vol. 112, no. 2, 2012. [Online]. Available: http://scitation.aip.org/content/aip/journal/jap/112/2/10.1063/1.4739715

[4] A. P. Sgouros, M. R. Neupane, M. M. Sigalas, N. Aravantinos-Zafiris, and R. K. Lake, "Nanoscale phononic interconnects in THz frequencies," *Phys. Chem. Chem. Phys.*, vol. 16, pp. 23 355–23 364, 2014. [Online]. Available: http://dx.doi.org/10.1039/C4CP02328E

[5] Y. Huang, E. Sutter, J. T. Sadowski, M. Cotlet, O. L. Monti, D. A. Racke, M. R. Neupane, D. Wickramaratne, R. K. Lake, B. A. Parkinson, and P. Sutter, "Tin disulfide An Emerging Layered Metal Dichalcogenide Semiconductor: Materials Properties and Device Characteristics," *ACS Nano*, vol. 8, no. 10, pp. 10 743–10 755, 2014. [Online]. Available: http://dx.doi.org/10.1021/nn504481r

[6] R. Ionescu, W. Wang, Y. Chai, Z. Mutlu, I. Ruiz, Z. Favors, D. Wickramaratne, M. Neupane, L. Zavala, R. Lake, M. Ozkan, and C. Ozkan, "Synthesis of atomically thin MoS_2 triangles and hexagrams and their electrical transport properties," *Nanotechnology, IEEE Transactions on*, vol. 13, no. 4, pp. 749–754, July 2014.

[7] M. R. Neupane, R. Rahman, and R. K. Lake, "Effect of strain on the electronic and optical properties of Ge-Si dome shaped nanocrystals," *Phys.*

Chem. Chem. Phys., vol. 17, pp. 2484–2493, 2015. [Online]. Available: http://dx.doi.org/10.1039/C4CP03711A

[8] R. Dhall, M. R. Neupane, D. Wickramaratne, M. Mecklenburg, Z. Li, C. Moore, R. K. Lake, and S. Cronin, "Direct bandgap transition in Many-layer MoS_2 by plasma-induced layer decoupling," *Advanced Materials*, vol. 27, no. 9, pp. 1573–1578, 2015. [Online]. Available: http://dx.doi.org/10.1002/adma.201405259

[9] P. Y. Huang, C. S. Ruiz-Vargas, A. M. van der Zande, W. S. Whitney, M. P. Levendorf, J. W. Kevek, S. Garg, J. S. Alden, C. J. Hustedt, Y. Zhu, J. Park, P. L. McEuen, and D. A. Muller, "Grains and grain boundaries in single-layer graphene atomic patchwork quilts," *Nature*, vol. 469, pp. 389–392, 2011.

[10] S. Benchabane, A. Khelif, J.-Y. Rauch, L. Robert, and V. Laude, "Evidence for complete surface wave band gap in a piezoelectric phononic crystal," *Phys. Rev. E*, vol. 73, p. 065601, Jun 2006. [Online]. Available: http://link.aps.org/doi/10.1103/PhysRevE.73.065601

[11] L. Lindsay, D. A. Broido, and T. L. Reinecke, "First-principles determination of ultrahigh Thermal Conductivity of Boron Arsenide: A Competitor for Diamond?" *Phys. Rev. Lett.*, vol. 111, p. 025901, Jul 2013. [Online]. Available: http://link.aps.org/doi/10.1103/PhysRevLett.111.025901

[12] F. Xia, H. Wang, D. Xiao, M. Dubey, and A. Ramasubramaniam, "Two-dimensional material nanophotonics," *Nature Photonics*, vol. 8, pp. 899–907, 2014.

[13] Y. M. Niquet, G. Allan, C. Delerue, and M. Lannoo, "Quantum Confinement in germanium nanocrystals," *Applied Physics Letters*, vol. 77, no. 8, pp. 1182 – 1184, 2000.

[14] K. Liu, L. Liu, Y. Luo, and D. Jia, "One-step synthesis of metal nanoparticle decorated graphene by liquid phase exfoliation," *J. Mater. Chem.*, vol. 22, pp. 20 342–20 352, 2012. [Online]. Available: http://dx.doi.org/10.1039/C2JM34617F

[15] J. Kang, S. Tongay, J. Zhou, J. Li, and J. Wu, "Band offsets and heterostructures of two-dimensional semiconductors," *Applied Physics Letters*, vol. 102, no. 1, pp. –, 2013. [Online]. Available: http://scitation.aip.org/content/aip/journal/apl/102/1/10.1063/1.4774090

[16] International Technology Roadmap for Semiconductors, Emerging Research Devices, 2011 ed., p. 24.

[17] J. kerman, "Toward a universal memory," *Science*, vol. 308, no. 5721, pp. 508–510, 2005. [Online]. Available: http://www.sciencemag.org/content/308/5721/508.short

[18] M. Wuttig and N. Yamada, "Phase-change materials for rewriteable data storage," *Nature*, vol. 6, no. 11, pp. 824–832, November 2007.

[19] S. Paul, "Realization of nonvolatile memory devices using small organic molecules and polymer," *Nanotechnology, IEEE Transactions on*, vol. 6, no. 2, pp. 191–195, March 2007.

[20] M. L. Ostraat, J. W. De Blauwe, M. L. Green, L. D. Bell, M. L. Brongersma, J. Casperson, R. C. Flagan, and H. A. Atwater, "Synthesis and characterization of aerosol silicon nanocrystal nonvolatile floating-gate memory devices," *Applied Physics Letters*, vol. 79, no. 3, pp. 433–435, 2001. [Online]. Available: http://scitation.aip.org/content/aip/journal/apl/79/3/10.1063/1.1385190

[21] D. Kahng and S. Sze, "A floating gate and its application to memory devices," *The Bell System Technical Journal*, no. 6, 1967.

[22] S. Tiwari, F. Rana, H. Hanafi, A. Hartstein, E. F. Crabb, and K. Chan, "A silicon nanocrystals based memory," *Applied Physics Letters*, vol. 68, no. 10, pp. 1377–1379, 1996. [Online]. Available: http://scitation.aip.org/content/aip/journal/apl/68/10/10.1063/1.116085

[23] J. D. Blauwe, "Nanocrystal nonvolatile memory devices," *IEEE Transactions on Nanotechnology*, vol. 1, no. 1, pp. 72 – 77, 2002.

[24] H. Zhou, Z. Li, J.-G. Zheng, and J. Liu, "Rapid thermal oxygen annealing formation of nickel silicide nanocrystals for nonvolatile memory," *Applied Physics A*, vol. 109, no. 3, pp. 535–538, 2012. [Online]. Available: http://dx.doi.org/10.1007/s00339-012-7299-2

[25] C. L. Yuan, P. Darmawan, Y. Setiawan, and P. S. Lee, "Formation of sio 2 nanocrystals in lu 2 o 3 high- k dielectric by pulsed laser ablation and application in memory device," *Nanotechnology*, vol. 17, no. 13, p. 3175, 2006. [Online]. Available: http://stacks.iop.org/0957-4484/17/i=13/a=016

[26] D. Zhao, Y. Zhu, R. Li, and J. Liu, "Simulation of a Ge-Si Hetero-Nanocrystal Memory," *IEEE Transaction on Nanotechnology*, vol. 5, no. 1, pp. 37 – 41, 2006.

[27] W. Wu, J. Gu, H. Ge, C. Keimel, and S. Y. Chou, "Room-temperature Si single-electron memory fabricated by nanoimprint lithography," *Applied Physics Letters*, vol. 83, no. 11, pp. 2268 – 2270, 2003.

[28] D. Zhao, Y. Zhu, R. Li, and J. Liu, "Transient processes in a Ge/Si hetero-nanocrystal p-channel memory," *Solid-State Electronics*, vol. 50, no. 3, pp. 362 – 366, 2006.

[29] H. G. Yang, Y. Shi, L. Pu, S. L. Gu, B. Shen, and P. Han, "Numerical investigation of characteristics of p-channel Ge/Si hetero-nanocrystal memory," *Microelectron Journal*, vol. 34, no. 1, pp. 71 – 75, 2003.

[30] K. S. Novoselov, A. K. Geim, S. V. Morozov, D. Jiang, M. I. Katsnelson, I. V. Grigorieva, S. V. Dubonos, and A. A. Firsov, "Two-dimensional gas of massless dirac fermions in graphene," *Nature*, vol. 438, no. 7065, pp. 197–200, November 2005.

[31] J. C. Meyer, A. K. Geim, M. I. Katsnelson, K. S. Novoselov, T. J. Booth, and S. Roth, "The structure of suspended graphene sheets," *Nature*, vol. 446, pp. 60 – 63, 2007.

[32] Y. Zhang, Y.-W. Tan, H. L. Stormer, and P. Kim, "Experimental observation of the quantum hall effect and Berry's phase in graphene," *Nature*, vol. 438, pp. 201 – 204, 2005.

[33] K. Bolotin, K. Sikes, Z. Jiang, M. Klima, G. Fudenberg, J. Hone, P. Kim, and H. Stormer, "Ultrahigh electron mobility in suspended graphene," *Solid State Communications*, vol. 146, no. 910, pp. 351 – 355, 2008. [Online]. Available: http://www.sciencedirect.com/science/article/pii/S0038109808001178

[34] S. Z. Butler, S. M. Hollen, L. Cao, Y. Cui, J. A. Gupta, H. R. Gutirrez, T. F. Heinz, S. S. Hong, J. Huang, A. F. Ismach, E. Johnston-Halperin, M. Kuno, V. V. Plashnitsa, R. D. Robinson, R. S. Ruoff, S. Salahuddin, J. Shan, L. Shi, M. G. Spencer, M. Terrones, W. Windl, and J. E. Goldberger, "Progress, challenges, and opportunities in two-dimensional materials beyond graphene," *ACS Nano*, vol. 7, no. 4, pp. 2898–2926, 2013.

[35] S. Z. Butler, S. M. Hollen, L. Cao, Y. Cui, J. A. Gupta, H. R. Gutirrez, T. F. Heinz, S. S. Hong, J. Huang, A. F. Ismach, E. Johnston-Halperin, M. Kuno, V. V. Plashnitsa, R. D. Robinson, R. S. Ruoff, S. Salahuddin, J. Shan, L. Shi, M. G. Spencer, M. Terrones, W. Windl, and J. E.Goldberger, "Progress, challenges, and opportunities in two-dimensional materials beyond graphene," *ACS Nano*, vol. 7, no. 4, pp. 2898–2926, 2013, pMID: 23464873. [Online]. Available: http://dx.doi.org/10.1021/nn400280c

[36] J. N. Coleman, M. Lotya, A. ONeill, S. D. Bergin, P. J. King, U. Khan, K. Young, A. Gaucher, S. De, R. J. Smith, I. V. Shvets, S. K. Arora, G. Stanton, H.-Y. Kim, K. Lee, G. T. Kim, G. S. Duesberg, T. Hallam, J. J. Boland, J. J. Wang, J. F. Donegan, J. C. Grunlan, G. Moriarty, A. Shmeliov, R. J. Nicholls,

J. M. Perkins, E. M. Grieveson, K. Theuwissen, D. W. McComb, P. D. Nellist, and V. Nicolosi, "Two-dimensional nanosheets produced by liquid exfoliation of layered materials," *Science*, vol. 331, no. 6017, pp. 568–571, 2011.

[37] Y. Shi, W. Zhou, A.-Y. Lu, W. Fang, Y.-H. Lee, A. L. Hsu, S. M. Kim, K. K. Kim, H. Y. Yang, L.-J. Li, J.-C. Idrobo, and J. Kong, "van der Waals Epitaxy of MoS_2 layers using graphene as growth templates," *Nano Letters*, vol. 12, no. 6, pp. 2784–2791, 2012. [Online]. Available: http://dx.doi.org/10.1021/nl204562j

[38] B. Radisavljevic, A. Radenovic, J. Brivio, V. Giacometti, and A. Kis, "Single-layer MoS_2 transistors," *Nature Nanotechnology*, vol. 6, pp. 147 – 150, 2011.

[39] Y. Yoon, K. Ganapathi, and S. Salahuddin, "How good can monolayer MoS_2 transistors be?" *Nano Letters*, vol. 11, no. 9, pp. 3768–3773, 2011.

[40] A. Splendiani, L. Sun, Y. Zhang, T. Li, J. Kim, C.-Y. Chim, G. Galli, and F. Wang, "Emerging photoluminescence in Monolayer MoS_2," *Nano Letters*, vol. 10, no. 4, pp. 1271–1275, 2010.

[41] D. Xiao, G.-B. Liu, W. Feng, X. Xu, and W. Yao, "Coupled spin and valley physics in monolayers of mos_2 and other group-vi dichalcogenides," *Phys. Rev. Lett.*, vol. 108, p. 196802, May 2012.

[42] X. Wu, X. Li, Z. Song, C. Berger, and W. A. de Heer, "Weak antilocalization in epitaxial graphene: Evidence for chiral electrons," *Phys. Rev. Lett.*, vol. 98, p. 136801, Mar 2007. [Online]. Available: http://link.aps.org/doi/10.1103/PhysRevLett.98.136801

[43] J. Hass, F. Varchon, J. Millán-Otoya, M. Sprinkle, N. Sharma, W. de Heer, C. Berger, P. First, L. Magaud, and E. Conrad, "Why Multilayer Graphene on 4H-SiC($000\bar{1}$) behaves like a single sheet of graphene," *Phys. Rev. Lett.*, vol. 100, Jan 2008.

[44] A. M. van der Zande, J. Kunstmann, A. Chernikov, D. A. Chenet, Y. You, X. Zhang, P. Y. Huang, T. C. Berkelbach, L. Wang, F. Zhang, M. S. Hybertsen, D. A. Muller, D. R. Reichman, T. F. Heinz, and J. C. Hone, "Tailoring the Electronic Structure in Bilayer Molybdenum Disulfide via Interlayer Twist," *Nano Letters*, vol. 14, no. 7, pp. 3869–3875, 2014.

[45] B. Lopes dos Santos J. M., R. Peres N. M., and H. Castro Neto A., "Graphene Bilayer with a Twist: Electronic Structure," *Phys. Rev. Lett.*, vol. 99, p. 256802, Jan 2007.

[46] S. Latil, V. Meunier, and L. Henrard, "Massless fermions in multilayer graphitic systems with misoriented layers: Ab initio calculations and experimental fingerprints," *Phys. Rev. B*, vol. 76, p. 201402, Jan 2007.

[47] S. Shallcross, S. Sharma, and O. A. Pankratov, "Quantum interference at the twist boundary in graphene," *Phys. Rev. Lett.*, vol. 101, no. 5, p. 056803, Aug 2008.

[48] A. Luican, G. Li, A. Reina, J. Kong, R. R. Nair, K. S. Novoselov, A. K. Geim, and E. Y. Andrei, "Single-layer behavior and its breakdown in twisted graphene layers," *Phys. Rev. Lett.*, vol. 106, no. 12, p. 126802, Mar 2011.

[49] E. Suárez Morell, P. Vargas, L. Chico, and L. Brey, "Charge redistribution and interlayer coupling in twisted bilayer graphene under electric fields," *Phys. Rev. B*, vol. 84, p. 195421, Nov 2011. [Online]. Available: http://link.aps.org/doi/10.1103/PhysRevB.84.195421

[50] L. Xian, S. Barraza-Lopez, and M. Chou, "Effects of electrostatic fields and charge doping on the linear bands in twisted graphene bilayers," *Phys. Rev. B*, vol. 84, Jan 2011.

[51] K. M. M. Habib, S. S. Sylvia, S. Ge, M. Neupane, and R. K. Lake, "The coherent interlayer resistance of a single, rotated interface between two stacks of AB graphite," *Applied Physics Letters*, vol. 103, no. 24, pp. –, 2013. [Online]. Available: http://scitation.aip.org/content/aip/journal/apl/103/24/10.1063/1.4841415

[52] I. Maasilta and A. J. Minnich, "Heat under the microscope," *PHYSICS TODAY*, vol. 67, no. 8, pp. 27–32, 2014.

[53] D. Hatanaka, I. Mahboob, K. Onomitsu, and H. Yamaguchi, "Phonon waveguides for electromechanical circuits," *Nature Nano*, vol. 9, no. 7, pp. 520–524, November 2014. [Online]. Available: http://dx.doi.org/10.1038/nnano.2014.107

[54] J. Petrus, R. Mathew, and J. Stotz, "A gaas phononic crystal with shallow noncylindrical holes," *Ultrasonics, Ferroelectrics, and Frequency Control, IEEE Transactions on*, vol. 61, no. 2, pp. 364–368, February 2014.

[55] M. Galeti, M. Rodrigues, J. Martino, N. Collaert, E. Simoen, and C. Claeys, "{GIDL} behavior of p- and n-MuGFET devices with different tin metal gate thickness and high-k gate dielectrics," *Solid-State Electronics*, vol. 70, no. 0, pp. 44 – 49, 2012, selected Full-Length Papers from the {EUROSOI} 2011 Conference. [Online]. Available: http://www.sciencedirect.com/science/article/pii/S0038110111004114

[56] E. Gnani, A. Gnudi, S. Reggiani, and G. Baccarani, "Theory of the junctionless nanowire FET," *Electron Devices, IEEE Transactions on*, vol. 58, no. 9, pp. 2903–2910, September 2011.

[57] M. Kim, Y. K. Wakabayashi, M. Yokoyama, R. Nakane, M. Takenaka, and S. Takagi, "Ge/Si heterojunction tunnel field-effect transistors and their post metallization annealing effect," *Electron Devices, IEEE Transactions on*, vol. 62, no. 1, pp. 9–15, January 2015.

[58] B. D. Gaynor and S. Hassoun, "Fin shape impact on finfet leakage with application to multithreshold and ultralow-leakage $fin fet$ design," *Electron Devices, IEEE Transactions on*, vol. 61, no. 8, pp. 2738–2744, August 2014.

[59] S. S. Sylvia, K. M. M. Habib, M. A. Khayer, K. Alam, M. Neupane, and R. K. Lake, "Effect of random, discrete source dopant distributions on nanowire tunnel FETs," *Electron Devices, IEEE Transactions on*, vol. 61, no. 6, pp. 2208–2214, June 2014.

[60] S. Datta, H. Liu, and V. Narayanan, "Tunnel {FET} technology: A reliability perspective," *Microelectronics Reliability*, vol. 54, no. 5, pp. 861 – 874, 2014. [Online]. Available: http://www.sciencedirect.com/science/article/pii/S0026271414000456

[61] S. S. Sylvia, M. A. Khayer, K. Alam, and R. K. Lake, "Doping, tunnel barriers, and cold carriers in InAs and InSb nanowire tunnel transistors,," *Electron Devices, IEEE Transactions on*, vol. 59, November 2012.

[62] T. Georgiou, R. Jalil, B. B. an L. Britnell, R. Gorbachev, S. Morozov, Y.Kim, A. Gholina, S. Haigh, O. Makarovsky, L. Ponomarenko, A. Geim, K. Novoselov, and A. Mischenko, "Vertical field-effect transistor based on graphene-ws2 heterostructures for flexible and transparent electronics," *Nature Nanotech.*, vol. 8, pp. 100–103, 2013.

[63] F. K. Perkins, A. L. Friedman, E. Cobas, P. M. Campbell, G. G. Jernigan, and B. T. Jonker, "Chemical vapor sensing with monolayer MoS_2," *Nano Letters*, vol. 13, no. 2, pp. 668–673, 2013, pMID: 23339527. [Online]. Available: http://dx.doi.org/10.1021/nl3043079

[64] A. K. Geim and I. V. Grigorieva, "Van der waals heterostructures," *Nature*, vol. 499, no. 7459, pp. 419–425, July 2013. [Online]. Available: http://dx.doi.org/10.1038/nature12385

[65] K. S. Novoselov, V. I. Falko, L. Colombo, P. R. Gellert, M. G. Schwab, and K. Kim, "A roadmap for graphene," *Nature*, vol. 490, no. 11, pp. 192–200, October 2012.

[66] M. Gilbert and J. Shumway, "Probing quantum coherent states in bilayer graphene," *Journal of Computational Electronics*, vol. 8, no. 2, pp. 51–59, 2009. [Online]. Available: http://dx.doi.org/10.1007/s10825-009-0286-y

[67] J. Junquera and P. Ghosez, "Critical thickness for ferroelectricity in perovskite ultrathin films," *Nature*, vol. 422, pp. 506–509, 2007.

[68] J. Li, P. Ndai, and S. Salahuddin, "Design paradigm for robust spin-torque transfer magnetic RAM (STT MRAM) from circuit/architecture perspective," *Very Large Scale Integration (VLSI) Systems, IEEE Transactions on*, vol. 18, no. 12, pp. 1710 – 1723, November 2009.

[69] M. Villafuerte, S. P. Heluani, G. Jurez, G. Simonelli, G. Braunstein, and S. Duhalde, "Electric-pulse-induced reversible resistance in doped zinc oxide thin films," *Applied Physics Letters*, vol. 90, no. 5, pp. –, 2007. [Online]. Available: http://scitation.aip.org/content/aip/journal/apl/90/5/10.1063/1.2437688

[70] L. P. Balet, S. A. Ivanov, A. Piryatinski, M. Achermann, and V. I. Klimov, "Inverted Core/Shell Nanocrystals Continuously Tunable between Type-I and Type-II Localization Regimes," *Nano Letters*, vol. 4, no. 8, pp. 1485 – 1488, 2004.

[71] J. Lu, Z. Zuo, Y. Chen, Y. Shi, L. Pu, and Y. Zheng, "Charge storage characteristics in metal-oxide-semiconductor memory structure based on gradual $ge_{1-x}si_x$/si heteronanocrystals," *Applied Physics Letters*, vol. 92, no. 1, p. 013105, 2008.

[72] J. S. de Sousa, V. N. Freire, and J.-P. Leburton, "Hole-versus electron-based operations in SiGe nanocrystal nonvolatile memories," *Applied Physics Letters*, vol. 90, no. 22, p. 223504, 2007.

[73] H. G. Yang, Y. Shi, L. Pu, R. Zhang, B. Shen, P. Han, S. L. Gu, and Y. D. Zheng, "Nonvolatile memory based on Ge/Si hetero-nanocrystals," *Applied Surface Science*, vol. 224, no. 1, pp. 394 – 398, 2004.

[74] E. S. Kannan, G.-H. Kim, and D. A. Ritchie, "Charge trapping in quantum dot memory devices with different dot densities," *J. Phys. D: Appl. Phys*, vol. 43, no. 22, p. 225101, 2010.

[75] K. K. Likharev, "Layered tunnel barriers for nonvlatile meory devices," *Applied Physics Letters*, vol. 73, no. 15, pp. 2137 – 2139, 1998.

[76] J. S. de Sousa, R. Peibst, M. Erenburg, G. Farias, and J.-P. Leburton, "Single-Electron Charging and Discharging Analyses in Ge-Nanocrystal Memories," *IEEE Trans. on Electron Devices*, vol. 58, no. 2, pp. 376 – 383, 2011.

[77] R. Peibst, J. S. de Sousa, and K. Hofmann, "Determination of the Ge-nanocrystal/SiO2 matrix interface trap density from the small signal response pf charge stored in nanocrystals," *Phys. Rev. B.*, vol. 82, no. 19, p. 195415, 2010.

[78] R. Peibst, M. Erenburg, E. Bugiel, and K. Hofmann, "Effects influencing electron and hole retention times in Ge nanocrystal memory structures operating in the direct tunneling regime," *Journal of Applied Physics*, vol. 108, no. 54316, 2010.

[79] A. A. Balandin, "Thermal properties of graphene and nanostructured carbon materials," *Nature Mater*, vol. 10, pp. 569–581, 2011. [Online]. Available: http://dx.doi.org/10.1038/nmat3064

[80] K. S. Novoselov, A. K. Geim, S. V. Morozov, D. Jiang, Y. Zhang, S. V. Dubonos, I. V. Grigorieva, and A. A. Firsov, "Electric Field Effect in Atomically Thin Carbon Films," *Science*, vol. 306, no. 5696, pp. 666–669, 2004.

[81] A. H. Castro Neto, F. Guinea, N. M. R. Peres, K. S. Novoselov, and A. K. Geim, "The electronic properties of graphene," *Rev. Mod. Phys.*, vol. 81, pp. 109–162, Jan 2009. [Online]. Available: http://link.aps.org/doi/10.1103/RevModPhys.81.109

[82] T. Ando, "Exotic electronic and transport properties of graphene," *Physica E: Low-dimensional Systems and Nanostructures*, vol. 40, no. 2, pp. 213 – 227, 2007.

[83] M. Y. Han, B. Özyilmaz, Y. Zhang, and P. Kim, "Energy band-gap engineering of graphene nanoribbons," *Phys. Rev. Lett.*, vol. 98, p. 206805, May 2007. [Online]. Available: http://link.aps.org/doi/10.1103/PhysRevLett.98.206805

[84] X. Li, X. Wang, L. Zhang, S. Lee, and H. Dai, "Chemically Derived, Ultrasmooth Graphene Nanoribbon Semiconductors," *Science*, vol. 319, no. 5867, pp. 1229–1232, 2008.

[85] K.-T. Lam and G. Liang, "An ab initio study on energy gap of bilayer graphene nanoribbons with armchair edges," *Applied Physics Letters*, vol. 92, no. 22, p. 223106, 2008.

[86] D. C. Elias, R. R. Nair, T. M. G. Mohiuddin, S. V. Morozov, P. Blake, M. P. Halsall, A. C. Ferrari, D. W. Boukhvalov, M. I. Katsnelson, A. K. Geim, and K. S. Novoselov, "Control of graphene's properties by reversible hydrogenation: Evidence for graphane," *Science*, vol. 323, no. 5914, pp. 610–613, 2009. [Online]. Available: http://www.sciencemag.org/content/323/5914/610.abstract

[87] K. Brenner and R. Murali, "Single step, complementary doping of graphene," *Applied Physics Letters*, vol. 96, no. 6, p. 063104, 2010. [Online]. Available: http://dx.doi.org/doi/10.1063/1.3308482

[88] D. B. Farmer, Y.-M. Lin, A. Afzali-Ardakani, and P. Avouris, "Behavior of a chemically doped graphene junction," *Applied Physics Letters*, vol. 94, no. 21, p. 213106, 2009. [Online]. Available: http://dx.doi.org/doi/10.1063/1.3142865

[89] C. L. Lu, C. P. Chang, Y. C. Huang, J. M. Lu, C. C. Hwang, and M. F. Lin, "Low-energy electronic properties of the ab-stacked few-layer graphites," *Journal of Physics: Condensed Matter*, vol. 18, no. 26, p. 5849, 2006. [Online]. Available: http://stacks.iop.org/0953-8984/18/i=26/a=005

[90] H. Min, B. Sahu, S. K. Banerjee, and A. H. MacDonald, "Ab initio theory of gate induced gaps in graphene bilayers," *Phys. Rev. B*, vol. 75, no. 15, p. 155115, Apr 2007.

[91] Y. Zhang, T.-T. Tang, C. Girit, Z. Hao, M. C. Martin, A. Zettl, M. F. Crommie, Y. R. Shen, and F. Wang, "Direct observation of a widely tunable bandgap in bilayer graphene," *Nature*, vol. 459, no. 7248, p. 820, 2009.

[92] P. Gava, M. Lazzeri, A. M. Saitta, and F. Mauri, "*Ab initio* study of gap opening and screening effects in gated bilayer graphene," *Phys. Rev. B*, vol. 79, p. 165431, Apr 2009. [Online]. Available: http://link.aps.org/doi/10.1103/PhysRevB.79.165431

[93] W. Liu, H. Li, C. Xu, Y. Khatami, and K. Banerjee, "Synthesis of high-quality monolayer and bilayer graphene on copper using chemical vapor deposition," *Carbon*, vol. 49, no. 13, pp. 4122 – 4130, 2011. [Online]. Available: http://www.sciencedirect.com/science/article/pii/S0008622311004106

[94] S. Shallcross, S. Sharma, E. Kandelaki, and A. Pankratov O., "Electronic structure of turbostratic graphene," *Phys. Rev. B*, vol. 81, p. 165105, Apr 2010. [Online]. Available: http://adsabs.harvard.edu/abs/2010PhRvB..81p5105S

[95] L. Jiao, L. Zhang, L. Ding, J. Liu, and H. Dai, "Aligned graphene nanoribbons and crossbars from unzipped carbon nanotubes," *Nano Research*, vol. 3, pp. 387–394, Jan 2010.

[96] H. Li, H. Ying, X. Chen, D. L. Nika, A. I. Cocemasov, W. Cai, A. A. Balandin, and S. Chen, "Thermal conductivity of twisted bilayer graphene," *Nanoscale*, vol. 6, pp. 13 402–13 408, 2014. [Online]. Available: http://dx.doi.org/10.1039/C4NR04455J

[97] J.-W. Jiang, B.-S. Wang, and T. Rabczuk, "Acoustic and breathing phonon modes in bilayer graphene with Moir patterns," *Applied Physics Letters*, vol. 101, no. 2, pp. –, 2012. [Online]. Available: http://scitation.aip.org/content/aip/journal/apl/101/2/10.1063/1.4735246

[98] R. Ruskov and C. Tahan, "On-chip cavity quantum phonodynamics with an acceptor qubit in silicon," *Phys. Rev. B*, vol. 88, p. 064308, Aug 2013. [Online]. Available: http://link.aps.org/doi/10.1103/PhysRevB.88.064308

[99] T. A. Kelf, W. Hoshii, P. H. Otsuka, H. Sakuma, I. A. Veres, R. M. Cole, S. Mahajan, J. J. Baumberg, M. Tomoda, O. Matsuda, and O. B. Wright, "Mapping gigahertz vibrations in a plasmonicphononic crystal," *New Journal of Physics*, vol. 15, no. 2, p. 023013, 2013. [Online]. Available: http://stacks.iop.org/1367-2630/15/i=2/a=023013

[100] M. M. Sigalas and E. N. Economou, "Elastic and acoustic wave band structure," *Journal of Sound Vibration*, vol. 158, pp. 377–382, 1992.

[101] Y. Lozovik and V. Yudson, "Feasibility of superfluidity of paired spatially separated electrons and holes; a new superconductivity mechanism," *JETP Lett.*, vol. 22, pp. 274–275, 1975.

[102] T. Kamizato and M. Matsuura, "Excitons in double quantum wells," *Phys. Rev. B*, vol. 40, pp. 8378–8384, Oct 1989. [Online]. Available: http://link.aps.org/doi/10.1103/PhysRevB.40.8378

[103] D. K. Kim and D. S. Citrin, "Strong excitonic mixing effect in asymmetric double quantum wells: On the optimization of electroabsorption modulators," *Phys. Status Solidi C*, vol. 5, pp. 2400–2403, Jan 2008.

[104] K. Sivalertporn, L. Mouchliadis, A. L. Ivanov, R. Philp, and E. A. Muljarov, "Direct and indirect excitons in semiconductor coupled quantum wells in an applied electric field," *Phys. Rev. B*, vol. 85, p. 045207, Jan 2012. [Online]. Available: http://link.aps.org/doi/10.1103/PhysRevB.85.045207

[105] E. E. Mendez, L. Esaki, and L. L. Chang, "Quantum hall effect in a Two-Dimensional Electron-hole Gas," *Phys. Rev. Lett.*, vol. 55, pp. 2216–2219, Nov 1985. [Online]. Available: http://link.aps.org/doi/10.1103/PhysRevLett.55.2216

[106] U. Sivan, P. M. Solomon, and H. Shtrikman, "Coupled electron-hole transport," *Phys. Rev. Lett.*, vol. 68, pp. 1196–1199, Feb 1992. [Online]. Available: http://link.aps.org/doi/10.1103/PhysRevLett.68.1196

[107] M. Pohlt, M. Lynass, J. G. S. Lok, W. Dietsche, K. v. Klitzing, K. Eberl, and R. Muhle, "Closely spaced and separately contacted two-dimensional electron and hole gases by in situ focused-ion implantation," *Applied Physics Letters*, vol. 80, no. 12, pp. 2105–2107, 2002.

[108] J. A. Seamons, D. R. Tibbetts, J. L. Reno, and M. P. Lilly, "Undoped electron-hole bilayers in a GaAs/AlGaAs double quantum well," *Applied Physics Letters*, vol. 90, no. 5, p. 052103, 2007.

[109] C.-H. Zhang and Y. N. Joglekar, "Excitonic condensation of massless fermions in graphene bilayers," *Phys. Rev. B*, vol. 77, p. 233405, Jun 2008. [Online]. Available: http://link.aps.org/doi/10.1103/PhysRevB.77.233405

[110] H. Min, R. Bistritzer, J.-J. Su, and A. H. MacDonald, "Room-temperature superfluidity in graphene bilayers," *Phys. Rev. B*, vol. 78, p. 121401, Sep 2008. [Online]. Available: http://link.aps.org/doi/10.1103/PhysRevB.78.121401

[111] S. K. Banerjee, L. Register, E. Tutuc, D. Reddy, and A. MacDonald, "Bilayer pseudospin field-effect transistor (bisfet): A proposed new logic device," *Electron Device Letters, IEEE*, vol. 30, no. 2, pp. 158–160, 2009.

[112] J.-J. su and A. H. MacDonald, "How to make a bilayer exciton condensate flow," *Nature Physics*, vol. 4, pp. 799 – 802, 2008.

[113] R. Rapaport, G. Chen, D. Snoke, S. H. Simon, L. Pfeiffer, K. West, Y. Liu, and S. Denev, "Charge Separation of Dense Two-Dimensional Electron-Hole Gases: Mechanism for Exciton Ring Pattern Formation," *Phys. Rev. Lett.*, vol. 92, p. 117405, Mar 2004. [Online]. Available: http://link.aps.org/doi/10.1103/PhysRevLett.92.117405

[114] D. Reddy, L. Register, and S. Banerjee, "Bilayer graphene vertical tunneling field effect transistor," in *Device Research Conference (DRC), 2012 70th Annual*, June 2012, pp. 73–74.

[115] G. Klimeck, S. Ahmed, H. Bae, N. Kharche, S. Clark, B. Haley, Sunhee, M. Naumov, H. Ryu, F. Saied, M. Prada, Korkusinski, T. B. Boykin, and R. Rahman, "Atomistic Simulation of Realistically Sized Nanodevices Using NEMO 3-D Part I– models and Benchmarks," *IEEE Transactions on Electron Devices*, vol. 54, no. 9, pp. 2090 – 2099, 2007.

[116] S. Plimpton and J. Comp, "Fast parallel algorithms for short-range molecular dynamics," *Journal of Computational Physics*, vol. 117, pp. 1–19, 1995.

[117] G. Kresse and J. Furthmüller, "Efficient iterative schemes for *ab initio* total-energy calculations using a plane-wave basis set," *Phys.*

Rev. B, vol. 54, pp. 11 169–11 186, Oct 1996. [Online]. Available: http://link.aps.org/doi/10.1103/PhysRevB.54.11169

[118] G. Bastard, "Theoretical investigations of superlattice band structure in the envelope function approximation," *Phys. Rev. B*, vol. 25, no. 12, pp. 7584–7597, 1982.

[119] D. S. L. Abergel, R. Sensarma, and S. Das Sarma, "Density fluctuation effects on the exciton condensate in double-layer graphene," *Phys. Rev. B*, vol. 86, p. 161412, Oct 2012. [Online]. Available: http://link.aps.org/doi/10.1103/PhysRevB.86.161412

[120] T. B. Boykin, G. Klimeck, and F. Oyafuso, "Valence band effective-mass expressions in the $sp^3d^5s^*$ empirical tight-binding model applied to a Si and Ge parametrization," *Phys. Rev. B*, vol. 69, no. 11, p. 115201, 2004.

[121] D. P. Sellan, E. S. Landry, J. E. Turney, A. J. H. McGaughey, and C. H. Amon, "Size effects in molecular dynamics thermal conductivity predictions," *Phys. Rev. B*, vol. 81, p. 214305, Jun 2010. [Online]. Available: http://link.aps.org/doi/10.1103/PhysRevB.81.214305

[122] W. Li, R. K. Kalia, and P. Vashishta, "Dynamical fracture in sise2 nanowires a molecular-dynamics study," *Europhys. Lett.*, vol. 35, pp. 103–108, July 1996.

[123] J. Gsponer and A. Caflisch, "Molecular dynamics simulations of protein folding from the transition state," *Proceedings of the National Academy of Sciences*, vol. 99, no. 10, pp. 6719–6724, 2002. [Online]. Available: http://www.pnas.org/content/99/10/6719.abstract

[124] J. A. Sanchez and M. P. Mengüç, "Phase-change phenomena during electron-beam heating: Molecular dynamics simulations," *Phys. Rev. B*, vol. 76, p. 224104, Dec 2007. [Online]. Available: http://link.aps.org/doi/10.1103/PhysRevB.76.224104

[125] E. A. Walker, "Influence of phon modes on the thermal conductivity of single-wall, double-wall and functionalized carbon nanotubes," Ph.D. dissertation, Vanderbilt University, 2012.

[126] C. Z. Wang, C. T. Chan, and K. M. Ho, "Tight-binding molecular-dynamics study of phonon anharmonic effects in silicon and diamond," *Phys. Rev. B*, vol. 42, pp. 11 276–11 283, Dec 1990. [Online]. Available: http://link.aps.org/doi/10.1103/PhysRevB.42.11276

[127] F. Keil, *Multiscale Modelling in Computational Heterogeneous Catalysis*, ser. Topics in Current Chemistry. Springer Berlin Heidelberg, 2012, vol. 307, pp. 69–107. [Online]. Available: http://dx.doi.org/10.1007/128.2011.128

[128] J. Tersoff, "New empirical approach for the structure and energy of covalent systems," *Phys. Rev. B*, vol. 37, pp. 6991–7000, Apr 1988. [Online]. Available: http://link.aps.org/doi/10.1103/PhysRevB.37.6991

[129] D. W. Brenner, "Empirical potential for hydrocarbons for use in simulating the chemical vapor deposition of diamond films," *Phys. Rev. B*, vol. 42, pp. 9458–9471, Nov 1990. [Online]. Available: http://link.aps.org/doi/10.1103/PhysRevB.42.9458

[130] S. J. Stuart, A. B. Tutein, and J. A. Harrison, "A reactive potential for hydrocarbons with intermolecular interactions," *The Journal of Chemical Physics*, vol. 112, no. 14, pp. 6472–6486, 2000. [Online]. Available: http://scitation.aip.org/content/aip/journal/jcp/112/14/10.1063/1.481208

[131] J. H. Los and A. Fasolino, "Intrinsic long-range bond-order potential for carbon: Performance in monte carlo simulations of graphitization," *Phys. Rev. B*, vol. 68, p. 024107, Jul 2003. [Online]. Available: http://link.aps.org/doi/10.1103/PhysRevB.68.024107

[132] L. T. Kong and Comp, "Phonon dispersion measured directly from molecular dynamics simulations," *Comp. Phys. Comm.*, vol. 10, pp. 2201–2207, 2011.

[133] L. T. Kong and L. J. Lewis, "Structure and energetics of c-*sia*-sio_2 systems: Planar interfaces and embedded si nanocrystals," *Phys. Rev. B*, vol. 77, 2008.

[134] *Anharmonic Phonon Dispersion Relations, Group Velocities, and Branch-Dependent Specific Heat Capacities Measured Directly from Molecular Dynamics Simulations at Finite Temperatures*, vol. 1, no. HT2012-58459. ASME, June 2012.

[135] P. Hohenberg and W. Kohn, "Inhomogeneous electron gas," *Phys. Rev.*, vol. 136, pp. B864–B871, Nov 1964. [Online]. Available: http://link.aps.org/doi/10.1103/PhysRev.136.B864

[136] W. Kohn and L. J. Sham, "Self-consistent equations including exchange and correlation effects," *Phys. Rev.*, vol. 140, pp. A1133–A1138, Nov 1965. [Online]. Available: http://link.aps.org/doi/10.1103/PhysRev.140.A1133

[137] J. P. Perdew and A. Zunger, "Self-interaction correction to density-functional approximations for many-electron systems," *Phys. Rev. B*, vol. 23, pp. 5048–5079, May 1981. [Online]. Available: http://link.aps.org/doi/10.1103/PhysRevB.23.5048

[138] D. M. Ceperley and B. J. Alder, "Ground state of the electron gas by a Stochastic Method," *Phys. Rev. Lett.*, vol. 45, pp. 566–569, Aug 1980. [Online]. Available: http://link.aps.org/doi/10.1103/PhysRevLett.45.566

[139] J. P. Perdew and W. Yue, "Accurate and simple density functional for the electronic exchange energy: Generalized gradient approximation," *Phys. Rev. B*, vol. 33, pp. 8800–8802, Jun 1986. [Online]. Available: http://link.aps.org/doi/10.1103/PhysRevB.33.8800

[140] J. P. Perdew, K. Burke, and M. Ernzerhof, "Generalized gradient approximation made simple," *Phys. Rev. Lett.*, vol. 77, pp. 3865–3868, Oct 1996. [Online]. Available: http://link.aps.org/doi/10.1103/PhysRevLett.77.3865

[141] J. Heyd, G. E. Scuseria, and M. Ernzerhof, "Hybrid functionals based on a screened coulomb potential," *The Journal of Chemical Physics*, vol. 118, no. 18, pp. 8207–8215, 2003. [Online]. Available: http://scitation.aip.org/content/aip/journal/jcp/118/18/10.1063/1.1564060

[142] Y. Zheng, C. Rivas, R. Lake, K. Alam, T. B. Boykin, and G. Klimeck, "Electronic properties of silicon nanowires," *IEEE Trans. Electron Dev.*, vol. 52, no. 6, pp. 1097–1103, 2005.

[143] S. Lee, F. Oyafuso, P. von Allmen, and G. Klimeck, "Boundary conditions for the electronic structure of finite-extent embedded semiconductor nanostructures," *Phys. Rev. B*, vol. 69, no. 4, p. 045316, 2004.

[144] R. Rahman, C. J. Wellard, F. R. Bradbury, M. Prada, J. H. Cole, G. Klimeck, and L. C. L. Hollenberg, "High precision quantum control of single donor spins in silicon," *Phys. Rev. Lett.*, vol. 99, no. 3, p. 036403, 2007.

[145] H. Schneider and K. v. Klitzing, "Thermionic emission and Gaussian transport of holes in $GaAs/A_xGa_{1-x}As$ multiple–quantum–well structure," *Phys. Rev. B*, vol. 38, no. 9, pp. 6160–6165, 1988.

[146] I. A. Larkin, S. Ujevic, and E. A. Avrutin, "Tunneling escape time from a semiconductor quantum well in an electric field," *Journal of Applied Physics*, vol. 106, no. 11, p. 113701, 2009.

[147] D. J. Griffiths, *Introduction to Quantum Mechanics*, 4th ed. New York: Pearson Education, 2008.

[148] H.-Y. Shen, R. R. Zeng, Y.-P. Zhou, G. F. Yu, C.-H. Huang, Z.-D. Zeng, W. J. Zhang, and Q. J. Ye, "Simultaneous Multiple Wavelength Laser Action in Various Neodymium Host Crystals," *IEEE Journal of Quantum Electronics*, vol. 27, no. 10, pp. 2315 – 2318, 1991.

[149] http://www.ioffe.rssi.ru/SVA/NSM/Semicond/.

[150] O. V. Vakulenko, S. V. Kondratenko, A. S. Nikolenko, S. L. Golovinskiy, Y. NKozyrev, M. Y. Rubezhanska, and A. I. Vodyanitsky, "Photoconductivity spectra of Ge/Si heterostructures with Ge QDs," *Nanotechnology*, vol. 18, no. 185401, pp. 1 – 5, 2007.

[151] S. Takeoka, M. Fujii, S. Hayashi, and K. Yamamoto, "Size-dependent near-infrared photoluminescence from Ge nanocrystals embedded in sio_2 matrices," *Phys. Rev. B*, vol. 58, no. 12, p. 7921 7925, 1998.

[152] B. Brar, G. Wilk, and A. Seabaugh, "Direct extraction of the electron tunneling effective mass in ultrathin SiO2," *Applied Physics Letters*, vol. 69, no. 18, pp. 2728 – 2730, 1996.

[153] A. Sakai, A. Ishida, S. Uno, and Y. Kamakura, "Calculation of direct tunneling current throught ultra–thin gate oxides using complex band models for SiO2," *Journal of Computational Electronics*, vol. 1, pp. 195 – 199, 2002.

[154] T.-X. Nie, J.-H. Lin, Z.-G. Chen, Y.-M. Shao, Y.-Q. Wu, X.-J. Yang, Y.-L. Fan, Z.-M. Jiang, and J. Zou, "Thermally oxidized formation of new ge dots over as-grown ge dots in the si capping layer," *Journal of Applied Physics*, vol. 110, no. 11, p. 114304, 2011. [Online]. Available: http://link.aip.org/link/?JAP/110/114304/1

[155] A. I. Yakimov, A. A. Bloshkin, V. A. Timofeev, A. I. Nikiforov, and A. V. Dvurechenskii, "Effect of overgrowth temperature on the mid-infrared response of Ge/Si(001) quantum dots," *Applied Physics Letters*, vol. 100, no. 5, p. 053507, 2012. [Online]. Available: http://link.aip.org/link/?APL/100/053507/1

[156] A. I. Yakimov, A. A. Bloshsin, and A. V. Dvurechenskii, "Enhanced oscillator strength of interband transitions in coupled Ge/Si quantum dots," *Applied Physics Letters*, vol. 93, no. 13, p. 132105, 2008. [Online]. Available: http://link.aip.org/link/?APL/93/132105/1

[157] A. I. Yakimov, N. P. Stepina, A. V. Dvurechenskii, A. I. Nikiforov, and A. V. Nenashev, "Excitons in charged Ge/Si type-II quantum dots," *Semiconductor Science and Technology*, vol. 15, no. 12, p. 1125, 2000. [Online]. Available: http://stacks.iop.org/0268-1242/15/i=12/a=305

[158] J. S. de Sousa, V. N. Freire, and E. F. da Silva Jr., "Quantum dot electronic devices: modeling and simulation," *Physica Status Solidi (C)*, vol. 1, no. S2, pp. S173 – S180, 2004.

[159] H. Zhou and J. Liu, "Performance enhancement of $TiSi_2$ coated Si nanocrystal memory device," *Mater. Res. Soc. Symp. Proc*, vol. 1160, pp. H01–H05, 2009.

[160] B. Li, J. Liu, G. F. Liu, and J. A. Yarmoff, "Ge/Si heteronanocrystal floating gate memory," *Applied Physics Letters*, vol. 91, no. 13, p. 132107, 2007. [Online]. Available: http://link.aip.org/link/?APL/91/132107/1

[161] A. I. Yakimov, G. Y. Mikhalyov, A. V. Dvurechenskii, and A. I. Nikiforov, "Hole states in Ge/Si quantum-dot molecules produced by strain-driven self-assembly," *Journal of Applied Physics*, vol. 102, no. 9, p. 093714, 2007. [Online]. Available: http://link.aip.org/link/?JAP/102/093714/1

[162] A. Rastelli, E. Müller, and H. von Känel, "Shape preservation of Ge/Si(001) islands during Si capping," *Applied Physics Letters*, vol. 80, no. 8, pp. 1438–1440, 2002. [Online]. Available: http://link.aip.org/link/?APL/80/1438/1

[163] M. R. Neupane, R. Rahman, and R. K. Lake, "Carrier leakage in Ge/Si core-shell nanocrystals for lasers: core size and strain effects," *Nanoengineering: Fabrication, Properties, Optics, and Devices VIII*, vol. 8102, no. 1, p. 81020, 2011. [Online]. Available: http://link.aip.org/link/?PSI/8102/81020P/1

[164] J. Stangl, A. Hesse, V. Hol, G. Bauer, U. Denker, O. G. Schmidt, O. Kirfel, and D. Grutzmacher, "Structural properties of SiGe islands: Effect of capping," *MRS Proceedings*, vol. 749, no. 21, p. 11, 2002.

[165] N. Kharche, M. Prada, T. B. Boykin, and G. Klimeck, "Valley splitting in strained silicon quantum wells modeled with 2^o miscuts, step disorder, and alloy disorder," *Applied Physics Letters*, vol. 90, no. 9, p. 092109, 2007.

[166] M. Usman, "In-plane polarization anisotropy of ground state optical intensity in InAs/GaAs quantum dots," *Journal of Applied Physics*, vol. 110, no. 9, p. 094512, 2011. [Online]. Available: http://link.aip.org/link/?JAP/110/094512/1

[167] A. A. Tonkikh, G. E. Cirlin, V. G. Talalaev, N. D. Zakharov, and P. Werner, "Room temperature electroluminescence from multilayer GeSi heterostructures," *physica status solidi (a)*, vol. 203, no. 6, pp. 1390–1394, 2006. [Online]. Available: http://dx.doi.org/10.1002/pssa.200566130

[168] Z. C. Holman and U. R. Kortshagen, "Quantum confinement in germanium nanocrystal thin films," *physica status solidi (RRL) Rapid Research Letters*, vol. 5, no. 3, pp. 110–112, 2011. [Online]. Available: http://dx.doi.org/10.1002/pssr.201105031

[169] A. Yakimov, A. Dvurechenskii, A. Nikiforov, and G. Mikhalev, "The Meyer-Neldel rule in the processes of thermal emission and hole capture in Ge/Si quantum dots," *JETP Letters*, vol. 80, pp. 321–325, 2004. [Online]. Available: http://dx.doi.org/10.1134/1.1825114

[170] V. G. Talalaev, G. E. Cirlin, A. A. Tonkikh, N. D. Zakharov, P. Werner, U. Gsele, J. W. Tomm, and T. Elsaesser, "Miniband-related 1.4-1.8 μm luminescence of Ge/Si quantum dot superlattices," *Nanoscale Research Letters*, vol. 1, no. 2, pp. 137–153, 2006.

[171] X. Yan, X. Zhang, X. Ren, X. Lv, J. Li, Q. Wang, S. Cai, and Y. Huang, "Formation mechanism and optical properties of InAs quantum dots on the surface of GaAs nanowires," *Nano Letters*, vol. 12, no. 4, pp. 1851–1856, 2012. [Online]. Available: http://pubs.acs.org/doi/abs/10.1021/nl204204f

[172] M. Usman, V. Tasco, M. T. Todaro, M. D. Giorgi, E. P. O. Reilly, G. Klimeck, and A. Passaseo, "The polarization response in InAs quantum dots: theoretical correlation between composition and electronic properties," *Nanotechnology*, vol. 23, no. 16, p. 165202, 2012. [Online]. Available: http://stacks.iop.org/0957-4484/23/i=16/a=165202

[173] Y. Yu, M.-F. Li, J.-F. He, Y.-M. He, Y.-J. Wei, Y. He, G.-W. Zha, X.-J. Shang, J. Wang, L.-J. Wang, G.-W. Wang, H.-Q. Ni, C.-Y. Lu, and Z.-C. Niu, "Single InAs quantum dot grown at the junction of branched gold-free GaAs nanowire," *Nano Letters*, vol. 13, no. 4, pp. 1399–1404, 2013. [Online]. Available: http://pubs.acs.org/doi/abs/10.1021/nl304157d

[174] A. M. Smith, A. M. Mohs, and S. Nie1, "Tuning the optical and electronic properties of colloidal nanocrystals by lattice strain," *Nature Nanotechnology*, vol. 4, pp. 56 – 63, 2008.

[175] R. Mahadevu, A. R. Yelameli, B. Panigrahy, and A. Pandey, "Controlling light absorption in charge-separating core/shell semiconductor nanocrystals," *ACS Nano*, vol. 7, no. 12, pp. 11 055–11 063, 2013. [Online]. Available: http://pubs.acs.org/doi/abs/10.1021/nn404749n

[176] L. J. Lauhon, M. S. Gudiksen, D. Wang, and C. M. Lieber, "Epitaxial core-shell and core-multishell nanowire heterostructures," *Nature*, vol. 420, pp. 57–61, Nov 2002. [Online]. Available: http://dx.doi.org/10.1038/nature01141

[177] G. Liang, J. Xiang, N. Kharche, G. Klimeck, C. M. Lieber, and M. Lundstrom, "Performance analysis of a Ge/Si core/shell nanowire field-effect transistor," *Nano Letters*, vol. 7, no. 3, pp. 642–646, 2007. [Online]. Available: http://pubs.acs.org/doi/abs/10.1021/nl062596f

[178] M. Friesen, S. Chutia, C. Tahan, and S. N. Coppersmith, "Valley splitting theory of SiGe/Si/SiGe quantum wells," *Phys. Rev. B*, vol. 75, no. 11, p. 115318, 2007.

[179] J. Lu, Z. Zuo, Y. Chen, Y. Shi, L. Pu, and Y. Zheng, "Charge storage characteristics in metal-oxide-semiconductor memory structure based on gradual $Ge_{1-x}Si_x$/Si heteronanocrystals," *Applied Physics Letters*, vol. 92, no. 1, p. 013105, 2008.

[180] M. Friesen and S. N. Coppersmith, "Theory of valley-orbit coupling in a Si/SiGe quantum dot," *Phys. Rev. B*, vol. 81, p. 115324, Mar 2010. [Online]. Available: http://link.aps.org/doi/10.1103/PhysRevB.81.115324

[181] B. M. Maune, M. G. Borselli, B. Huang, T. D. Ladd, P. W. Deelman, K. S. Holabird, A. A. Kiselev, I. Alvarado-Rodriguez, R. S. Ross, A. E. Schmitz, M. Sokolich, C. A. Watson, M. F. Gyure, and A. T. Hunter, "Coherent singlet-triplet oscillations in a silicon-based double quantum dot," *Nature*, vol. 481, pp. 344–347, Jan 2012. [Online]. Available: http://dx.doi.org/10.1038/nature10707

[182] Y. Hu, F. Kuemmeth, C. Lieber, and C. M. M. Marcus, "Hole spin relaxation in Ge-Si core-shell nanowire qubits," *Nature*, vol. 7, pp. 47–50, Jan 2012. [Online]. Available: http://dx.doi.org/10.1038/nnano.2011.234

[183] S. Kwon, Z. C. Y. Chen, J.-H. Kim, and J. Xiang, "Misfit-Guided Self-Organization of Anticorrelated Ge quantum dot arrays on Si nanowires," *Nano Letters*, vol. 12, no. 9, pp. 4757–4762, 2012. [Online]. Available: http://pubs.acs.org/doi/abs/10.1021/nl302190e

[184] J. K. Gamble, M. A. Eriksson, S. N. Coppersmith, and M. Friesen, "Disorder-induced valley-orbit hybrid states in si quantum dots," *Phys. Rev. B*, vol. 88, p. 035310, Jul 2013. [Online]. Available: http://link.aps.org/doi/10.1103/PhysRevB.88.035310

[185] Y. J. Ma, Z. Zhong, Q. Lv, T. Zhou, X. J. Yang, Y. L. Fan, Y. Q. Wu, J. Zou, and Z. M. Jiang, "Formation of coupled three–dimensional GeSi quantum dot crystals," *Applied Physics Letters*, vol. 100, no. 15, p. 153113, 2012. [Online]. Available: http://link.aip.org/link/?APL/100/153113/1

[186] S.-W. Lee, H.-T. Chang, J.-K. Chang, and S.-L. Cheng, "Formation mechanism of self-assembled Ge/Si/Ge composite islands," *Journal of The Electrochemical Society*, vol. 158, no. 11, pp. H1113–H1116, 2011. [Online]. Available: http://link.aip.org/link/?JES/158/H1113/1

[187] J. Yang, Y. Jin, C. Wang, L. Li, D. Tao, and Y. Yang, "Evolution of self-assembled Ge/Si island grown by ion beam sputtering deposition," *Applied Surface Science*, vol. 258, no. 8, pp. 3637 – 3642, 2012. [Online]. Available: http://www.sciencedirect.com/science/article/pii/S0169433211018885

[188] A. Alkhatib and A. Nayfeh, "A Complete Physical Germanium-on-Silicon Quantum Dot Self-Assembly Process," *Sci. Rep.*, vol. 3, Jun 2013. [Online]. Available: http://dx.doi.org/10.1038/srep02099

[189] J. Zhang, A. Rastelli, O. G. Schmidt, and G. Bauer, "Site-controlled SiGe islands on patterned Si(001): Morphology, composition profiles, and devices," *Physica Status Solidi (b)*, vol. 249, no. 752-763, p. 12, 2012.

[190] A. I. Yakimov, A. V. Dvurechenskii, Y. Y. Proskuryakov, A. I. Nikiforov, O. P. Pchelyakov, S. A. Teys, and A. K. Gutakovskii, "Normal-incidence infrared photoconductivity in Si p-i-n diode with embedded Ge self-assembled quantum dots," *Applied Physics Letters*, vol. 75, no. 10, pp. 1413–1415, 1999. [Online]. Available: http://link.aip.org/link/?APL/75/1413/1

[191] T. Tayagaki, K. Ueda, S. Fukatsu, and Y. Kanemitsu, "Recombination dynamics of high-density photocarriers in type-ii ge/si quantum dots," *Journal of the Physical Society of Japan*, vol. 81, no. 6, p. 064712, 2012. [Online]. Available: http://journals.jps.jp/doi/abs/10.1143/JPSJ.81.064712

[192] T. Tayagaki, Y. Hoshi, and N. Usami, "Investigation of the open-circuit voltage in solar cells doped with quantum dots," *Sci. Rep.*, vol. 3, Sep 2013. [Online]. Available: http://dx.doi.org/10.1038/srep02703

[193] X.-J. Hao, T. Tu, G. Cao, C. Zhou, H.-O. Li, G.-C. Guo, W. Y. Fung, Z. Ji, G.-P. Guo, and W. Lu, "Strong and Tunable Spin-Orbit coupling of one-dimensional holes in Ge/Si core/shell nanowires," *Nano Letters*, vol. 10, no. 8, pp. 2956–2960, 2010. [Online]. Available: http://pubs.acs.org/doi/abs/10.1021/nl101181e

[194] A. F. Zinovieva, A. V. Dvurechenskii, N. P. Stepina, A. S. Deryabin, A. I. Nikiforov, R. M. Rubinger, N. A. Sobolev, J. P. Leitão, and M. C. Carmo, "Spin resonance of electrons localized on Ge/Si quantum dots," *Phys. Rev. B*, vol. 77, p. 115319, Mar 2008. [Online]. Available: http://link.aps.org/doi/10.1103/PhysRevB.77.115319

[195] L. A. Montoro, M. S. Leite, D. Biggemann, F. G. Peternella, K. J. Batenburg, G. MedeirosRibeiro, and A. J. Ramirez, "Revealing quantitative 3D chemical arrangement on Ge-Si nanostructures," *The Journal of Physical Chemistry C*, vol. 113, no. 21, pp. 9018–9022, 2009. [Online]. Available: http://pubs.acs.org/doi/abs/10.1021/jp902480w

[196] M. R. McKay, J. Venables, and J. Drucker, "Kinetic frustration of Ostwald ripening in Ge/Si(100) hut ensembles," *Solid State Communications*, vol. 149, no. 35-36, pp. 1403 – 1409", 2009. [Online]. Available: http://www.sciencedirect.com/science/article/pii/S003810980900252X

[197] B. Cho, J. Bareno, I. Petrov, and J. E. Greene, "Enhanced Ge/Si(001) island areal density and self-organization due to P predeposition," *Journal of Applied Physics*, vol. 109, no. 9, p. 093526, 2011.

[198] M.-I. Richard, T. U. Schülli, and G. Renaud, "In situ x-ray study of the formation of defects in Ge islands on Si(001)," *Applied Physics Letters*, vol. 99, no. 16, p. 161906, 2011. [Online]. Available: http://link.aip.org/link/?APL/99/161906/1

[199] M. S. Leite, T. I. Kamins, R. S. Williams, and G. MedeirosRibeiro, "Intermixing during Ripening in Ge/Si incoherent epitaxial nanocrystals," *The Journal of Physical Chemistry C*, vol. 116, no. 1, pp. 901–907, 2012. [Online]. Available: http://pubs.acs.org/doi/abs/10.1021/jp2092016

[200] D. Grtzmacher, T. Fromherz, C. Dais, J. Stangl, E. Mller, Y. Ekinci, H. H. Solak, H. Sigg, R. T. Lechner, E. Wintersberger, S. Birner, V. Hol, and G. Bauer, "Three-dimensional Si/Ge quantum dot crystals," *Nano Letters*, vol. 7, no. 10, pp. 3150–3156, 2007, pMID: 17892317. [Online]. Available: http://pubs.acs.org/doi/abs/10.1021/nl0717199

[201] M. D. Seta, G. Capellini, F. Evangelisti, C. Ferrari, L. Lazzarini, G. Salviati, R. W. Peng, and S. S. Jiang, "Effect of interlayer strain interaction on the island composition and ordering in Ge/Si(001) island superlattices," *Journal of Applied Physics*, vol. 102, no. 4, p. 043518, 2007. [Online]. Available: http://link.aip.org/link/?JAP/102/043518/1

[202] S. Leea, H. Changa, C. Leeb, S. Chengc, and C. Liub, "Composition redistribution of self–assembled Ge islands on Si(001) during annealing," *Thin Solid Films*, vol. 518, no. 6, pp. S196–S199, 2010. [Online]. Available: http://dx.doi.org/10.1016/j.tsf.2009.10.087

[203] Z. F. Krasilnik, A. V. Novikov, D. N. Lobanov, K. E. Kudryavtsev, A. V. Antonov, S. V. Obolenskiy, N. D. Zakharov, and P. Werner, "SiGe nanostructures with self–assembled islands for Si–based optoelectronics," *Semiconductor Science and Technology*, vol. 26, no. 1, p. 014029, 2011. [Online]. Available: http://stacks.iop.org/0268-1242/26/i=1/a=014029

[204] M. V. Shaleev, A. V. Novikov, A. N. Yablonskiy, Y. N. Drozdov, D. N. Lobanov, Z. F. Krasilnik, and O. A. Kuznetsov, "Photoluminescence of dome and hut shaped Ge(Si) self-assembled islands embedded in a tensile-strained Si layer," *Applied Physics Letters*, vol. 91, no. 2, p. 021916, 2007. [Online]. Available: http://link.aip.org/link/?APL/91/021916/1

[205] E. Mateeva, P. Sutter, and M. G. Lagally, "Spontaneous self-embedding of three-dimensional SiGe islands," *Applied Physics Letters*, vol. 74, no. 4, pp. 567–569, 1999. [Online]. Available: http://link.aip.org/link/?APL/74/567/1

[206] M. V. Shaleev, A. V. Novikov, A. N. Yablonskiy, Y. N. Drozdov, D. N. Lobanov, Z. F. Krasilnik, and O. A. Kuznetsov, "Photoluminescence of Ge(Si) self-assembled islands embedded in a tensile-strained Si layer," *Applied Physics Letters*, vol. 88, no. 1, p. 011914, 2006. [Online]. Available: http://link.aip.org/link/?APL/88/011914/1

[207] M. Shaleev, A. Novikov, N. Baydakova, A. Yablonskiy, O. Kuznetsov, D. Lobanov, and Z. Krasilnik, "Photoluminescence line width of self-assembled Ge(Si) islands arranged between strained Si layers," *Semiconductors*, vol. 45, pp. 198–202, 2011, 10.1134/S1063782611020199. [Online]. Available: http://dx.doi.org/10.1134/S1063782611020199

[208] J. T. Teherani, W. Chern, D. A. Antoniadis, J. L. Hoyt, L. Ruiz, C. D. Poweleit, and J. Menéndez, "Extraction of large valence-band energy offsets and comparison to theoretical values for strained-Si/strained-Ge type-II heterostructures on relaxed SiGe substrates," *Phys. Rev. B*, vol. 85, p. 205308, May 2012. [Online]. Available: http://link.aps.org/doi/10.1103/PhysRevB.85.205308

[209] P. Klenovský, M. Brehm, V. Křápek, E. Lausecker, D. Munzar, F. Hackl, H. Steiner, T. Fromherz, G. Bauer, and J. Humlíček, "Excitation intensity dependence of photoluminescence spectra of sige quantum dots grown on prepatterned si substrates: Evidence for biexcitonic transition," *Phys. Rev. B*, vol. 86, p. 115305, Sep 2012. [Online]. Available: http://link.aps.org/doi/10.1103/PhysRevB.86.115305

[210] A. V. Nenashev, A. V. Dvurechenskii, and A. F. Zinovieva, "Wave functions and g factor of holes in Ge/Si quantum dots," *Phys. Rev. B*, vol. 67, p. 205301, May 2003. [Online]. Available: http://link.aps.org/doi/10.1103/PhysRevB.67.205301

[211] G. Bester and A. Zunger, "Cylindrically shaped zinc-blende semiconductor quantum dots do not have cylindrical symmetry: atomistic symmetry, atomic relaxation, and piezoelectric effects," *Phys. Rev. B*, vol. 71, p. 045318, Jan 2005. [Online]. Available: http://link.aps.org/doi/10.1103/PhysRevB.71.045318

[212] G. Pizzi, M. Virgilio, and G. Grosso, "Tight-binding calculation of optical gain in tensile strained [001]-Ge/SiGe quantum wells," *Nanotechnology*, vol. 21, no. 5, p. 055202, 2010. [Online]. Available: http://stacks.iop.org/0957-4484/21/i=5/a=055202

[213] N. Skoulidis and H. Polatoglou, "Modeling the optical properties of Si-capped germanium quantum dots," *Computational Materials Science*, vol. 33, pp. 303 – 309, 2005. [Online]. Available: http://www.sciencedirect.com/science/article/pii/S0927025604003234

[214] B. Julsgaard, P. Balling, J. L. Hansen, A. Svane, and A. N. Larsen, "Luminescence decay dynamics of self-assembled germanium islands in silicon," *Applied Physics Letters*, vol. 98, no. 9, p. 093101, 2011. [Online]. Available: http://link.aip.org/link/?APL/98/093101/1

[215] V. M. Lavchiev, U. Schade, G. Hesser, G. Chen, and W. Jantsch, "Ellipsometry and spectroscopy on 1.55 μm emitting Ge islands in Si for photonic applications," *Phys. Rev. B*, vol. 86, p. 125421, Sep 2012. [Online]. Available: http://link.aps.org/doi/10.1103/PhysRevB.86.125421

[216] M. Usman, S. Heck, E. Clarke, P. Spencer, H. Ryu, R. Murray, and G. Klimeck, "Experimental and theoretical study of polarization-dependent optical transitions in InAs quantum dots at telecommunication-wavelengths (1300–1500 nm)," *Journal of Applied Physics*, vol. 109, no. 10, p. 104510, 2011. [Online]. Available: http://link.aip.org/link/?JAP/109/104510/1

[217] M. Usman, Y.-H. M. Tan, H. Ryu, S. S. Ahmed, H. J. Krenner, T. B. Boykin, , and G. Klimeck, "Quantitative excited state spectroscopy of a single InGaAs quantum dot molecule through multi–million–atom electronic structure calculations," *Nanotechnology*, vol. 22, no. 315709, July 2011. [Online]. Available: stacks.iop.org/Nano/22/315709

[218] H. Zhou, R. Gann, B. Li, J. Liu, and J. A. Yarmoff, "Performance enhancement of $TiSi_2$ coated Si nanocrystal memory device," in *Mater. Res. Soc. Symp.*, vol. 1160. Mater. Res. Soc, 2009.

[219] H. Zhou, B. Li, Z. Yang, N. Zhan, D. Yan, R. K. Lake, and J. Liu, "$TiSi_2$ nanocrystal metal oxide semiconductor field effect transistor memory," *IEEE Trans. on Nanotechnology*, vol. 10, no. 3, pp. 499 – 505, 2011.

[220] A. Tonkikh, N. Zakharov, V. Talalaev, and P. Werner, "Ge/si(100) quantum dots grown via a thin sb layer," *physica status solidi (RRL) Rapid Research Letters*, vol. 4, no. 8-9, pp. 224–226, 2010. [Online]. Available: http://dx.doi.org/10.1002/pssr.201004259

[221] A. Yakimov, A. Nikiforov, A. Bloshkin, and A. Dvurechenski, "Electromodulated reflectance study of self-assembled ge/si quantum dots," *Nanoscale Research Letters*, vol. 208, p. 136602, 2011. [Online]. Available: http://www.nanoscalereslett.com/content/6/1/208

[222] P. Klenovský, M. Brehm, V. Křápek, E. Lausecker, D. Munzar, F. Hackl, H. Steiner, T. Fromherz, G. Bauer, and J. Humlíček, "Excitation intensity dependence of photoluminescence spectra of sige quantum dots grown on prepatterned si substrates: Evidence for biexcitonic transition,"

Phys. Rev. B, vol. 86, p. 115305, Sep 2012. [Online]. Available: http://link.aps.org/doi/10.1103/PhysRevB.86.115305

[223] V. Yuryev, L. Arapkina, M. Storozhevykh, V. Chapnin, K. Chizh, O. Uvarov, V. Kalinushkin, E. Zhukova, A. Prokhorov, I. Spektor, and B. Gorshunov, "Ge/si(001) heterostructures with dense arrays of ge quantum dots: morphology, defects, photo-emf spectra and terahertz conductivity," *Nanoscale Research Letters*, vol. 7, no. 1, p. 414, 2012. [Online]. Available: http://www.nanoscalereslett.com/content/7/1/414

[224] Z. Liu, W. Hu, S. Su, C. Li, C. Li, C. Xue, Y. Li, Y. Zuo, B. Cheng, and Q. Wang, "Enhanced photoluminescence and electroluminescence of multilayer gesi islands on si(001) substrates by phosphorus-doping," *Opt. Express*, vol. 20, no. 20, pp. 22 327–22 333, Sep 2012. [Online]. Available: http://www.opticsexpress.org/abstract.cfm?URI=oe-20-20-22327

[225] A. V. Baranov, A. V. Fedorov, T. S. Perova, R. A. Moore, V. Yam, D. Bouchier, V. Le Thanh, and K. Berwick, "Analysis of strain and intermixing in single-layer Ge/Si quantum dots using polarized raman spectroscopy," *Phys. Rev. B*, vol. 73, p. 075322, Feb 2006. [Online]. Available: http://link.aps.org/doi/10.1103/PhysRevB.73.075322

[226] Y. Ogawa, T. Toizumi, F. Minami, and A. V. Baranov, "Nanometer-scale mapping of the strain and Ge content of Ge/Si quantum dots using enhanced raman scattering by the tip of an atomic force microscope," *Phys. Rev. B*, vol. 83, p. 081302, Feb 2011. [Online]. Available: http://link.aps.org/doi/10.1103/PhysRevB.83.081302

[227] H. Ryu, S. Lee, B. Weber, S. Mahapatra, L. C. L. Hollenberg, M. Y. Simmons, and G. Klimeck, "Atomistic modeling of metallic nanowires in silicon," *Nanoscale*, vol. 5, pp. 8666–8674, 2013. [Online]. Available: http://dx.doi.org/10.1039/C3NR01796F

[228] G. P. Lansbergen, R. Rahman, C. J. Wellard, J. Caro, N. Collaert, S. Biesemans, G. Klimeck, L. C. L. Hollenberg, and S. Rogge, "Gate-induced quantum-confinement transition of a single dopant atom in a silicon FinFET," *Nature*, vol. 4, pp. 656–661, Aug 2008. [Online]. Available: http://dx.doi.org/10.1038/nphys994

[229] B. Weber, S. Mahapatra, H. Ryu, S. Lee, A. Fuhrer, T. C. G. Reusch, D. L. Thompson, W. C. T. Lee, G. Klimeck, L. C. L. Hollenberg, and M. Y. Simmons, "Ohms Law Survives to the Atomic Scale," *Science*, vol. 335, no. 6064, pp. 64–67, 2012. [Online]. Available: http://www.sciencemag.org/content/335/6064/64.abstract

[230] H. Bch, S. Mahapatra, R. Rahman, A. Morello, and M. Y. Simmons, "Spin readout and addressability of phosphorus-donor clusters in silicon," *Nat Commun*, vol. 4, Jun 2013. [Online]. Available: http://dx.doi.org/10.1038/ncomms3017

[231] C. Pryor, J. Kim, L. W. Wang, A. J. Williamson, and A. Zunger, "Comparison of two methods for describing the strain profiles in quantum dots," *Journal of Applied Physics*, vol. 83, no. 5, pp. 2548–2554, 1998. [Online]. Available: http://scitation.aip.org/content/aip/journal/jap/83/5/10.1063/1.366631

[232] G. Klimeck, F. Oyafuso, T. B. Boykin, R. C. Bowen, and P. von Allmen, "Development of a nanoelectronic 3-d (nemo 3-d) simulator for multimillion atom simulations and its application to alloyed quantum dots," *CMES*, vol. 3, no. 5, pp. 601–642, 2002.

[233] F. Oyafuso, G. Klimeck, P. Allmen, T. Boykin, and R. Bowen, "Strain effects in large-scale atomistic quantum dot simulations," *physica status solidi (b)*, vol. 239, no. 1, 2003, phys. Stat. Sol. (b), Vol. 239, p 71-79 (2003); doi: 10.1002/pssb.200303238.

[234] A. Paul, M. Luisier, and G. Klimeck, "Modified valence force field approach for phonon dispersion: fromzinc-blende bulk to nanowires," *Journal of Computational Electronics*, vol. 9, no. 3-4, pp. 160–172, 2010. [Online]. Available: http://dx.doi.org/10.1007/s10825-010-0332-9

[235] T. B. Boykin, G. Klimeck, R. C. Bowen, and F. Oyafuso, "Diagonal parameter shifts due to nearest-neighbor displacements in empirical tight-binding theory," *Phys. Rev. B*, vol. 66, p. 125207, Sep 2002. [Online]. Available: http://link.aps.org/doi/10.1103/PhysRevB.66.125207

[236] R. Rahman, S. H. Park, J. H. Cole, A. D. Greentree, R. P. Muller, G. Klimeck, and L. C. L. Hollenberg, "Atomistic simulations of adiabatic coherent electron transport in triple donor systems," *Phys. Rev. B*, vol. 80, p. 035302, Jul 2009. [Online]. Available: http://link.aps.org/doi/10.1103/PhysRevB.80.035302

[237] J. Salfi, J. A. Mol, R. Rahman, G. Klimeck, M. Y. Simmons, L. C. L. Hollenberg, and S. Rogge, "Spatially resolving valley quantum interference of a donor in silicon," *Nature Materials*, vol. 13, pp. 605 – 610, 2014.

[238] M. Naumov, S. Lee, B. Haley, H. Bae, S. Clark, R. Rahman, H. Ryu, F. Saied, and G. Klimeck, "Eigenvalue solvers for atomistic simulations of electronic structures with NEMO-3D," *Journal of Computational Electronics*, vol. 7, no. 297-300, pp. 297–300, 2008. [Online]. Available: http://dx.doi.org/10.1007/s10825-008-0223-5

[239] T. B. Boykin, G. Klimeck, and F. Oyafuso, "Valence band effective-mass expressions in the $sp^3d^5s^*$ empirical tight-binding model applied to a Si and Ge parametrization," *Phys. Rev. B*, vol. 69, p. 115201, Mar 2004. [Online]. Available: http://link.aps.org/doi/10.1103/PhysRevB.69.115201

[240] T. B. Boykin, N. Kharche, and G. Klimeck, "Brillouin-zone unfolding of perfect supercells having nonequivalent primitive cells illustrated with a Si/Ge tight-binding parameterization," *Phys. Rev. B*, vol. 76, p. 035310, Jul 2007. [Online]. Available: http://link.aps.org/doi/10.1103/PhysRevB.76.035310

[241] H. Ryu, D. Nam, B.-Y. Ahn, J. R. Lee, K. Cho, S. Lee, G. Klimeck, and M. Shin, "Optical {TCAD} on the net: A tight-binding study of inter-band light transitions in self-assembled InAs/GaAs quantum dot photodetectors," *Mathematical and Computer Modelling*, vol. 58, pp. 288 – 299, 2013. [Online]. Available: http://www.sciencedirect.com/science/article/pii/S0895717712003354

[242] K. Wang, C. Payette, Y. Dovzhenko, P. W. Deelman, and J. R. Petta, "Charge relaxation in a single-electron Si/SiGe double quantum dot," *Phys. Rev. Lett.*, vol. 111, p. 046801, Jul 2013. [Online]. Available: http://link.aps.org/doi/10.1103/PhysRevLett.111.046801

[243] A. B. Talochkin, V. A. Markov, and V. I. Mashanov, "Inelastic strain relaxation in the Ge quantum dot array," *Applied Physics Letters*, vol. 91, no. 9, p. 093127, 2007. [Online]. Available: http://link.aip.org/link/?APL/91/093127/1

[244] G. G. D. Walle, "Band lineups and deformation potentials in the model-solid theory," *Phys. Rev. B*, vol. 39, no. 3, pp. 1871 – 1883, 1989.

[245] R. Quhe, J. Ma, Z. Zeng, K. Tang, J. Zheng, Y. Wang, Z. Ni, L. Wang, Z. Gao, J. Shi, and J. Lu, "Tunable band gap in few-layer graphene by surface adsorption," *Sci. Rep.*, vol. 3, May 2013.

[246] A. J. Samuels and J. D. Carey, "Molecular doping and band-gap opening of Bilayer Graphene," *ACS Nano*, vol. 7, no. 3, pp. 2790–2799, 2013. [Online]. Available: http://pubs.acs.org/doi/abs/10.1021/nn400340q

[247] S. Y. Zhow, A. Gweon, P. N. First, W. A. de Heer, D. H. Lee, F. Guinea, A. H. Castro Neto, and A. Lanzara, "Substrate-induced bandgap opening in epitaxial graphene," *Nature materials*, vol. 6, no. 10, 2007. [Online]. Available: http://dx.doi.org/10.1038/nmat2003

[248] J. Borysiuk, J. Sotys, J. Piechota, S. Krukowski, J. M. Baranowski, and R. Stpniewski, "Structural defects in epitaxial graphene layers synthesized on C-terminated 4H-SiC (0001) surfaceTransmission

electron microscopy and density functional theory studies," *Journal of Applied Physics*, vol. 115, no. 5, 2014. [Online]. Available: http://scitation.aip.org/content/aip/journal/jap/115/5/10.1063/1.4863644

[249] A. A. Balandin, S. Ghosh, W. Bao, I. Calizo, D. Teweldebrhan, F. Miao, and C. N. Lau, "Superior Thermal Conductivity of Single−layer Graphene," *Nano Letters*, vol. 8, no. 3, pp. 902–907, 2008. [Online]. Available: http://dx.doi.org/10.1021/nl0731872

[250] J. H. Seol, I. Jo, A. L. Moore, L. Lindsay, Z. H. Aitken, M. T. Pettes, X. Li, Z. Yao, R. Huang, D. Broido, N. Mingo, R. S. Ruoff, and L. Shi, "Two-Dimensional Phonon Transport in Supported Graphene," *Science*, vol. 328, no. 5975, pp. 213–216, 2010. [Online]. Available: http://www.sciencemag.org/content/328/5975/213.abstract

[251] A. I. Cocemasov, D. L. Nika, and A. A. Balandin, "Phonons in twisted bilayer graphene," *Phys. Rev. B*, vol. 88, p. 035428, Jul 2013. [Online]. Available: http://link.aps.org/doi/10.1103/PhysRevB.88.035428

[252] Y. Kim, H. Yun, S.-G. Nam, M. Son, D. S. Lee, D. C. Kim, S. Seo, H. C. Choi, H.-J. Lee, S. W. Lee, and J. S. Kim, "Breakdown of the Interlayer Coherence in Twisted Bilayer Graphene," *Phys. Rev. Lett.*, vol. 110, p. 096602, Feb 2013. [Online]. Available: http://link.aps.org/doi/10.1103/PhysRevLett.110.096602

[253] E. Moreau, S. Godey, X. Wallart, I. Razado-Colambo, J. Avila, M.-C. Asensio, and D. Vignaud, "High-resolution angle-resolved photoemission spectroscopy study of monolayer and bilayer graphene on the c-face of sic," *Phys. Rev. B*, vol. 88, p. 075406, Aug 2013. [Online]. Available: http://link.aps.org/doi/10.1103/PhysRevB.88.075406

[254] S. C. Xu, B. Y. Man, S. Z. Jiang, C. S. Chen, C. Yang, M. Liu, X. G. Gao, Z. C. Sun, and C. Zhang, "Direct synthesis of graphene on sio2 substrates by chemical vapor deposition," *CrystEngComm*, vol. 15, pp. 1840–1844, 2013. [Online]. Available: http://dx.doi.org/10.1039/C3CE27029G

[255] J. Hicks, M. Sprinkle, K. Shepperd, F. Wang, A. Tejeda, A. Taleb-Ibrahimi, F. Bertran, P. Le Fèvre, W. A. de Heer, C. Berger, and E. H. Conrad, "Symmetry breaking in commensurate graphene rotational stacking: Comparison of theory and experiment," *Phys. Rev. B*, vol. 83, p. 205403, May 2011. [Online]. Available: http://link.aps.org/doi/10.1103/PhysRevB.83.205403

[256] K. Kim, S. Coh, L. Z. Tan, W. Regan, J. M. Yuk, E. Chatterjee, M. F. Crommie, M. L. Cohen, S. G. Louie, and A. Zettl, "Raman spectroscopy study of rotated double-layer graphene: Misorientation-angle dependence of

electronic structure," *Phys. Rev. Lett.*, vol. 108, p. 246103, Jun 2012. [Online]. Available: http://link.aps.org/doi/10.1103/PhysRevLett.108.246103

[257] G. Trambly de Laissardiere, D. Mayou, and L. Magaud, "Localization of dirac electrons in rotated graphene bilayers," *Nano Letters*, vol. 10, no. 3, pp. 804–808, 2010, pMID: 20121163. [Online]. Available: http://pubs.acs.org/doi/abs/10.1021/nl902948m

[258] A. Luican, G. Li, A. Reina, J. Kong, R. R. Nair, K. S. Novoselov, A. K. Geim, and E. Y. Andrei, "Single-layer behavior and its breakdown in twisted graphene layers," *Phys. Rev. Lett.*, vol. 106, p. 126802, Mar 2011. [Online]. Available: http://link.aps.org/doi/10.1103/PhysRevLett.106.126802

[259] G. Trambly de Laissardière, D. Mayou, and L. Magaud, "Numerical studies of confined states in rotated bilayers of graphene," *Phys. Rev. B*, vol. 86, p. 125413, Sep 2012. [Online]. Available: http://link.aps.org/doi/10.1103/PhysRevB.86.125413

[260] W.-Y. He, Y. Su, M. Yang, and L. He, "Creating in-plane pseudomagnetic fields in excess of 1000 t by misoriented stacking in a graphene bilayer," *Phys. Rev. B*, vol. 89, p. 125418, Mar 2014. [Online]. Available: http://link.aps.org/doi/10.1103/PhysRevB.89.125418

[261] S. Ahsan, K. M. Masum Habib, M. R. Neupane, and R. K. Lake, "Interlayer magnetoconductance of misoriented bilayer graphene ribbons," *Journal of Applied Physics*, vol. 114, no. 18, pp. –, 2013. [Online]. Available: http://scitation.aip.org/content/aip/journal/jap/114/18/10.1063/1.4830019

[262] V. Perebeinos, J. Tersoff, and P. Avouris, "Phonon-mediated interlayer conductance in twisted graphene bilayers," *Phys. Rev. Lett.*, vol. 109, p. 236604, Dec 2012. [Online]. Available: http://link.aps.org/doi/10.1103/PhysRevLett.109.236604

[263] V. Carozo, C. M. Almeida, E. H. M. Ferreira, L. G. Canado, C. A. Achete, and A. Jorio, "Raman signature of graphene superlattices," *Nano Letters*, vol. 11, no. 11, pp. 4527–4534, 2011. [Online]. Available: http://dx.doi.org/10.1021/nl201370m

[264] K. Kim, S. Coh, L. Z. Tan, W. Regan, J. M. Yuk, E. Chatterjee, M. F. Crommie, M. L. Cohen, S. G. Louie, and A. Zettl, "Raman spectroscopy study of rotated double-layer graphene: Misorientation-angle dependence of electronic structure," *Phys. Rev. Lett.*, vol. 108, p. 246103, Jun 2012. [Online]. Available: http://link.aps.org/doi/10.1103/PhysRevLett.108.246103

[265] R. W. Havener, H. Zhuang, L. Brown, R. G. Hennig, and J. Park, "Angle-resolved raman imaging of interlayer rotations and interactions in twisted bilayer graphene," *Nano Letters*, vol. 12, no. 6, pp. 3162–3167, 2012. [Online]. Available: http://dx.doi.org/10.1021/nl301137k

[266] S. Ghosh, W. Bao, D. L. Nika, S. Subrina, E. P. Pokatilov, C. N. Lau, and A. A. Balandin, "Dimensional crossover of thermal transport in few-layer graphene," *Nature Materials*, vol. 9, pp. 555–558, 2010.

[267] F. Herziger, P. May, and J. Maultzsch, "Layer-number determination in graphene by out-of-plane phonons," *Phys. Rev. B*, vol. 85, p. 235447, Jun 2012. [Online]. Available: http://link.aps.org/doi/10.1103/PhysRevB.85.235447

[268] A. L. Rakhmanov, A. V. Rozhkov, A. O. Sboychakov, and F. Nori, "Instabilities of the AA-stacked graphene bilayer," *Phys. Rev. Lett.*, vol. 109, p. 206801, Nov 2012. [Online]. Available: http://link.aps.org/doi/10.1103/PhysRevLett.109.206801

[269] N. Ashcroft and N.Mermin, *Solid State Physics*. Saunders College Publishing, Fort Worth, 1976.

[270] J. Los and A. Fasolino, "Monte Carlo simulations of carbon-based structures based on an extended Brenner potential," *Computer Physics Communications*, vol. 147, no. 12, pp. 178 – 181, 2002, proceedings of the Europhysics Conference on Computational Physics Computational Modeling and Simulation of Complex Systems. [Online]. Available: http://www.sciencedirect.com/science/article/pii/S0010465502002400

[271] J. Maultzsch, S. Reich, C. Thomsen, H. Requardt, and P. Ordejón, "Phonon Dispersion in Graphite," *Phys. Rev. Lett.*, vol. 92, p. 075501, Feb 2004. [Online]. Available: http://link.aps.org/doi/10.1103/PhysRevLett.92.075501

[272] L. Wirtz and A. Rubio, "The phonon dispersion of graphite revisited," *Solid State Communications*, vol. 131, no. 34, pp. 141 – 152, 2004. [Online]. Available: http://www.sciencedirect.com/science/article/pii/S0038109804003424

[273] R. He, T.-F. Chung, C. Delaney, C. Keiser, L. A. Jauregui, P. M. Shand, C. C. Chancey, Y. Wang, J. Bao, and Y. P. Chen, "Observation of Low Energy Raman Modes in Twisted Bilayer Graphene," *Nano Letters*, vol. 13, no. 8, pp. 3594–3601, 2013. [Online]. Available: http://dx.doi.org/10.1021/nl4013387

[274] J.-W. Jiang, B.-S. Wang, and T. Rabczuk, "Acoustic and breathing phonon modes in bilayer graphene with Moir patterns," *Applied Physics Letters*, vol. 101, no. 2, pp. –, 2012. [Online]. Available: http://scitation.aip.org/content/aip/journal/apl/101/2/10.1063/1.4735246

[275] D. L. Nika, A. I. Cocemasov, and A. A. Balandin, "Specific heat of twisted bilayer graphene: Engineering phonons by atomic plane rotations," *Applied Physics Letters*, vol. 105, no. 3, pp. –, 2014. [Online]. Available: http://scitation.aip.org/content/aip/journal/apl/105/3/10.1063/1.4890622

[276] Y. Ni, Y. A. Kosevich, S. Xiong, Y. Chalopin, and S. Volz, "Substrate-induced cross-plane thermal propagative modes in few-layer graphene," *Phys. Rev. B*, vol. 89, p. 205413, May 2014. [Online]. Available: http://link.aps.org/doi/10.1103/PhysRevB.89.205413

[277] A. A. Balandin and D. L. Nika, "Phononics in low-dimensional materials," *Materialstoday*, vol. 15, pp. 266–275, 2012.

[278] M. Maldovan, "Sound and heat revolutions in phononics," *Nature*, vol. 503, pp. 209–217, 2013.

[279] M. S. Kushwaha, P. Halevi, L. Dobrzynski, and B. Djafari-Rouhani, "Acoustic band structure of periodic elastic composites," *Phys. Rev. Lett.*, vol. 71, pp. 2022–2025, Sep 1993. [Online]. Available: http://link.aps.org/doi/10.1103/PhysRevLett.71.2022

[280] C. W. Chang, D. Okawa, A. Majumdar, and A. Zettl, "Solid-state thermal rectifier," *Science*, vol. 314, pp. 1121–1124, 2006.

[281] D. Segal, "Single mode heat rectifier: Controlling energy flow between electronic conductors," *Phys. Rev. Lett.*, vol. 100, p. 105901., 2008.

[282] N. Boechler, G. Theocharis, and C. Daraio, "Bifurcation-based acoustic switching and rectification," *Nature Materials*, vol. 10, pp. 665–668, 2011.

[283] S. R. Sklan and J. C. Grossman, "Phonon diodes and transistors from magneto-acoustics," *New J. Phyics*, vol. 16, 2014.

[284] L. Wang and B. Li, "Thermal memory: A storage of phononic information," *Phys Rev. Lett.*, vol. 101, p. 267203, 2008.

[285] J. Khan, C. M. Nolen, D. Teweldebrhan, D. Wickramaratne, R. K. Lake, and A. A. Balandin, "Anomalous electron transport in back-gated field-effect transistors with tite2 semimetal thin-film channels," *Appl. Phys. Lett.*, vol. 100, p. 043109, 2012.

[286] P. Goli, J. Khan, D. Wickramaratne, R. K. Lake, and A. A. Balandin, "Charge density waves in exfoliated films of van der waals materials: Evolution of raman spectrum in $tise_2$," *Nano Lett.*, vol. 12, pp. 5941–5945, 2012.

[287] P. E. Hopkins, C. M. Reinke, M. F. Su, R. H. Olsson, E. A. Shaner, Z. C. Leseman, J. R. Serrano, L. M. Phinney, and I. El-Kady, "Reduction in the thermal conductivity of single crystalline silicon by phononic crystal patterning," *Nano Lett.*, vol. 11, pp. 107–112, 2011.

[288] J. Cuffe, E. Chvez, A. Shchepetov, P. O. Chapuis, E. H. E. Boudouti, F. Alzina, T. Kehoe, J. Gomis-Bresco, D. Dudek, Y. Pennec, D.-R. B, M. Prunnila, J. Ahopelto, and C. M. S. Torres, "Phonons in slow motion: dispersion relations in ultrathin si membranes," *Nano Lett.*, vol. 12, pp. 3569–3573, 2012.

[289] M. Maldovan, "Narrow low-frequency spectrum and heat management by thermocrystals," *Phys. Rev. Lett.*, vol. 110, p. 025902, Jan 2013. [Online]. Available: http://link.aps.org/doi/10.1103/PhysRevLett.110.025902

[290] B. L. Davis and M. I. Hussein, "Nanophononic metamaterials: Thermal conductivity reduction by local resonance," *Phys. Rev. Lett.*, vol. 112, p. 055505., 2014.

[291] A. W. Fang, B. R. Koch, D. Liang, H. Park, M. N. Sysak, and J. E. Bowers, "Hybrid silicon photonics for optical interconnects," *J. Sel. Top. Quantum Electronics*, vol. 17, pp. 333–346, 2011.

[292] P. Chaisakul, D. Marris-Morini, J. Frigerio, D. Chrastina, M. S. Rouifed, S. Cecchi, P. Crozat, G. Isella, and L. Vivien, "Integrated germanium optical interconnects on silicon substrates," *Nature Photonics*, vol. 8, pp. 482–488, 2014.

[293] S. Dakshinamurthy, N. R. Quick, and A. Kar, "Temperature-dependent optical properties of silicon carbide for wireless temperature sensors," *Journal of Phys. D: Appl. Phys.*, vol. 40, 2007.

[294] P. cajev, M. Kato, and K. Jaraiunas, "A diffraction-based technique for determination of interband absorption coefficients in bulk 3c-, 4h- and 6h-sic crystals," *Journal of Physics D: Applied Physics*, vol. 44, no. 36, p. 365402, 2011. [Online]. Available: http://stacks.iop.org/0022-3727/44/i=36/a=365402

[295] L. Huet, M. Ammar, E. Morvan, N. Sarazin, J. P. Pocholle, J. Reichel, C. Guerlin, and S. Schwartz, "Experimental investigation of transparent silicon carbide for atom chips," *Appl. Phys. Lett.*, vol. 100, p. 121114., 2012.

[296] H. Kraus, V. A. Soltamov, D. Riedel, S. Vth, F. Fuchs, A. Sperlich, P. G. Baranov, V. Dyakonov, and G. V. Astakhov, "Room-temperature quantum microwave emitters based on spin defects in silicon carbide," *Nature Physics*, vol. 10, pp. 157–162, 2014.

[297] S. Castelletto, B. C. Johnson, V. Ivdy, N. Stavrias, T. Umeda, A. Gali, and T. Ohshima, "A silicon carbide room-temperature single-photon source," *Nature Materials*, vol. 13, pp. 151–156, 2013.

[298] Z. Zhong, W. Schwinger, F. Schffler, G. Bauer, G. Vastola, F. Montalenti, and L. Miglio, "Delayed plastic relaxation on patterned si substrates: Coherent sige pyramids with dominant 111 facets," *Phys. Rev. Lett.*, vol. 98, p. 176102, 2007.

[299] S. M. George, "Atomic layer deposition: An overview," *Chem. Rev.*, vol. 110, pp. 111–131, 2010.

[300] Z. Zhong, H. Gong, Y. Ma, Y. Fan, and Z. Jiang, "A promising routine to fabricate gesi nanowires via self-assembly on miscut si (001) substrates," *Nanoscale Research Letters*, 2011.

[301] Y. Luo, X. Zheng, G. Li, I. Shubin, H. Thacker, J. Yao, J. H. Lee, D. Feng, J. Fong, C. C. Kung, S. Liao, R. Shafiiha, M. Asghari, K. Raj, A. V. Krishnamoorthy, and J. E. Cunningham, "Strong electro-absorption in gesi epitaxy on silicon-on-insulator (soi)," *Micromachines*, vol. 3, pp. 345–363, 2012.

[302] A. Sgouros, M. M. Sigalas, G. Kalosakas, K. Papagelis, and N. I. Papanicolaou, "Phononic band gap engineering in graphene," *Journal of Appl. Phys.*, vol. 112, p. 094307, 2012.

[303] M. M. Sigalas and E. N. koukaras, "Band gap effects in a two-dimensional regular polygonal graphene-like structure," *Appl. Phys. Lett.*, vol. 100, p. 203109, 2012.

[304] M. Fuechsle, J. A. Miwa, S. Mahapatra, H. Ryu, S. Lee, O. Warschkow, L. C. L. Hollenberg, G. Klimeck, and M. Y. Simmons, "A single-atom transistor," *Nature Nanotech.*, pp. 242–246, 2012.

[305] B. W. S. Mahapatra, H. Ryu, S. Lee, A. Fuhrer, T. C. G. Reusch, D. L. Thompson, W. C. T. Lee, G. Klimeck, L. C. L. Hollenberg, and M. Y. Simmons, "Ohm's law survives to the atomic scale," *Science*, pp. 64–67, 2012.

[306] J. Tersoff, "New empirical approach for the structure and energy of covalent systems," *Phys. Rev. B*, vol. 37, p. 6991, 1998.

[307] ——, "Modeling solid-state chemistry: Interatomic potentials for multicomponent systems," *Phys. Rev. B*, vol. 39, p. 5566, 1989.

[308] J. P. Perdew, K. Burke, and M. Ernzerhof, "Generalized gradient approximation made simple," *Phys. Rev. Lett.*, vol. 77, p. 3865, 1996.

[309] G. Gopalakrishnan, M. V. Holt, K. M. McElhinny, J. W. Spalenka, D. A. Czaplewski, T. U. Schlli, and P. G. Evans, "Thermal diffuse scattering as a probe of large-wave-vector phonons in silicon nanostructures," *Phys. Rev. Lett.*, vol. 110, p. 20550, 2013.

[310] D. Vanderbilt and Phys, "Soft self-consistent pseudopotentials in a generalized eigenvalue formalism," *Phys. Rev. B*, vol. 41, 1990.

[311] P. Giannozzi, S. Baroni, N. Bonini, M. Calandra, R. Car, C. Cavazzoni, D. Ceresoli, G. L. Chiarotti, M. Cococcioni, I. Dabo, A. D. Corso, S. Fabris, G. Fratesi, S. de Giron-coli, R. Gebauer, U. Gerstmann, C. Gougoussis, A. Kokalj, M. Lazzeri, L. Martin-Samos, N. Marzari, F. Mauri, R. Mazzarello, S. Paolini, A. Pasquarello, L. Paulatto, C. Sbraccia, S. Scandolo, G. Sclauzero, A. P. Seitsonen, A. Smogunov, P. Umari, and R. M. Wentzcovitch, "Quantum espresso: a modular and open-source software project for quantum simulations of materials," *Journal of Phys. : Cond. Mat.*, vol. 21, p. 395502, 2009.

[312] S. Nose, "A unified formulation of the constant-temperature molecular dynamics method," *J. Chem. Phys.*, vol. 81, pp. 511–519, 1984.

[313] W. G. Hoover, "Canonical dynamics: Equilibrium phase-space distributions," *Phys. Rev. A*, vol. 31, pp. 1695–1697, 1985.

[314] L. V. Keldysh and Y. V. Kopaev, *Sov. Phys. Solid State*, vol. 6, p. 2219, 1965.

[315] D. Nandi, A. Finck, J. Eisenstein, L. Pfeiffer, and K. West, "Exciton condensation and perfect coulomb drag," *Nature*, vol. 488, pp. 481–484, 2012.

[316] A. Perali, D. Neilson, and A. R. Hamilton, "High-temperature superfluidity in double-bilayer graphene," *Phys. Rev. Lett.*, vol. 110, p. 146803, Apr 2013. [Online]. Available: http://link.aps.org/doi/10.1103/PhysRevLett.110.146803

[317] C.-H. Zhang and Y. N. Joglekar, "Excitonic condensation of massless fermions in graphene bilayers," *Phys. Rev. B*, vol. 77, p. 233405, Jun 2008. [Online]. Available: http://link.aps.org/doi/10.1103/PhysRevB.77.233405

[318] H. Fang, C. Battaglia, C. Carraro, S. Nemsak, B. Ozdol, J. S. Kang, H. A. Bechtel, S. B. Desai, F. Kronast, A. A. Unal, G. Conti, C. Conlon, G. K. Palsson, M. C. Martin, A. M. Minor, C. S. Fadley, E. Yablonovitch, R. Maboudian, and A. Javey, "Strong interlayer coupling in van der waals heterostructures built from single-layer chalcogenides," *Proceedings of the National Academy of Sciences*, vol. 111, no. 17, pp. 6198–6202, 2014. [Online]. Available: http://www.pnas.org/content/111/17/6198.abstract

[319] G. Nardin, G. Moody, R. Singh, T. M. Autry, H. Li, F. m. c. Morier-Genoud, and S. T. Cundiff, "Coherent excitonic coupling in an asymmetric double InGaAs Quantum Well arises from Many-body effects," *Phys. Rev. Lett.*, vol. 112, p. 046402, Jan 2014. [Online]. Available: http://link.aps.org/doi/10.1103/PhysRevLett.112.046402

[320] A. Filinov, P. Ludwig, Y. E. Lozovik, M. Bonitz, and H. Stolz, "Strongly correlated indirect excitons in quantum wells in high electric fields," *Journal of Physics: Conference Series*, vol. 35, no. 1, p. 197, 2006. [Online]. Available: http://stacks.iop.org/1742-6596/35/i=1/a=018

[321] Y. Lozovik and A. Sokolik, "Electron-hole pair condensation in a graphene bilayer," *JETP Letters*, vol. 87, no. 1, pp. 55–59, 2008. [Online]. Available: http://dx.doi.org/10.1134/S002136400801013X

[322] Y. E. Lozovik, S. L. Ogarkov, and A. A. Sokolik, "Condensation of electron-hole pairs in a two-layer graphene system: Correlation effects," *Phys. Rev. B*, vol. 86, p. 045429, Jul 2012. [Online]. Available: http://link.aps.org/doi/10.1103/PhysRevB.86.045429

[323] P. Rivera, J. R. Schaibley, A. M. Jones, J. S. Ross, S. Wu, G. Aivazian, P. Klement, N. J. Ghimire, J. Yan, D. G. Mandrus, W. Yao, and X. Xu, "Observation of long-lived interlayer excitons in monolayer $MoSe_2$-WSe_2 heterostructures," *CoRR*, vol. arXiv:1403.4985, 2015.

Appendix A

Ge/Si QD Laser

A.1 Introduction

A nanocrystal or quantum dot (QD) laser is a semiconductor laser in which electrons and holes are injected from 3D contact regions, where carriers are free, into an active region with QDs, where lasing transition take place and carriers are confined in all directions. The main motivation behind the idea of a QD laser was to conceive a design for a low-threshold, single-frequency, and temperature-insensitive lasing operation due to the quantum confinement effect. Ge/Si core-shell (Type-II heterostructure) QD laser has been proposed due to its capability to use existing Si based fabrication scheme and exhibiting size dependent stimulated emission. Recent experimental reports also suggested an increase in the light emission probability of such laser by increasing radiative lifetimes due to an extra Si-shell layer around Ge QD acting as an auxiliary quantum well (QW) coupled to the quantum dots by tunneling via a thin barrier and hence, suppressing the carrier leakage current. This structure overcomes the limitations of carrier collection, lateral transport, and thermalization of the quantum dots. The carrier (hole) current leakage mechanism in Ge/Si core-shell

QD is governed by thermionic lifetime of the confined carrier in the Ge core region. Thermionic barrier height is a key parameter that governs the thermionic emission mechanism, which is calculated by finding the difference between the energy levels. Depending on the core/shell size, the barrier heights for electrons and holes can be varied independently. This tunability nature of the barrier height allows the optimization of the structure by minimizing thermal emission, a fundamental operational requirement for the QD based lasing device

A.1.1 Optical Properties

An intersubband transition in the Ge/Si QD based laser has unique properties such as large dipole moment, relaxation time of nanoseconds, large tunability of the transition wavelength, which are obtained by choosing suitable parameters, such as external field, strain and core-size. With external field set to zero, strain and core-size directly impact the transition energies and oscillator strengths within the active region of the laser.

Momentum Matrix Elements (MME)

Optical momentum matrix for lowest electron state to the first six highest hole states are calculated using Eq. A.1.

$$\|M_{if}\| = \langle \psi_i^*(x,y,z)|e(x,y,z).p|\psi_f(x,y,z)\rangle \tag{A.1}$$

where $\langle \psi_i(x,y,z)$, $|\psi_f(x,y,z)\rangle$, $e(x,y,z)$, and p are the wave functions of initial and final states, the polarization vector, and electron momentum operator, respectively.

Due to the spherical symmetry of QDs, the light polarization along the x-direction is considered. In order to understand the qualitative behavior of the MME, as it ap-

plies to the gain calculation, we consider the quantity $|M^2_{total}|$, which is the modulus squared of the MME summed over degenerate spin states. Fig. A.1 shows the calculated $|M^2_{total}|$ with both the Ge core size and the energy level variation only for the light polarized along the x-direction. Since the shape of the QDs considered here are spherically symmetric, the matrix elements for each light polarized direction (x,y or z) are equivalent. As evident from the Fig. A.1, $|M^2_{total}|$ initially increases with the core size for each transitions before reaching a peak value beyond which it decreases rapidly. The magnitude of the matrix element for smaller core size, when the isotropic strain is applied to the Ge/Si heterostructure QDs, increases by the factor of three because of the increased overlap integral between electrons and holes due to increased quantum confinement effect. However for the larger core size, the strain has no or minimal effect in the matrix element mainly due to the increased localization of the holes in the Ge core region and electrons in the Si shell region.

The oscillator strength (OS_{if}) is also a fundamental, but important, physical parameter during the study of the luminescence properties of any optical device, and are related to the electronic dipole-allowed transition. The concentration of oscillator strength in discrete energy levels of QDs make QDs a promising candidate for electro-optic and nonlinear optical application. The amplitude of the OS depends on the light polarization directions in accordance with the coordinate axes, and should be equal in each direction for the symmetric/spherical QD. Generally, the oscillator strength OS_{if} between initial $|i\rangle$ and final $|f\rangle$ electronic states is defined as,

$$OS_{if} = \frac{2}{m^*_w \hbar \omega_{if}} \|M_{if}\|^2 \tag{A.2}$$

where m^*_w and $\|M_{if}\|$ are the effective mass of the hole in the Ge core region and MME between initial and final electronic states. The m^*_w is approximated using

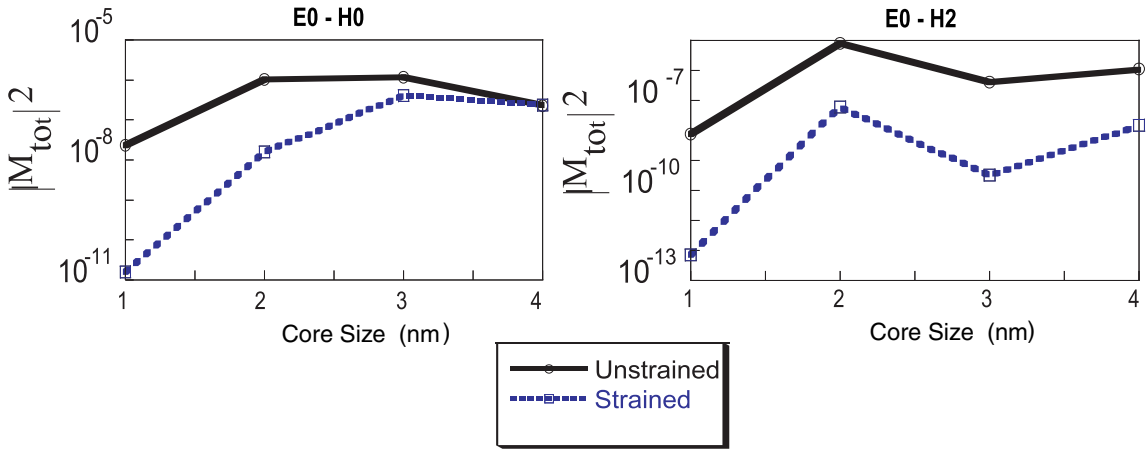

Figure A.1: (Color online) Magnitude of the modulus squared of the optical matrix element $|M_{total}|^2$ plotted against the Ge core size for (a) unstrained and (b) strained case. The units for $|M_{total}|^2$ is given in eV/c, where c is speed of light.

using the expression for the lowest energy level in a three-dimensional box with infinite potential confinement. The $\hbar\omega_{if}$ is the transition energy between initial $|i\rangle$ and final $|f\rangle$ electronic states and defined as, $\hbar\omega_{if} = \Delta E_{if} = E_i - E_f$, where E_i and E_f are the energy levels of the initial and final transitional states. The required photon transition rate (Γ_{if}) between these states are strongly dependent on the MME and $\hbar\omega_{if}$ as follows,

$$\Gamma_{if} = \frac{2\pi}{\hbar}\frac{e^2A^2}{4m_0^2}\|M_{if}\|^2\delta(E_f - E_i + E) \tag{A.3}$$

where e, A, and $\hbar$ are electron charge, vector potential, and reduced Plank's constant, respectively. In a QD laser, the gain is effected by not only the density of states, but also by the amplitude of the optical MME. This reduction leads to the inefficient lasing involving ground states due to the reduced overlap between the hole and electron wave functions. However, recent theoretical studies predicted that the magnitude of the MME could be engineered in order to optimize the optical gain in QD lasers and optical amplifiers

Similarly, achieving low threshold current is one of the fundamental requirements of QD based SCH laser. In this type of laser, carrier leakage processes are shown experimentally as one of the factors contributing to the threshold current and temperature sensitiveness. Higher material gain due to the reduction in the hole-leakage process in the Type-II SCH was reported earlier. In order to analyze the leakage due to the heavy hole escape mechanism in the Ge/Si core-shell QD laser, we calculate the thermionic escape times of holes from the Ge core region. The thermionic emission lifetime (τ^{th}) is determined by the height of the barrier over which the hole is emitted, and it is approximated using the expression derived by Schneider and von Klitzing. The minimal thermionic carrier escape out of the core will lead to an increase in the injection efficiency and the temperature sensitivity. The thermionic leakage current (J_h) from the edge of the single quantum well to either side of the barrier is related to the thermionic emission lifetime (τ_h^{th}) as follows,

$$J_h = \frac{Nq}{\tau_h^{th}} \tag{A.4}$$

where, q, N and τ_h^{th} represent the electron charge, number of hole in the QD, and thermionic emission carrier lifetime, respectively. τ_h^{th} is defined as,

$$\tau_h^{th} = W\sqrt{\frac{2\pi m_w^*}{k_B T}}\exp\left(\frac{\Phi_b}{k_B T}\right) \tag{A.5}$$

where, m_w^* is the effective mass of the hole in the Ge core, k_B is Boltzmann's constant, and Φ_b is the potential barrier height. The potential barrier height is calculated from the energy difference between the localized ground and delocalized state of the hole,

$$\Phi_b = E_0 - E_n. \tag{A.6}$$

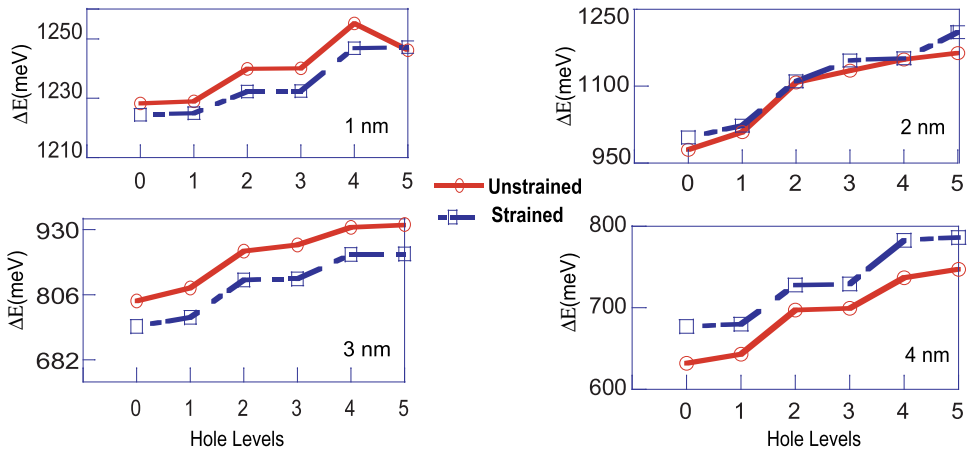

Figure A.2: (Color online) Transition energies (ΔE_{if}), in meV, between lowest electron state and first six highest hole states, as a function of strain and Ge core size (nm), with a fixed Si shell thickness of 5 nm.

where, E_0 is the ground state hole energy and E_n is the highest energy of the hole state that does not exponentially decay in the Si shell, i.e. it is delocalized throughout the Ge/Si NC, where the quantum number n varies depending on the size of the Ge core.

Interband Transition Energies and Rates

The transition energies or photon energies (ΔE) is calculated by taking the difference between eigen energies of corresponding electron and hole states. The photon energies emitted by the lowest electron state during the transition to the first six highest hole states is plotted in Fig. A.2. The strain, as expected, shifts the hole energy states by reducing the required emitted photon energies. Eventually, when the core-size increases beyond the 3 nm, bulk-like behavior becomes dominant and required transition energies decreases with increasing core-size. This behavior is consistent with the predicted behavior for the infinite potential well system. Similarly, the interband transition rate (Γ_{if}) between electron and hole states is calculated using the

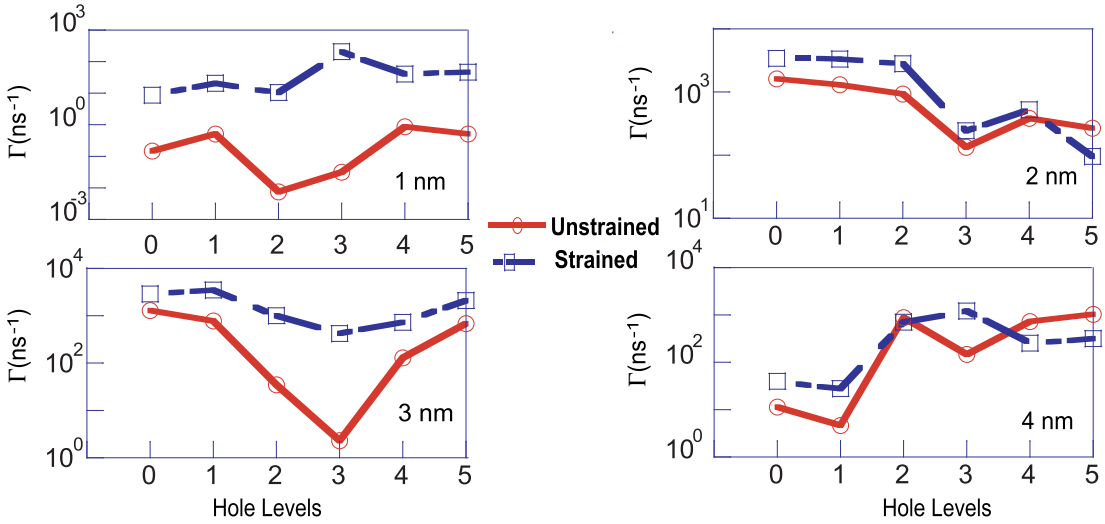

Figure A.3: (Color online) Transition rates between lowest electron level and first six highest holes states, as a function of strain and the Ge core size (nm) with a fixed 5 nm Si shell.

modulus squared of the optical matrix element of electron and hole states transition summed over the degenerate spin states using the Eq. A.3 and plotted in Fig. A.3. For all the core sizes, the transition rate between lowest electron state and first hole state, Γ_{01}, is faster than the unstrained counterparts, mainly due to the observed shifting of the hole energy states. Similarly, the observed transition rate (Γ_{01}) for the QD with 1 nm core size is few orders of magnitude faster than that of QD with 4 nm core size owing it to the increased transition energy (ΔE_{01}) due to quantum confinement effect.

Oscillator Strength

The oscillator strength for the transition between lowest electron state ground state electron to the first five highest hole states as a function of strain and Ge core size is calculated using Eq. A.2. Fig. A.4 shows the oscillator strength, OS_{if}, for a range of Ge core size from 1 nm to 4 nm for light polarized in the x-direction. The

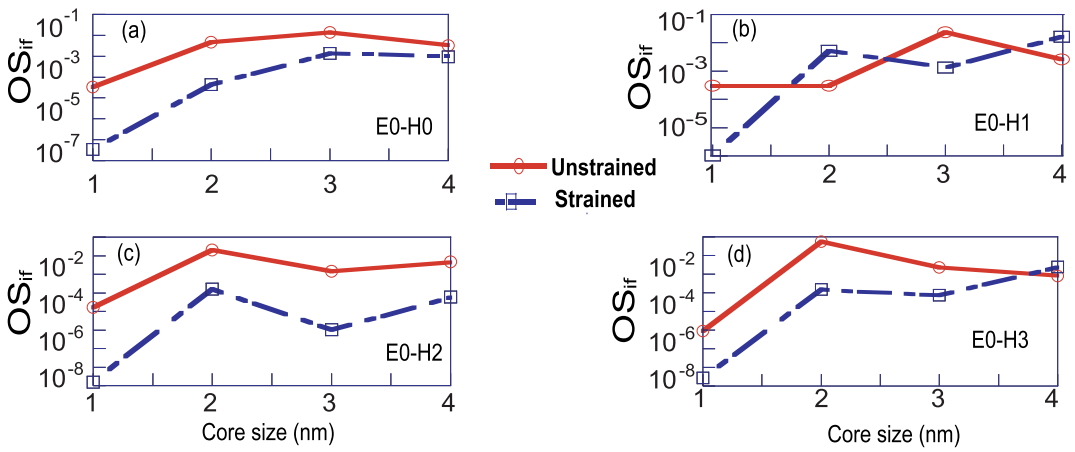

Figure A.4: (Color online) Magnitude of Oscillator strength (OS_{if}) as a function of Ge core size and strain for the lowest electron state (E0) to a)Hole ground state (H0) b) First hole state (H1) c) Second hole state (H2), and d) Third hole state (H3).

oscillator strength mainly depends on two parameters: energy difference ($\hbar\omega$) and the momentum matrix element (MME) between initial and final states. As can be seen in Fig. A.4(a), the oscillator strength increases with the core size and reaches maximum values at 3 nm, and it reaches a characteristics constant value beyond the Ge core size of 3 nm for both strained and unstrained conditions. In small Ge core size, the energy difference ($\hbar\omega$) between lowest electron state(E0) and hole ground state(H0) is high, the overlapping between the electron and hole wavefunctions is small, i.e. the momentum matrix element ($\|M\|^2$) is small. When the Ge core size increases, the $\|M\|^2$ increases, while the energy difference ($\hbar\omega$) decreases. However, the overall effect remains constant, and hence the OS_{if} remains constant. This size dependent characteristic for OS_{if} is in good agreement with other published theoretical and experimental results for other materials.

Thermionic Hole Lifetime and Leakage Current

The thermionic lifetime (τ_h^{th}) due to the thermionic emission from the Ge/Si QD as SCH laser is calculated for Ge core size of 1 to 4 nm, using Eq. A.5. The thermionic lifetime dependence on the temperature, core size, and strain is illustrated in Fig. A.5(a, b). At smaller Ge core sizes, the thermal energy is much larger than the barrier height and hence, the lifetimes remain constant through out the analyzed temperature range. In addition, the strain has little impact on lifetime and carrier densities due to the small number of Ge atoms. However at the larger Ge core sizes, the lifetimes shows exponential decay behavior because barrier height is much larger than the thermal energies at different temperatures. Since the energy barrier height increases with the core size, the lifetimes at room temperature, varies by several orders of magnitude with the core size. When strain is applied, the thermionic lifetime increases by an order of magnitude, owing it to the valence band shift due to the applied isotropic strain.

Furthermore, the thermal leakage current (J_h), which is inversely proportional to the thermionic lifetime, is calculated using Eq. A.4, by assuming number of hole(N) in the QD as 1. The thermionic current dependence on the temperature, core size, and strain is illustrated in Fig. A.5(c, d). The J_h shows the exponential dependence on increasing core size. Due to the significantly smaller τ_h^{th}(1 picosecond) at room temperature, the J_h for 2 nm core size, for unstrained QD, is around 10 *picoAmpere*. However, when strain is applied, the J_h decreases by three orders of magnitude. For the temperature beyond room temperature, the thermal energies become larger than the energy barriers and hence, J_h is linear and constant.

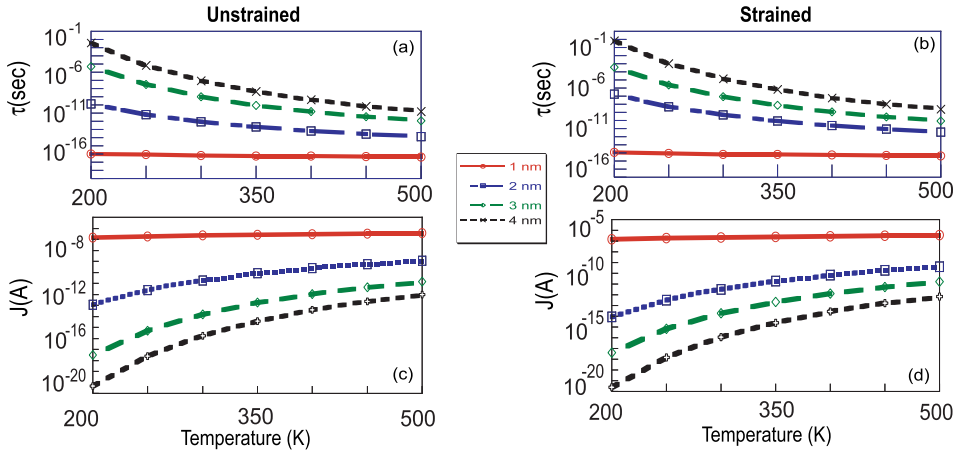

Figure A.5: (Color online) Lifetimes (a,b) and Current Densities (c,d) as a function of core size and temperature for both unstrained (left) and strained (right) conditions.

A.2 Conclusion

The electronic properties of Ge-core/Si-shell NCs are calculated for a fixed 5 nm Si shell and Ge-core ranging from 1 nm - 4 nm in diameter. Electronic calculations are performed atomistically using a nearest-neighbor, $sp^3d^5s^*$ tight-binding model as implemented in NEMO3D, with and without strain. The electron-hole wavefunctions and wave vectors are then used to calculate momentum matrix element, oscillator strength, transition rates using Fermi's Golden rule. The momentum matrix elements, transition energies and transition rates between lowest electron state and highest hole state are linearly dependent with the core-size and strain. The oscillator strength shows the exponential dependence on the smaller core sizes ($\leq$3 nm) and strain due to the prominent quantum confinement effect. However for the larger core size ($\geq$3 nm), the exponential dependence vanishes because of nominal quantum confinement effect.

The calculated thermionic lifetime and leakage current shows exponential dependence with the fundamental design parameters such as, temperature, core-size and

strain. At room temperature, the thermionic leakage current reduces by five orders of magnitude when the core size is increased from 2 nm to 4 nm, for both strained and unstrained conditions. Therefore, a careful modulation of these design parameters will lead to the low leakage current and hence, threshold current density during lasing operation.

Appendix B

Capping and core layer-dependent carrier dynamics on Ge/Si NC memory

B.1 Introduction and Motivation

Nonvolatile memory devices based on Ge/Si core-shell nanocrystals (NCs) [23], have attracted attention due to their ability to handle the trade-off between the programming speed and the retention time by minimizing tunnel oxide thickness. Recently, several experimental groups have highlighted the effect of Si-cap (Ge-core) thickness and overall size distribution of Ge/Si dome shaped structure on various device parameters, including retention lifetime of the charge (hole) [28]. Theoretical groups tried to analyze the effect of confinement on these structures using effective mass and pseudopotential methods by assuming bulk band alignment and valence band offset between the Ge and Si region. To understand the effect of capping and core layer thickness on the electronic structure, carrier lifetimes, and other operating parame-

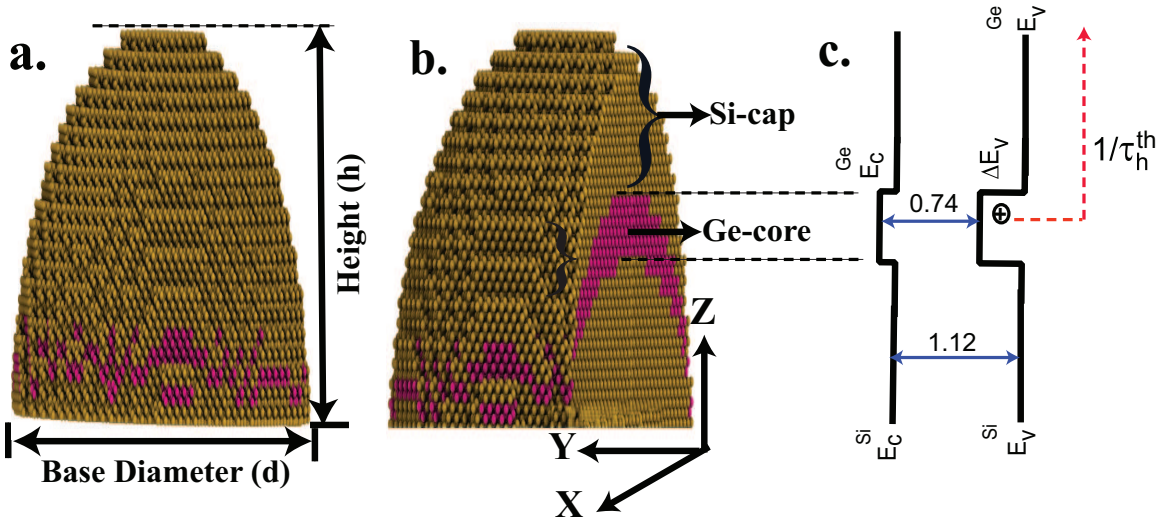

Figure B.1: (Color online) Front-view (a) and cross-sectional-view (b) of a dome-shaped Ge/Si NC with a Ge-core and Si-cap thickness of 3nm. The base diameter and the inner Si layer height is maintained at 5nm. The lighter gray (red) dots are Ge atoms and the darker (yellow) dots are Si atoms. (c) Bulk energy level lineups. The energy values shown correspond to the band gap of the bulk Si and Ge materials. The valence and conduction band edges for the Ge and Si materials are labeled as E_V^{Ge} and E_V^{Si}, E_C^{Ge} and E_C^{Si}, respectively. Similarly, the valence band offset is identified as ΔE_V. The dotted arrow shows the thermionic hole escape mechanism with an escape rate of $1/\tau^{th}$.

ters of these NCs, a detailed atomistic model is necessary to capture the atomic scale inhomogeneities of the devices. Often, atomistic models of the NCs are severely size-limited, hindering a direct comparison of simulations with the experimental devices.

B.2 Model and Methods

In this work, we carry out a computational study of the low-energy electronic states in dome-shaped Ge/Si core shell NCs using a full-band, $sp^3d^5s^*$ nearest neighbour empirical-tight-binding model including spin-orbit (SO) coupling as implemented in NEMO3D [115]. The front and dissected views of simulated NC model is shown in the Fig. ??.a. The strain due to the lattice mismatch between Ge and Si is

calculated using the valence-force-field (VFF) model with Keating Potentials. The energy difference between the ground and excited first delocalized hole state is defined as the barrier height (ϕ_b). ϕ_b is calculated by analyzing probability densities ($|\psi|^2$) of these states in the Ge core layer obtained from the tight-binding method. Using these barrier heights, the thermionic lifetimes (τ) that govern the overall retention characteristics are calculated as a function of capping layer and core layer thickness. In doing so, the height of the dome shaped QD is varied from 6.5 nm to 10 nm. The base size of the NC is maintained at 5 nm.

B.3 Results and Discussion

The energy gap (E_g) decreases from 1.125 eV for the 0.5 nm Ge core thickness and reached the bulk Ge bandgap value of 0.7 eV for 3 nm Ge core thickness. This reduction in the energy gap is mainly attributed to the increasing hole energy levels, where the electron energy levels remain unchanged. This behaviour is attributed to the TYPE-II band line up as shown in Fig. **??**.c In these systems, as shown in Fig. B.2, quantum confinement energy (E_c) and the effective mass of the hole also show a strong dependency on the Ge core thickness, consistent with that found in other theoretical work [2, 3, 77, 163]. However, the effect of the capping layer thickness on these parameters is negligible. Similarly, the barrier heights and the thermionic lifetimes demonstrate a strong dependence on the core thickness. As illustrated in Fig. B.3.c, the lifetime reaches desirable lifetime of few microseconds when the Ge core thickness increases beyond 2 nm.

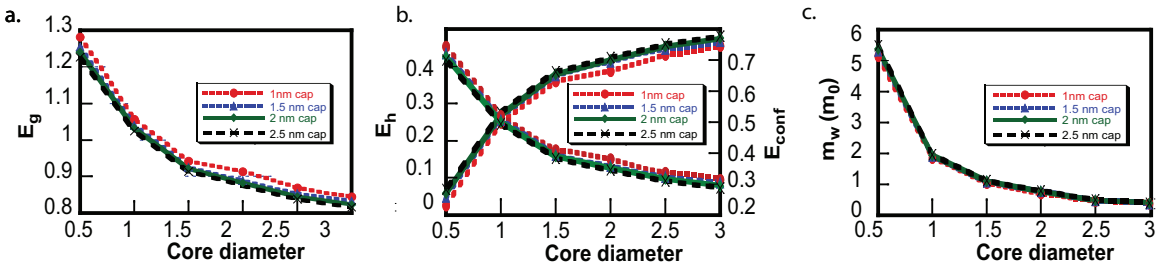

Figure B.2: (Color online)(a) Minimum energy gap (E_g) as a function of as a function of Ge core and Si cap thickness. (b) Ground state hole energy (E_h) and Confinement energy (E_c) as a function of Ge core and Si cap thickness. The confinement energy (E_c) is defined as $E_c = E_v$ (Ge) - E_h, where E_v (Ge) is the bulk valence band edge of Ge. (c) Effective mass of hole inside the Ge core layer.

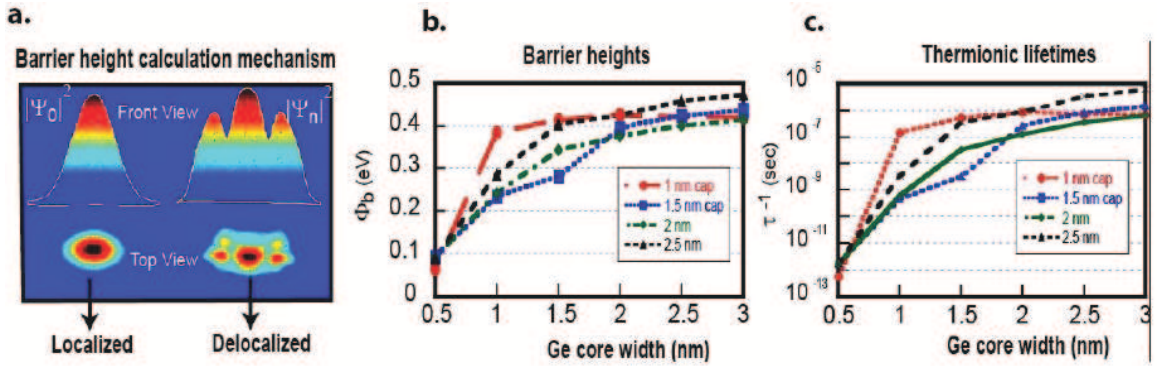

Figure B.3: (Color online) (a) Probability densities ($|\psi|^2$) of localized and first delocalized hole states in the Ge core layer of a dome shaped Ge/Si core shell NC with Ge core and Si cap thicknesses of 3 nm and 2.5 nm, respectively. The n in the delocalized probability density represents the index of the first delocalized hole state. (b) The barrier height (ϕ_b) i.e. E_0 E_n, where E_0 is the ground state hole energy and En is the energy of the first delocalized hole states, as a function of Ge core and Si cap thickness.(c) Thermionic lifetime as function of Ge core and Si cap thickness

B.4 Conclusion

In conclusion, we have performed a comprehensive study on the effect of varying Si capping and Ge core layers on the carrier dynamics of the dome shaped Ge/Si core shell NCs using the atomistic tight-binding method including strain using the VFF model. Various carrier dynamic related parameters, such as confinement energies, bandgap, and effective masses, were also analyzed and these parameters match closely with the experimental measurements and follow intuition, showing that atomistic details of the devices are crucial to fully understand these devices. Our study also finds that the Ge core layer thickness dominates the carrier dynamics over the Si capping thickness, providing optimized design parameters for the devices.